An Investigation of Extraocular and Intraocular Wireless Communication Techniques on a Retinal Prosthesis System

Hans Permana

Doctor of Philosophy

2013

RMIT

An Investigation of Extraocular and Intraocular Wireless Communication Techniques on a Retinal Prosthesis System

A dissertation submitted in fulfilment of the requirements for the Doctor of Philosophy

Hans Permana
B.Eng, Hons

School of Electrical and Computer Engineering
College of Science, Engineering, and Health
RMIT University
April 2013

Genius is 1% inspiration and 99% perspiration…

- Thomas Alva Edison

Declaration

I certify that except where due acknowledgement has been made, the work is that of the author alone; the work has not been submitted previously, in whole or in part, to qualify for any other academic award; the content of the thesis is the result of work which has been carried out since the official commencement date of the approved research program; and, any editorial work, paid or unpaid, carried out by a third party is acknowledged.

Hans Permana

12 April 2013

Acknowledgement

First and foremost, this thesis would not have been possible without the continuous supports of people around me, of whom only a few can be specifically mentioned here.

I would like to express my most sincere appreciation to my primary supervisor, ***Dr. John Fang***, who had always been supportive from the moment I decided to do a PhD, right until the writing of my thesis. With his patience and understanding, he guided me in finishing my candidature according to schedule. I would also like to thank ***Dr. Wayne Rowe*** for his expertise in the antenna design process. Thank you for your time in sharing your extensive knowledge and experience, also for your comments about my antenna experiments. Without his help, my candidature would not have reached up to this level. I also owe sincere and earnest thankfulness to ***Prof. Irena Cosic***, whom at my early days of my candidature had been source of inspiration as well as motivation in pursuing my degree.

Mr. David Welch, one of the Technical Officers in RMIT University, has provided me tremendous assistance with his kind and patient nature throughout my research. He has particularly managed the fabrication of the antennas, organized the anechoic chamber availability, as well as provided countless feedbacks on the antenna design with his vast knowledge and experience.

This is also a great opportunity for me to express my deepest gratitude to my girlfriend, ***Ms. Aurelia Trisliana***, for her day to day support and motivation and also to ***my parents*** and ***my little sister*** who had been behind my back from the day one of my candidature. Without them, I would not have been strong enough to hurdle all the obstacles until the finish line.

I would like to acknowledge the financial, academic, and technical support of ***RMIT University***, Melbourne, Australia. I am pleased to thank the university especially for the RMIT PhD Scholarship that was awarded to me to provide financial aid in this research. Also, my appreciation goes to two separate travel grants from the university, which allowed me to attend two big conferences in San Diego and Tainan and to present my work there while at the same time gaining more new information that undoubtedly enriched my knowledge.

I would like to express my sincere gratitude on the generosity of ***Mr. Chris Zombolas*** and ***Mr. Peter Jakubiec*** from EMC Technologies, Melbourne, Victoria, Australia, for

assisting this project by supplying Vitreous Humour mimicking fluid. The fluid was indispensable in the measurement process in this research.

Mr. Charan Shah, a fellow PhD candidate, also deserved a mention in this section due to his kind assistance in developing a Polydimethylsiloxane (PDMS) encapsulation for my antenna as well as in sharing his expertise about the material.

Mr. Zhe Zhang, another fellow PhD candidate, has been a great company since he started his candidature. Thank you for wonderful time together in the lab, in the office, in the staff room, or during the usual Friday lunch at Rose Garden, which were always very refreshing and enjoyable.

Last but not least, I would like to thank all my colleagues, who at any stage of my researches had provided some assistance to me, whether just by being a listener to me or as someone who provided my some useful information. I wish you all the best towards the completion of your candidatures.

Table of Contents

List of Tables

List of Figures

Abbreviations

WHO	: World Health Organization
AMD	: Age-related Macular Degeneration
RP	: Retinitis Pigmentosa
LGN	: Lateral Geniculate Nucleus
SAR	: Specific Absorption Rate
HFSS	: High Frequency Structure Simulator
FDA	: Food and Drug Administration
MRI	: Magnetic Resonance Imaging
RPE	: Retinal Pigment Epithelium
NLM	: National Library of Medicine
FDTD	: Finite Difference Time Domain
VPU	: Video Processing Unit
PFM	: Pulse Frequency Modulator
STS	: Suprachoroidal Transretinal Stimulation
EEP	: Electrically Evoked Potential
CT	: Computer Tomography
ASIC	: Application Specific Integrated Circuit
OIS	: Optical imaging of Intrinsic Signals
PI	: Phosphene Image
IBSN	: Implantable Body Sensor Network
HF	: High Frequency
MICS	: Medical Implant Communication Service
ISM	: Industrial Scientific and Medical
FCC	: Federal Communications Commission
ICNIRP	: International Commission on Non-Ionizing Radiation Protection
ASK	: Amplitude Shift Keying
PWM	: Pulse-Width Modulation
CMOS	: Complimentary Metal-oxide Semiconductor
EMF	: Electromagnetic Field
RFID	: Radio Frequency Identification
NFC	: Near Field Communication

GSM : Global System for Mobile Communications

CST : Computer Simulation Technology

PIFA : Planar Inverted-f Antenna

CSF : Cerebro Spinal Fluid

FIT : Finite Integration Technique

GPS : Global Positioning System

ZOR : Zeroth-order Resonance

DC : Direct Current

RCS : Radar Cross Section

FEM : Finite Element Method

LCP : Liquid Crystal Polymer

PDMS : Polydimethylsiloxane

PCB : Printed Circuit Board

MMTC : Microelectronics and Materials Technology Centre

AUT : Antenna under Test

Abstract

Retinitis Pigmentosa (RP) and Age-related Macular Degeneration (AMD) are two genetic ocular diseases that cause gradual visual impairments which will eventually lead to blindness as a result of damage in the retina. In the cases of people suffering from RP and AMD, it has been found out that 95% of the photoreceptors are damaged, while interestingly majority of the bipolar and ganglion cells that are responsible for the nerve stimulation remain intact. This is where a retinal prosthesis system comes into the picture. Retinal prosthesis is a prosthetic device that is aimed to assume the functionality of the damaged photoreceptors and produce stimulations to the bipolar and ganglion cells for a visual perception. Typically, a retinal prosthesis system comprises of two major components: an image capturing unit and an array of microelectrode. While a lot of studies have been conducted on each major component, the development of the wireless link between the two components has been mostly overlooked. It is clear that the two components are not physically connected and a data exchange is required between the two. This thesis aims to bridge the knowledge gap in this area by addressing the following research questions: "What is the most suitable frequency band for a wireless link in a retinal prosthesis system?" and "What kind of antenna would generate the most optimal performance under the constraints introduced by a retinal prosthesis system?"

The study was initiated by a literature review on the latest system design of retinal prosthesis as well as a review on other implantable antennas to gain knowledge on the typical performance of similar antennas. It was followed by a comparison of various frequency bands based on bandwidth, possible external interference, antenna size, as well as Specific Absorption Rate (SAR) values to find the best match for a retinal prosthesis system. The selected frequency band was employed as the solution frequency in the antenna design and simulation process in High Frequency Structure Simulator (HFSS) software. A set of optimisation techniques was applied to the antenna to achieve a certain level of performance. The resulting antenna was fabricated and measured to obtain three different parameters: return loss, radiation, and gain. At the end of the thesis, the data collected from both simulation and measurement was analysed and the performance of the antenna was finalised. The discrepancies on the results were discussed and an explanation was given as the response. Potential future works as a continuation of this study were also presented at the end of this dissertation.

List of Publication

Following is the list of papers that have been submitted or accepted during the candidature period (the newest first):

- **Permana, H**., Fang, Q., Lee, S.Y., "*Comparison study on specific absorption rate of three implantable antennas designed for retinal prosthesis systems*"
  Published in IET Microwaves, Antennas & Propagation, Vol. 7, Issue 11, pp. 1-8, 2013.

- **Permana, H**., Fang, Q., Lee, S.Y., "*A microstrip antenna designed for implantable body sensor network*"
  Published in ICOT 2013 – 1st International Conference on Orange Technologies, art. no. 6521168, pp. 103-106.

- **Permana, H**., Fang, Q., Rowe, W.S.T., "*Hermetic implantable antenna inside vitreous humour simulating fluid*"
  Published in Progress In Electromagnetic Research, Vol. 133, 591-605, 2013.

- **Permana, H**., Fang, Q., Rowe, W.S.T., "*Implantable Multilayer Microstrip Antenna for Retinal Prosthesis: Antenna Testing*"
  Published in Proceedings of the Annual International Conference of the IEEE Engineering in Medicine and Biology Society, EMBS, art. no. 6346270 , pp. 1679-1682.

- **Permana, H**., Fang, Q., Cosic, I., "*3-layer Implantable Microstrip Antenna Optimised for Retinal Prosthesis System in MICS Band*"
  Published in Proceedings of 2011 International Symposium on Bioelectronics and Bioinformatics, ISBB 2011, art. no. 6107646 , pp. 65-68.

- Fang, Q., Lee, S.Y., **Permana, H**., Ghorbani, K., Cosic, I., "*Developing a Wireless Implantable Body Sensor Network in MICS Band*"
  Published in IEEE Transactions on Information Technology in Biomedicine vol.15 no.4 page 567-576.

- **Permana, H**., Fang, Q., Cosic, I., " *Simulation of EMF Absorption on Human Head at 402 MHz, 900 MHz, and 2.4 GHz*"
  Accepted for International Symposium on Bioelectronics and Bioinformatics in Melbourne, Australia, 9-11 December 2009.

Chapter 1
Introduction

1.1. Background

Based on a research conducted by World Health Organization (WHO), Age-related Macular Degeneration (AMD) ranked third as the cause of blindness worldwide, with a prevalence of 8.7% [1]. Retinitis Pigmentosa (RP), on the other hand, has an incidence of 1 in 4000 people worldwide [2], while the number varies in different races like Navajo Indians (1 in 1800) [3]. Both diseases are predicted to burden the government with a US$ 75-833 million annually [4]. Without proper solution, these problems will deliver a massive hit to the health bill, money which could be better spent elsewhere. The first step to achieve a concrete solution is to fully understand the diseases. What are AMD and RP? What are the causes and which technologies may provide a solid answer to resolve these problems?

AMD and RP are both genetic diseases that cause gradual visual impairments as a result of damage in the retina [2, 5]. In the case of AMD, the symptom starts with what looks like a small mark at the central vision, which grows progressively until the subject's vision is completely blocked. In RP, peripheral vision lost is common as an early symptom and it eventually leads to a permanent loss of the central vision. To gain an insight on how the diseases affect the visual recognition, one has to understand the light perception process inside the human eye. The light perception process involves retina, optic nerve, optic chiasm, optic tract, Lateral Geniculate Nucleus (LGN), optic radiations, and striate cortex [6]. The light comes into the eyeball and through to the retina layer, in which it will be detected by photoreceptors [7]. The photoreceptors convert light energy into a neuronal signal that is passed to the bipolar cell and the amacrine cell, and then to the ganglion cell. The signal is then transmitted to the optic nerve and is subsequently passed onto the brain [6]. In the case of people who suffer from AMD and RP, it was found out that at the later stage of the disease, up to 95% of the photoreceptors are damaged, which means the majority of incoming lights could not be detected [8]. The study also revealed that in most of the cases, the bipolar and ganglion cells, which are responsible for the nerve stimulation,

have remained intact. This is where a technology can be proposed to provide a solution to both diseases.

Retinal prosthesis is a prosthetic device aimed at helping to partially restore the vision of people who suffer RP and AMD by either bypassing or replacing the function of the defective photoreceptors and creating stimulation to the neurons. Although there are different types of the systems, a retinal prosthesis system basically comprises of two components: an image capturing unit and an array of microelectrode. The positioning of the latter component with respect to the retinal layer is what differentiates one type to another. With the assistance of this system, patients would be able to recognize nearby objects by detecting the reflection of the objects' edges. A preliminary study has revealed that such system would allow patients to perform a cutting task, a pouring task, a reading task, and a symbol recognition task [9]. The benefit that would be generated by such a system is clearly significant.

Currently there are several research groups who are working on a retinal prosthesis system development with their own distinct approaches. Second Sight group, Sylmar, USA, has been developing an epiretinal prosthesis, a kind of retinal prosthesis system in which the electrode array is attached on the inner layer of the retina, with an emphasize on the electrode material, the phosphene shapes in relation to the stimulation amplitude, the possible thermal elevation caused by the system, as well as the wireless link that connects the extraocular and intraocular components [10-18]. Clinical trials have also been conducted by this company. Another group is from Nara, Japan, and the prominent feature of this study has been in the photosensor design, which can be applied in both epiretinal and subretinal system [20-25]. In contrary to the epiretinal system, subretinal prosthesis is a retinal prosthesis system where the electrode array placement is at the outer layer of the human retina. The system has been tested inside rabbits' eyes. There is also collaboration between University of New South Wales and Bionic Vision Australia, Australia, in an attempt to build a retinal prosthesis system. This group has done rigorous studies on the neurophysiology aspect to gain the knowledge of the biological response to the implanted device. Several testings have been conducted *in vivo* using cats [26].

The previous paragraphs showcased the development of retinal prosthesis systems by three leading groups of researchers. There has been plenty of coverage on the photosensors, microelectrode arrays, tissue behaviour post-implantation, the material selection, or the manufacturing technique of the system. However, one issue is seemingly overlooked: the wireless link between the extraocular and the intraocular components. It is

clear that the two major components of the system cannot be physically connected and there has to be a data communication between the two. The lack of studies in this area raises questions such as “what frequency should the data be modulated in?” or “how big is the antenna?” or “what type of the antenna is the most suitable for the system?” or “will the transmission be the same as a free space transmission?”. These are the questions that fundamentally motivated this research.

1.2. Rationale

The rationale of this research was to obtain an answer to these two research questions: “what is the most suitable frequency band for a wireless link in a retinal prosthesis system?” and “what kind of antenna would generate the most optimal performance under the constraints introduced by a retinal prosthesis system?”. In order to answer these two questions, the following research framework is proposed. The research was initiated by the frequency band analysis in order to determine the most optimal frequency range for the wireless communication link of the system. This was implemented by designing an antenna for three different frequency bands and observation of its performance and characteristic in terms of maximum allowable bandwidth, ideal antenna aperture, as well as the maximum specific absorption rate (SAR) value. The fundamental design of the antennas was based on the antenna designs that had been published in literatures with some adjustments to achieve optimal performance at the desired frequency band. The whole process would be discussed comprehensively in Chapter 3 of this dissertation. After a series of evaluations, a frequency band was selected for the operation of the wireless communication link of the system. The next step of this research was the design of the implantable antenna to be operated inside the eyeball at the selected frequency band. This process involved the development of the antenna based on experimental approach with the aid of High Frequency Structure Simulator (HFSS) simulation software. The antenna underwent various modifications in order to achieve the most optimal performance. Once a simulation produced a satisfying result, the antenna was fabricated for the data validation. The study was concluded by a discussion on the discrepancies between the simulation and the measurement as well as an observation on how the antenna performed in comparison to other implantable antennas.

1.3. Thesis Organization

This thesis investigates the realization of an implantable antenna for an operation inside Vitreous Humour liquid, which resembles its operation in a retinal prosthesis system. An introduction about a retinal prosthesis system is presented in Chapter 2 of this thesis. A rationale behind a retinal prosthesis system is stated at the beginning of the chapter, followed by the information on the system mechanism. Current technologies on the system as well as the wireless communication components are also covered to conclude the chapter. Chapter 3 explores possible frequency bands for an optimal implementation of wireless communication link in the retinal prosthesis system. A selection process based on multiple aspects such as bandwidth, possible external interference, antenna size, as well as SAR values, is presented in this chapter. At the end of the chapter, the most suitable frequency band is selected to bring the project to the next step, antenna design. Chapter 4 explores the basic principle of an antenna as well as its operation in free space and in a high dielectric and conductive medium. Past literatures about implantable antenna designs are brought into the picture as a basic reference for the current design. At the end of this chapter, the process of the antenna design is initialized, starting with the constraints encountered by the antenna, the antenna model selection, as well as the miniaturization of the antenna. The last part of this Section shows the final antenna design for this project. In Chapter 5, the simulation aspect of the project is showcased. A selection of numerical solver tool for solving Maxwell's Equations associated with the antenna design is presented, followed by the design procedure using HFSS software. The chapter also discloses the simulation results of the final antenna design after a series of optimisation process. The manufacturing process of the antenna is demonstrated in Chapter 6 as part of measurement process. The measurement in two different conditions, free space and inside Vitreous Humour liquid is conducted and the antenna performance is presented in three different parameters: return loss, radiation pattern, and gain. The configuration for each measurement is also covered in this chapter. Chapter 7 summarizes the simulation and measurement results and includes analyses on the resulting antenna performance. Discrepancies are identified and discussed for a more comprehensive knowledge about the behaviour of the antenna. At the end, the antenna is compared against previously designed antennas to observe the actual level of the antenna performance. In Chapter 8, a derivative study of this research in the implantable antenna design for an Implantable Body Sensor Network (IBSN) is presented. It covers the antenna design as well as the simulation and

measurement results of the antenna. Chapter 9 concludes the thesis by signifying the major findings in this project as well as possible future works as a continuation of this study.

Chapter 2
Retinal Prosthesis

In this chapter, the introduction to a retinal prosthesis system would be covered extensively. A number of important facts will provide the readers an interesting perspective on the essentiality of the system. Subsequently, the mechanism of the system will be explained, including what significance it would bring to the prospective users. This information would provide a thorough introduction to the core part of this chapter, a compilation of current technologies developed by several leading researchers on the field. This Section would allow the reader to have an insight on various types of the system, in which this thesis will be focused on. Ultimately, at the latter part of this chapter, the attention will be intensified on the wireless communication components of the system, which is specifically narrowed down to implantable antennas. A short review on existing wireless communication techniques for other medical purpose implantable systems will provide a useful idea on the design procedure of the retinal prosthesis system.

2. 1. Overview

2. 1. 1. Background

Retinitis Pigmentosa (RP) and Age-related Macular Degeneration (AMD) are two major ocular diseases that are genetically inherited. RP is a form of visual impairment as a result of degenerative retinal cells, which initially impacts the peripheral vision of the patient progressively and it eventually leads to a permanent loss of the central vision (Figure 2.1a) [27]. The prevalence of RP is 1 in 4000 people worldwide [2]. AMD is another disease caused by defective retinal cell and it is marked by a symptom of progressive worsening of central vision with distortion of straight lines or a dark patch in the central vision, or both (Figure 2.1c) [28].

According to World Health Organisation (WHO), AMD is the third greatest cause of visual impairment with blindness prevalence of 8.7% [1]. On 2000, AMD was estimated to affect 1.75 million people over 40 years old in USA, and was predicted to increase by 71%

by 2020 [29] and approximately 10 times by the year of 2050 [30] with total annual direct cost of US$ 75-733 million [4]. Without a proper solution, RP and AMD could become a big financial burden worldwide in the future.

(a) (b) (c)

Figure 2.1. The visual perception of (a) people suffering from RP, (b) normal people, and (c) people suffering from AMD.

2. 1. 2. Human Eyeball Anatomy

A human eyeball has an average diameter of 25 mm and it comprises of cornea, iris, lens, vitreous body, and retina, along with many more minor components (Figure 2.2).

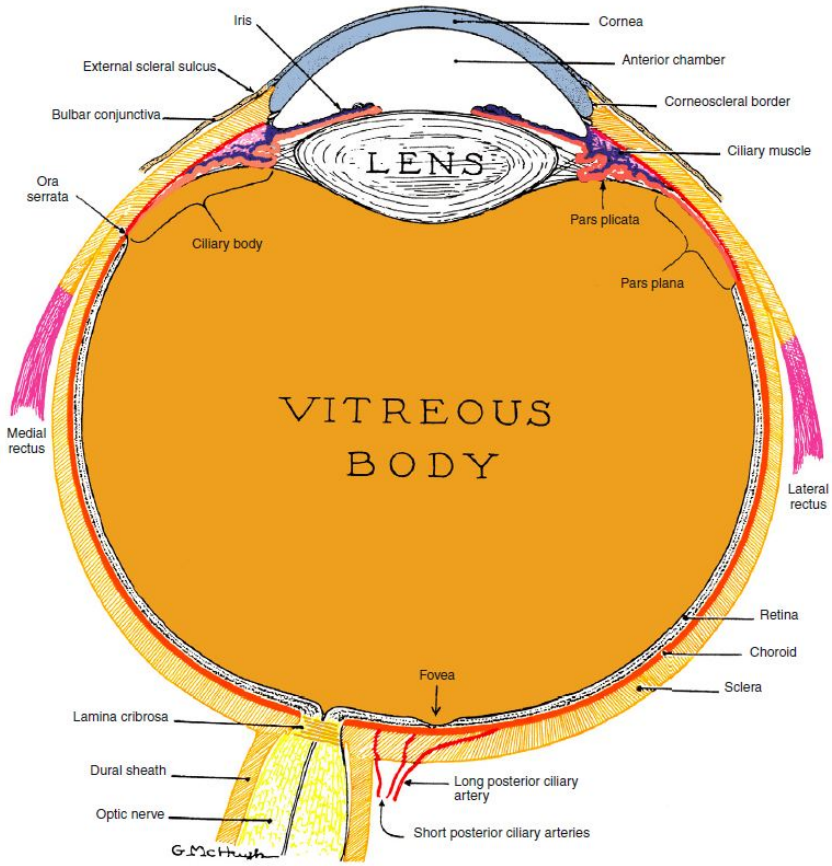

Figure 2.2. Human eyeball anatomy (from Kronfeld PC: *The human eye*, Rochester, NY, 1943, Bausch & Lomb Press).

From the eyeball diagram, it is clear that Vitreous cavity forms majority of the eyeball. It is filled with clear fluid called Vitreous Humour, which is composed of 99% physiological saline and 1% hylaruonic acid [6, 31]. When a foreign object is inserted into the cavity, a portion of the fluid has to be removed, which can be done with a vitrectomy procedure [32]. The volume of the removed fluid should be equivalent to the object's volume.

The light perception process involves retina, optic nerve, optic chiasm, optic tract, Lateral Geniculate Nucleus (LGN), optic radiations, and striate cortex [6]. The light comes into the eyeball and through to the retina layer, in which it will be detected by photoreceptors (Figure 2.3) [7]. The photoreceptors convert light energy into a neuronal signal that is passed to the bipolar amacrine cell, and then to the ganglion cell. The signal is subsequently transmitted to the optic nerve and is ultimately passed onto the brain [6].

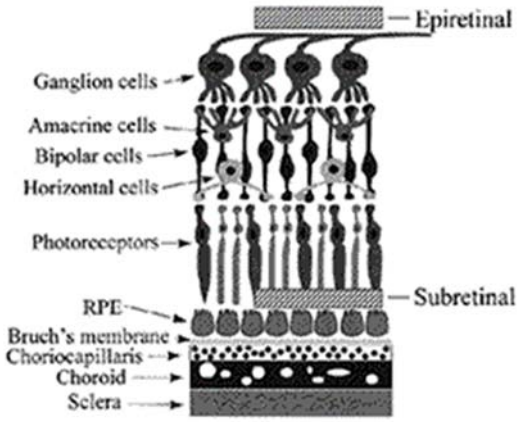

Figure 2.3. Retinal layer anatomy, signifying the subretinal and epiretinal side of the layer (Peachey, N. S., 1999).

In the case of people who suffer RP and AMD, it was found out that up to 95% of the photoreceptors are damaged, which means the majority of incoming lights could not be detected [8]. Interestingly, the study also revealed that in most of the cases, the bipolar and ganglion cells, responsible for the nerve stimulation, remain undamaged [33]. This brings the idea of a retinal prosthesis system, where it will function as a replacement of the damaged photoreceptors in detecting the inbound light wave and will eventually produce stimulations to the bipolar and ganglion cells for visual perception.

2. 2. Retinal Prosthesis

2. 2. 1. What is Retinal Prosthesis?

Retinal prosthesis is a prosthetic device aimed at helping to restore partial vision of people who suffer from RP and AMD by either bypassing or replacing the function of the defective photoreceptors and creating stimulation to the neurons. Based on the electrode placement, there are several variations of retinal prosthesis system: suprachoroidal retinal prosthesis, subretinal prosthesis, as well as epiretinal prosthesis [31]. By looking at the retina layer diagram (Figure 2.3), it is easier to comprehend the basic idea of where the stimulators are located for each system. The ***suprachoroidal*** type is an approach of a retinal prosthesis system by placing the stimulator on the choroidal pocket of the eyeball.

In ***subretinal*** prosthesis system, a set of electrode arrays are attached to the retinal layer from the outer side. It means the whole set of circuitry is attached to the outermost layer of the eyeball, which is called sclera (Figure 2.4). The advantages of this approach include good biocompatibility, simpler non-invasive surgical procedure, as well as more flexibility to the size of the implant [34]. However, the down side of this technique is the inability to adjust the stimulation parameters such as amplitude, duration, and frequency. Moreover, only lights with an adequate energy level can be detected and converted effectively into stimulation impulses [35, 36]. Hence, the device must have an internal power supply to amplify the weak incoming lights. One prominent group of researchers

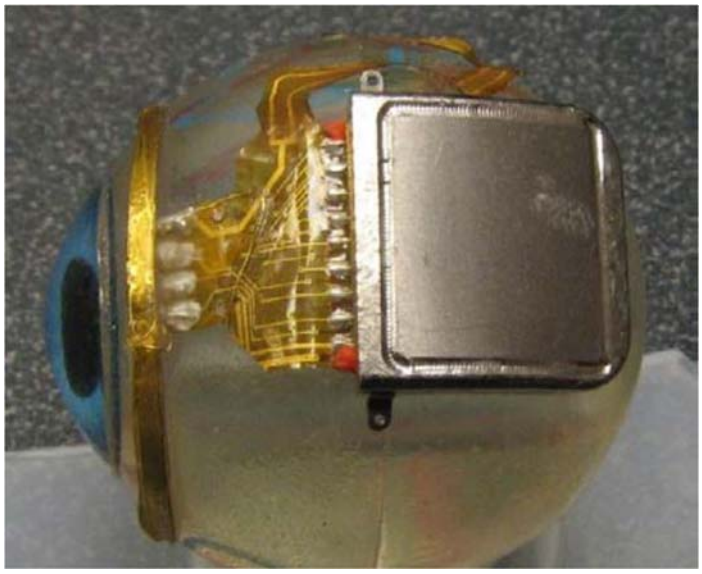

Figure 2.4. The placement of subretinal implant in regards to the eyeball. Inside the titanium case are the electrode array and the gold coil is responsible for the data and power transfer (Kelly, S. K., 2009).

has been pursuing this technique [119], where a number of human trials have been successfully conducted by implementing subretinal prosthesis system of 1500 photodiodes.

In ***epiretinal*** system, the stimulation occurs at the inner layer of the retina, inside the Vitreous cavity. It means the whole circuitry that includes image processor, electrode array, and even receiving antenna, is placed completely inside the eyeball [35, 37]. In this configuration, the image data is transmitted wirelessly between the extraocular and intraocular part of the system (Figure 2.5). The data is subsequently processed by the implantable image processor, to form a suitable stimulation pattern. Since this system is powered externally, it offers more flexibility in adjusting some parameters of the system wirelessly [35]. Also, since it is intended to be fully implanted inside the Vitreous cavity, it produces minimal discomfort for the patient once the device is installed. However, the main challenge for this approach is the difficulty in implementing surgical procedure to implant the whole device inside the eyeball as well as the fixation of the stimulator to the retina layer to generate the desired stimulation pattern.

Until now, there are no findings suggesting that one approach is better than another, and both are currently being developed by leading research groups as presented in Section 2.2.3. However, due to the limited applicability of this study to only epiretinal prosthesis systems, all the terms "retinal prosthesis" in this document will refer to epiretinal prosthesis system.

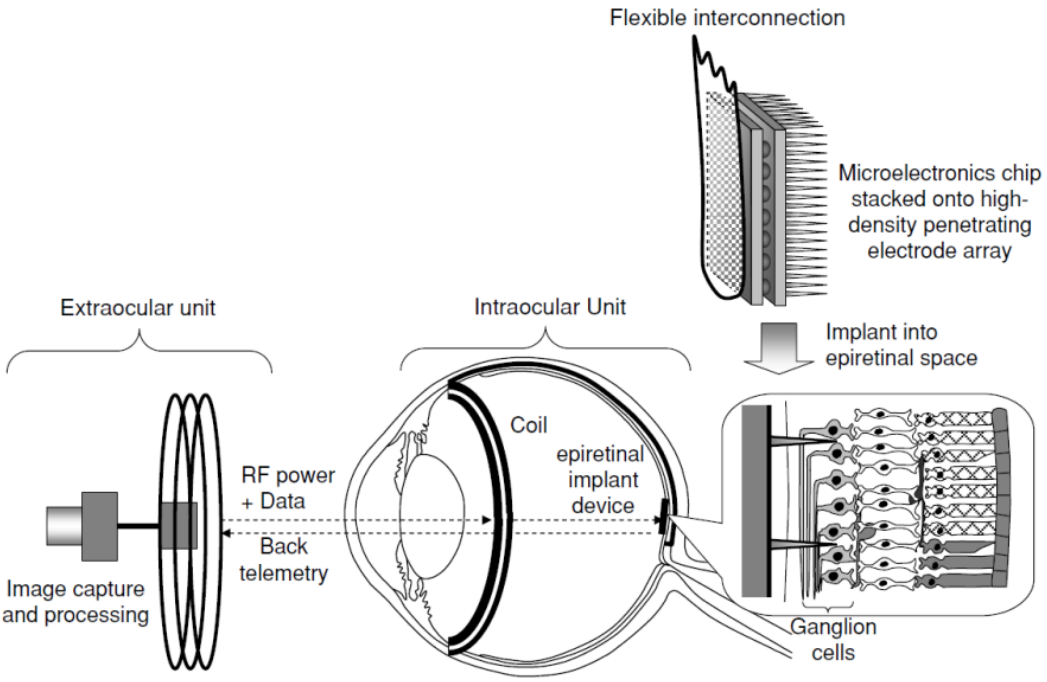

Figure 2.5. Epiretinal prosthesis system configuration. Extraocular component includes a combination of camera and transmitter unit while the intraocular component consists of implantable antenna, image processing unit, and electrode array (Ng, D., 2009).

2. 2. 2. Significance

The system will be beneficial for people who are visually impaired due to RP and AMD with healthy bipolar and ganglion cells. The system will assist the patients to actually recognize nearby objects by detecting the reflection of the objects' edges.

There have been a number of studies on different tasks that can be performed or different objects that can be identified with a variation of electrode numbers. Most experiments were conducted by covering healthy subjects' eyes with perforated masks and there were different requirement on the number of electrodes depending on the requested tasks, which vary from wandering around a room to identifying objects and faces [8, 38, 39]. In this study [38], it was hypothesized that an array of 25 x 25 electrodes within an area of 1 cm2 could produce a visual perception that could be useful for pattern recognition. In another experiment [9], the subjects' visions were masked by 4 x 4, 6 x 10, and 16 x 16 dots to resemble the electrode patterns, and they were made to perform a set of tasks including a cutting task, a pouring task, symbol recognition, and also reading tasks. The result showed that the highest performance was expectedly achieved on the 16 x 16. However, the most interesting finding from this experiment was that even by using the lowest resolution array of 4 x 4, the subjects could still manage to do symbol identification and cutting task with the spontaneously developed response to overcome the device limitation. For example, in the case of symbol recognition and cutting task, scanning and tactile information was used by the subjects, respectively.

Another study focused on the effect of different phosphene shape and grid parameters to find the best configuration [39]. Sixteen conditions were created by modifying the array size from 10 x 10 to 32 x 32, as well as varying the grid size, dot size, gap width, dot dropout rate, and greyscale resolution. It is obvious that the best accuracy was achieved by the highest number configuration (32 x 32). However, the most valuable information that could be extracted from the study is that the size of each phosphene was very influential to the accuracy level of the response. For a dot size of 2.3 times bigger on the same electrode number, the accuracy was about two times higher.

These results showed that a retinal prosthesis system, even at the very low level in terms of the number of electrodes, could assist people who are visually impaired as a result of RP and AMD. It is obvious that higher electrode number corresponds to better image perception, but the limiting factor would be the size [36] as well as the complexity in data multiplexing [40]. The promising results even by 4 x 4 arrays shows that even at the very basic level, this device could have a significant influence for people who are visually

impaired. Combined with a proper training and supervision, this device would improve the quality of life of the users.

2. 2. 3. Current Technologies

Retinal prosthesis system is currently developed by multiple research groups with each group putting the focus on different aspects. Here is the summary on the progress of each group from the technical as well as clinical perspective.

2.2.3.1. Second Sight Group, California, USA

Second Sight is a company based in Sylmar, California, USA, and is focused on building retinal prosthesis system to assist people who suffer RP and AMD. Until now, this company has developed two products, named Argus I and Argus II. The first clinical trial for Argus I was conducted on 2002 while the 2nd generation device's trial was initiated on 2006. Thirty subjects who suffered severe outer retinal degeneration had been enrolled between June 2007 and August 2009 with follow-up cares of up to 2 years and 8 months [41]. This latest product has also been tested on 21 patients with RP with the objective of guiding fine hand movements [42]. The device was waiting for a regulatory approval from Food and Drug Administration (FDA) for commercial use, which was expected to come by late 2012 [43].

Feasibility studies had been conducted prior to the prototype design to gain a deep understanding about the predicted system behaviour and the effect to the surrounding environment. The studies covered the investigation of the electrode array substrate material [10], phosphene amplitude variation in relation to the visual perception [11], the effect of the system to the surrounding tissues as part of the safety measure [12-14], as well as the investigation of the wireless link between the extraocular and the intraocular components [16-17]. Post-production study has also been conducted to understand the device behaviour when it is exposed to Magnetic Resonance Imaging (MRI) [19].

Electrode substrate is a crucial component in an electrode array where its main purpose is to provide a mechanically steady platform for all the electrodes. The task of selecting the substrate material is therefore very crucial. Three polymer materials were investigated in this study [10]: polyimide, parylene, and silicone. Each material was manufactured with its specific process and was individually tested in canine eye. The testing revealed that polyimide has the advantage of being the easiest to fabricate due to the already matured phase of this material in the market. However, polyimide is also the least flexible material,

which requires special treatment during the implantation process. Parylene, on the other hand, requires a slightly more complex manufacturing process, but resulted in an exceptional biocompatible property. The fabrication of the substrate using silicone material is less common and a new, untested, production technique was conducted for the testing purpose in this investigation. It resulted in the most biocompatible material, in terms of damage inflicted to the retina. However, the implementation of this material reduced the performance of the system, marked with the presence of the distortion on the signal. Based on the testing results, it was agreed that parylene has the best properties, even though it is still not ideal. An alternative solution would be a multi-polymer approach for a single substrate, which would require a further investigation.

An investigation on the effect of stimulation amplitude variation to the phosphene shapes was launched [11]. The experiment was conducted on the test subjects who had been implanted with a 4 x 4 electrode array and stimulator. The stimulation patterns were produced by a PC and the data was transmitted to the implant using a serial cable. Each subject was then required to reconstruct the phosphene data on a grid screen using a tracked digital pen to see the actual perception. The input current to the electrodes was subsequently varied to four different levels. The findings from this experiment suggested that the phosphenes change in form and size due to amplitude variation. Although it could not be guarantee that the shapes drawn by the subjects were 100%, it was clear that there was a uniform change at the size of the patterns. This information would provide a useful insight on how the retina reacts as a response of the stimulations.

Several studies about the safety aspect had been conducted to gain a better understanding on the thermal elevation effect due to the retinal prosthesis system. In this study [15], the relationship between the heat and power dissipation effect on the retina was investigated. A custom intraocular heater probe was attached to 5 different areas on the retinal layer of dog with various power levels. It was found out that the liquid environment of the eye acts as a heat sink that is capable of dissipating a significant amount of power. As a result, a heat source that was located further away from the retina boasted higher power allowance. On a further study, a single platinum microelectrode was inserted into the vitreous cavity of rats and was supplied with different level of input current pulses (0.05 to 0.2 μC/phase) [14]. The placement of the microelectrode was also repeatedly altered to understand its mechanical impact to the retina. The experiment suggested that retinal damage was greatest when the retina was directly contacted by the electrode, whether or not electrical stimulation was applied. The combination of retinal contact and

electrical stimulation produced the most damage. High charge density stimulation from an epiretinal electrode in normal rats damages photoreceptors more severely than the inner retina and ganglion cells. Moderate to severe changes were noted in the retina, Retinal Pigment Epithelium (RPE), and choroid, only when the electrode was in contact with the retina. Contact with no electrical stimulation still resulted in retinal damage. The results imply that a successful retinal prosthesis design will consider carefully both electrical and mechanical safety issues.

The study about the thermal elevation was extended further by involving the prototype of the retinal prosthesis system. These papers [12, 13] investigated a temperature increase on eye components due to the first and the second generation epiretinal prosthesis. Human head and eye models were constructed based on the Visible Man Project from the National Library of Medicine (NLM, Bethesda, USA) with the resolution of 1 mm. An implant model was inserted into the head and eye model and was numerically calculated using Bio-Heat Equation and finite difference time domain (FDTD) as the solver. The results were verified by implanting a temperature sensor fitted chip package into canine eyes for an *in vivo* measurement. The measurement result of the first generation implant revealed that a temperature elevation of 0.26°C was observed in the vitreous cavity after 26 minutes of continuous operation while the chip's temperature itself raised by 0.82°C [13]. Table 2.1 shows the resulting temperature increase in multiple eye components due to the implanted coil on the second generation implant [12].

This group has also spent some efforts on investigating the wireless link between the extraocular and the intraocular components of the system. In this study [18], the group investigated the feasibility of data telemetry link at the frequency 1.45 GHz and 2.45 GHz with the internal antenna dimension 6 x 6 mm. Microstrip antennas were designed for each frequency and were calculated using FDTD technique. The measurement was executed by immersing the manufactured antenna into an eye phantom, which was mimicked by a mix of water, sugar, and salt at a certain proportion. At a separation of 25 mm between the external and internal antenna, in the frequency band of 1.45 GHz, the coupling was measured to be 42.5 dB in free space, and it was improved to 37.2 dB when the intraocular antenna was immersed in the eye phantom. At 2.45 GHz, the corresponding experimental free-space coupling was 32 dB, and it was improved to 31.1 dB in the presence of the eye phantom. Numerical and experimental values agreed well for all cases at a separation of 25 mm [18]. In separate experiment, a 3D dipole antenna was designed and tested to be operating inside Vitreous Humour mimicking solution at 1.9 to 2.33 GHz frequency [16].

The idea of using 3D dipole antenna was proposed to reduce the planar dimension of the antenna while improving the bandwidth performance. The hypothesis was confirmed by the measurement inside the phantom.

Table 2.1. Thermal Effects due to Operation of the Secondary Coil

Tissue/Material	Max ΔT (°C)
Sclera	0.22
Choroid	0.19
Retina	0.17
Vitreous Humour	0.18
Fat	0.23
Coil	0.39
Silicone	0.38

There have been two retinal prosthesis devices built by this company, the Argus I and the Argus II. Argus I was the first generation device, employing 4 x 4 electrodes and was launched a decade ago. Argus II is their most recent product(currently waiting for approval from FDA [43]) and it is more relevant to discuss about it here. The Argus II Retinal Prosthesis is an epiretinal prosthesis that includes a receiving coil, electronics case and an electrode array that are to be surgically implanted in and around the eye (Figure 2.6).

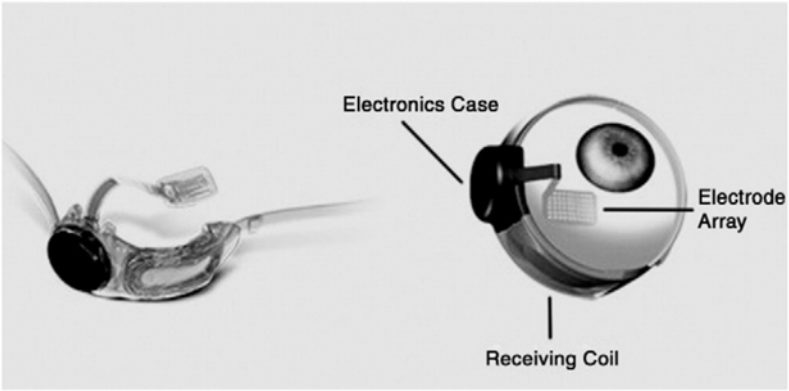

Figure 2.6. Illustration of Argus II retinal prosthesis device and its placement during the operation. The images were retrieved from Gizmag (http://www.gizmag.com/argus-ii-retinal-implant-european-approval/18758/, date accessed: 18January 2013)

The array is attached to the retina over the macula with a retinal tack. The external equipment includes glasses, a Video Processing Unit (VPU) with rechargeable battery and a cable connecting the VPU to the glasses. The glasses include a miniature video camera, which captures video images, and a coil that sends data and stimulation commands to the implant. The VPU converts the video images into stimulation commands and is body-worn. The Argus II System operates by converting video images into electrical energy that

activates retinal cells, delivering the signal through the optic nerve to the brain where it is perceived as light [19].

Clinical tests have been conducted to characterize the device behaviour as well as to comprehend if the device was indeed significant for the test subjects. In this particular test [44], the 4 x 4 retinal prosthesis system was implanted into three test subjects suffering RP. The objective was to see how electrodes proximity affected the subjects' perception. First of all, it was discovered that the subjects who were chronically implanted with prototype retinal prostheses have perceptual thresholds lower than those obtained during acute studies. It was also revealed that the proximity to the retina played a role in determining the threshold and impedance, but only for electrodes that were greater than 0.5 mm from the retina. Within this distance, perception thresholds and impedances did not seem to be strongly dependent on the proximity of the electrode to the retina. Thresholds did not seem to depend on the diameter of the electrode either [44]. In another clinical trial, thirty subjects were enrolled in the United States and Europe between June 6, 2007, and August 11, 2009 and all subjects were followed up for a minimum of 6 months and up to 2.7 years [41]. The results suggested that subjects performed statistically better with the system for the following tasks: object localization (96% of subjects), motion discrimination (57%), and discrimination of oriented gratings (23%). The best recorded visual acuity was 20/1260 [41].

An additional post-production study was conducted on the second generation device to test the device compliance (the intraocular part) under the exposure of MRI equipment [19]. A patient with Argus II retinal prosthesis device implanted underwent an MRI with the magnetic strength of 1.5 T and 3 T. The experiment revealed that there was no significant divergence on the magnetic field interaction on MRI equipment and the retinal prosthesis device, which consequently means that patients are not required to remove the intraocular component in order to undergo MRI scanning.

In summary, the Second Sight group has managed to build two products, Argus I and II, both with the concept of epiretinal prosthesis system. Numerous studies had been conducted prior to the design process for each prototype on the electrode substrate material, the phosphene shapes in relation to the stimulation amplitude, the possible thermal elevation, as well as the wireless link between the intraocular and the extraocular parts. Clinical trials have been conducted to verify the functionality of the product and satisfying responses were obtained. Post-production testing was also conducted to investigate the compatibility of the intraocular component of the system with the MRI

equipment. It was found out that an MRI operation with the magnetic strength of up to 3 T is sufficiently safe for the device.

2.2.3.2. Nara Institute of Science and Technology, Nara, Japan

A group from Nara Institute of Science and Technology, Nara, Japan, has done a rigorous study on the retinal prosthesis system, with the emphasis on the photosensor development. They had attempted creating a direct replacement of the defective photoreceptors by designing a photosensor that detects the incoming light and converts it to electrical stimulation for neuron stimulation.

In this study [20], a single pixel pulse frequency modulation photosensor was designed and fabricated using standard 0.6 μm CMOS process technology for a subretinal prosthesis system. It was integrated with digital adjustable photosensitivity feature for inbound light adaptation. Experimental results showed that the dynamic range of the sensor was about 120 dB and the photosensitivity could be adjusted from 0 dB to around -40 dB. In another development [21], a back-illuminated photosensor with silicon-on-sapphire technology was investigated to be integrated in an epiretinal prosthesis system. Unlike in subretinal system, the neuron stimulations from epiretinal is electronically more complicated due to the sensor circuits placement being on the other side of the plane where the electrodes are placed to be able to capture the inbound lights. To overcome this problem, a transparent substrate was developed to enable back-illuminated Pulse Frequency Modulator (PFM) photosensor, resulting in the silicon-on-sapphire technology. The experiment results indicated that the sensor was twice as sensitive as the previous photosensor with a dynamic range of 30 dB.

In a more advanced study, a multi-chip electrode with the material of silicone was developed for a neuro-stimulation device such as retinal prosthesis system [22]. Each chip unit consisted of nine electrodes and a control circuit. The chip was intended to be functional either as a standalone unit or as part of a multichip network. The advantage of employing this architecture was not only to have a mechanically stronger and more flexible packaging, but also to have a more expandable architecture. The unit chip was initially moulded with epoxy resin layer at the final assembly process to make it hermetic (Figure 2.7). However, the epoxy gap at the electrode widened over time due to the electrical stimulation by the electrodes. A solution was proposed to achieve a better seal quality [23], by slightly modifying the assembly process, involving the use of Si dummy wafers. The technique was named flip-chip bonding technology.

The chip was subsequently fabricated in a configuration of 1 x 4 unit chips and was tested in an *in vivo* measurement [24]. The flexible chip was implanted into a rabbit eye's sclera pocket for a Suprachoroidal Transretinal Stimulation (STS) configuration. The experiment was intended more for testing the chip prototype rather than a chronic use. To verify that the stimulators were working as supposed to, an Electrically Evoked Potential (EEP) reading was recorded by inserting a screw electrode through the skull of the rabbit ant onto the visual cortex. A clear reading of EEP signals was obtained, which respectively confirmed the performance of the stimulator chip.

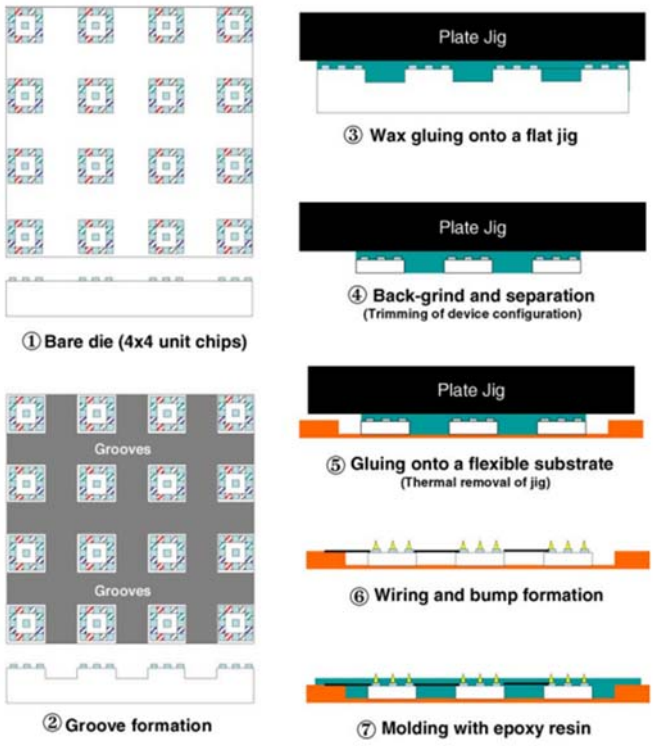

Figure 2.7. Assembly process of the multi-chip neural interface device on a polyimide substrate (Tokuda, T., 2005).

Another chip was developed based on the knowledge of the previous experiment to accommodate more functions such as realization of multichip stimulation, light-controlled stimulation, as well as conformability to the eyeball shape [25]. The significant improvement in this experiment was the incorporation of photodiode to the stimulating electrode chip for an independent light detection. Initially the chip was tested by an exposing it to a certain light pattern in a free space condition. Satisfactory response was obtained and it led the path to the *in vivo* testing inside a rabbit's eye. The same procedure was applied to the implantation process, except that this time the stimulation will be based on the incoming light instead of the externally generated electrical signal, due to the implementation of the photodiodes. It was verified that the retinal stimulations were

correctly corresponding to the inbound light judging by the relationship between the EEP traces and the light source.

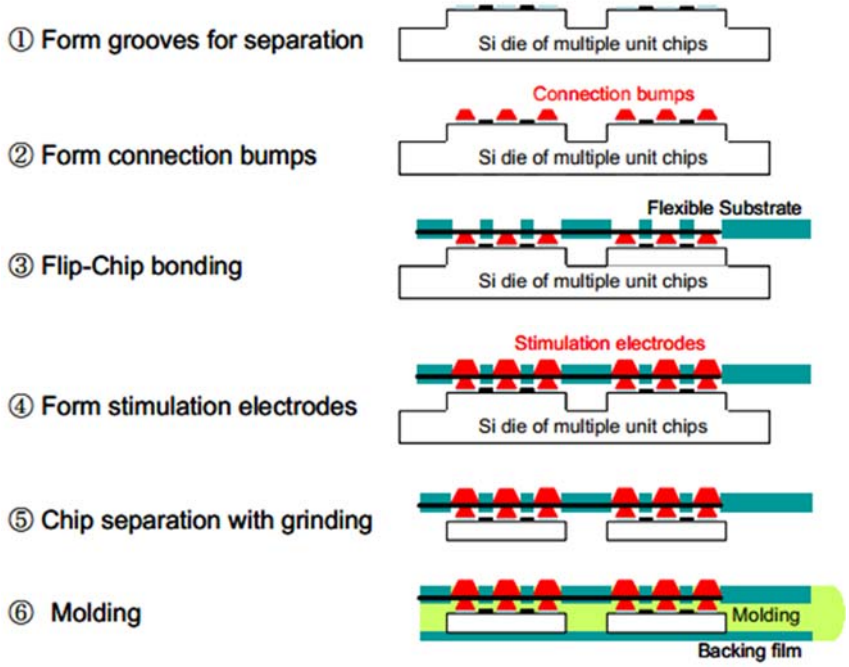

Figure 2.8. The improved assembly process of the electrode array for a better encapsulation (Tokuda, T., 2006). The technique is called flip-chip bonding technology.

In summary, this group proposed a different approach on designing a retinal prosthesis system. The main focus was the design of photosensor using a pulse frequency modulation, intended for both subretinal and epiretinal system. Multichip electrodes were also developed in an effort to provide a robust, flexible, and biocompatible chip. Both technologies, the photosensor and the electrode chip, were combined to create a real retinal prosthesis system. The system was tested *in vivo* using rabbits' eyes, but no clinical trials on human to date.

2.2.3.3. University of New South Wales and Bionic Vision Australia

This group is based in Australia and started the retinal prosthesis study following the success of their cochlear implant product. The group began the study from the neurophysiological approach, by investigating the response of various stimulations to the visual cortex activity. Different types of stimulator array in regards to their positions have been fabricated and tested: subretinal, epiretinal, and suprachoroidal array. Most of the device has been manufactured and implanted into cats' eyes to obtain the *in vivo* performance.

The study was initiated by an investigation on retinal prosthesis system implementation from the surgical point of view. An ovine eyeball was selected for a surgical simulation on visual prosthesis implantation [45] due to its similar shape to a human's eyeball. The visual prosthesis device was inoperative and was manufactured to specifically emulate the actual anticipated device. The surgical procedure included transplanar port-hole lensectomy and vitrectomy, insertion of the model implant through a limbal incision, and fixation of the Perspex subunit close to the location of the native crystalline lens. Figure 2.9 shows the expected position of the retinal prosthesis and subsequently what was aimed from the procedures.

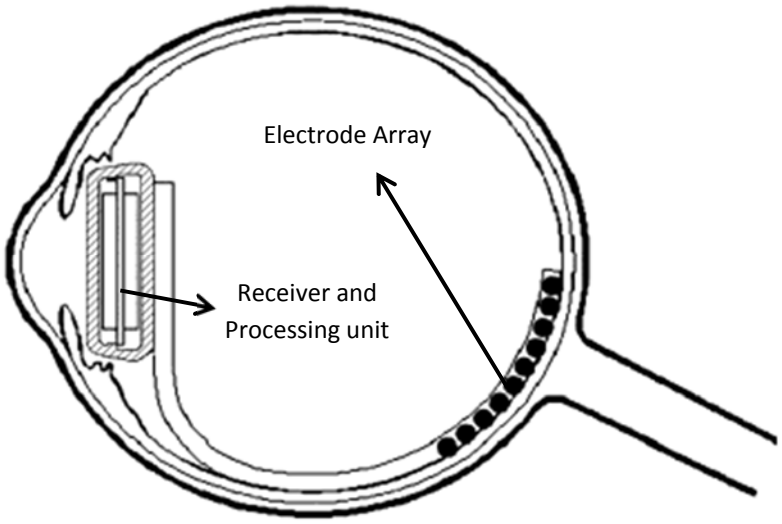

Figure 2.9. The desired position of the implant. The surgical procedure was executed with a dummy device (Kerdraon, Y. A., 2002)

A surgical technique was discovered to successfully implant the intraocular component of the retinal prosthesis system with the placement verified by the computer tomography (CT). The following criteria have also been met using this approach: no substantial haemorrhage, no damage to the retina layer, no trauma observed in any part of the globe, and most importantly, the wounds were successfully closed.

On a more advance step, the group developed an application specific integrated circuit (ASIC) neurostimulator for the purpose of creating simultaneous multi electrode stimulation on the neurons [46]. Simultaneous multi electrode stimulation creates electrical cross-talk which consequently reduces the current flowing through to the neurons. As a solution to overcome that problem, a neurostimulator using a unique configuration of electrodes was proposed. Instead of using just a conventional one pair of electrodes, one stimulating and one return electrode, a set of return electrodes forming a hexagon ring

surrounding each stimulating electrode was implemented. This configuration was intended to isolate one stimulating electrode from another to avoid any electrical cross-talks. The system was built and tested to operate well within the specifications. The principle was then applied to drive 100 electrodes in 14 different locations [47].

In another attempt to improve the neural stimulation responses, an optical imaging of intrinsic signals (OIS imaging), in addition to EEP, was employed to record the activity at the visual cortex [48]. This technique allowed a better resolution data recording over large area of tissue, which would be beneficial to the further neurophysiological analysis of prosthetic vision. In this study, adult cats were anesthetized and were exposed to corneal, intra-vitreal, as well as visual stimulations.

A feasibility study was conducted to verify the possibility of retinal stimulation from suprachoroidal [49]. This marked a shift of research direction from the previous epiretinal approach. The advantages of the suprachoroidal stimulation technique included reduced long term risk as a result of indirect contact to the retina tissue, as well as relative practicality in the surgical procedure. The down side of this technique was the higher power threshold on the electrodes, which translated to higher power requirement for the implant. Both 6-return and 1-return electrode systems were implanted to cats' eyes and it was found out that the use of 6-return electrode system resulted in a lower recorded signal amplitude at the cortex compared to the single-return system. The study was followed up by a suprachoroidal electrode array design [26], which was manufactured using a flexible polyimide substrate material and was coated with silicone. The device was implanted inside an adult cat's eye by accommodating a pocket within the suprachoroidal space. The experiment was conducted to obtain the antenna performance in terms of impedance, thresholds and input-output function slopes with variations on the number of return electrodes, electrode sizes, the number of simultaneous stimulating electrode, and the pulse widths. The result suggested that the introduction of suprachroidal approach is feasible for a retinal prosthesis system, as the implant induced visual cortex activity. A new knowledge was also obtained for reducing the voltage requirement by employing larger diameter electrodes and wider pulse widths for monopolar stimulation.

A study on image analysis was conducted in an attempt to model the most efficient algorithm to convert a raw image to a phosphine image (PI) [50]. A mutual-information function was employed to determine the amount of information to be passed through to the PI observer (device user) based on visual stimuli. The parameters of the function included the number of phosphenes and their locations, the number of levels of phosphene

quantification, and also the image analysis scheme. An implementation of the image processing algorithm has been demonstrated in a prototype wearable real-time image processor [51]. The device, which was to be attached on the user's waist, featured dual-core OMAP5912 microprocessor from Texas Instruments (Dallas, TX, USA). The image processing procedure was divided into 4 steps: image acquisition by the camera, image enhancements, image pixelation, and command generation. It was concluded that using the proposed image processing technique, the use of general-purpose embedded micro-processors would not be sufficient for a real-time visual prosthesis.

To summarize, this group has done rigorous studies about the retinal prosthesis from the neurophysiological approach. A lot of efforts were spent on the experiment to gain the knowledge of the biological response to the implanted device. To date, no human trials have been reported on the journals and cats were regularly involved in the *in vivo* testing.

2. 3. Existing Implants Communication Methods

In epiretinal prosthesis system (Figure 2.5), there is a data communication exchange between the extraocular and the intraocular components. The specific communication methodology for the retinal prosthesis system has not been rigorously investigated, but there has been relatively more research about wireless link on other implantable medical applications, such as capsule endoscope and implantable body sensor network.

2. 3. 1. Capsule Endoscope

In the capsule endoscope system, a capsule-sized camera module that is an integration of antenna, sensors, and the camera itself is ingested. As the capsule travels following the digestion path, the camera repeatedly captures images of the internal section of the organs while actively transmits the images to the external receiver wirelessly. In any wireless communications, antenna is a very crucial component, transforming electric signals to electromagnetic waves. In this scenario, the role of an antenna is even more important due to severe challenges of the surrounding.

Instead of operating at free space, just like other standard antennas, the antenna in this system has to transmit the signal from inside the body, which in this case has a dielectric constant of 56 and conductivity of 0.83 S/m [52]. Moreover, the antenna is also subjected to the dimensional as well as orientation constraints which as a result create a demand of a small, wide bandwidth, and omnidirectional characteristic.

In this experiment, a printed spiral antenna with a diameter of 10.1 mm and height of 3 mm was proposed for a capsule endoscopy system [52]. The selection of the spiral shape was to improve the bandwidth of the antenna. The antenna was intended for operation at 450 MHz, but measurement inside a tissue simulating fluid reflected a shift to 465 MHz with a bandwidth of 70 MHz. In a further development, the bandwidth of the antenna was improved even more by the implementation of thick arm spiral [53]. The width of the arm and its gap from one another were varied to study their effects on the resulting bandwidth. The antenna was tested inside a cylinder filled with liquid human phantom and produced a bandwidth of 104 MHz at 500 MHz resonant frequency.

2. 3. 2. Implantable Body Sensor Network

The advancement of sensor technology introduces the possibilities of various implantable sensors for the purpose of measuring as well as monitoring physiological signals *in vivo*. Implantable sensors for measuring SvO_2, blood oxygen, blood glucose, neural activity, as well as internal imaging, are currently investigated comprehensively. In an implantable body sensor network (IBSN), all the sensors were designed to exchange data wirelessly by employing master-slave mechanism [54]. To realize this, implantable communication must be considered at the core design of the architecture.

Although the medium surrounding the implantable antenna is different to the one in capsule endoscope system, the constraints remain the same because generally human tissues have high dielectric constant and high conductivity which translates to high propagating loss. In this study [54], a microstrip antenna with the dimension of 22 mm x 18 mm x 9.5 mm was designed and simulated to be operating at MICS band. The implementation of high permittivity substrate material was done as an approach for a miniaturization. The antenna was simulated inside the fat layer in a 3-layer tissue model and Specific Absorption Rate (SAR) values were recorded.

2. 3. 3. Retinal Prosthesis

Back to the retinal prosthesis system, the same constraints of the implantable antenna that were applied to the previous two systems are also applied here. However, in retinal prosthesis, the surrounding medium (Vitreous Humour) is particularly more challenging, with its relative permittivity of 69 and conductivity of 1.53 S/m at MICS band and the cavity diameter of only 25 mm.

In this study [55], a system with a pair of coils was designed for a wireless data telemetry and power transfer between the extraocular and the intraocular components. The external antenna was placed at the front of the cornea while the internal coil is at the middle of the eyeball. The operating frequency was 6 MHz, hence both antennas were operating at each other's near field zone.

As already discussed at the Second Sight Group development, a 3D dipole antenna was designed and tested to be operating inside Vitreous Humour mimicking solution at 1.9 to 2.33 GHz frequency [16]. The idea of using 3D dipole antenna was proposed to reduce the planar dimension of the antenna while improving the bandwidth performance. The hypothesis was confirmed by the measurement inside the phantom.

2.4. Summary

It is clear that human body characteristic is naturally very complex as it has very high dielectric and conductivity values and they are frequency dependent. It makes it difficult to design an antenna for multiple implantation scenarios in different medium. Therefore, implantable antenna design requires a careful planning to gather all the exact information needed to resemble the real operating condition of the antenna. The design procedure starts from the operating frequency selection, followed by the design of the antenna, design of the surrounding medium(s), simulation, and verification of the results.

In this chapter, information regarding retinal prosthesis system, including the rationale of the system, how the system works, and the current developments, has been presented. The focus was then intensified on the wireless communication component of the system for the relevance to the thesis topic. Existing technologies employed by other medical implants were reviewed to obtain more knowledge about the design challenges of the implantable antenna. The information gathered would be essential in the frequency selection process, which will be presented in the next chapter.

Chapter 3
Frequency Selection

Frequency selection is an integral part in the design phase of any wireless communication systems due to its significance in determining the antenna design. However, choosing a frequency band for a specific purpose is not a straightforward task considering there are various aspects that need to be looked at, such as bandwidth, possible external interference, antenna size, and SAR value. In this chapter, all these factors will be individually investigated for subsequent feasibility study on several frequency bands for the retinal prosthesis system that include High Frequency (HF) band, Medical Implant Communication Service (MICS) band, and Industrial Scientific and Medical (ISM) band. Simulation results on SAR values calculation will be presented next, and ultimately a frequency band will be selected based on the analysis test on all possible frequency bands.

3.1. Important factors in frequency selection

As mentioned previously, there are four aspects that would be influential in the selection process: bandwidth, external interference, antenna size, and SAR value.

3.1.1. Bandwidth

There are numerous definitions of the term bandwidth depending on the specific applications. In this thesis, however, the term's interpretation will be narrowed down for two different scenarios: in the frequency selection process and in the antenna design process.

The first definition of bandwidth is an authorized bandwidth parameter assigned by a legal communication body to specify the spectrum allowed in the data transmission process [56]. The two most recognized communication bodies include Federal Communications Commission (FCC) from USA and International Commission on Non-Ionizing Radiation Protection (ICNIRP), based in Germany, and their standards have been commonly adopted by other countries. The bodies basically govern the maximum bandwidth, or in this case spectrum slot, to avoid any inter-signal interference during the transmission. The signal

bandwidth of a transmission depends on the modulation technique employed and it is proportional to the data rate, as suggested by the Nyquist's Theorem in which sampling rate has to be at least twice the size of the bandwidth [56]. Therefore, higher data rate in a transmission will translate to larger bandwidth requirement for the same modulation approach.

In retinal prosthesis system, the number of electrodes will drive the data rate requirement. However, modulation technique also plays a big part in controlling the data rate of the transmission. In this study [57], a neuro-stimulus chip of 100 electrodes was manufactured. Data rate at operating frequency of 1-10 MHz was ranged from 25 to 250 kbps with Amplitude Shift Keying (ASK) controlled by Pulse-width Modulation (PWM) technique. Another retinal prosthesis chip was manufactured with a CMOS-only technology, operating at 5-9 MHz. The achieved data rate was 25 to 714 kbps with ASK modulation when 15 electrodes were operating [58].

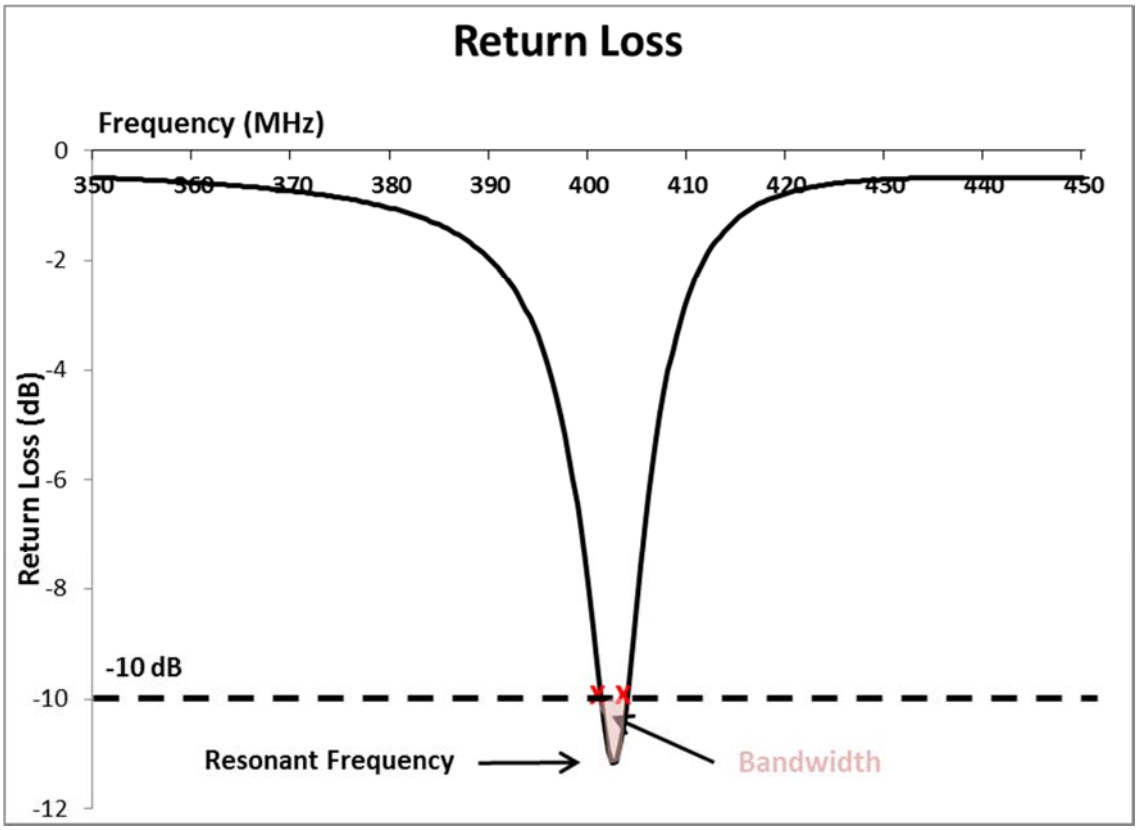

Figure 3.1. Return loss of an antenna. The red cross signs mark the part where the return loss of the antenna crosses the -10 dB level. The pink area in between represents the antenna bandwidth in Hz. The resonant frequency is the point where return loss is at its lowest value.

From the antenna design perspective, bandwidth is defined as the range of frequencies within which the performance of the antenna conforms to a specified standard [59]. Usually there is a distinction on the radiation patterns as a result of input impedance

variations. Therefore, input impedance is adopted as an indicator of the antenna performance. Generally, a value of lower than -10 dB indicates a good performance of an antenna and the region between the two points where the return loss crossed the -10 dB mark is the bandwidth of the antenna, as represented by the pink area in Figure 3.1.

In the antenna design process, some applications require a very wide bandwidth while for the others it is insignificant. It is also important that the bandwidth of the antenna is large enough to maximize the spectrum allocated for the transmission. As discussed in the previous Section, in retinal prosthesis the bandwidth requirement is affected by the number of electrodes as well as the modulation technique. A successful antenna design will need to incorporate the bandwidth requirement of the system into the consideration.

3.1.2. External interference

External electromagnetic interference comes as a result of multiple usages of the frequency band by different devices. To overcome this problem, implementation of higher power or special shielding is required. Selecting a frequency with the least possible external interference is desirable to minimize the need of dealing with the radio frequency signal interference.

3.1.3. Antenna size

Antenna size is very closely related to the frequency selection process in the way that an antenna aperture's size has to be at least a quarter wavelength to achieve ideal radiation efficiency. Wavelength in itself is inversely proportional to the signal frequency, which means that low frequency operation will require bigger antenna size to achieve an ideal performance. However, in the case of retinal prosthesis system, there is a limiting factor on the size of the antenna due to its anticipated position inside the eyeball.

3.1.4. SAR values

SAR is the rate at which electromagnetic field (EMF) energy is absorbed by the human body and it has become a standard to identify the limit of safe EMF exposure level to the human body. Every device that produces EMF will cause thermal and non-thermal effect to living tissues [60]. The non-thermal effect, due to its complexity and lack of published reports, is not considered in this investigation. The thermal effect relates directly to the temperature increase on parts of human body due to EMF absorption. SAR is used as an indication whether the EMF exposure is maintained at the safe level. It is important and

necessary to investigate the SAR distribution pattern for an implanted retinal prosthesis system. The implanted device, which will be in a continuous operation for uninterrupted vision, will be put inside a human eye that is only a few centimetres away to the most vital human organ, the brain. The basic formula for SAR calculation can be defined as:

$$SAR = \frac{\sigma}{\rho} E^2 = \frac{1}{\rho} \omega \varepsilon E^2 \tag{3.1}$$

where E is the electric field at a point in the body (V/m), σ is the conductivity (S/m), ρ is the mass density of the body (kg/m^3), ω is the angular frequency (ω = 2πf radians), and ε is the permittivity of the body part (F/m). According to ICNIRP [60], the limit of SAR value is 2 W/kg over 10g of body tissue (for frequency range of 100 kHz to 10 GHz), whereas based on FCC standard, the limit of SAR value is 1.6 W/kg over 1g of body tissue [61]. The SAR value difference between those two standards is very little, but the fact is that in the ICNIRP standard, the SAR value is obtained as an average of 10g body tissue surrounding the emitter, while in the FCC standard, it is an average of 1g body tissue. What this means is that the ICNIRP standard allows higher point SAR value within the measured volume than the FCC standard. FCC and ICNIRP standards have been adopted by a majority of countries around the world, which was the reason why the 10g and 1g SAR threshold values were used in this experiment as the reference of the standard safety level.

The analysis of each frequency band in the following Sections will be based on evaluating each factor. At the end of the chapter, a summary on the performance of each band will be presented and the operating frequency is ultimately selected.

3.2. High Frequency (HF)

HF band is a radio frequency band with the range of 3-30 MHz. Within this frequency range, there are three radio bands allocated by FCC for licensed uses: 6.78 MHz, 13.56 MHz, and 27.12 MHz [62]. Maximum bandwidth has been set by FCC for licensed usages to avoid interferences between each device. The maximum bandwidth of 30 kHz, 14 kHz, and 326 kHz were set for the radio bands of 6.78 MHz, 13.56 MHz, and 27.12 MHz, respectively [62].

Common applications for High Frequency band include shortwave radio, Radio-frequency Identification (RFID), and Near Field Communication (NFC) standard. For the

unlicensed operation, this band has been regularly used for amateur radio activities. Short wave radio applications utilize frequency band between 1.8 MHz to 30 MHz and it is typically associated with international and domestic broadcasting with the spacing for each channel is 5 kHz. RFID is another application that operates at HF band, specifically at 13.56 MHz. Due to its low cost and compact shape, RFID is currently being implemented on massive range of applications from different areas that include commerce, transportation, logistics, personal identification, sports, and telemetries. NFC is another technology that employs 13.56 MHz frequency and it is largely based on the RFID technology. However, in addition to RFID's read or write operation mode, the technology is also incorporated with card emulation and peer-to-peer modes [63]. NFC technology is currently still at the early stage, which explains low adoption rate, but future possible applications in the public transportation, office, money transaction, or sport sectors will make NFC the new RFID.

Ideal antenna size for free space operation in this frequency is 2.5 to 25 m based on the condition mentioned on Section 3.1.3. However, the nature of retinal prosthesis system requires the antenna to be surrounded by Vitreous Humour. The relative permittivity and the conductivity of the fluid (ε_r = 70, σ = 1.5 S/m at HF [64]) affect the minimum aperture requirement of the antenna due to resonant frequency shift [65]:

$$f_r \approx \frac{1}{\sqrt{\varepsilon_r}} \tag{3.2}$$

According to formula (3.2), the resonant frequency is shifted by the factor $\frac{1}{\sqrt{\varepsilon_r}}$. Hence, the minimum free space aperture is also shifted by the same factor to obtain the minimum aperture inside the medium. In this scenario, the minimum aperture was calculated to be 0.3 to 3 m, down from 2.5 to 25 m.

3.3. Medical Implant Communication Service (MICS)

MICS band is a frequency band that is allocated specifically for medical implant purposes with the frequency range of 401 to 406 MHz [66]. In this band, the maximum bandwidth is divided into 2 categories: 300 kHz for the 402 to 405 MHz and 100 kHz for both 401-402 MHz and 405-406 MHz [66].

MICS band is currently utilized for medical systems like cardiac pacemaker [67] and implantable body sensor network (IBSN) [54], which can comprise of implantable sensors

for the measurement of SvO_2, blood oxygen, blood glucose, neural activity, as well as internal imaging.

The dielectric property of Vitreous Humour at MICS band is like the following: ε_r = 69, σ = 1.53 S/m at 402 MHz [64]. By using Equation (3.2), the ideal antenna aperture inside the Vitreous Humour at MICS band is 22.46 mm, down from 186.57 mm at free space environment.

3.4. Industrial, Scientific, and Medical (ISM) 915 MHz

This band, just like the other ISM bands, is dedicated to the industrial, scientific, and medical purposes other than telecommunications. The frequency range of this band is from 902 to 928 MHz with the maximum licensed bandwidth of around 4.58 MHz [68] depending on the centre frequency.

The only major licensed usage for this band is Global System for Mobile Communications (GSM) 900, a standard developed for cellular phone network. GSM-900 is being utilized globally except for some countries like USA and Canada. In GSM-900, the uplink frequency is 890-915 MHz and the downlink is 935-960 MHz with the spacing between each channel 200 kHz [69]. It is clear that the uplink frequency of the GSM-900 overlaps with the part of the ISM 915 MHz band and it will probably cause interference during the transmission.

For this band, the ideal free space antenna aperture using the quarter wavelength method is 82 mm. When the antenna is operating inside the Vitreous Humour liquid with ε_r = 68.9 and σ = 1.64 S/m at 915 MHz [64], the minimum antenna size is reduced to 9.87 mm.

3.5. Industrial, Scientific, and Medical (ISM) 2.45 GHz

Probably the most popular ISM band, this band has a frequency range of 2.4 to 2.5 GHz. With the range of 100 MHz, the maximum bandwidth imposed for each transmission is around 12.25 MHz, depending on the centre frequency [68].

There are plenty of applications utilizing this frequency band, namely Bluetooth (IEEE 802.15.1), Wi-Fi (802.11), ZigBee (IEEE 802.15.4), cordless phones, baby monitors, and microwave ovens. These are everyday applications and therefore the signal interferences in this band are practically everywhere.

The ideal free space minimum aperture based on the calculation in 3.1.3 is 30.6 mm. With the introduction of Vitreous Humour as the surrounding medium (ε_r = 68.2 and σ = 2.48 S/m at 2.45 GHz [64]), the required antenna aperture for ideal radiation is smaller at 3.71 mm.

3.6. SAR Values Calculation

SAR values for each frequency band (except the HF band) were calculated with the aid of Computer Simulation Technology (CST) Microwave Studio® software. First of all, an antenna was designed to be operating in each frequency for the purpose of understanding the SAR values of each frequency band. Microstrip antenna is considered as the most suitable for the retinal prosthesis system due to its low cost, compact, and low profile nature. Microstrip antenna can also be made to conform to the shape of human tissue using some specific material [70].

A microstrip antenna normally consists of a ground plane, a substrate, and the microstrip line/patch itself. A superstrate is sometimes added to protect the patch or microstrip line from the undesirables. Besides, a superstrate can affect the resonant frequency of the antenna. In the case of implantable antenna, a superstrate is highly essential to prevent the patch to be in contact with the human tissue. In the antenna design process, there are several parameters that are influential to the performance of the antenna, namely physical dimension, position of the feed, material, as well as the surrounding material. A parametric study for each component mentioned above has been done [71] and the knowledge was used as the reference for the design of each microstrip antenna.

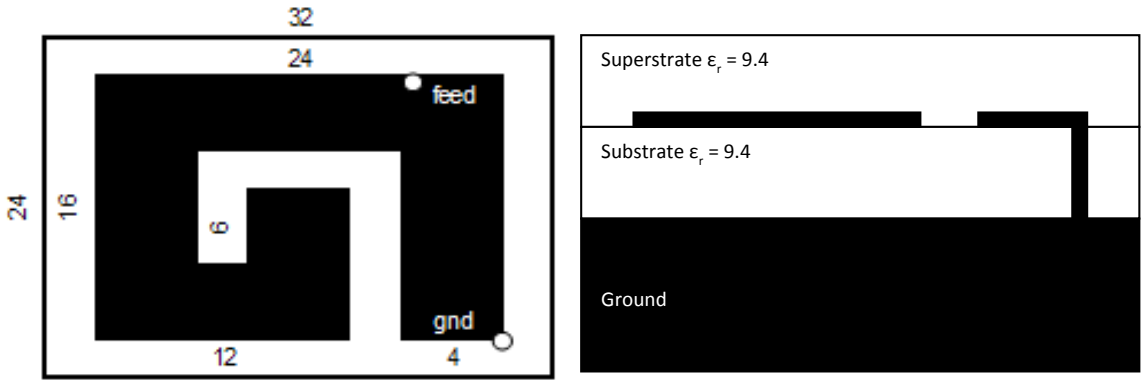

(a) (b)

Figure 3.2. (a) Top view and (b) side view of 402 MHz antenna. All the numbers are in mm.

Figure 3.2a and 3.2b show the design of the antenna that was optimised to work in MICS band. In Figure 3.2a, the dark line is the microstrip line which is made of copper material with the thickness of 0.1 mm. The feed and ground pins were also made of copper material with the cylinder diameter of 0.5 mm. With the ground pin included in the design, this antenna can be categorised as a Planar Inverted F Antenna (PIFA).

The design of this microstrip antenna was generally based on the antenna in this study [72] with some additional modifications on the substrate thickness as well as the material to suit different surrounding environment. The fine tune process to get the intended frequency accurately was done using experimental approach. This antenna is optimised to work on 402 MHz frequency.

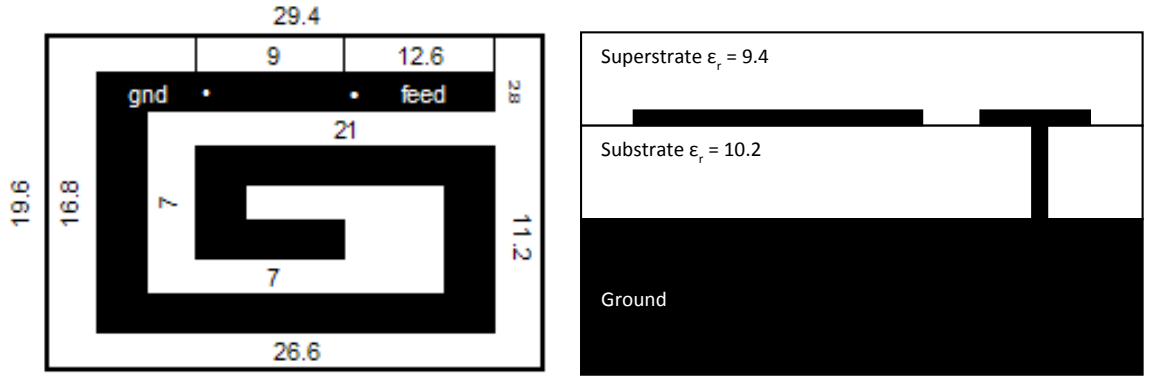

Figure 3.3. (a) Top view and (b) side view of 915 MHz antenna. All the numbers are in mm.

Figure 3.3a and 3.3b show the blueprint of an antenna that was designed to suit the ISM 915 MHz frequency band. The basic structure of this antenna originated from [71]. Modifications on the antenna material and dimensions were made to optimise the antenna performance at 915 MHz. It can be observed that there is a ground pin that connects microstrip to the ground. Therefore this antenna is also classified as PIFA model. For this antenna, a material with higher dielectric constant was used for the substrate. Other than that, all the materials used were identical as the previous ones. The feed and ground pin also have the same size and material as the previous model. This antenna is resonant at 911 MHz, which is still in the range of 915 MHz ISM band.

For the 2.4 GHz band, the antenna design is very similar with the one discussed before. However, it has to be emphasised that the physical dimension, including the feed and ground pin diameter, of this antenna is smaller by a factor of 2 (Figure 3.4). The thickness of each layer was also reduced. It is very logical taking into consideration the relationship between frequency and wavelength. When the frequency is higher, the wavelength

becomes shorter proportionally. Consequently, the required dimension of the antenna to accommodate that resonant frequency is also smaller. Other than physical dimension modification of this antenna compared to the previous one, the material superstrate for this antenna was also changed. Lower dielectric constant material, which in this case was mica ($\varepsilon_r = 6$) was used in place of Rogers RO3210. The resonance frequency of this antenna is 2.47 GHz.

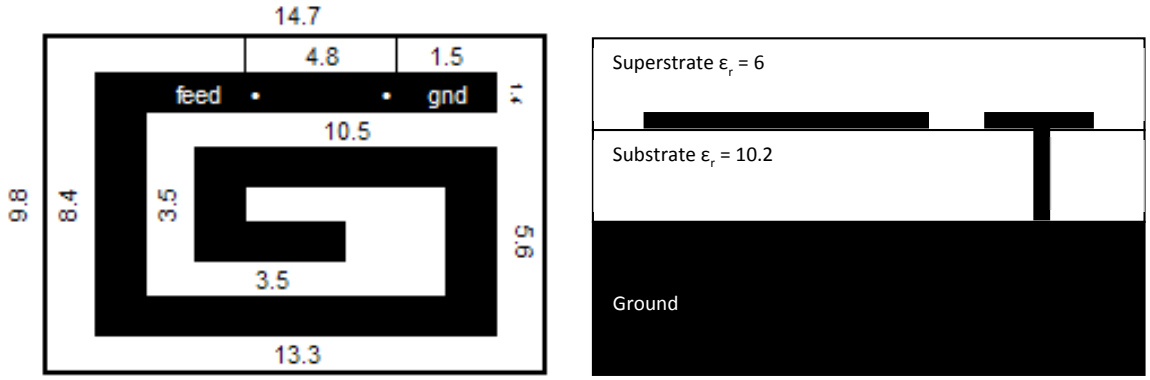

(a) (b)

Figure 3.4. (a) Top view and (b) side view of 2.4GHz antenna. All the numbers are in mm.

The three antenna models that had been presented before were placed inside a 6 layer human head model proposed by [72], shown in Figure 3.5. The head model consists of 6 layers (from outer to inner): skin, fat, bone, Dura, Cerebro Spinal Fluid (CSF), and brain.

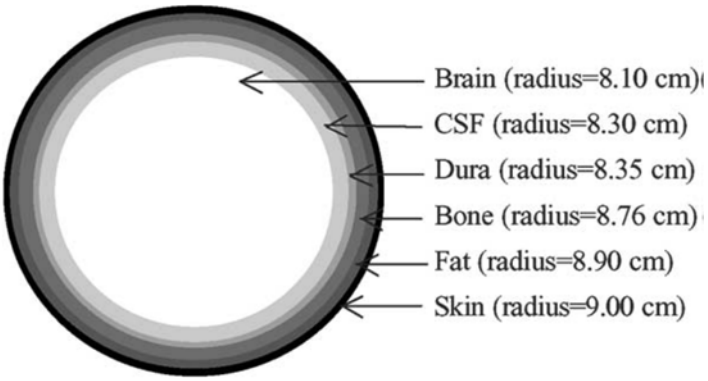

Figure 3.5. Spherical head model used for the simulation

Each layer of the human head model above has its own electrical properties and they are frequency dependent. The two most important electrical properties that will influence the simulation results are dielectric constant (ε_r) and conductivity (σ). Table 3.1 shows the electrical properties of each material that compose human head model in three different frequency bands [64]. Horizontally, each antenna was placed facing out of the front side of the head model. Vertically, the antenna was set slightly above the centre line. Refer to

Figure 3.6a and 3.6b to get more detail about the antenna and head model configuration. The configuration was implemented to specifically simulate the implanted antenna used in retinal prosthesis. The presence of eyeballs as well as ear, nose, and throat parts were ignored at this investigation since this experiment is focused more on the relation of antenna radiation to the human brain, the most vital part in human body.

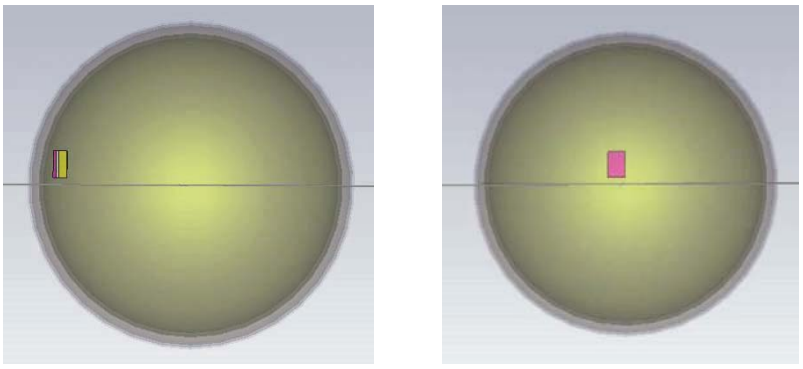

(a) (b)

Figure 3.6. The position of the antenna with respect to the head model seen from (a) side view and (b) front view.

Table 3.1. Electrical Characteristics of Human Head Components at 402, 915, and 2400 MHz Frequency Band

Material	f = 402 MHz		f = 915 MHz		f = 2.4 GHz	
	Relative Permittivity (ε_r)	Conductivity (σ) S/m	Relative Permittivity (ε_r)	Conductivity (σ) S/m	Relative Permittivity (ε_r)	Conductivity (σ) S/m
Air	1	0	1	0	1	0
Brain	49.7	0.59	45.75	0.77	42.61	1.48
CSF	70.97	2.25	68.61	2.42	66.32	3.41
Dura	46.65	0.83	44.39	0.97	42.1	1.64
Bone	13.14	0.09	12.44	0.15	11.41	0.38
Fat	5.58	0.04	5.46	0.05	5.29	0.1
Skin	46.74	0.69	41.33	0.87	38.06	1.44

The simulation was run with the aid of CST Microwave Studio software, which uses Finite Integration Technique (FIT) as its mathematical solver. FIT is a numerical technique to solve Maxwell's Equation, the basic equation for all electromagnetic problem. It basically works using the same equations as the popularly known Finite Difference Time Domain (FDTD) technique, but using different solving approach (matrix and scalar). In a test conducted by Leithon [73], FIT performed much faster than FDTD to solve non-homogeneous material, which is exactly the nature of the models used in this experiment.

The frequency range was set to 0-1 GHz for the first two antennas, and 0-3 GHz for the last one. Transient solver was used in all the simulations because the return loss of each antenna is needed to be acquired and transient solver, which is based on frequency domain,

will run a sweep of every frequency from the range specified to get the return loss value for each frequency. By knowing the return loss pattern, it would be clear which operating frequency is the best for each antenna.

After the simulations were executed, it was learnt that the SAR distribution pattern for each frequency remained the same even when the power source was altered, but the maximum values are different. As the source power was increased, the maximum SAR value also increased. This phenomenon occurred on both the 10g and 1g average SAR calculation. With the safety level standing at 2 W/kg (10g average SAR) and 1.6 W/kg (1g average SAR), the 100 mW and 1 W power sources cannot be considered due to their over-limit absorption values (refer to Table 3.2). Figures 3.7 – 3.12 show the results of antenna simulation inside the human head model using CST Microwave Studio software for each frequency at the power level of 10 mW.

Figure 3.7 shows the average 1g SAR of human head model with the 402 MHz microstrip antenna implanted into the brain layer in two different views: (a) full 3D front view and (b) cross-sectional view from the same angle. The highest SAR value obtained in this case is 0.51 W/kg. It can be clearly seen, especially on the cross-sectional view that the highest SAR value intensity occurs at the front end of the antenna. Average 10g SAR of 402 MHz antenna is shown in Figure 3.8 also in two different views. This time, CST calculated the maximum number of 0.341 W/kg. In terms of SAR distribution pattern, it spreads more through to the most outer layer of the model, unlike in the average 1g case where the higher SAR values mostly occur only on the brain layer.

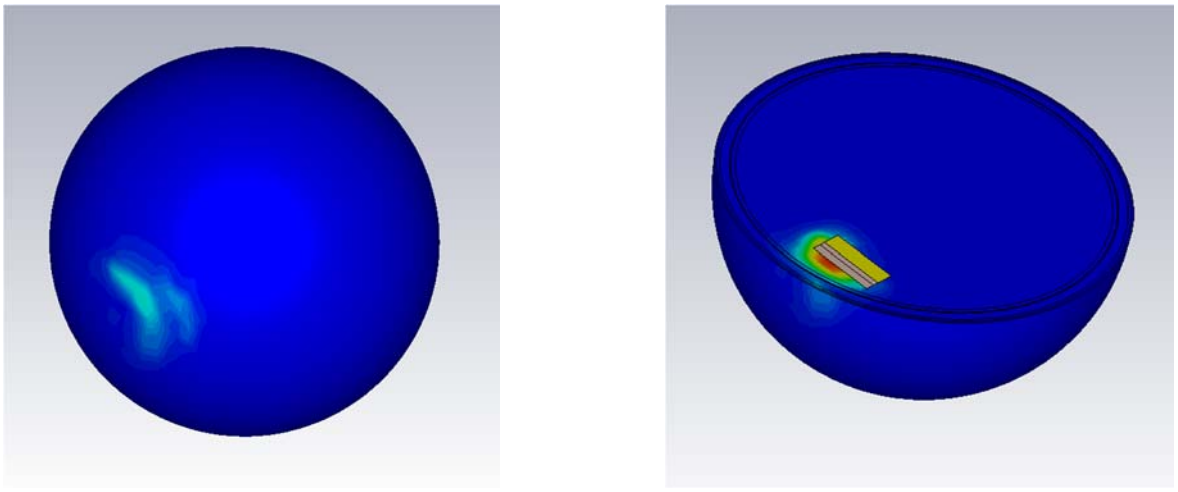

(a) (b)

Figure 3.7. Average 1g SAR of 402 MHz antenna from (a) front view and (b) cross-sectional view, both from the same angle.

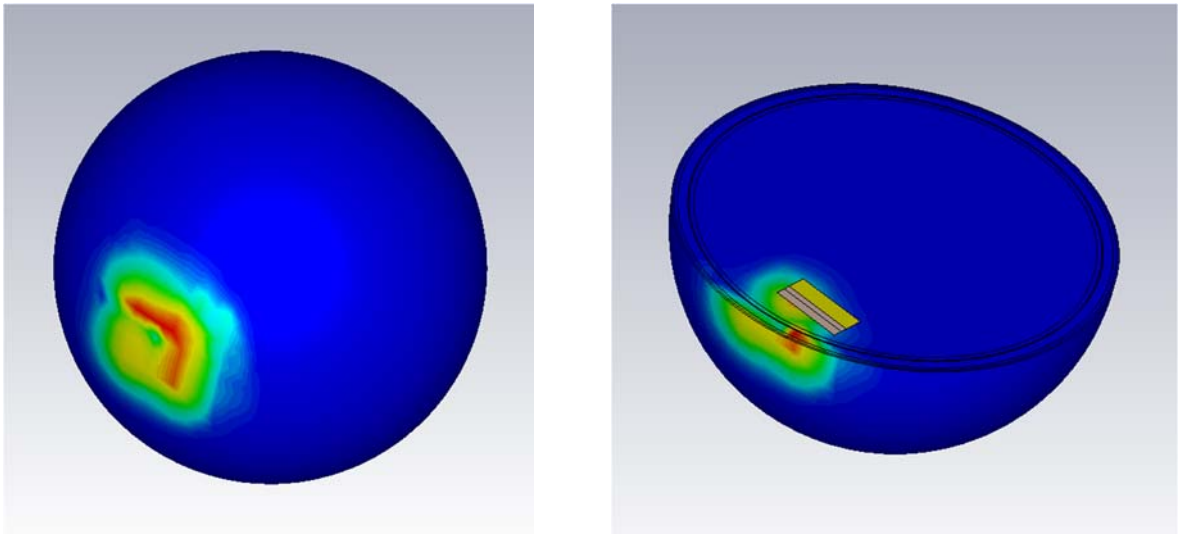

(a) (b)

Figure 3.8. Average 10g SAR of 402 MHz antenna from (a) front view and (b) cross-sectional view, both from the same angle.

Observing the 3D view of the simulation result for the 915 MHz antenna (Figure 3.9a), it can be seen that the SAR values at the outer surface of the model are very small. Exploring the 2D view (Figure 3.9b), it becomes clearer that the higher SAR values mostly occupy the inner layer, which is the brain. The maximum SAR value calculated in this set up was 0.779 W/kg. Still using 10 mW power source, the average 10g SAR pattern of the 915 MHz antenna is similar to that of 402 MHz antenna, with the maximum magnitude is slightly lower at 0.275 W/kg (Figure 3.10a and b).

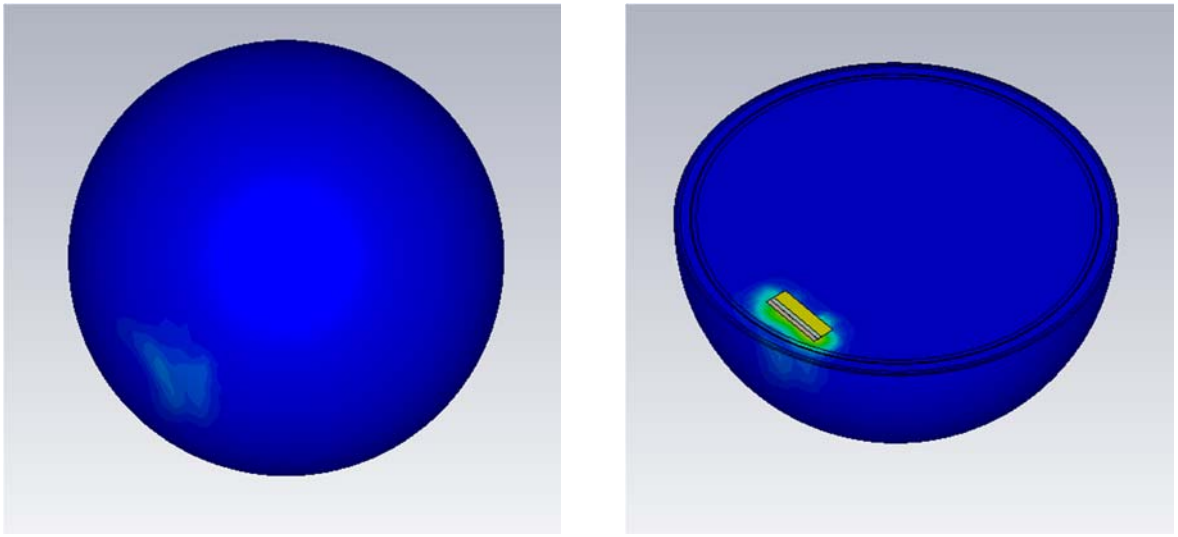

(a) (b)

Figure 3.9. Average 1g SAR of 915 MHz antenna from (a) front view and (b) cross-sectional view, both from the same angle.

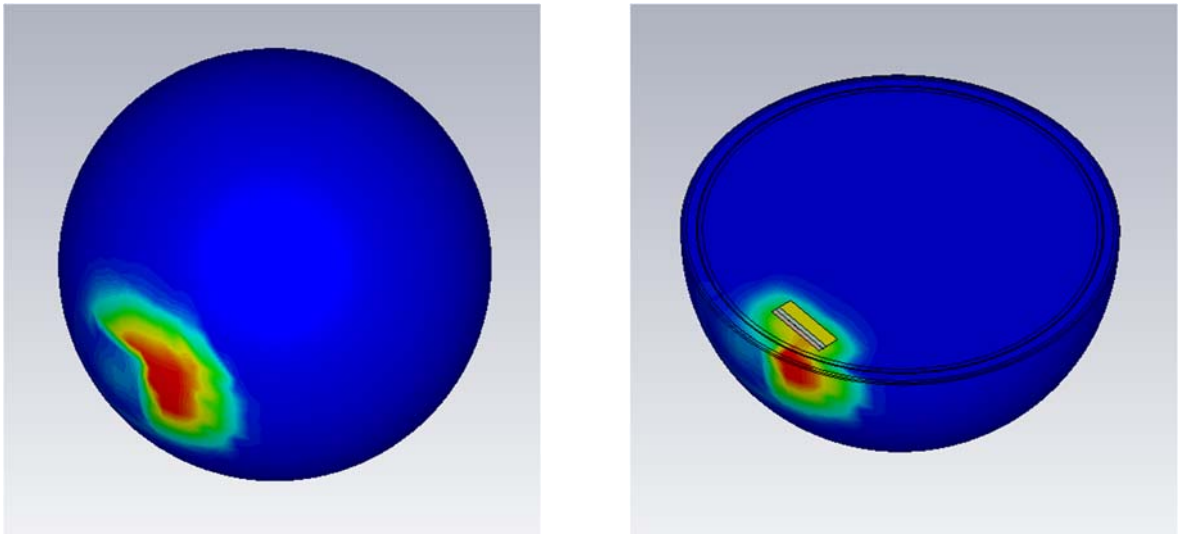

(a) (b)

Figure 3.10. Average 10g SAR of 915 MHz antenna from (a) front view and (b) cross-sectional view, both from the same angle.

Referring to Table 3.2, the antenna absorbed electric field at the highest rate in this frequency, both using 10g averaging and 1g averaging method. The 10g average value is 0.679 W/kg and the 1g average value is 3.468 W/kg. With regard to the distribution pattern, the area covered by this antenna is relatively small compared with other frequencies for the 1g average SAR (Figure 3.11). However, for the 10g average SAR, it is very clear that the value distribution is concentrated more on the outer layer (Figure 3.12).

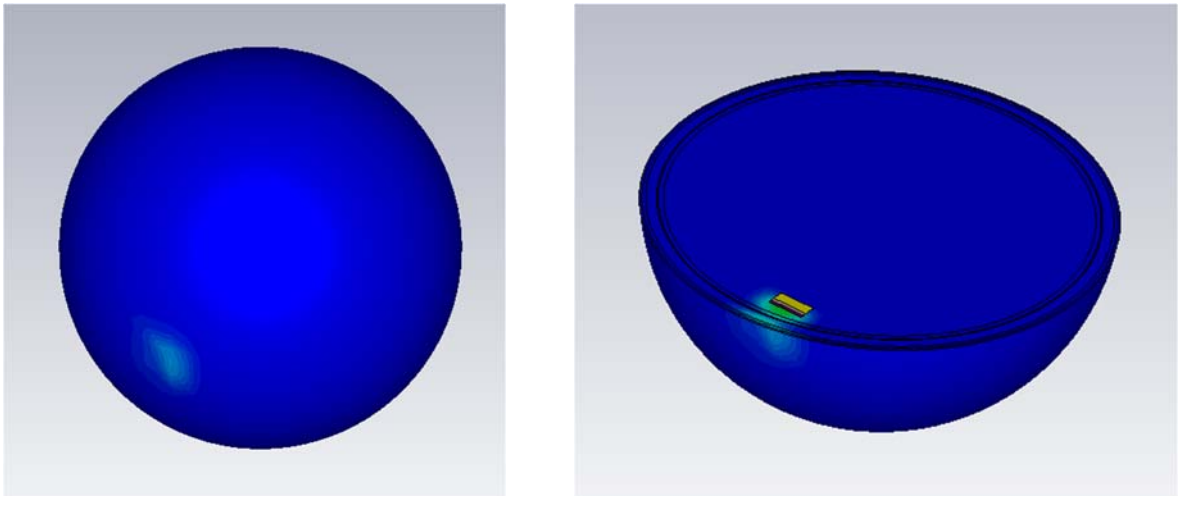

(a) (b)

Figure 3.11. Average 1g SAR of 2.4 GHz antenna from (a) front view and (b) cross-sectional view, both from the same angle.

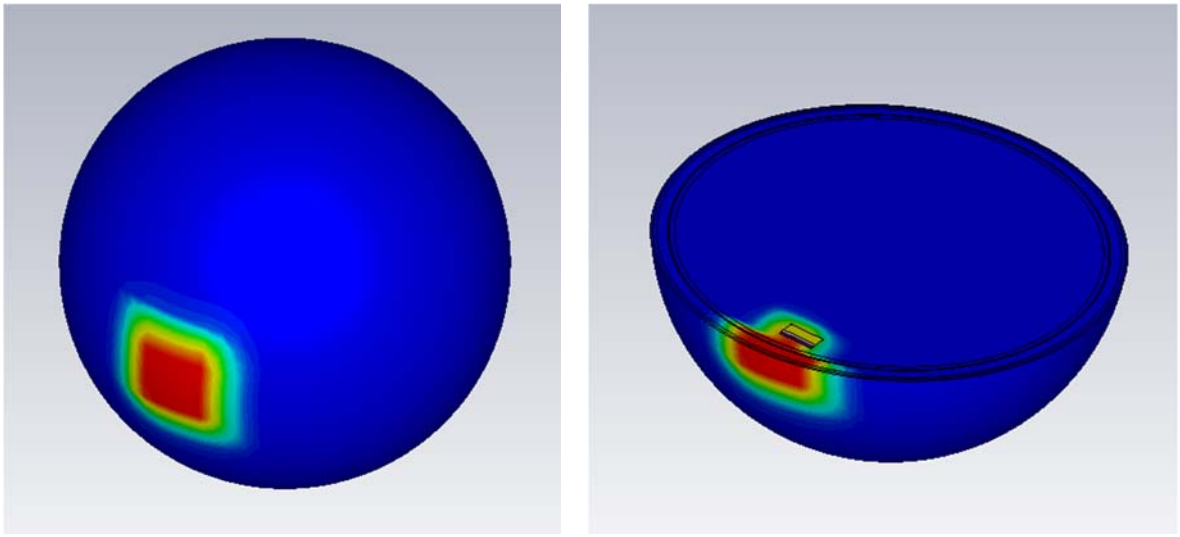

(a) (b)

Figure 3.12. Average 10g SAR of 2.4 GHz antenna from (a) front view and (b) cross-sectional view, both from the same angle.

In Table 3.2, the 1g and 10g average SAR values for each band are presented. The logarithmic variations on the input power can be observed as having proportional outcomes on the SAR values. This is due to the corresponding relationship between electric field strength and SAR value based on Equation (3.1), which can be translated to the proportionate input power. Maximum allowable power to the antenna can also be solved based on the combination of this knowledge and the simulation data. Based on the maximum SAR values of each frequency band, the maximum legitimate power levels to satisfy both regulations are 31.39 mW, 20.54 mW, and 4.61 mW for 402 MHz, 915 MHz, and 2.4 GHz bands, respectively.

Table 3.2. Summary of simulation SAR values for 3 different antenna designs in 4 different power levels (orange shade means the value exceeds the safety limit)

SAR Value (W/kg)	402 MHz		915 MHz		2.4 GHz	
	10g	1g	10g	1g	10g	1g
Prms = 1 mW	0.01	0.02	0.01	0.04	0.03	0.17
Prms = 10 mW	0.11	0.17	0.14	0.39	0.34	1.72
Prms = 100 mW	1.14	1.7	1.36	3.86	3.37	17.18
Prms = 1 W	11.37	17	13.63	38.62	33.66	171.8
SAR Limit	2	1.6	2	1.6	2	1.6

3.7. Frequency Selection

Based on the analysis on each frequency band, the results can be compiled in Table 3.3.

Table 3.3. Summary of antenna attributes and performances in different frequency bands

	HF	MICS	ISM (A)	ISM (B)
Range	3-30 MHz	401 - 406 MHz	902 - 928 MHz	2.4 - 2.5 GHz
Common Usage	short wave AM RFID Amateur Radio NFC	Pacemakers Medical Implants	GSM	Bluetooth Wi-Fi ZigBee Cordless Phone Baby Monitor Microwave Oven
Maximum Bandwidth	39, 14, 326 kHz	300 kHz	4.8 MHz	12.25 MHz
Ideal Antenna Aperture (free space)	2.5 - 25 m	0.19 m	82 mm	30.6 mm
Ideal Antenna Aperture (Vit. Humour)	0.3 – 3 m	22.46 mm	9.87 mm	3.71 mm
Max SAR 1g	-	17 W/kg	38.62 W/kg	171.8 W/kg
Max SAR 10g	-	11.37 W/kg	13.63 W/kg	33.66 W/kg

Table 3 provides a summary of the analysis of each frequency band with regards to maximum bandwidth, possible external interferences, antenna size, and SAR values. According to the table above, the main barrier of employing HF band is the fact that bigger antenna size is required to maintain the antenna performance. In this retinal prosthesis system, it is crucial that antenna size does not exceed the human eyeball diameter of 25 mm. This will prove very difficult even with the implementation of miniaturization technique. Another aspect that will undermine HF band's case is the low maximum bandwidth imposed by the regulators of 14 and 39 kHz. Based on the chip performance, the modulation technique will require up to 250 kHz and 714 kHz for 100 and 15 electrodes, respectively [57, 58]. That rules out the feasibility of this frequency band for the retinal prosthesis system.

MICS band is naturally the first choice frequency band for this system due to its specific allocation for implantable medical devices. In this band, there are relatively less external interferences that would affect the performance of this system. The relatively low maximum usable bandwidth of 300 kHz may cause a slight concern for future development that will incorporate higher number of electrodes. However, it has been proven that with a certain modulation technique, the data rate of the transmission can be suppressed [57]. The

ideal antenna aperture for this frequency band will barely fit into the human eyeball, but with a certain miniaturization technique, this problem will find its solution. Regarding the SAR value, this band caused the least electromagnetic absorption on the surrounding tissues compared to the two ISM bands, due to lower conductivity value of the tissues at that frequency band.

The ISM 915 MHz band is also a good candidate to be utilized for the retinal prosthesis system due to its high bandwidth (4.8 MHz) and smaller minimum antenna aperture (9.87 mm). The calculated SAR values for this frequency band are slightly higher than the ones in MICS band, but the maximum allowable power for the antenna is only reduced by 34.5%. The down side of this frequency band is the partial overlapping with the GSM in some countries. GSM-900 band is a communication platform which forms an integral part to people's daily life and is popularly used everywhere. The overlapping with this band, albeit only the uplink component, would give undesirable results to the system. Unlicensed uses are also available in this band which means even more interferences may be generated.

The ISM 2.4 GHz is undoubtedly the most popular band out of the four. The implementation of this frequency band would mean that the compatibility with other devices in the future would be very smooth. However, from different perspective, the number of applications operating in this band means that signal interferences will present very frequently. Bluetooth and Wi-Fi are just two of the applications occupying the band and they are available almost on every device at this time. On the positive side, this ISM band will allow generous 12.25 MHz bandwidth and the required antenna aperture inside Vitreous Humour is 3.71 mm, well below the eyeball diameter. However, as a result of high conductivities of human tissues at this band, the resulting SAR values become high. Consequently, the maximum allowable input power to the antenna is very low (maximum 9.3 mW, based on the 1g SAR value) in order not to damage the surrounding tissues.

Based on the analysis of each frequency band, it has been decided that MICS band is the most suitable candidate for the retinal prosthesis system. This frequency band will be employed as the reference in the design process of the antenna as well as the tissue modelling at the electromagnetic simulation software.

3.8. Summary

In this chapter, a feasibility study on utilization of frequency bands for the retinal prosthesis system was conducted. Four frequency bands were investigated, including HF band, MICS band, ISM band 915 MHz, and ISM band 2.4 GHz, with respect to their performance in terms of maximum bandwidth, possible external interference, minimum antenna aperture, as well as SAR values. These factors were selected due to their influence to the performance of the proposed implantable antenna. MICS band was selected as the best candidate for this system due to its specific allocation at the frequency spectrum, lower chance of external interferences, as well as its low SAR values. On the next chapter, an antenna will be designed to be operating at MICS band inside the human eyeball.

Chapter 4
Antenna Design

In the previous chapter, the investigation on the most suitable frequency for the retinal prosthesis system was conducted. The next step is to comprehend the basic theory underlying the antenna design since this is the component that has paramount importance in the wireless communication link between the extraocular and the intraocular components of the system. In this chapter, the basic principle of an antenna will be discussed and it is followed by the operation of an antenna in free space as well as inside dispersive and conductive medium. A set of reviews on previously designed implantable antennas will also be presented to provide a reference on typical antenna designs and their performance. Ultimately, a series of analysis will be executed to determine the most suitable antenna geometry and structure to produce a strong performance despite the constraints.

4.1. Antenna

4.1.1. Basic Principle

It is a common courtesy that antenna is always associated with a wireless communication system. But what exactly is an antenna? An antenna is defined as "transitional structure between free-space and a guiding device, which may take the form of a coaxial line or a hollow pipe (waveguide)" [70]. By this definition, any conductors can serve this function with a guided electromagnetic wave input. However, a proper antenna is designed to radiate or receive electromagnetic wave with a certain direction and minimal reflection to/from the transmission line [74]. Hence, impedance matching between an antenna and its connecting circuitry is very important in the antenna design process.

The mechanism is based on the underlying principle of electromagnetic theory, particularly Maxwell's Equations. There are four equations that define Maxwell's theorem:

$$\nabla \cdot D = \rho_V \tag{4.1}$$

$$\nabla \cdot B = 0 \tag{4.2}$$

$$\nabla \times E = -\frac{\partial B}{\partial t} \tag{4.3}$$

$$\nabla \times H = \frac{\partial D}{\partial t} + J \tag{4.4}$$

where D is electric flux density (Coulomb/m^2), ρV is electric charge density (coulomb/m^3), B is magnetic flux density (T), E is electric field (V/m), H is magnetic field (A/m), and J is electric current density (A/m^3).

Equation (4.1) is called Gauss' Law and it states that the electric flux out of any closed surface is proportional to the total charge enclosed within the surface. Equation (4.2) is called Gauss' Law for magnetism and the equation can be interpreted as the magnetic field flowing into a closed surface will have the same magnitude flowing out of the same surface, or in another word the total cumulative flux B through a closed surface equals to zero. The equation also implies that there are no magnetic monopoles. Equation (4.3) is normally called Faraday's Law and it expresses that a variation of magnetic flux within a closed loop produces a circular loop of electric field around it. Equation (4.4) is named Ampere's Law and it is interpreted as electric current J and varying electric flux density D produces a magnetic field circulation around the closed loop. The combination of Equations (4.3) and (4.4) presents an infinite circulation of electric and magnetic field, consecutively, and that is the basic principle of electromagnetic wave propagation. It is axiomatic that antenna propagation is derived from this theory. Figure 4.1 shows graphical representation of the concept.

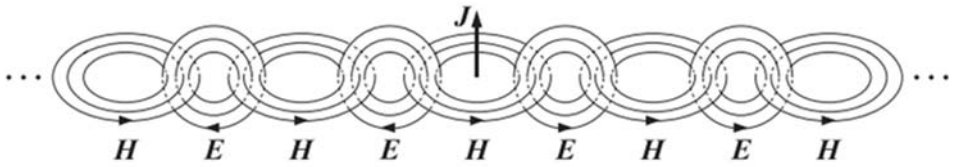

Figure 4.1. Electromagnetic wave propagation mechanism based on Maxwell's theorems (Orfanidis, S. J., 2010).

As an indicator to the antenna performance, various parameters are defined. There are numerous antenna parameters that can be calculated or measured from a single antenna, but for the purpose of this study, only a certain parameters will be investigated. They are radiation pattern, gain, bandwidth, input impedance.

Antenna radiation pattern is a graphical representation of the radiation properties of the antenna as a function of space coordinates [59]. Typically radiation pattern is used for far field measurement to represent 2-dimension or 3-dimension power level of the particular antenna. Logarithmic scale is usually used to highlight the parts with low values, known as minor lobes of the antenna. More information about the interpretation of the radiation pattern can be found on the measurement section in Chapter 6.

Antenna gain is another important parameter that defines the antenna performance. In basic term, gain is interpreted as the ratio of the radiation intensity in a particular direction to the radiation intensity of antenna if it were isotropic, which is generally expressed as the input power over 4π [59]. However, in most cases, gain is interpreted as the ratio of power gain in a certain direction to the power gain of a reference antenna in its referenced direction. The second interpretation will be adopted for the design and measurement process of the antenna throughout the thesis.

As described in the previous chapter, bandwidth is defined as the range of frequencies within which the performance of the antenna conforms to a specified standard, usually the radiation patterns. Antenna bandwidth is typically associated with the range of frequency at which the return loss of the antenna is lower than 10 dB. This parameter is important to determine if the antenna is of wide-band or narrow-band category.

Input impedance is defined as the impedance presented by an antenna at its terminals [59]. In any transmission line system, impedance matching is very crucial to determine the power delivery to/from a specific terminal. Impedance mismatch will result in lower power delivery to/from the antenna due to reflection, which ultimately results in lower efficiency. Typically, antenna is designed to have 50 Ω to be matched with standard coaxial cable.

It is also important to understand that in most antennas reciprocity theorem exists. It means that when a given antenna transmits in direction A 100 times more than in direction B, it will also be 100 times more sensitive in direction A compared to B when acting as a receiver. From the antenna design perspective, it implies that the radiation pattern of an antenna is identical regardless whether it is acting as a transmitter or a receiver. However, this reciprocity theory may not be applicable for antenna with nonlinear materials such as diode and semiconductors [74].

4.1.2. Antenna in Free Space

To understand the electromagnetic wave propagation in free space, it is essential to obtain the understanding of medium properties such as permittivity (ε) and permeability (μ). In

free space condition, permittivity (ε_0) has a value of 8.85 x 10^{-12} F/m and it is used as the basic reference of finding other mediums' permittivity (ε_r). Permeability is related to permittivity by the function [74]:

$$c = \frac{1}{\sqrt{\mu_0 \varepsilon_0}} \tag{4.5}$$

where c is the speed of light in vacuum (3 x 10^8 m/s), μ_0 is the vacuum permeability (H/m), and ε_0 is the vacuum permittivity (F/m). The free space permeability has a quantity of 4π x 10^{-7} or approximately 1.26 x 10^{-6} H/m and its application is analogous to the free space permittivity (ε_0).

Back to Maxwell's Equation, particularly Equation (4.3) and (4.4), they can be rewritten as the following Equations [75]:

$$\hat{z} \times \frac{\partial E}{\partial z} = -\mu \frac{\partial H}{\partial t} \tag{4.6}$$

$$\hat{z} \times \frac{\partial H}{\partial z} = \varepsilon \frac{\partial E}{\partial t} \tag{4.7}$$

Assuming that D = εE and B = μH, with J omitted for source-free condition. From Equation (4.6) and (4.7), it is clear that permittivity and permeability affect the signal propagation. Free space condition has the lowest permittivity value.

4.1.3. Antenna inside High Dielectric and Conductive Medium

In an electromagnetic propagation, wavelength λ is defined as the distance by which the phase of the sinusoidal wave changes by 2π radians [75]. In free space medium, a formula can be derived from the definition:

$$\lambda_0 = \frac{c_0}{f} \tag{4.8}$$

where λ_0 is the free space wavelength (m), c_0 is the free space speed of light (m/s), and f is the propagation frequency (Hz). In a high dielectric but non-magnetic (μ=μ_0) medium, the speed of light is reduced by a factor of $\sqrt{\varepsilon_r}$ and subsequently, the wavelength λ inside the medium is also reduced. The reduction of the signal wavelength will consequently reduce the ideal dimension requirement of the antenna.

In a conducting medium such as water or other liquids, part of the power carried by the electromagnetic wave is converted into heat [74]. An examination has to be conducted to determine which category the medium belongs to by using the following formula [74]:

$$\frac{\varepsilon''}{\varepsilon'} \tag{4.9}$$

Where:

$$\varepsilon' = \varepsilon \tag{4.10}$$

$$\varepsilon'' = \frac{\sigma}{\omega} \tag{4.11}$$

The medium is categorized as a low-loss dielectric if $\frac{\varepsilon''}{\varepsilon'}$< 0.01, a good conductor if $\frac{\varepsilon''}{\varepsilon'}$> 100, and a quasi-conductor if 0.01 <$\frac{\varepsilon''}{\varepsilon'}$< 100 [74]. The Equation (4.9) has been used to calculate the human tissues involved in this study and it can be observed in Table 4.1 that all of them fall under category of quasi-conductor.

Table 4.1. Dielectric properties of human tissues in terms of conductivity (S/m) and relative permittivity. The $\frac{\varepsilon''}{\varepsilon'}$ ratio has been calculated to determine if the medium is categorized as a dielectric, a conductor, or a quasi-conductor.

Medium	σ (S/m)	ε_r	ε''/ε'
Air	0	1	0
Vitreous Humour	1.53	69	0.99
Brain	0.59	49.7	0.53
CSF	2.25	70.97	1.42
Dura	0.83	46.65	0.80
Bone	0.09	13.14	0.31
Fat	0.04	5.58	0.32
Skin	0.69	46.74	0.66

Attenuation constant for each medium can be solved by using the following Equation [74]:

$$\alpha = \omega \sqrt{\frac{\mu\varepsilon}{2}\left[\sqrt{1+\frac{\sigma}{\varepsilon\omega}}-1\right]} \tag{4.12}$$

Implementing this formula for different values of permittivity and conductivity depending on the human tissues has given a deeper comprehension about how both parameters affect the attenuation. Higher dielectric constant and/or higher conductivity result in higher attenuation constant. This will ultimately result lower gain on the propagating signal.

4.2. Previous Implantable Antenna Designs

After gaining a valuable insight on the fundamental principle of how an implantable antenna works, this Section will present a review on published literatures about implantable antenna designs. The focus will be on the antenna parameters as well as the simulation and measurement technique in each experiment. The obtained knowledge will provide a good direction on the design and simulation process of the proposed antenna.

In a study conducted by **Soontornpipit (2004)** [71], microstrip antenna parameters such as shape, length, size, feeding placement, materials, and layer thickness were investigated to accomplish a useful knowledge for antenna optimisation. Microstrip antenna type was selected and simulation inside both 2/3 human muscle and human shoulder model was executed using finite-difference time-domain (FDTD) technique at 402-405 MHz frequency band. The parametric study determined that a microstrip planar inverted-F (PIFA) antenna with a dimension of 29.4 x 19.6 x 6 mm^3 was the most optimized geometry implantable antenna. The simulation inside 2/3 human muscle (ε_r = 42.8, σ = 0.65 S/m at 402 MHz) produced a good return loss of -30 dB at 402 MHz. However, a switch of the medium to a heterogeneous shoulder model developed by University of Utah, the resonant frequency was shifted to approximately 430 MHz. The proposed antenna produced a bandwidth of 20 MHz and maximum gain of -38 dB.

In a study by **Kim (2004)** [72], the adoption of PIFA geometry is investigated and compared against the conventional microstrip antenna. Both models were identical except for the presence of a pin connecting the conductor to the ground layer. The dimension of the antenna was 40 x 36 x 4 mm^3 and the material of both substrate and superstrate was high permittivity Rogers RO3210 (ε_r = 10.2). Both antenna configuration was simulated and measured inside a human tissue simulating fluid with dielectric characteristic of ε_r = 49.6, σ = 0.51 S/m at 402 MHz. The simulation using FDTD technique produced a return loss of -20 dB at 402 MHz (PIFA) and 413 MHz (Microstrip) inside the tissue simulating fluid. However, the resonant frequencies from the measurement were shifted to 438 MHz and 427 MHz for the microstrip and the PIFA antenna, respectively. From the simulation, the radiation efficiency of the antenna was 0.25% for the PIFA and 0.16% for the microstrip antenna. The results indicated that the implementation of PIFA geometry for the same microstrip antenna pattern lowers the resonance frequency and increases the radiation efficiency.

In another research by **Azad (2009)** [76], an implantable antenna was designed for the purpose of integration to global positioning system (GPS) as part of Alzheimer's disease telemetry system. The PIFA microstrip antenna occupied a volume of 20 x 20 x 6 mm^3 with the conductor line resembling Hilbert pattern. Biocompatible materials such as Silicone and Macor were selected for the substrate and superstrate of the antenna, respectively. In this experiment, the antenna was immersed into a block of human muscle with dielectric properties of $\varepsilon_r = 42.81$ and $\sigma = 0.65$ S/m. The simulation achieved a return loss of -12 dB at 1.575 GHz with a bandwidth span of 44.1 MHz.

An implantable printed spiral antenna was designed, simulated, and tested to be integrated into a capsule endoscope system **(Kwak, 2006)** [52]. Due to the nature of the transmission, which requires a high data rate for high resolution image data transfer, a wideband antenna is proposed. A spiral conductor with a diameter of 10.1 mm was printed on RF 35-A with relative permittivity (ε_r) of 3.5 and thickness of 3 mm. The proposed antenna was simulated inside a tissue-simulating fluid ($\varepsilon_r = 56$, $\sigma = 0.83$ S/m) at the operating frequency of 450 MHz with the aid of CST Microwave Studio software. The simulation achieved a return loss of -23 dB at 450 MHz, with the measurement verification showed a 30 MHz discrepancy on the resonant frequency. The proposed antenna also had a wide bandwidth characteristic of 70 MHz, which spans from 430 to 500 MHz.

A different approach of antenna miniaturization was proposed by **Lee (2007)** [77] by incorporating a multilayer microstrip antenna design. In this study, three substrate layers with thickness of 0.635 mm and material of RO3210 were selected as dielectric materials in between each conductor layer. The overall dimension of the antenna was $\pi \times (7.5)^2 \times 1.9$ mm^3 and is intended to be operating at MICS band. The antenna was immersed inside human tissue fluid ($\varepsilon_r = 46.7$, $\sigma = 0.69$ S/m at 402 MHz) in the HFSS simulation. For the verification of the simulation, a tissue liquid composed of deionized water, sugar, salt, and cellulose was created. The proposed antenna achieved return loss of -44 dB at 402 MHz, verified by the measurement result of -28 dB at 402 MHz. The radiation pattern was omnidirectional with maximum gain and radiation efficiency achieved were -26 dB and 0.31%, respectively. The antenna also produced a large bandwidth of 50 MHz, as a result of the multilayer technique. Another microstrip antenna was proposed by the same author **Lee (2008)** [78] with a focus on wider bandwidth realization. A π-shaped microstrip PIFA antenna with a substrate dimension of 22.5 x 22.5 x 1.27 mm^3 was proposed to operate on the same human tissue fluid at the same frequency band (MICS band). The 10 dB bandwidth of the antenna was 80 MHz, in which two dips were observed, and the

maximum gain was -25 dB. In terms of volume occupied by the antenna geometry, this antenna required twice as much space compared to the first antenna. A further improvement to this antenna was proposed by the implementation of additional substrate layer to obtain wider bandwidth and smaller dimension **(2009)** [79]. The π-shaped conductor was still preserved in this design and the dimension of the antenna was slightly modified to 22.5 x 18.5 x 1.9 mm^3. A HFSS simulation inside a grinded pork leg (ε_r = 54, σ = 0.8 S/m) produced a return loss of -24 dB at 440 MHz and it was validated by the measurement result (-34 dB at 440 MHz). The achievable bandwidth in this configuration was 132 MHz with the maximum gain achieved was -27 dB.

A three dimensional dipole antenna was developed as part of a retinal prosthesis system by **Soora (2008)** as part of the Second Sight Group [16]. In this study, the proposed antenna occupied 5.25 x 5.25 x 4 mm^3 and it was simulated inside a human eye phantom (ε_r = 65.67, σ = 1.8 to 2.6 S/m at 2 to 2.6 GHz), which was created by mixing salt and sugar into water. Measurement inside the tissue simulating fluid produced a return loss of -32.4 dB at 2.33 GHz, with a bandwidth of 151 GHz and maximum gain of -32.4 dB.

In a more recent study, an implantable serpentine microstrip antenna was designed for the purpose of continuous glucose monitoring **(Karacolak, 2008)** [80]. With a dimension of 22.5 x 22.5 x 2.5 mm^3, the antenna achieved a dual-band operation at MICS band and ISM 2.4 GHz, with the return loss values of -25 dB and -26 dB at 402 MHz and 2.4 GHz, respectively. This was achieved after the implementation of particle swarm optimisation for finding the best geometry of the antenna. The verification of the antenna was executed inside a mixture of deionized water, sugar, salt, and agarose to mimic the skin characteristic at 402 MHz and 2.4 GHz. The measurement inside the fluid was successful in replicating the simulation results by achieving -24 dB and -11 dB return loss at 402 MHz and 2.45 GHz, respectively. The maximum gain achieved at MICS band was -24 dB with a measured bandwidth 131.91 MHz. The next step of this study was the implementation of rat skin for a further testing of the antenna [81]. Slight modification was applied to the antenna design for an optimized operation inside the rat skin (ε_r = 33, σ = 0.5 S/m at 402 MHz). A verification process was then conducted by embedding the fabricated antenna into the real rat skin. The results showed an agreement with the antenna measurement inside the rat skin mimicking material. This antenna was further tested in an *in vivo* experiment involving rats supplied by Mississippi State University's College of Veterinary Medicine [82]. Before the implantation process, the antenna was encapsulated

by Silastic MDS4-4210 Biomedical-Grade Base Elastomer with ε_r = 3.3 for biocompatibility characteristic.

Another multi-layer configuration was investigated for an implantable microstrip antenna [83] by **Liu (2008)**. With a dimension of 10 x 10 x 1.9 mm^3, this antenna adopted PIFA configuration and featured 50 MHz bandwidth. The verification of the simulation was done by immersing the antenna to a cylinder filled with skin simulating fluid (ε_r = 46.7, σ = 0.69 S/m at 403 MHz). Maximum gain achieved by the antenna was -26 dB with the radiation efficiency of 0.61%. Another multilayer microstrip antenna was developed by **Liu (2009)** [84] for the purpose of increasing the bandwidth of the antenna. The new antenna design was implementing hooked-shaped slots at the edges of the radiating patches and occupied 8 x 8 x 1.9 mm^3 space. The bandwidth of the antenna was increased to 122 MHz, with a reduction on the radiation efficiency (0.55%) and the maximum gain (-37.96 dB) compared to the previous antenna. The measurement procedure for this antenna was identical with the previous one.

A study by **Abadia (2009)** highlighted an innovative implantable antenna miniaturization technique by connecting all the conductor path in 3D, resulting in a 3D microstrip antenna [85]. With a total dimension of 14 x 14 x 15 mm^3, this antenna achieved a return loss of -37 dB at 425 MHz for a simulation inside the muscle fluid. For the data validation, the antenna was submerged to a cylinder filled with muscle fluid (ε_r = 57.1 and σ = 0.796 S/m at 402 MHz). The measurement results generally agreed with the simulation data, with the return loss achieved was -39 dB at 427 MHz with a bandwidth 225 MHz. The maximum achievable gain was recorded at -28.5 dB. In another experiment, this group attempted another antenna design by maximizing the 3D structure of the packaging [86]. The proposed design was called multilayer pyramidal structure, which was basically a multilayer microstrip antenna with different substrate dimensions on each layer. The antenna, with total dimension of 13.1 x 8 x 5.2 mm^3, was operating on two frequency bands (MICS and ISM 2.4 GHz). Compared to the previous design, this antenna achieved a much lower bandwidth at 12 MHz with comparable maximum gain of -28.8 dB.

Another attempt to miniaturize an implantable antenna was done by employing a very high dielectric substrate **(Chien, 2010)** [87]. The antenna consisted of a substrate layer, which was created from ceramic substrate (ε_r = 28), and a monopole strip on top of it. No superstrate was included in the design. The antenna had a dimension of 18 x 16 x 1 mm^3 (just the antenna) and 18 x 16 x 1.4 mm^3 (with added Al_2O_3superstrate). Both antennas

were measured inside a skin mimicking liquid and achieved bandwidth and gain of 134 MHz and -24 dB (just the antenna) and 166 MHz and -26 dB (with the superstrate).

A study by **Sánchez-Fernández (2010)** proposed a multilayer implantable microstrip patch antenna with a capability of operating at double bands (MICS and ISM 2.4 GHz) [88]. This antenna incorporated a spiral printed with split ring resonator design, with the spiral radius of 6.7 mm and the total substrate height of 5.08 mm. At MICS band, the antenna produced a weak performance with a simulated return loss of around -9 dB at MICS band. The measurement provided a significantly better performance level with the achieved return loss of -16 dB at MICS band. The measurement was conducted with 1 layer MICS mimicking gel ($\varepsilon_r = 46$ and $\sigma = 0.7$ S/m at 402 MHz).

More advanced technique was investigated by **Ha (2011)** in an attempt to create a compact implantable antenna [89]. A novel zeroth-order resonance (ZOR) antenna, which was principally a patch antenna with addition of embedded inductors on the antenna conductor. With a dimension of 15.9 x 12.9 x 1.6 mm^3at 402 MHz in a single layer configuration, the antenna achieved a bandwidth of 9 MHz and maximum gain of -38 dB for a measurement inside homogeneous muscle phantom.

The most recent development from the implantable antenna design comes from this study by **Huang (2011)** [90], where a rectenna principle was implemented in the antenna design process. Rectenna is a rectifying antenna, a special antenna used to directly convert microwave energy to Direct Current (DC) electricity. This antenna employed a 4-layer microstrip antenna structure with the RO3210 selected for the substrate layers and a total dimension of 10 x 10 x 2.54 mm^3. At MICS band, this antenna produced a bandwidth of 115 MHz to cover both MICS band and 433 MHz band. The simulation was verified with minced pork medium, with dielectric characteristic of $\varepsilon_r = 55.2$ and $\sigma = 2.06$ S/m at 402 MHz.

A review of 18 implantable antenna designs has been presented to provide information about the implications of the shapes, dimensions, materials, configurations, and tissue materials to the antenna performances in terms of return loss, gain, bandwidth, and radiation efficiency. The following table (Table 4.2) will provide an easier access to compare each antenna model based on the review.

Table 4.2. Summary of antenna performance on the previous studies. The antenna parameters observed include dimensions, return losses, bandwidths, radiation efficiencies, maximum gains, and SAR values. Units are as stated.

Antenna	Resonant Frequency	Dimension (mm^3)	Model	Medium	Return Loss (dB)	Bandwidth (MHz)	Rad. Efficiency (%)	Gain (dB)	peak 1g avg SAR (W/kg)
[71]	402 MHz	29.4 x 19.6 x 6	MicrostripPIFA	2/3 Human Muscle	simulated: **-30** measured: **N/A**	20	N/A	-38	max input -30.6 dBW
[72]	402 MHz	40 x 32 x 8	MicrostripPIFA	human tissue fluid	simulated: **-20** measured: **-6**	40	0.25	N/A	209
[76]	1575 MHz	20 x 20 x 6	Hilbert PIFA	muscle	simulated: **-12** measured: **-N/A**	44.1	N/A	N/A	N/A
[52]	450 MHz	pi/4 x 10.1 x 10.1 x 3	Spiral Microstrip with capsule	human tissue fluid	simulated: **-23** measured: **-30**	70	N/A	N/A	N/A
[77]	402 MHz	pi x 7.5 x 7.5 x 1.9	3 layer MicrostripPIFA	human tissue fluid	simulated: **-44** measured: **-28**	50	0.31	-26	333
[78]	402 MHz	22.5 x 22.5 x 1.27	pi-shape MicrostripPIFA	skin-tissue simulating fluid	simulated: **-12** measured: **-20**	80	N/A	-25	215
[79]	402 MHz	22.5 x 18.5 x 1.9	meandered MicrostripPIFA	grinded pork leg	simulated: **-24** measured: **-34**	132	N/A	-27	280
[16]	2.33 GHz	5.25 x 5.25 x 4	3D Rotate Spiral	Vitreous Humour Liquid	measured: **-32.4**	151	N/A	-32.4	N/A
[80]	2-band 402 and 2400 MHz	22.5 x 22.5 x 2.5	Serpentine Microstrip	skin-mimicking gel	simulated: **-25** measured: **-24**	MICS: **141.91** ISM: **170.4**	N/A	MICS: **-24** ISM: **-8**	N/A
[81]	2-band 402 and 2400 MHz	23 x 23 x 2.5	Serpentine Microstrip	rat skin mimicking material	simulated: **-27** measured: **-10**	MICS: **27.3** ISM: **180.72**	N/A	MICS: **-27** ISM: **-10**	N/A
[83]	402 MHz	10 x 10 x 1.9	3 layer MicrostripPIFA	skin-tissue simulating fluid	simulated: **-30** measured: **-36**	50	0.61	-26	336
[84]	402 MHz	8 x 8 x 1.9	3 layer MicrostripPIFA	skin-tissue simulating fluid	simulated: **-26** measured: **-21**	122	0.55	-37.96	903

Table 4.2 continues…

Antenna	Resonant Frequency	Dimension (mm^3)	Model	Medium	Return Loss (dB)	Bandwidth (MHz)	Rad. Efficiency (%)	Gain (dB)	peak 1g avg SAR (W/kg)
[85]	402 MHz	14 x 14 x 15	3D Microstrip Spiral	muscle	simulated: **-63** measured: **-37**	225	N/A	-28.5	270
[86]	2-band 402 and 2400 MHz	13.1 x 8 x 5.2	multilayer pyramidal structure	Muscle	simulated: **-21** measured: **-22**	12	0.051	-28.8	289
[87]	402 MHz	18 x 16 x 1.4 18 x 16 x 1	CPW Fed Monopole	skin-tissue simulating fluid	measured: **-24** measured: **-25**	166 134	N/A	-50	741 797
[88]	2-band 402 and 2400 MHz	pi x 6.7 x 6.7 x …	Spiral Printed with Split Ring Resonator	1 layer skin model	simulated: **-9** measured: **-16**	MICS: **N/A** ISM: **500**	MICS: **23** ISM: **40**	N/A	N/A
[89]	402 MHz	15.9 x 12.9 x 1.6	ZOR Antenna	Muscle	simulated: **-18** measured: **-16**	9	N/A	-38	1.54
[90]	3-band 402, 433, and 2450 MHz	10 x 10 x 2.54	4 layer Microstrip	Minced Pork	simulated: **-20** measured: **-17**	MICS: **115** ISM: **70**	MICS: **39** ISM: **1.5**	MICS: **-7** ISM: **-15**	MICS: 341 ISM: 382

4.3. Antenna Model Selection

The review about various implantable antenna designs provided a good insight on factors affecting the implantable antenna operation. The knowledge gained from the articles was continually referred to during the design process. In this subchapter, an antenna model selection process will be presented. The process involved matching the antenna design with the constraints associated with the surrounding medium. The constraints will be defined and followed by the proposal of the most suitable design alternative.

4.3.1. Constraints

Designing an implantable antenna is a challenging task due to inevitable constraints that have to be considered, such as size, electrical characteristic of the surrounding materials, antenna material, as well as the SAR value limitation. In this case, the antenna is intended to be implanted inside a human eyeball with a diameter of around 24-25 mm. Consequently, an antenna that fits spherical dimension of 25 mm diameter is desirable.

Each part of human body has unique electrical characteristic, and the frequency dependability of each part makes it even more complicated. To satisfy the purpose of the antenna, Vitreous Humour was applied as the surrounding material in the simulation. As stated in Chapter 2, Vitreous Humour is a semisolid gel structure inside an eyeball that is based on water (98%) and contains small amount of solid matters in the form of collagen, vitrosin, and hyaluronic acids. Compared to other parts of human body, Vitreous Humour has a high relative permittivity and conductivity at 402 MHz (ε_r = 69, σ = 1.5296 S/m) [64], which makes it an inefficient medium for electromagnetic signal propagation. Due to the surrounding medium being a living tissue, it is imperative that the antenna has to be made of, or enclosed by, a biocompatible material. This is to avoid any bad reaction by the antenna's surrounding tissue.

Since the antenna is placed right in the middle of the tissue, the direct electromagnetic exposure to the surrounding tissue will result in higher SAR values. As mentioned in Chapter 3, the SAR values on any 10 g average of tissues must not exceed 2 W/kg.

4.3.2. Microstrip Antenna

Due to the constraints presented on the previous Section, it is inevitable that microstrip antenna model is adopted for the retinal prosthesis system purpose. A microstrip antenna consists of very thin metallic strip separated to a ground plane by a dielectric material,

typically referred to as substrate [70]. The advantages of microstrip antenna include compact and low profile characteristic, straightforward fabrication procedure, possibility of multiband operation, and low radar cross section (RCS – useful for military purposes) [91]. These aspects exist to compensate the fact that a microstrip antenna generally produces a narrow bandwidth, low power, and produces large insertion loss [70].

A microstrip antenna is a resonant-style radiator, which means one of its apertures has to have dimension around half of the wavelength. The resonant dimension of the antenna will also depend on the shape of the patch conductor. When a voltage is applied to the feeding point, a current will be excited on the patch and vertical electric fields will be generated between the patch and the ground plane. When the gap between the edge of the patch and the ground plane is half the wavelength, the radiated fields will create an efficient resonant radiator [91]. The feeding placement greatly influences the input impedance value, with a placement near the edge resulting high input impedance in contrast to low impedance when the feed is placed at the centre of the patch.

There are countless possibilities on the conductor shapes of the microstrip antenna and each pattern has its own characteristic. The most utilized conductor geometry is the rectangular and the square shapes. For this pattern, the length of the patch controls the resonant frequency while the width affects the impedance level as well as the bandwidth [91]. With this configuration, dual polarized radiation can be generated by placing the feeding pin along the diagonal plane. Due to the large area occupied by this geometry, rectangular and square patches generally produce higher bandwidth. Circular and elliptical shapes are also common in the microstrip antenna designs. With circular geometry, it has only one degree of freedom in its shape through its radius and it will affect the resonant frequency of the antenna. This pattern was rigorously investigated in the past due to its inherent symmetry which in turn allows more efficient computation on the full-wave analysis tool. With the advancement of full-wave design software, this geometry is becoming increasingly rare. Modern conductor geometries have evolved to something beyond the conventional shapes. In this case, traditional analysis on the geometry is very difficult due to the complex nature of current flow on the conductor. The utilization of electromagnetic solver is inevitable.

There are four excitation methods of microstrip antenna: edge fed, probe fed, aperture-coupled, and proximity-coupled. However, only the edge fed and probe fed techniques will be discussed in this Section. In the edge fed method, the microstrip feed-line is in direct contact with the patch conductor. The advantages of this approach include simple

fabrication, easy to model, and efficient, while the drawback is narrow bandwidth [91]. In the probe fed method, a probe extends through the ground plane and is connected to the conductor with the aid of soldering work. The probe is typically the inner conductor of a coaxial cable and its position on the conductor patch greatly influences the input impedance of the antenna. The advantages of implementing probe fed to a microstrip antenna are the isolation of the antenna to the ground plane and high efficiency. There are also issues in adopting this approach, namely low bandwidth, difficult to analyse accurately, and the generation of unintentional cross-polarized fields. However, despite these drawbacks, it has been decided that probe fed method will be adopted in the antenna design process to take advantage of the isolation between the antenna conductor and the ground plane. This would be useful in minimizing the spurious radiation.

4.3.3. Antenna Miniaturization

One of the constraints in the antenna design for the retinal prosthesis system is the size limitation. The diameter of a human eyeball is 25 mm, while the ideal antenna aperture for an operation inside Vitreous Humour at 402 MHz is 22.46 mm (Table 3.3). Although mathematically possible, the implementation of the ideal aperture is not very practical from the sustainability point of view. The potential implant will cause a lot of pressure to the surrounding eyeball components and there is little option for the placement of the antenna other than along the centre line.

The proposed solution to counteract this problem is to reduce the size of the antenna. The performance of the resized antenna would inevitably be inferior compared to the one in ideal size, but there are some miniaturization techniques to prevent significant penalty to the antenna performance. They are [92]: a) use lump-element loaded antenna, b) use high permittivity substrate or superstrate, c) short circuit to ground plane, and d) geometry optimisation.

The idea of using lump-element as an extension of the antenna conductor is raised to counteract strong reactive input impedance caused by the antenna dimension reduction to less than half a wavelength. The implementation of this technique will result in lower efficiency and smaller bandwidth. This technique has been applied in one of the previous antenna designs [89].

Modification on substrate material on a microstrip antenna will produce different antenna characteristic. The adoption of high permittivity material as a substrate will particularly lower the resonant frequency of the antenna based on the principle that the

wavelength is shorter inside the material. This advantage comes in expense of lower bandwidth and gain of the antenna. A high dielectric ceramic material $MgTa_{1.5}Nb_{0.5}O_6$ (ε_r = 28) has been specially developed for an implantable antenna.

The idea of creating a connection between a conductor and a ground plane is to utilize the ground plane as a virtual half of dipole arm in respect to the entire antenna. This method has been widely used (as PIFA) because it is very easy to implement. In Table 2, it can be seen that majority of the microstrips antenna incorporate PIFA configuration in their designs.

Geometry adjustment of an antenna, particularly microstrip antenna, includes modification on the patch pattern as well as substrate geometry and configuration. However, with this optimisation technique, the application of the antenna is limited to that specific purpose. Many studies have incorporated innovative geometry optimisation approach such as stacked pyramidal structure [86] or 3D rotated dipole antenna [16] to boost the performance of the antenna.

In addition to design problems, there are also problems associated with small antenna measurements. Due to the small ground size, the antenna is neither balanced nor unbalanced, makes it difficult to obtain an accurate measurement result. In addition, spurious radiations from the coaxial cable produce a great degree of distortion to the antenna characteristic. The polarizations are also difficult to define due to the conductor length being shorter than the wavelength [92].

4.4. Summary

This chapter has provided an insight on the underlying principle of an antenna, including its operation in free space as well as inside high dielectric and conductive medium like Vitreous Humour. An extensive review on the previous implantable antenna designs published on the journal articles were also presented for an indicator on how an implantable antenna should behave. The information obtained from the theory, combined with the past antenna designs, was applied in determining the design of the proposed antenna. Several constraints were listed as potential obstacles in the design process. As a result, microstrip antenna was selected as the antenna type and miniaturization technique was also discussed as a measure to comply the limited space available. On the next chapter, the simulation aspect of the study would be revealed. The evolution of the antenna design through multiple modifications would also be disclosed, followed by the simulation of the antenna in the real case scenarios.

Chapter 5
Simulation

Previously, the reader has been exposed to the basic principle of the antenna for its operation in both free space and in a high dielectric and conductive medium, which ultimately led to the introduction of the constraints associated with the antenna's circumstance. A study of the previous implantable antenna designs on the publications was also conducted to compile a typical antenna performance in similar conditions. It was decided that a microstrip antenna was the most suitable antenna model for this mission due to several reasons including its compactness and simplicity. In this chapter, the simulation algorithm of the proposed antenna based on the information gathered in Chapter 4 will be presented. It will be initiated with a brief review on the available techniques for solving the numerical calculation including their strengths and weaknesses, and then followed by a comprehensive process of designing the proposed antenna in the selected software package, including the defined assumptions and conditions. In the next part, the development process of the antenna will be presented systematically in order to obtain the final design of the proposed antenna. In the end, several real case situations will be applied to the antenna to understand the antenna characteristic in each circumstance, which will be of absolute importance prior to commencing the measurement procedure.

5.1. Electromagnetic Software Choices Based on Numerical Technique

Due to the complex geometry and structure of the proposed antenna, the adoption of a particular numerical technique to solve Maxwell's equations is inevitable. There are several techniques available to solve the equations, whether in differential or integration forms, and each technique provides optimal computation for different configurations. Three techniques have been investigated to gain fundamental knowledge about the strength and weakness of each approach and ultimately to decide the best solver for the proposed antenna. The techniques under investigation are Finite-different Time Domain (FDTD) method, Finite Element Method (FEM), and Finite Integration Technique (FIT).

5.1.1. FDTD

This method was first proposed by Allen Taflove and Morris E. Brodwin for the purpose of simulating EMF exposure on human tissues [93] by solving time-dependent Maxwell's equations in their differential forms. It has been discussed in Chapter 4 that the fundamental principle of electromagnetic wave propagation was based on the continuous variation of electric and magnetic flux (Equations (4.3) and (4.4)). By solving the value of electric and magnetic field at the present state, the next state of both fields can be determined. This will subsequently provide the propagation characteristic of the electromagnetic wave. When only one dimension is considered, the calculation is relatively simple. However, when it involves multiple dimensions, the calculation becomes more complicated.

With FDTD technique, a certain number of samples are created by segmenting the fields propagating in all directions over the volume of interest and over a period of time. This can be represented visually by a cube of grid voxels, which is popularly called Yee lattice (Figure 5.1) [94]. Each grid in this cube signifies a coordinate resembling the electric and magnetic field vectors in x, y, and z directions and the size of each grid must be only a fraction of its wavelength to produce an isotropic electromagnetic field. Yee used central finite-difference approximations that were second-order accurate in space and time to represent spatial and temporal derivatives of F, a function of space and time [94].

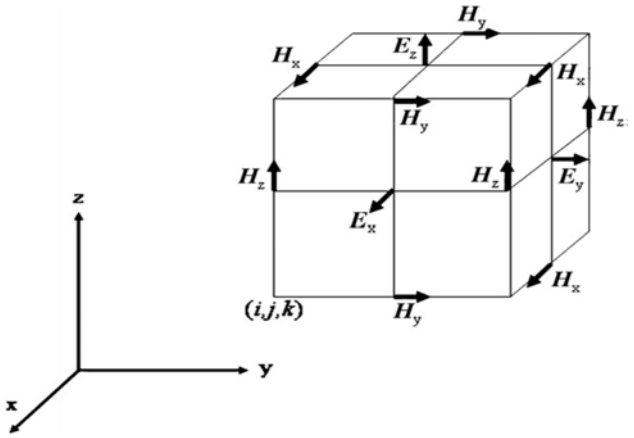

Figure 5.1. Electric and magnetic field components representation in Yee lattice (Kane, Y., 1966).

It can be observed from Figure 5.1 that Yee interleaved components of E and H at spatial intervals of δ/2. By applying explicit finite-difference equations to these components, the value of a component of E or H at any position on the lattice can be determined from its previous value and the previous values of the H or E components at adjacent grid positions [95]. Determining boundary condition of the geometry is essential

for FDTD solving technique to minimize reflections at the boundary due to finite computation domain [93].

The main weakness of FDTD is the handling of curved surfaces or irregular boundary shapes, which would result in "Staircasing Effect". To avoid that, an adaptive grid or a high spatial resolution grid would be needed, with a compromise of higher memory requirement. Another difficulty is that with this technique, the E and H fields are calculated everywhere within the computational domain. As a result, a calculation of far field values will require a very large computational space. This will subsequently result in a higher memory requirement [95].

Commercial software packages that employ FDTD as the numerical technique include CONCERTO by Vector Fields, EMPIRE XCcelTM by IMST GmbH, FIDELITY by Zeland Software, GEMS by 2COMU, SEMCAD X by SPEAG, as well as XFDTD by Remcom [93].

5.1.2. FIT

A different approach on solving Maxwell's Equation was introduced by Thomas Weiland [93], by transforming integral-form equations into a set of matrix equations on an orthogonal dual grid pair for spatial and temporal domain. In this technique, the integral form of the equations is discretised on a dual grid complex in space and time (Figure 5.2).

A typical transient simulation task is described by a known geometry and material configuration, as well as boundary conditions and antenna characteristics for the emitting and receiving modes. The application of FIT using a dual-cell complex in space and time can be visually represented by the geometry in Figure 5.3 [96]. The idea is to use the midpoint to approximate the integral appearing in the governing equations, as can be observed in Figure 5.3.

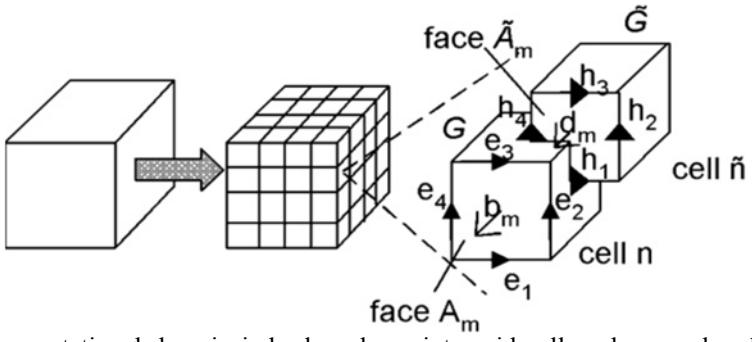

Figure 5.2. The computational domain is broken down into grid cells, where each cell comprises of a component in two orthogonal grids (Marklein, R., 2002).

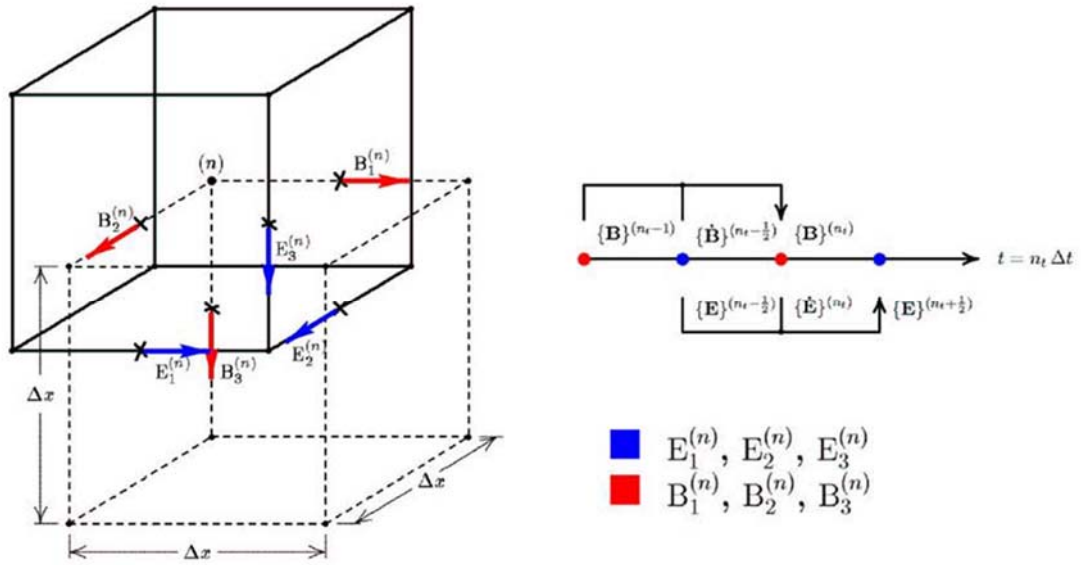

Figure 5.3. The spatial and temporal grid complex of FIT and the allocation of the local discrete field quantities (Marklein, R., 2002).

The main strength of this approach is the discrete time-stepping process, which is helpful in avoiding problems from simultaneous equations and matrix inversion. This would also enhance the accuracy of the calculation results as well as the ability to perform computation on an anisotropic non-linear medium. Microwave Studio® by CST GmbH is one example of electromagnetic software package that employs FIT as its numerical technique.

5.1.3. FEM

This approach attempts to solve Maxwell's Equations in their differential form by discretising all variables related to the problem that includes geometry, excitation, scatterers, and boundary constraints [93]. Adaptive meshing is implemented in this technique, which means that large mesh element is employed for larger and more uniform geometries, while smaller mesh is employed for smaller and more complex geometries to preserve their details.

The mechanism of computation using this technique can be divided into four steps: 1) discretization of the problem domain, 2) selection of interpolation functions, 3) formulation of the system of equations, and 4) solution of the system of equations [93]. The main strength of this technique is the adoption of adaptive meshing, which means that the computation of complex geometries will yield more accurate results. The disadvantages

of FEM include the fact that FEM obtains only approximate solutions as well as the need of the user to avoid grid dispersion errors during the design process. The latter implies that the user has to pay special attention when specifying the simulation parameters to obtain accurate results. HFSS^{TM} from Ansoft is one of the commercially available software packages that employ FEM approach and it will be utilised as the main antenna design and simulation tool in this project.

5.2. Simulation Configurations

The following flow chart will provide a clear idea on the process of designing and simulating an antenna using HFSS software package.

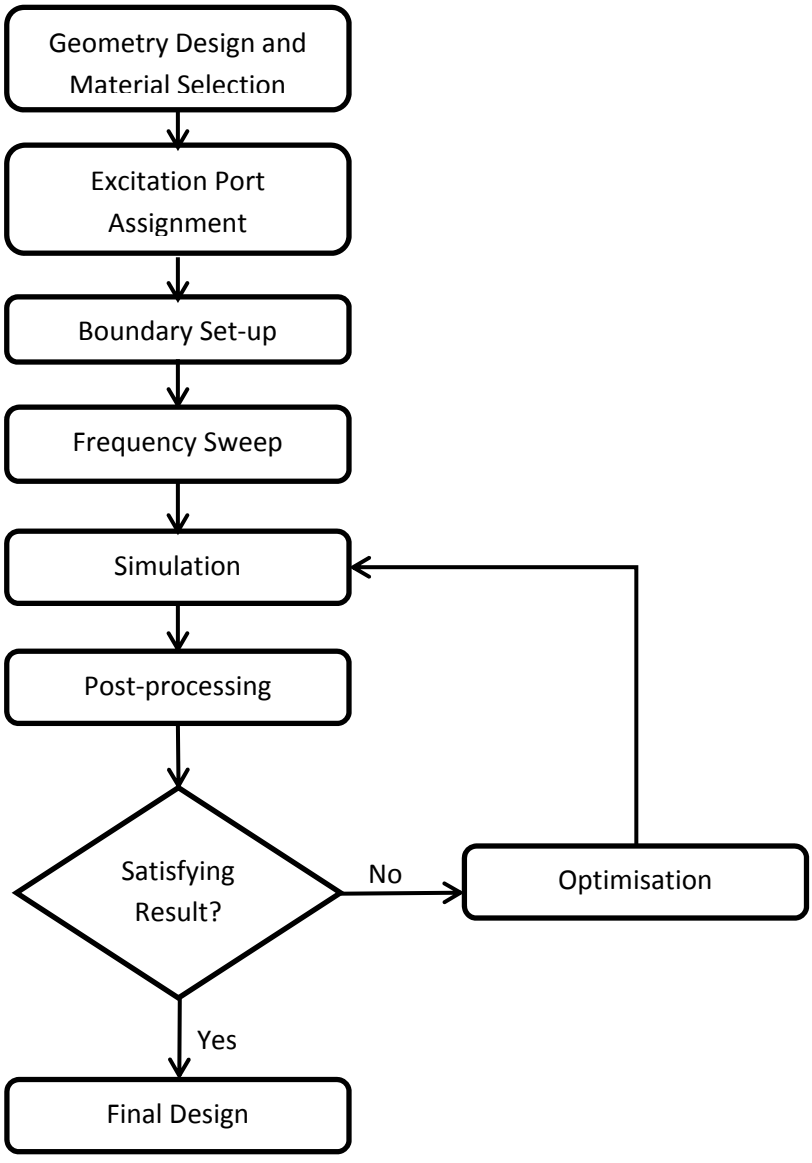

Figure 5.4. A flow chart representing the algorithm of designing and simulating an antenna in HFSS software package.

5.2.1. Geometry Design and Material Selection

The first step in the simulation process is to design all the geometries involved in the configuration, as presented in the flow chart above (Figure 5.4). The structure can either be designed with the aid of design tool provided by the HFSS software or imported from other 3D modeller software such as AutoCAD and SolidWorks. It is essential that the model is meticulously designed to resemble the actual operating condition of the device to obtain accurate results from the simulation. It could be seen in the latter part of this chapter that even a slight change in the structure geometry would create a great discrepancy to the final result.

A material has to be assigned for each three dimensional geometry built. HFSS provides a set of common metal and dielectric materials in its library. For other non-standard materials that are not listed on the library, such as human tissues or other special dielectric materials, a new entry can be added to the library by entering the electrical characteristic of the material that include relative permittivity, relative permeability, and conductivity. The list of materials that have been employed in the antenna and its simulating medium in this project is presented in Table 5.1.

Table 5.1. List of materials that were assigned to the antenna and medium geometry. The shaded cells signify custom materials added to the library.

Material	**ε_r**	**σ (S/m)**	**tan δ**
Silicone (PDMS) [from datasheet]	2.72	0	0.04
Liquid Crystal Polymer [83]	2.95	0	0.0023
Vitreous Humour (402 MHz) [64]	69	1.53	0.99
Celluloid [97]	4	0	0
Rogers 3210 [from HFSS]	10.2	0	0.003
Copper [from HFSS]	1	5.8×10^6	0
Silicon [from HFSS]	11.9	0	0
Teflon [from HFSS]	2.1	0	0.001
Air [from HFSS]	1.0006	0	0

5.2.2. Excitation Port Assignment

The next step is to assign an excitation port on the geometry to specify how the electromagnetic wave enters the structure. In HFSS, there are two types of excitation port that are applicable to this work: wave port and lumped port. Wave ports represent places in the geometry through which excitation signals enter and leave the structure. They are most

commonly used in waveguide structures. Lumped ports have the same function as wave ports except that they can be located internally and have complex user-defined impedance. They compute S-parameters directly at the port. For the specific purpose of this project, lumped port was selected as the excitation port due to the placement of the whole structure inside a conductive medium. As can be observed from Figures 5.5, the port was assigned on the outer face at the end of the coaxial connector.

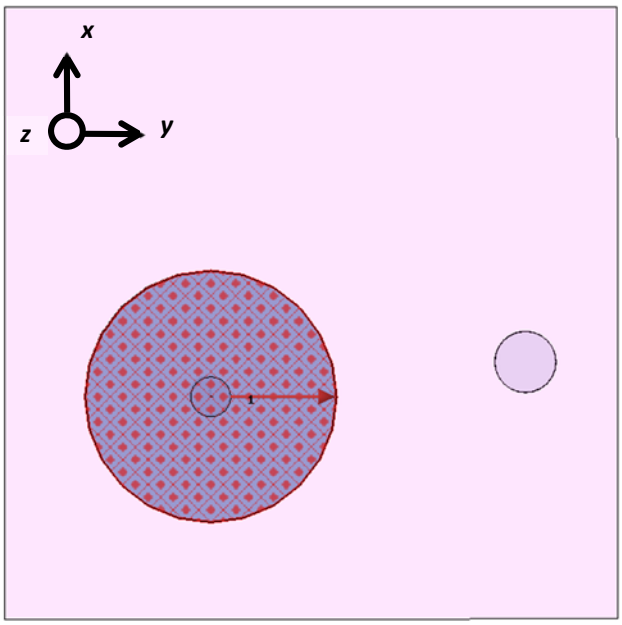

Figure 5.5. The wave port was positioned at the end of the coaxial connector.

5.2.3. Boundary Set-up

Boundary conditions specify the field behaviour at the edges of the problem region and object interfaces. In HFSS, there are different types of boundaries for implementation on different components of the device:

- *Perfect E*: Represents a perfect conductor surface. It is employed to simulate an ideal lossless system operation.
- *Finite Conductivity*: Represents an imperfect conductor with adjustable conductivity of the component. It is employed to simulate a realistic operation depending on the conductor material.
- *Radiation*: Represents an open surface from which energy can radiate. This boundary is useful for simulating a far field operation of the antenna with a limited simulation space.

Figure 5.6 to 5.9 show the assignment of boundary conditions to different component of the antenna.

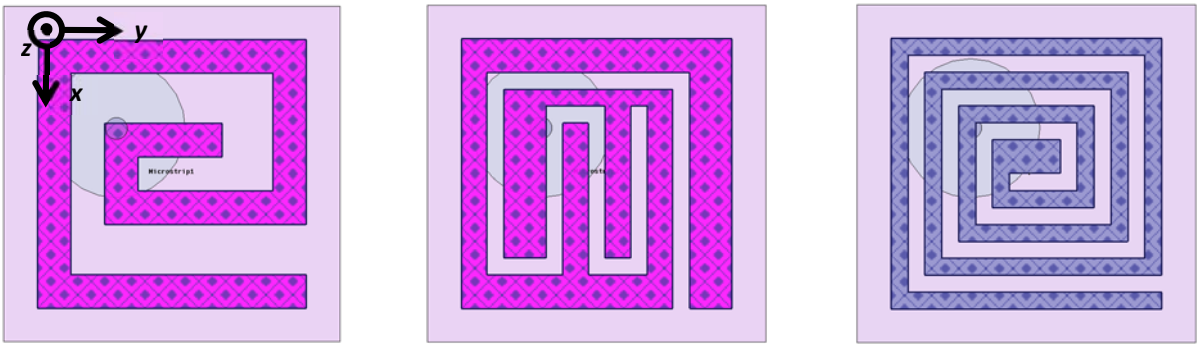

Figure 5.6. Finite conductivity boundary applied to the 3 microstrip conductor paths.

Finite conductivity boundary was assigned to all three microstrip conductors of this antenna (Figure 5.6). The decision of using finite conductivity instead of perfect E boundary for these conductors is based on the objective of obtaining the real performance results of the antenna. The conductivity of the conductor was set to 58.8 x 10^6 S/m to resemble the copper material. The same boundary condition was applied to the ground plane of the antenna (Figure 5.7).

Figure 5.7. Finite conductivity layer on the ground plane.

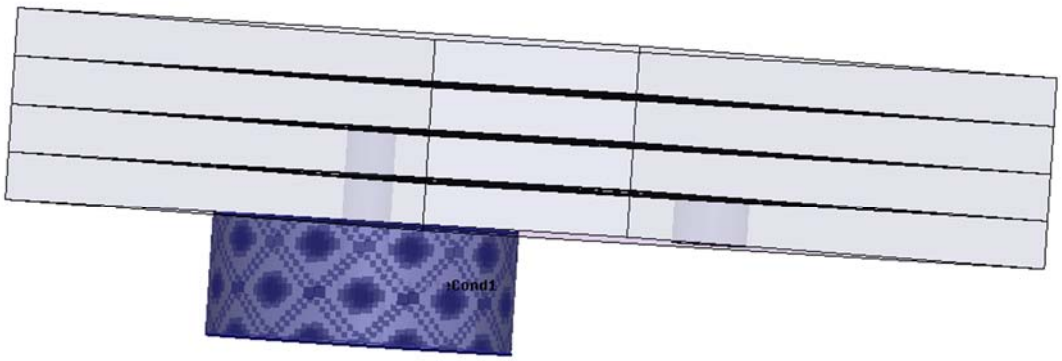

Figure 5.8. Finite conductivity boundary applied to the outer coaxial cylinder to resemble the outer conductor of the coaxial connector.

A conductive boundary layer was also assigned on the outer side of the coaxial connector to resemble the outer conductor of the connector and the cable (Figure 5.8). The outer face of the coax cylinder was selected, and then was assigned with a finite

conductivity boundary layer with copper's conductivity value to resemble the structure of a coaxial connector.

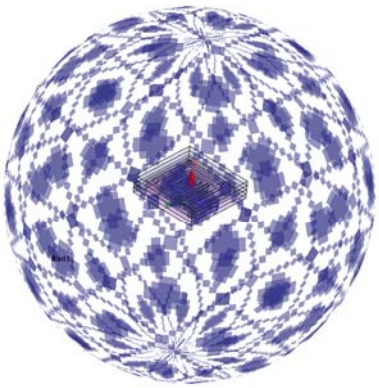

Figure 5.9. A vacuum or air-filled sphere was created as a platform of implementing radiation boundary to the structure.

Finally, a radiation boundary was set up in a sphere shape enclosing the entire antenna structure (Figure 5.9). The size of the sphere should ideally be a quarter wavelengths in every direction in addition to the dimension of the antenna to ensure full electromagnetic wave far field radiation. However, in this case, a quarter of free space wavelength is significantly longer (186.6 mm) relative to the antenna aperture (10 mm) and hence it requires large amount of memory. Hence, a smaller boundary diameter was specified with the condition that it does not compromise the performance of the antenna. The diameter of the sphere in this simulation was 23.32 mm.

5.2.4. Frequency Sweep

A solution frequency and its range have to be selected before executing the simulation. When specifying the frequency range, it is helpful to define a large range of frequency initially for a larger range observation on the resonance of the antenna. With a better knowledge on which range the antenna is operating, it is imperative to narrow down the range for a better data resolution. In this simulation, the operating frequency was set to 402 MHz with the sweeping range of 300 to 500 MHz.

5.2.5. Simulation and Post-processing

The next step is executing the simulation. When there are no errors, the simulation will run with varying time frame depending on the meshing. Once completed, antenna parameters such as return loss, gain, and radiation pattern can be presented in various display format. The return loss of the antenna is presented in dB unit according to the specified frequency range. For the gain and radiation pattern, the data can be presented in 2D or 3D views.

5.2.6. Optimisation

The flowchart in Figure 5.4 indicates that the simulation and the optimisation stages are done iteratively until the antenna performance meets the requirement. The optimisation process is generally done by adjusting one or more variables progressively and observing the response on the next simulation. There has been a study on antenna optimisation process by Soontornpipit [71] and it has served as a good guideline for optimizing the proposed antenna. It was stated that a serpentine antenna has higher resonant frequency compared to spiral antenna for the same physical length. Longer conductor path and higher permittivity substrate material would lower the resonant frequency of the antenna. The substrate thickness was also analysed in this study with a verdict that thicker substrate would make the antenna appear electrically longer and hence slightly lower resonant frequency.

5.3. Antenna Design Process

In this subchapter, the development of the antenna from the initial design until the final design would be presented, together with its justification based on the performance results of each stage. When the design was finalised, it would be configured in 4 different scenarios. More detail about this would be presented on Section 5.3.3.

5.3.1. Model Development Based on Empirical Approach

The characteristic of an implantable microstrip antenna is very difficult to predict due to the complex human tissue characteristic and as a consequence the basic antenna design principle for general antennas could not be applied, as evident later in this Section. Alternatively, an experiment based approach with the aid of electromagnetic simulation software was implemented in this work in order to produce a final implantable antenna design with a strong performance.

5.3.1.1. Modification #1 – Implementation of Liu's antenna [83]

Initially, a specific antenna design from [83] was adopted with a consideration of its strong performance relative to its compact size. This antenna, implemented with 3-layer microstrip antenna geometry, was designed for operation inside human skin tissues. Slight modifications were made by reducing the substrate dimension from 10 x 10 x 1.9 mm^3 to 9 x 9 x 1.8 mm^3 as well as the feed and ground pin radius to 0.1 mm to adjust with a change

of medium to Vitreous Humour liquid. The changes can be seen by comparing the original design by Liu [83] in Figure 5.10 and the modified antenna in Figure 5.11.

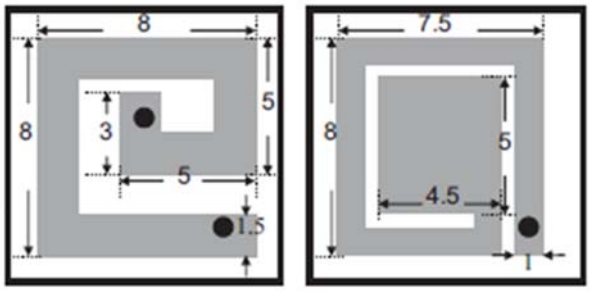

Figure 5.10. The conductor pattern on layer 2 and layer 3 of an implantable antenna design by Liu [83]. This design was employed as the initial design of the proposed antenna. All the units are in mm.

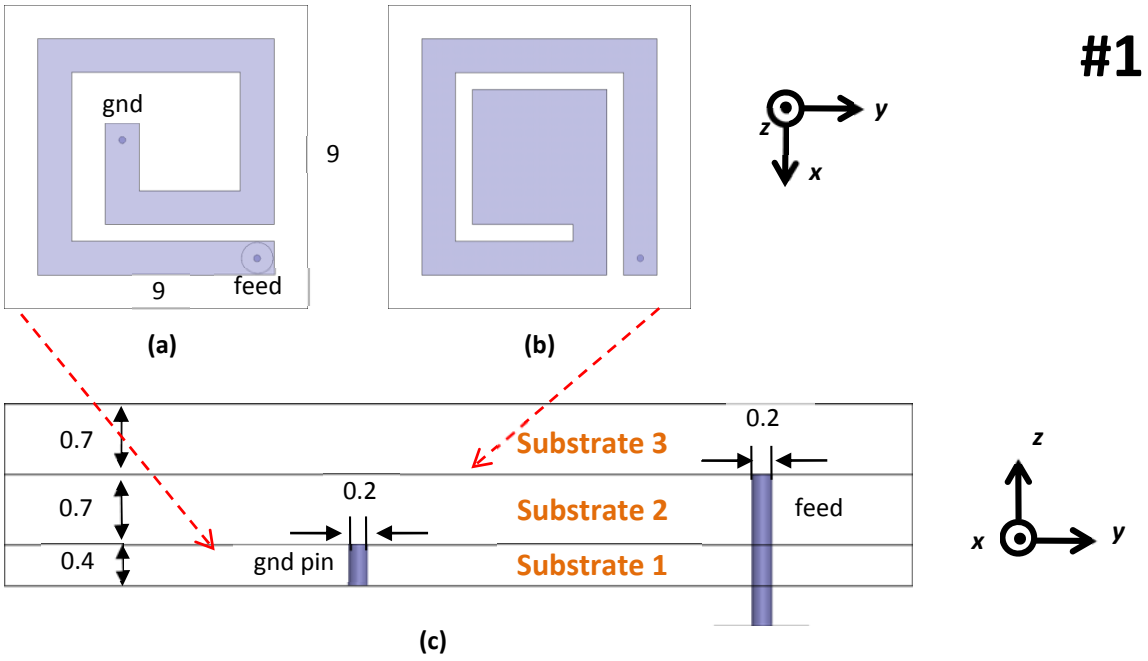

Figure 5.11. The implementation of Liu's antenna with some modifications including the substrates' dimension and the pins' sizes. The design can be observed on (a) layer 2, (b) layer 3, and (c) the side view of the structure. The first layer was just simply a ground layer from copper and was not shown in this image. All units are in mm.

Figure 5.11 shows the representation of the antenna design based on [83] with a slight modification. The red dashed line indicates the position of each layer with respect to the side view of the antenna. All the substrates were made of Rogers RO3210 material and the coaxial connector dielectric was of Liquid Crystal Polymer (LCP), as part of the MHF® mini coaxial connector implemented in [83]. The modified antenna was resonant at 403.5 MHz with a 10 dB bandwidth of 50.8 MHz, which was satisfying. However, the maximum gain of -51.58 dB was considered too low and therefore modifications were made to

improve this number. The radiation pattern of the antenna was as expected, an omnidirectional pattern around the z-axis.

5.3.1.2. Modification #2 – Conductor path modification on layer 2 and 3

The antenna #1 was modified by extending the conductor length on layer 2 as well as the slot length on layer 3 in an attempt to achieve higher maximum gain. The feed pin position was left at the same position, but the ground pin was slightly shifted in –x direction to achieve a more optimal resonance condition. The resulting pattern for each layer as well as the pins placement can be observed from Figure 5.12.

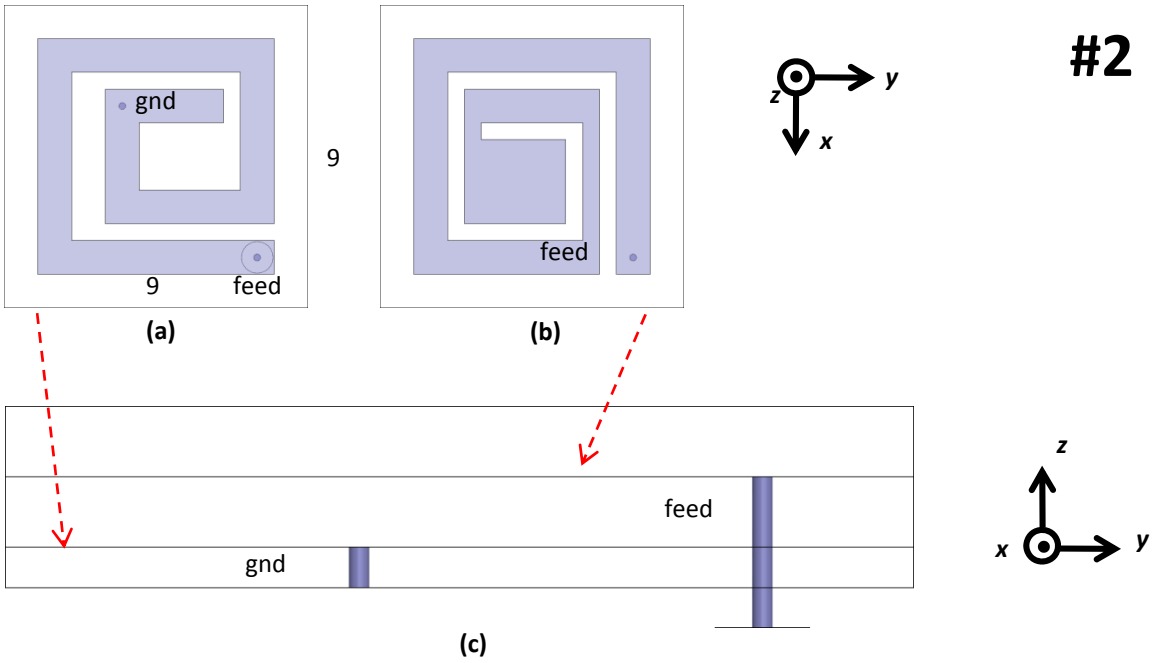

Figure 5.12. Longer conductor paths on both layer 2 and 3 were implemented in this modification. The design can be observed on (a) layer 2, (b) layer 3, and (c) the side view of the structure. The first layer was just simply a ground layer from copper and was not shown in this image. All units are in mm.

Modification #2 featured a slight improvement to the maximum gain (-50.98 dB), but at the same time it shifted the resonance frequency to 375 MHz with 44.8 MHz bandwidth. With the resonance frequency and the bandwidth, the antenna was able to perform optimally at the frequency range of 352.6 to 397.4 MHz, which was outside the MICS band range. The maximum gain improvement of 0.6 dB in this version was not very significant, but in this version a new knowledge was acquired, that longer conductor path in the implantable multilayer microstrip antenna resulted in a drop of resonance frequency. This information would be useful for the next modifications applied to the antenna.

5.3.1.3. Modification #3 – Conductor path modification on layer 3

In modification #3, the layer 2 of the antenna was kept identical to the previous version, but the slot pattern on layer 3 was altered (Figure 5.13). Another change in this version included the positioning of the feed pin at layer 3, which was directed to the slot instead of the conductor path. The result of this action was a shift of resonant frequency beyond 500 MHz. The maximum gain of the antenna was also negatively affected, with a 1.46 dB decrease to -52.44 dB. From modification #2 it had been understood that longer conductor path on the microstrip antenna lowered the resonant frequency. The action taken on modification #3 implied that the conductor path of the whole structure is shorter, with the feed pin only connected to the conductor path on layer 2. Based on this knowledge, the resulting geometry would create the opposite effect to what was present on the modification #2, a higher resonance frequency. The simulation results successfully verified the hypothesis.

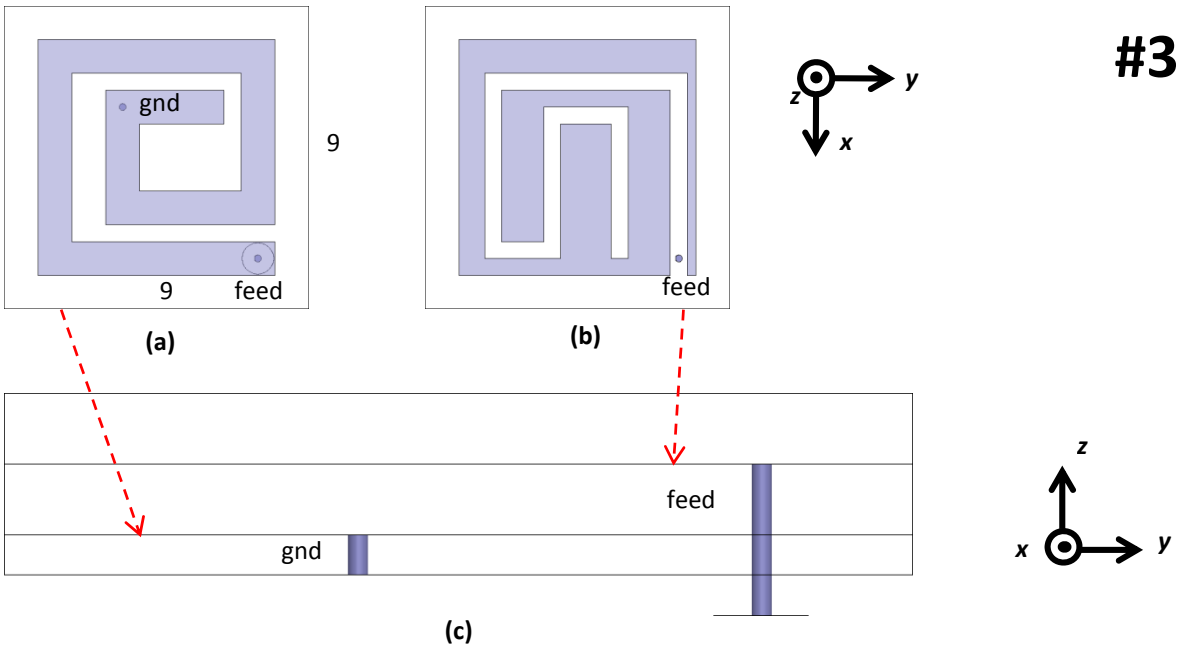

Figure 5.13. Modification #3 featured meandered slot on layer 3, with the rest of the structure kept the same. The design can be observed on (a) layer 2, (b) layer 3, and (c) the side view of the structure. The first layer was just simply a ground layer from copper and was not shown in this image. All units are in

5.3.1.4. Modification #4 – Longer slot path on layer 3

In modification #4, the slot pattern on layer 3 was remodelled to accommodate a connection between feed pin and the conductor, as can be seen in Figure 5.14. The solitary modification produced a geometry that was similar to the antenna on modification #2 with a longer meandered slot path on layer 3. From the results' point of view, this antenna was

resonant at 347.9 MHz with a bandwidth of 38.4 MHz which effectively meant that the antenna operation was beyond the MICS band. On the positive side, this antenna produced a strong performance in the maximum gain at -50.03 dB.

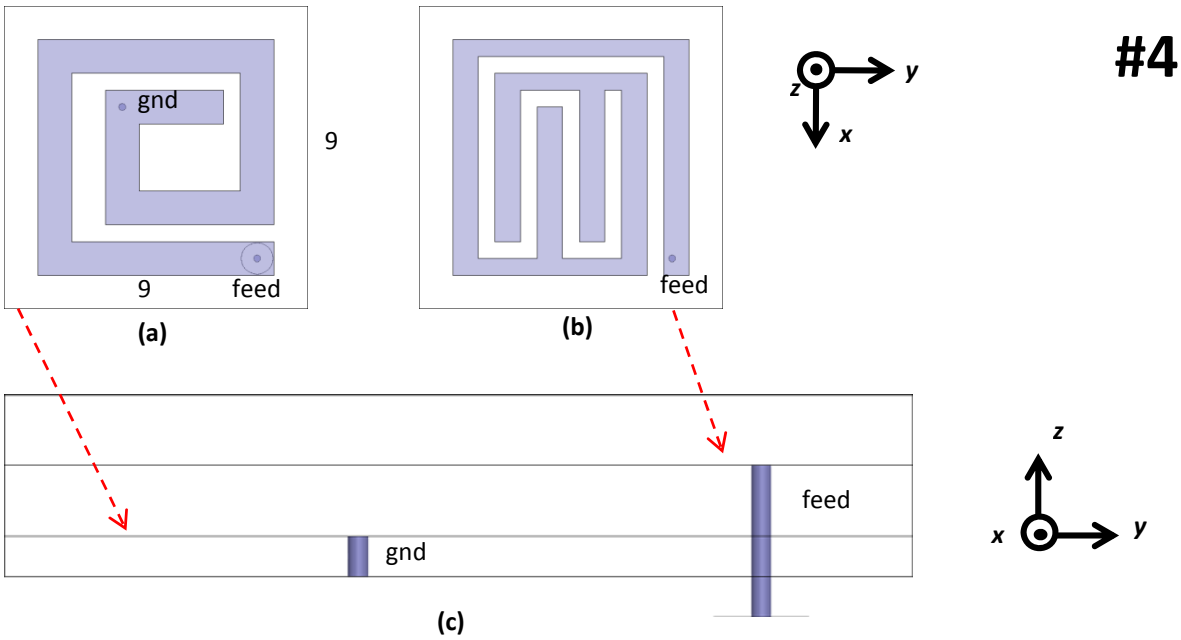

Figure 5.14. Longer slot path on layer 3 can be observed as a result of modification #4. Also, take a look at the feed pin position on layer 3, it was connected to the conductor instead of the slot path. The design can be observed on (a) layer 2, (b) layer 3, and (c) the side view of the structure. The first layer was just simply a ground layer from copper and was not shown in this image. All units are in mm.

5.3.1.5. Modification #5 – Change in substrate dimensions

The next modification, #5, the focus was to achieve an operating frequency band that covers the MICS band while maintaining the maximum gain of the antenna. The modifications applied in this stage included a change in the dimension of all three substrates (the length, the width, and the height) as well as new positions for both feed and ground pins (Figure 5.15). Each substrate layer was now 10 x 10 mm^2 large with a thickness of 0.635 mm, with the material remained the same. The conductor paths on both layer 2 and layer 3 were also modified by a small degree to conform to the larger substrate area. The change of substrate heights was implemented in order to comply with the standard height of RO3210 material, which is 0.635 mm. These set of changes produced a good resonance at 405.16 MHz with a bandwidth of 55.6 MHz. The maximum gain was slightly lower at -50.87 dB. Overall, the results showed a promising outcome, but the attempt to increase the antenna's gain had not yielded any significant breakthrough.

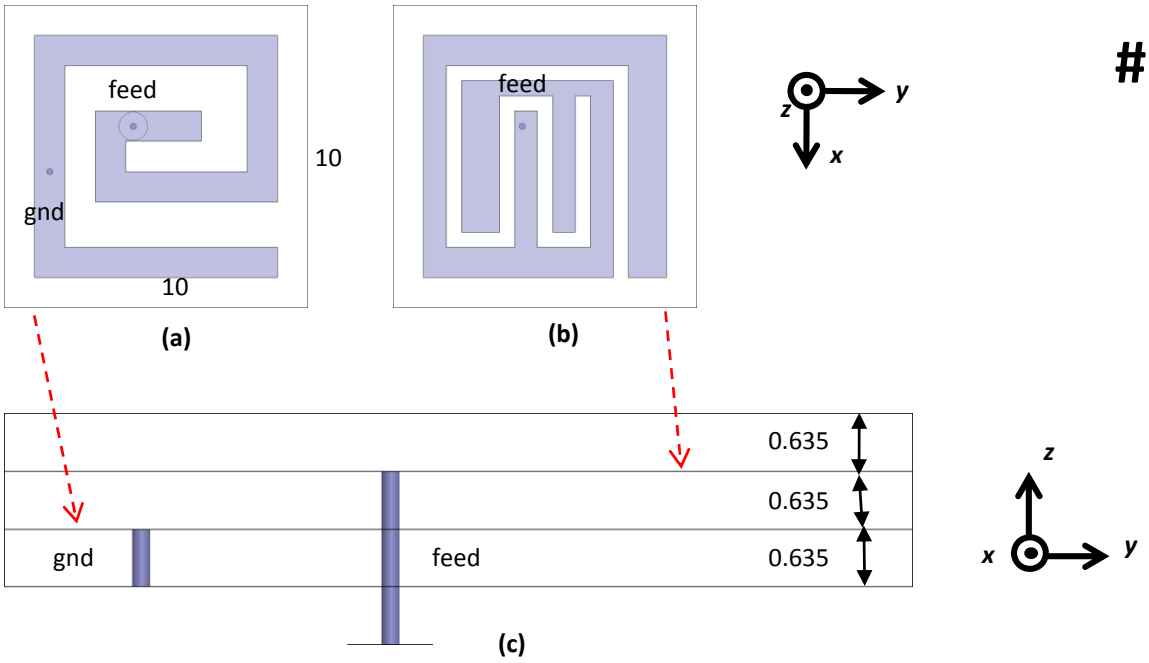

Figure 5.15. All the three substrates were modified to have the same heights, 0.635 mm, to comply with the default thickness of the material. Larger area of the entire substrate layer can also be observed as a result of this modification. The design can be observed on (a) layer 2, (b) layer 3, and (c) the side view of the structure. The first layer was just simply a ground layer from copper and was not shown in this image. All units are in mm.

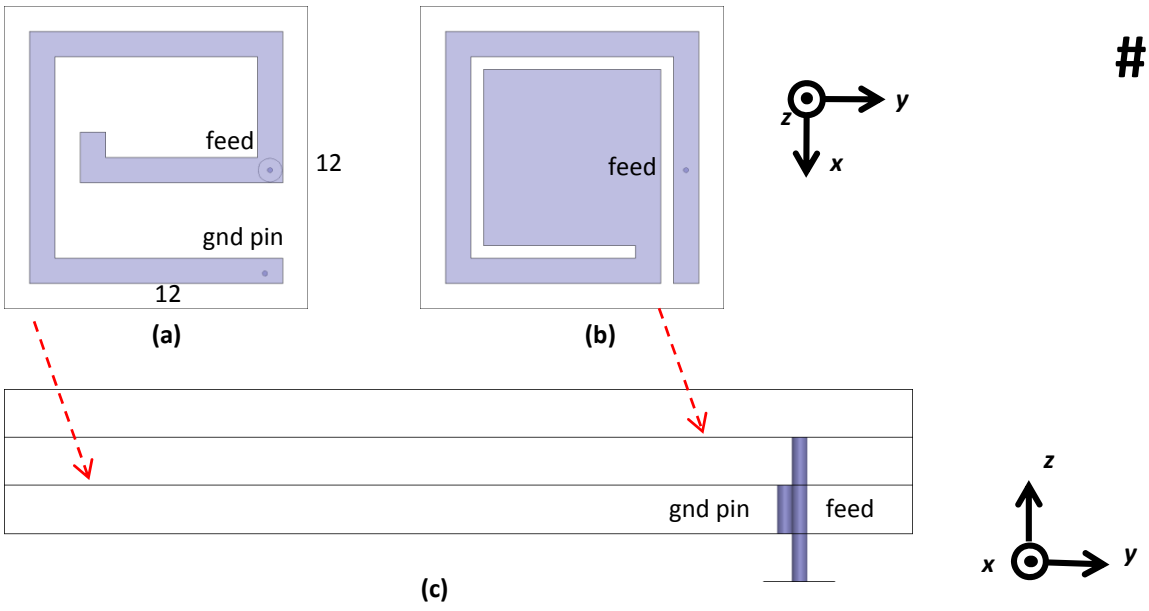

Figure 5.16. The conductor and slot path on layer 2 and 3, respectively, resembled the pattern on the initial model (Figure 5.15) with an enlarged substrate area from 9 x 9 mm^2 to 12 x 12 mm^2. This was done to study the effect of larger area to the overall antenna performance. The design can be observed on (a) layer 2, (b) layer 3, and (c) the side view of the structure. The first layer was just simply a ground layer from copper and was not shown in this image. All units are in mm.

5.3.1.6. Modification #6 – Larger substrate area

In the next modification, the substrate area was enlarged to 12 x 12 mm^2 to see if there was any connection between a larger area and an improved maximum gain of the antenna (Figure 5.16). The slot path pattern from antenna modification #1 was adopted with a change in both feed and ground pin placement. The results showed that the maximum gain of the antenna was greatly improved (-47.95 dB) but at a cost of lower resonant frequency at 362.74 MHz with 32.8 MHz bandwidth, which effectively ruled out the antenna operation at MICS band. The development of antenna geometry with the substrate size of 12 x 12 mm^2 was not continued due to a concern that the whole structure being oversize when an additional encapsulation layer was integrated into the geometry.

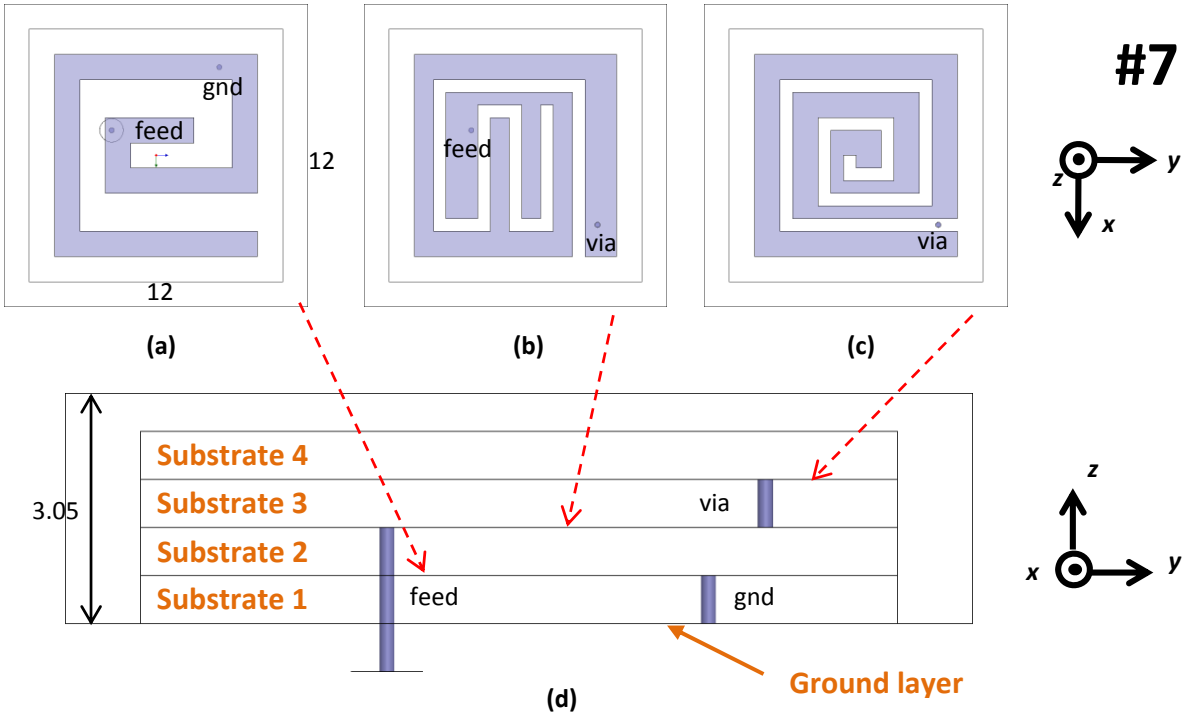

Figure 5.17. In modification #7, an extra substrate layer with the same material and dimension as the other three was added. The whole structure was encapsulated by Silicon material with the dimension of 12 x 12 x 3.05 mm^3 that covered the ground layer upwards. The design can be observed on (a) layer 2, (b) layer 3, (c) layer 4, and (d) the side view of the structure. The first layer was just simply a ground layer from copper and was not shown in this image. All units are in mm.

5.3.1.7. Modification #7 – Addition of a substrate layer and an encapsulation

For the first time, in modification #7, an encapsulation layer was introduced as an attempt to add biocompatibility attribute to the antenna. The material of the encapsulation layer was Silicon (ε_r = 11.9) with a dimension of 12 x 12 x 3.05 mm^3, completely encapsulating the antenna from the ground layer upwards (Figure 5.17d). An extra substrate layer was also added at the top of the structure with a rectangular spiral conductor path pattern

(Figure 5.17) as an attempt to improve the return loss performance. The feed and ground pins were repositioned to obtain the best return loss performance out of the geometry.

The 4-layer microstrip antenna with a Silicon encapsulation was resonant at 402 MHz with a bandwidth of 10.8 MHz and a maximum gain -44.44 dB. This was definitely a significant improvement from any of the previous antenna geometries. However, more modifications were conducted to further investigate the influence of each parameter for more optimal performance of the antenna.

5.3.1.8. Modification #8 – Removal of substrate 4 and enclosure enlargement

In modification #8, the fourth substrate layer was removed and the enclosure area was increased to 13 x 13 mm^2 (Figure 5.18). The position of the feed and ground pins was also rearranged to achieve the desired resonant frequency. The performance of this antenna geometry was slightly inferior in terms of maximum gain (-45.98 dB), but it was compensated with a higher bandwidth (19.2 MHz). This result implied that the presence of the 4^{th} substrate layer was important in achieving a greater gain, but in doing so, it also lowered the resonance frequency as well as the bandwidth of the antenna.

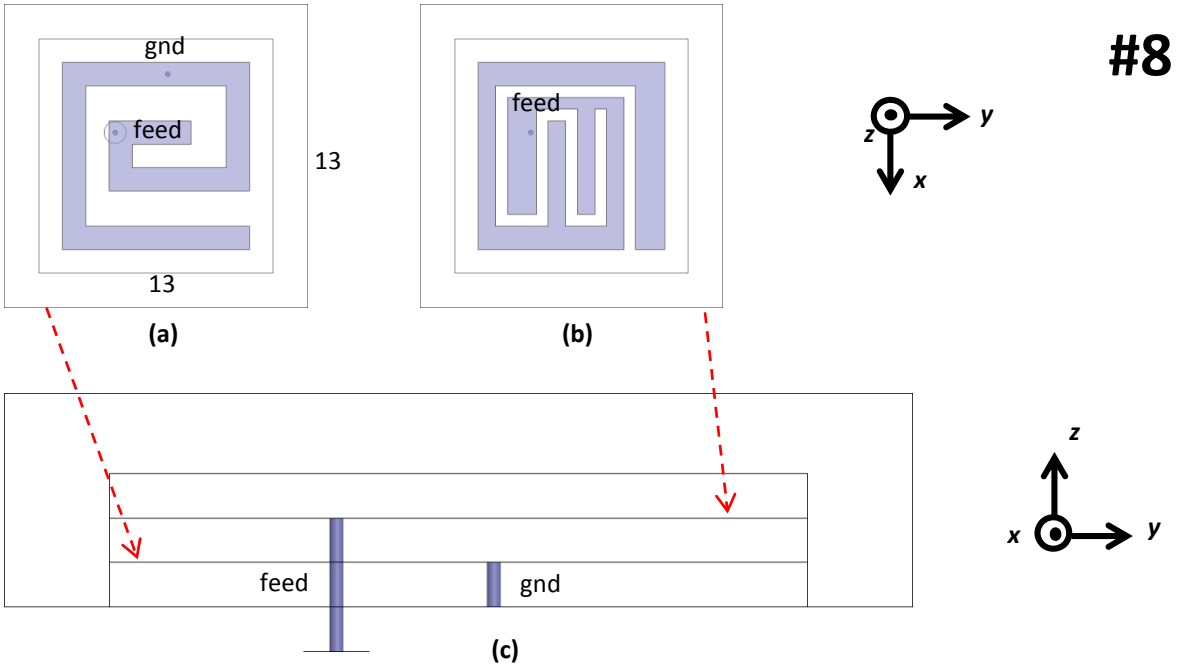

Figure 5.18. In this version, the substrate 4 was removed, but the encapsulation area was increased to 13 x 13 mm^2. The design can be observed on (a) layer 2, (b) layer 3, and (c) the side view of the structure. The first layer was just simply a ground layer from copper and was not shown in this image. All units are in mm.

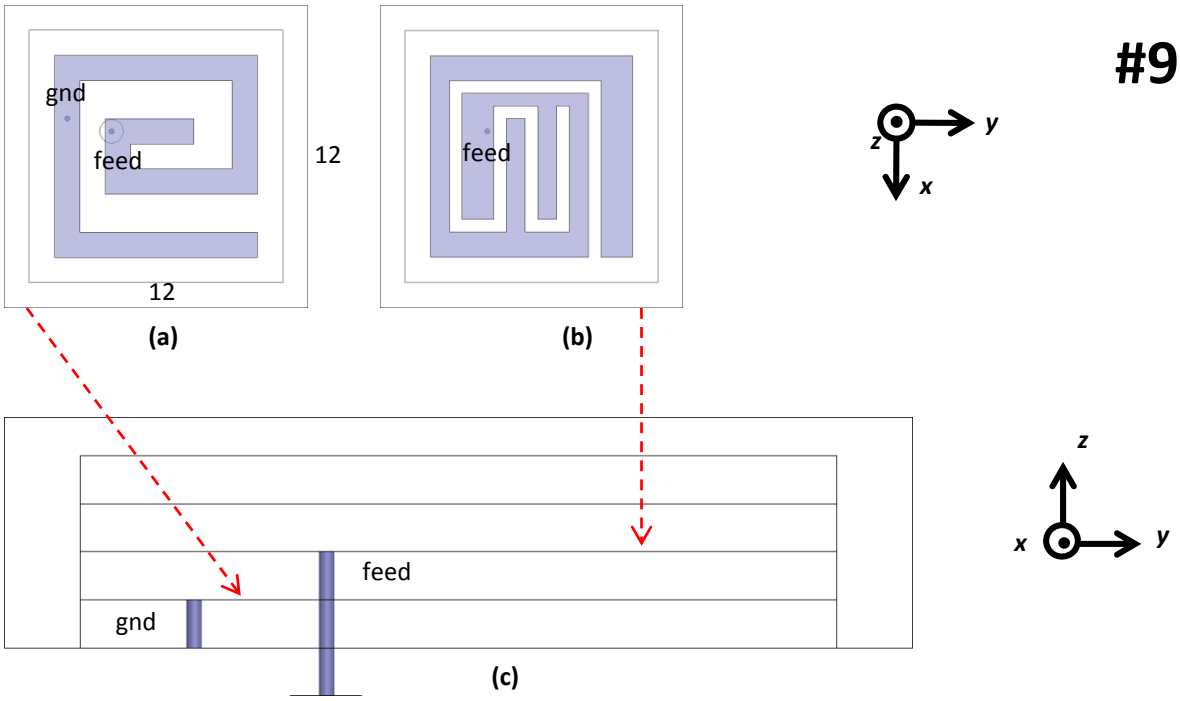

Figure 5.19. In this version, the substrate 4 was returned, but no additional conductor path was added. Substrate 3 and 4 served as suprestrates. The design can be observed on (a) layer 2, (b) layer 3, and (c) the side view of the structure. The first layer was just simply a ground layer from copper and was not shown in this image. All units are in mm.

5.3.1.9. Modification #9 – Addition of a substrate layer without any conductor path

A further investigation was conducted on the layer 4 conductor to gain knowledge on the effect of the slot path to the antenna performance. In modification #9, the additional 4th substrate layer was added, but no conductor line was attached on top of substrate 3, which effectively made the 3rd and 4th substrate layer superstrates (Figure 5.19). The feed and ground pins were also adjusted for better return loss performance. Compared to the results on antenna #7, this antenna was resonant at 391.13 MHz with a bandwidth of 14 MHz and produced a lower maximum gain at -46.13 dB. It was clear that the presence of the conductor path on top of substrate 3 provided a positive impact on the gain of the antenna, while at the same time lowered its resonance.

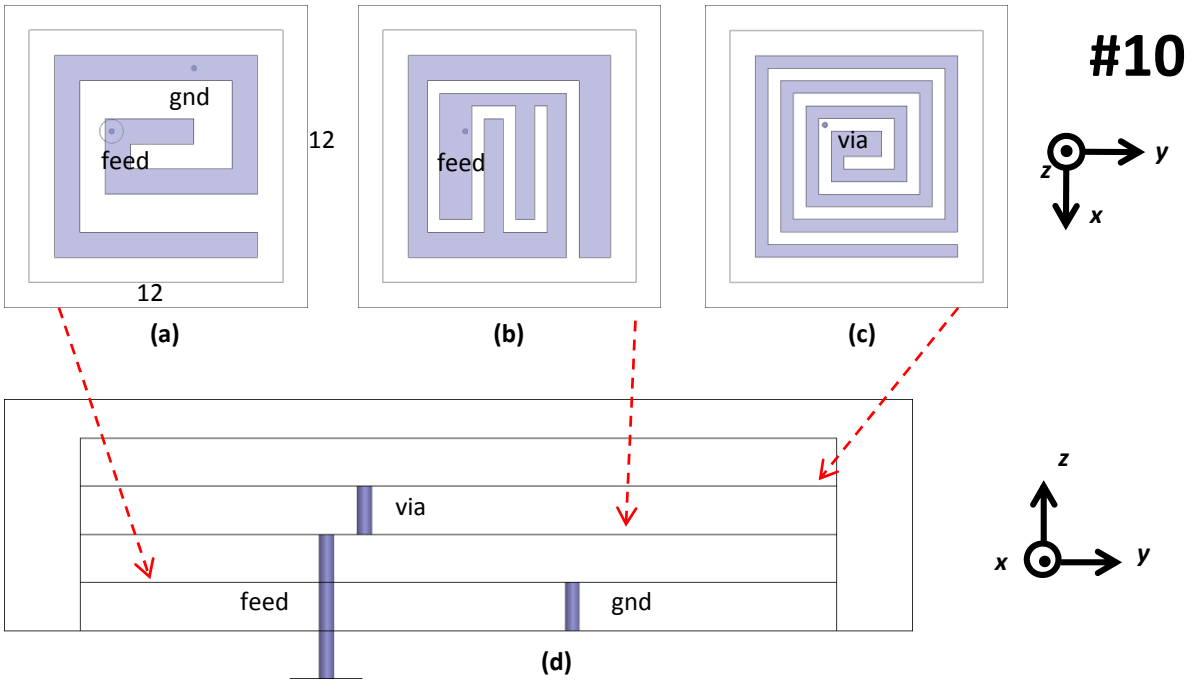

Figure 5.20. Modification #10 featured a rectangular spiral on top of substrate 3. A via pin was placed at the conductor layer on substrate 2 and was connected to the slot path on substrate 3. The design can be observed on (a) layer 2, (b) layer 3, (c) layer 4, and (d) the side view of the structure. The first layer was just simply a ground layer from copper and was not shown in this image. All units are in mm.

5.3.10. Modification #10 – Conductor path on top of substrate 3

The next step was to see if a longer slot path than the one on #7 would result in an even higher gain. Figure 5.20c showed an extended slot line, with the via pin directed to the slot as part of the modification #10, where everything else was kept identical with the antenna #7. The results were consistent with the previous findings in which a higher antenna gain was observed (-41.56 dB). The resulting gain was superior compared to all the previous results, but more modifications were required to improve the current resonant frequency (367.09 MHz with bandwidth 6.4 MHz), which was outside the MICS frequency range.

5.3.1.11. Modification #11 – Change of encapsulation material

In the next modification, #11, the only change was a substitution of the encapsulation material from Silicon to Polydimethylsiloxane (PDMS) with a relative permittivity of 2.72 based on the stated . The height of the enclosure was the same (3.05 mm) with a slightly larger x-y area at 13 x 13 mm^2 (Figure 5.21a). The change of the material was due to the difficulty of shaping Silicon material in manual fabrication process. PDMS, on the other hand, is inexpensive and easy to create through a mixing process, which will be discussed more in Chapter 6. PDMS is also a biocompatible material, an important attribute for this

implantable antenna. The simulation revealed a higher resonant frequency and bandwidth (390.8 MHz and 7.2 MHz, respectively) with a higher maximum gain at -40.77 dB.

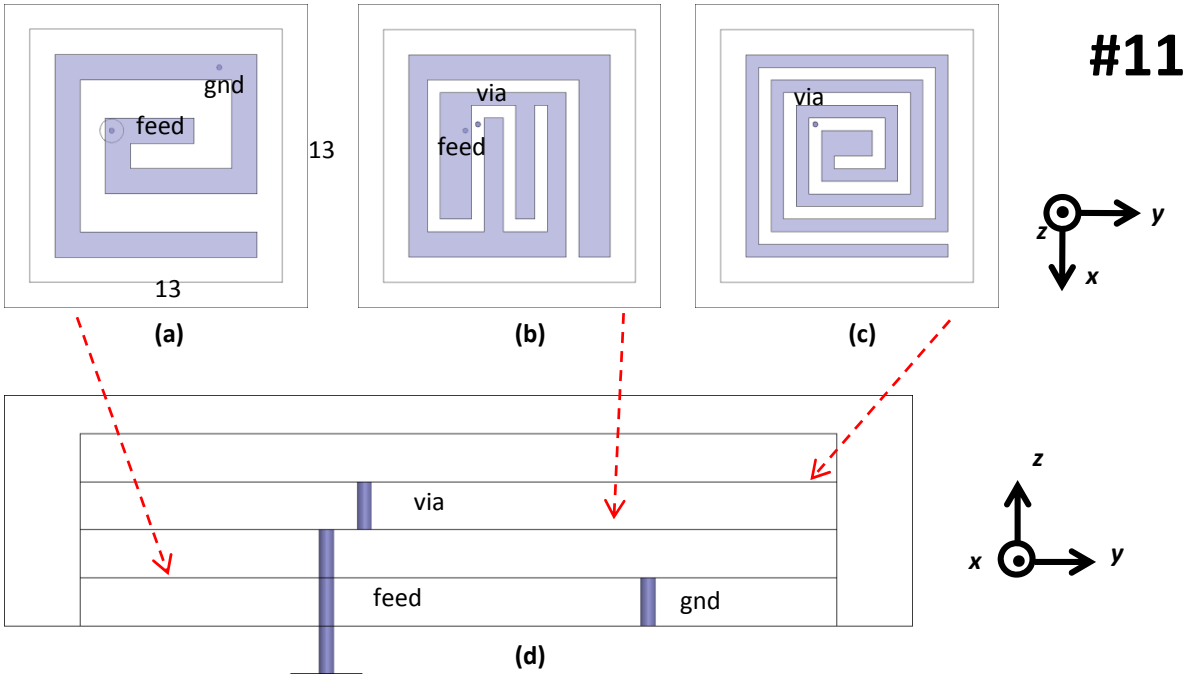

Figure 5.21. In this version, the encapsulation material was PDMS instead of Silicon. The design can be observed on (a) layer 2, (b) layer 3, (c) layer 4, and (d) the side view of the structure. The first layer was just simply a ground layer from copper and was not shown in this image. All units are in mm.

5.3.1.12. Modification #12 – Removal of the via pin

In modification #12, the only modification to the antenna was the removal of via probe which had connected layer 3 and layer 4 conductor paths (Figure 5.22). The simulation results showed no significant variation on the antenna performance (resonance: 391.2 MHz, bandwidth: 8 MHz, max gain: -40.77 dB).

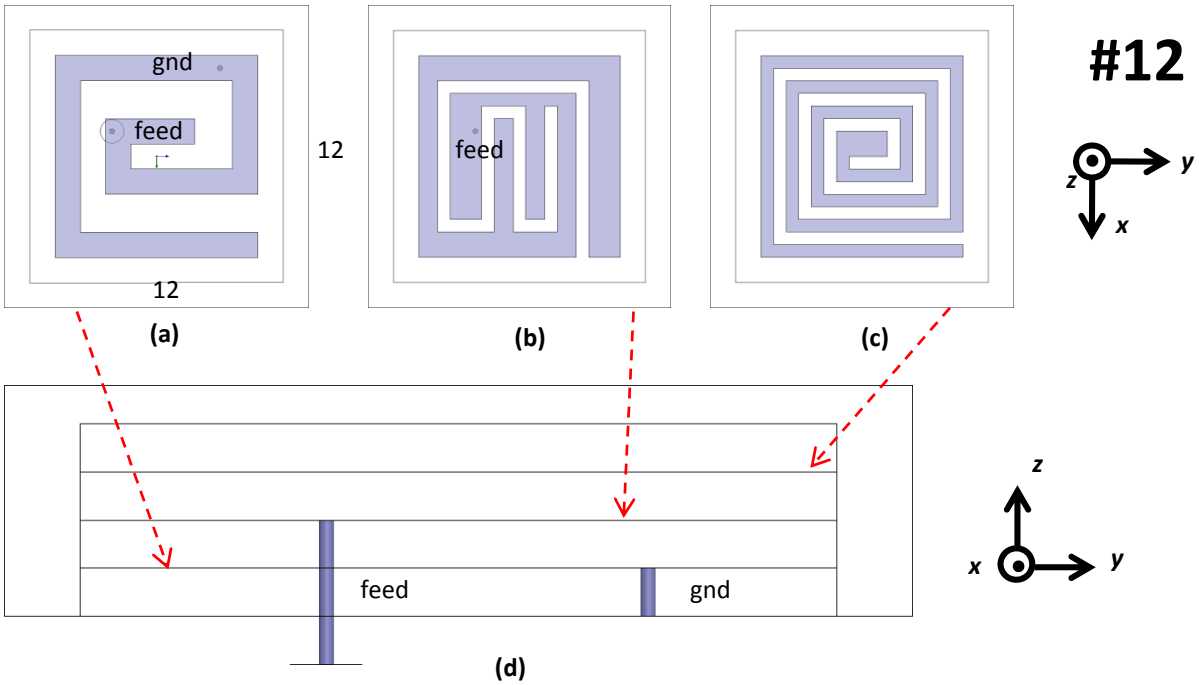

Figure 5.22. The only modification done in this version was the removal of via probe that had connected substrate 2 and substrate 3 previously. The design can be observed on (a) layer 2, (b) layer 3, (c) layer 4, and (d) the side view of the structure. The first layer was just simply a ground layer from copper and was not shown in this image. All units are in mm.

5.3.1.13. Modification #13 – The implementation of Radiall SMA Connector to the design

There was a hypothesis that higher encapsulation height would result in a better antenna gain because more proportion Vitreous Humour liquid with a high loss is removed to make room for the enclosure which is lossless. In modification #13, the enclosure height was increased to 4.06 mm and the area was made larger at 13 x 13 mm^2 (Figure 5.23d). Also included this modification version was re-configuration of the feed pin and radius enlargement for the ground pin. The radius of the feed pin and the coaxial connector were increased to 0.325 mm and 2.05 mm, respectively, to resemble the actual configuration of Radiall R125.463.000 SMA Connector (Appendix 1). The dielectric material of the connector was also changed to Teflon (ε_r = 2.1). The result of these alterations was a resonance at 402.8 MHz with a bandwidth of 2.2 MHz and a maximum gain of -40.35 dB. This result represented the best outcome that this antenna had achieved and this design was selected as the main design of the antenna and the fabrication and measurement process at the latter part of this research will be based on this model.

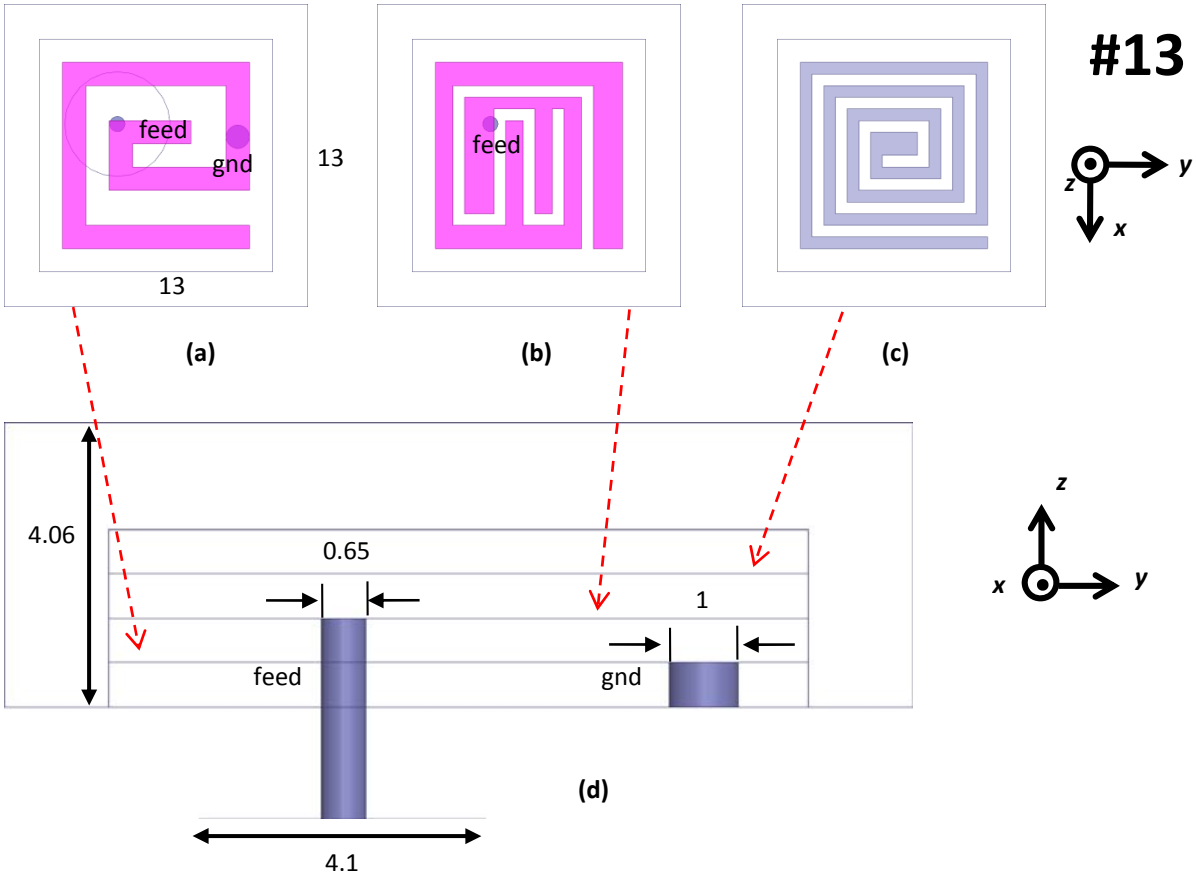

Figure 5.23. The radius of the feed pin was altered to match it with the real SMA Connector from Radiall. As part of the change, the coax dielectric material was also changed to Teflon. The design can be observed on (a) layer 2, (b) layer 3, (c) layer 4, and (d) the side view of the structure. The first layer was just simply a ground layer from copper and was not shown in this image. All units are in mm.

5.3.1.14. Modification #14 – Addition of steel arms around the connector (Final Design)

The finalization of the antenna structure was done by creating a pair of supporting arms around the coaxial connector as an attempt to resemble the SMA Connector from Radiall, as shown on the datasheet (Appendix 1). The supporting structure was made of steel (σ = 1100000 S/m) with all the dimensions acquired from the datasheet. As shown in Figure 5.24, modification #14 involved the addition of the supporting structure as well as longer coaxial dielectric. Otherwise, the structure and geometry of the antenna was identical to the previous version, #13. These modifications did not produce significant deviations to the previous results, with a resonant at 402.8 MHz and bandwidth 3.2 MHz. The gain was slightly lower at -41.02 dB.

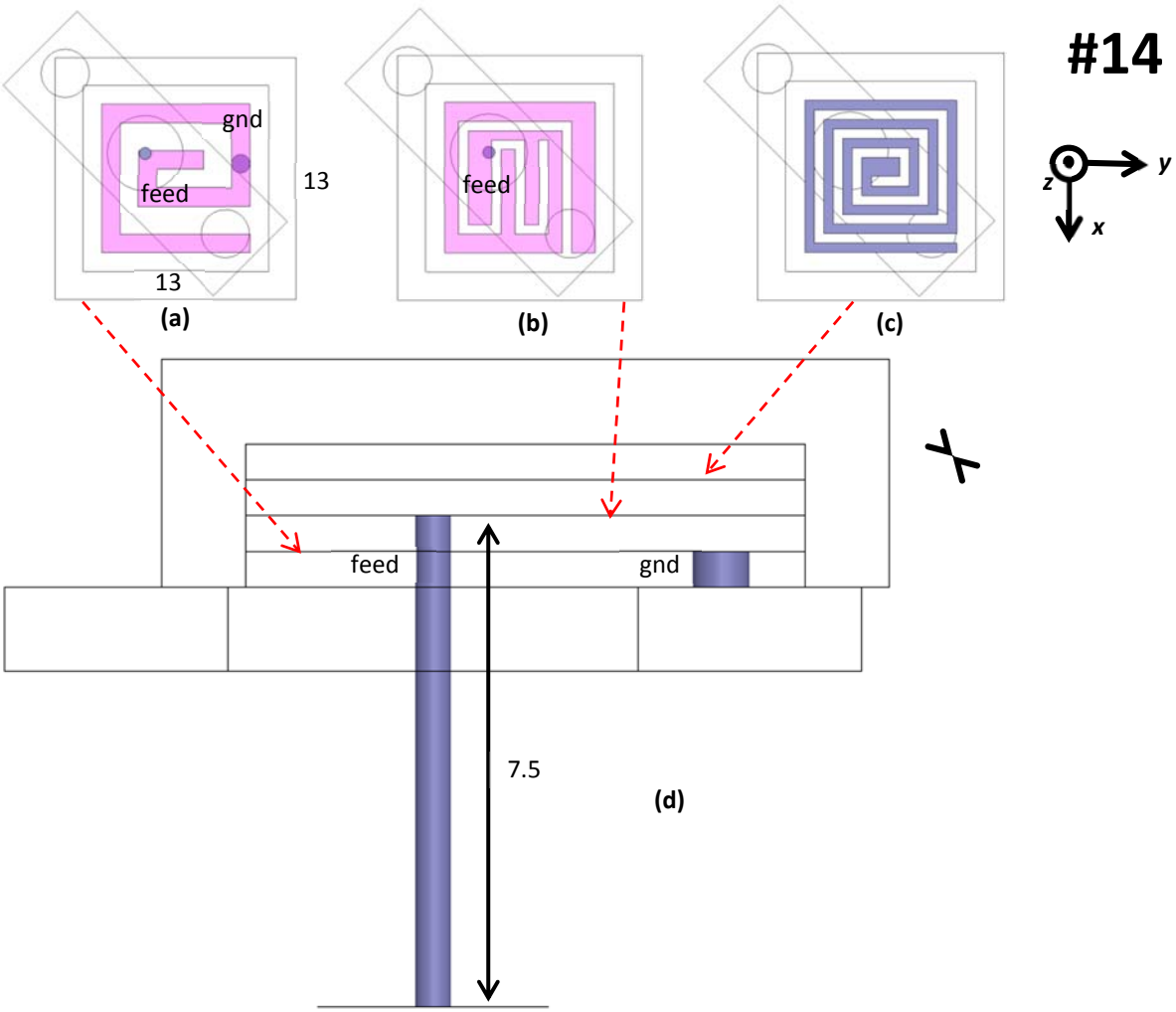

Figure 5.24. This is the final design of the antenna. The inclusion of a pair of steel arms was an attempt to resemble the real condition during the measurement, to provide high accuracy results. The design can be observed on (a) layer 2, (b) layer 3, (c) layer 4, and (d) the side view of the structure. The first layer was just simply a ground layer from copper and was not shown in this image. All units are in mm.

For more detailed information about each layer of the antenna, refer to Figure 5.25 to 5.28.

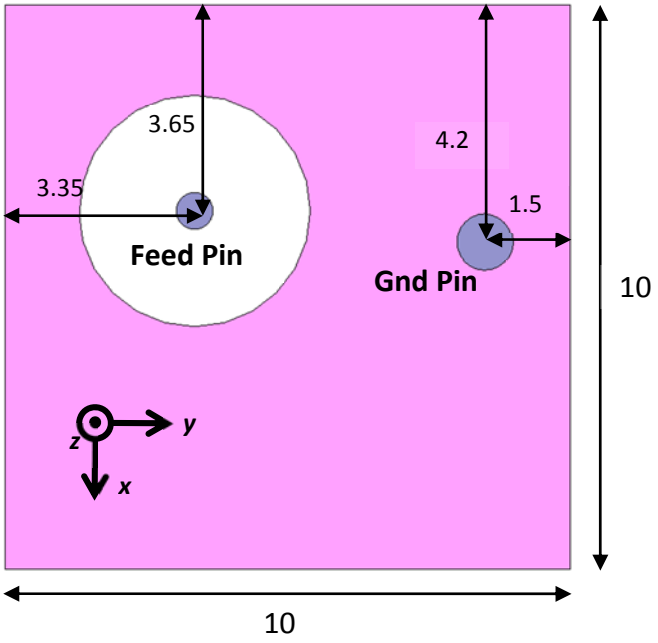

Figure 5.25. The ground plane of the antenna from the top view. It is located at the bottom of the first substrate. The steel arms are not included in this design for a more simplified look. All units are in mm.

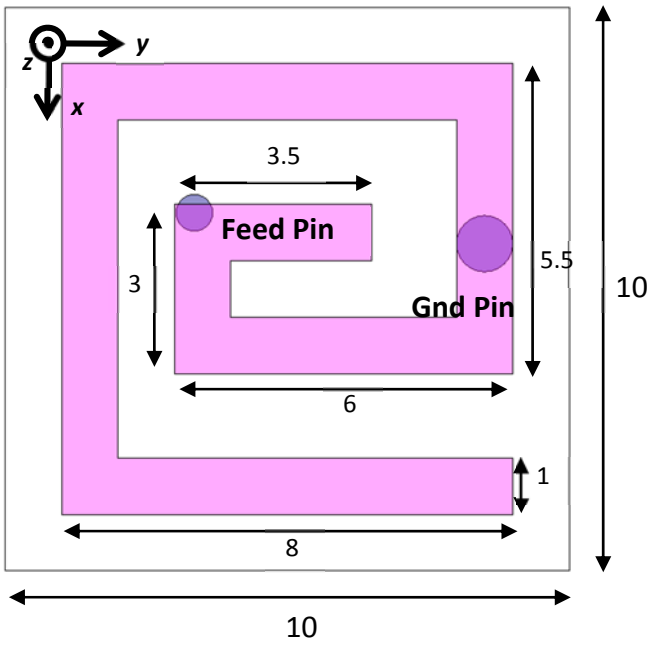

Figure 5.26. The first conductor layer of the antenna from the top view. It is sitting on top of the first substrate layer. The distance of both feed pin and ground pin from the edges of the substrate are identical to the ones in ground layer. The steel arms are not included in this design for a more simplified look. All units are in mm.

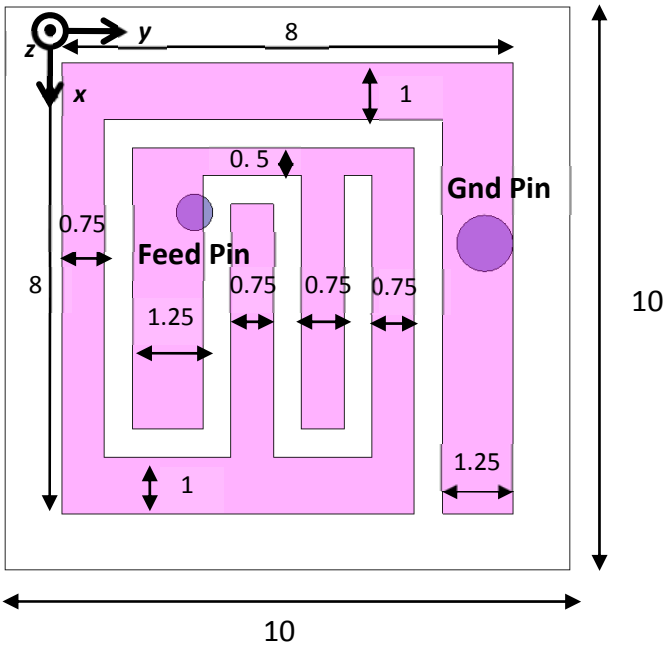

Figure 5.27. The second conductor layer of the antenna from the top view. It is sitting on top of the second substrate layer. The steel arms omitted in this design for a more simplified look. All units are in mm.

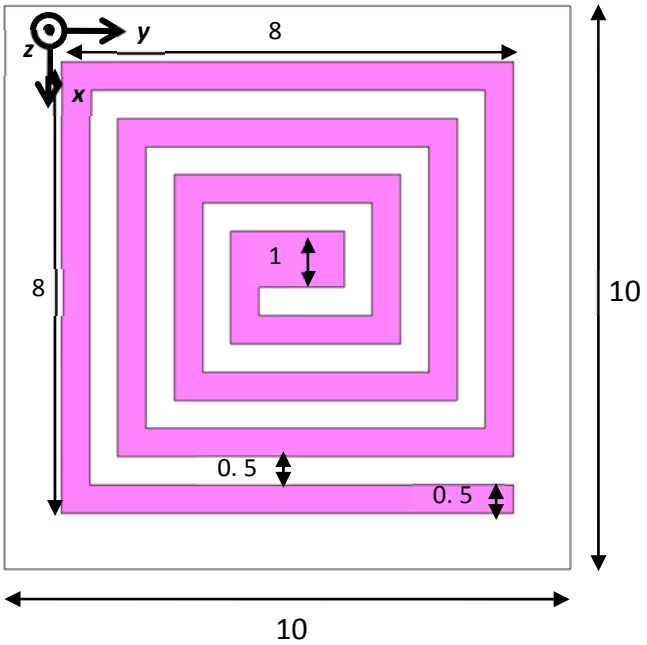

Figure 5.28. The third conductor layer of the antenna from the top view. It is sitting on top of the third substrate layer. The steel arms omitted in this design for a more simplified look. All units are in mm.

5.3.1.15. Summary

Table 5.2 summarizes 14 modifications that had been applied to the antenna with the resulting antenna performances. From this table, it could be clearly seen how each modification affected the antenna performance. Modification #14 was conducted as part of building an accurate model based on the detail of each component. The resulting simulated antenna performance was satisfying and the operation was within the range of MICS band. This antenna model was subsequently fabricated and measured in both free space and Vitreous Humour liquid to verify its performance.

Table 5.2. Summary of the antenna performance based on each modification. The antenna performances were obtained following HFSS simulation process.

#	Main modification	Dimension (mm^3)	Layers	Encl material	Enclosure h (mm)	Return Loss (dB)	Resonant Frequency (MHz)	10-dB Bandwidth (MHz)	Max Gain (dB)
1	Implementation of Liu's Antenna	9 x 9 x 1.8	3	-	-	-18.84	403.5	50.8	-51.58
2	Conductor pattern	9 x 9 x 1.8	3	-	-	-19.21	375	44.8	-50.98
3	Conductor pattern	9 x 9 x 1.8	3	-	-	-	-	-	-52.44
4	Conductor pattern	9 x 9 x 1.8	3	-	-	-29.75	347.9	38.4	-50.03
5	Substrate dimension	10 x 10 x 1.9	3	-	-	-25.71	405.16	55.6	-50.87
6	Substrate dimension	12 x 12 x 1.9	3	-	-	-11.69	362.74	32.8	-47.95
7	Extra substrate layer and encapsulation	12 x 12 x 1.9	4	Silicon	3.05	-16.04	402	10.8	-44.44
8	Removal of the 4^{th} substrate	13 x 13 x 1.9	3	Silicon	3.05	-25.7	409.84	19.2	-45.98
9	Removal of conductor on the 4^{th} substrate	12 x 12 x 1.9	4	Silicon	3.05	-11.17	391.13	14	-46.13
10	Conductor pattern	12 x 12 x 1.9	4	Silicon	3.05	-12.46	367.09	6.4	-41.56
11	Enclosure material	12 x 12 x 1.9	4	PDMS	3.05	-21.82	390.8	7.2	-40.74
12	Removal of via probe	12 x 12 x 1.9	4	PDMS	3.05	-22.38	391.2	8	-40.77
13	Feed and ground pin dimension	13 x 13 x 1.9	4	PDMS	4.06	-11	402.8	2.2	-40.35
14	Addition of steel arm to resemble the Radiall SMA Connector	13 x 13 x 1.9	4	PDMS	4.06	-12	402.8	3.2	-41.02

5.3.2. Variation on Encapsulation Height

A course of simulations were run with a variation on the thickness of the PDMS encapsulation layer on the final design of the antenna as an attempt to find the most optimal geometry for the antenna performance. The height variations (denoted by *h*) are presented in the first column of Table 5.3, with the antenna performance presented on the rest of the columns in terms of resonant frequency, minimum return loss, maximum gain, and radiation efficiency.

Table 5.3. Antenna Performance on Different Enclosure Height

h **(mm)**	**frequency (MHz)**	**Return Loss (dB)**	**Max Gain (dB)**	**Efficiency**
4.06	402.8	-10.86	-40.35	0.39%
3.81	401.6	-10.53	-40.3	0.39%
3.56	400.4	-9.99	-40.32	0.39%
3.3	398	-9.13	-40.34	0.38%
3.05	387.2	-6.94	-40.2	0.38%
0	359.6	-3.63	-43.5	0.17%

In the case of h = 0, no encapsulation was applied to the antenna, whereas the number of 3.05 mm to 4.06 mm corresponds to the height of the enclosure measured from the antenna ground layer. Values greater than 4.06 mm were not considered because part of the enclosure would exceed the eyeball structure with its 25 mm radius.

Based on the data in Table 5.3, the existence of PDMS enhanced return loss of the antennas. For the thinnest layer (h = 3.05 mm), an improvement of 3.31 dB was observed while 7.23 dB improvement was observed for the highest thickness simulated (h = 4.06 mm). According to this relationship, perpetual increment on the thickness would result in much better return loss property. However, space limitation will be an issue since the antenna will be implanted inside the eyeball that has typical diameter of 25 mm. Without the additional layer, the best return loss performance was -3.63 dB at 359.6 MHz, which is greater than the -10 dB threshold of reliable transmission. Based on the results in Table 5.3, the PDMS thickness of 4.06 mm was selected for further investigation for all 4 proposed cases.

5.3.3. Different Cases for Real Life Testing

The development process to achieve the final design of the antenna as shown in modification 1 to 14 employed a scenario where the antenna was submerged into a sphere

made of Vitreous Humour fluid (ε_r = 69, σ = 1.53 S/m [64]). This Vitreous Humour sphere was designed with a diameter of 25 mm to realistically resemble the human eyeball. The decision to use the simple eyeball model instead of a complex human head model for this study was based on the fact that the transmission between the intraocular and the extraocular parts always occur at the same unobstructed path from the inside to the distance of a few centimetres outwards the eyeball. This made the signal propagation analysis in that direction sufficed to obtain accurate representation of the antenna performance in respect to the system transmission for an *in vitro* testing. The presence of additional complex human head model would not produce a significant discrepancy. With a penalty on the time and resources needed for implementing the human head model, this scenario is deemed irrelevant at this stage. In regards to the antenna position inside the eyeball, it is located right at the centre of the sphere with the signal propagation perpendicular to the substrate layers (Figure 5.29). More information about this will be presented on the latter part of this Section.

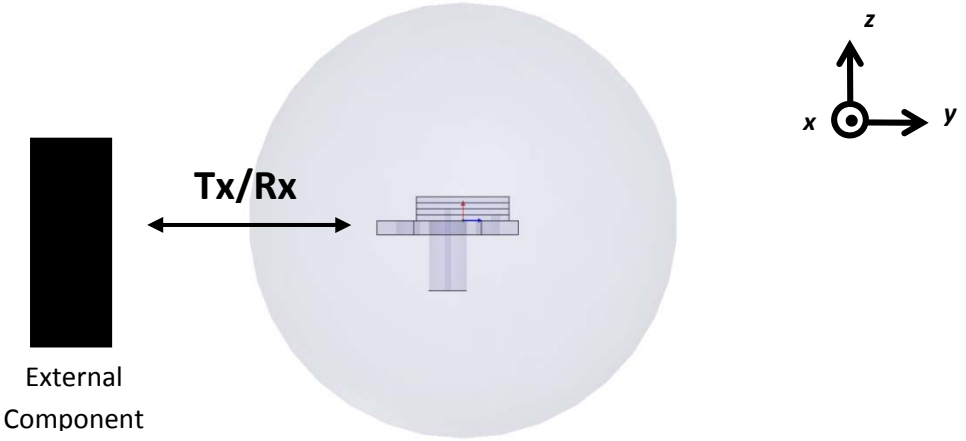

Figure 5.29. The position of the antenna with respect to the eyeball model and the direction of the signal propagation.

Even though the final purpose of this antenna was an operation inside a human eyeball, it was necessary to run simulations in different scenarios of surrounding medium. The objective was to obtain better knowledge on the antenna behaviour both in the simulation and the measurement. These are the proposed scenarios in which the antenna will be simulated and measured:

- **Case A**: an antenna in a free space sphere
- **Case B**: an encapsulated antenna in a free space sphere

- **Case C**: an encapsulated antenna in a Vitreous Humour sphere at the size of human eyeball
- **Case D**: an encapsulated antenna in a Vitreous Humour sphere at the size of table tennis ball with diameter 40 mm.

In *case A*, the presence of both Vitreous Humour liquid and the PDMS encapsulation is excluded and the antenna is positioned in the middle of an air-filled sphere. This case would be useful to know the characteristic of the antenna right after the fabrication process, before the encapsulation and immersion stage.

In *case B*, a PDMS encapsulation layer is incorporated to the antenna structure. The antenna would still be placed inside an air-filled sphere. This stage would provide an important information should the behaviour of the antenna is not as expected.

Case C is the condition in which the antenna was originally designed for. The encapsulated antenna structure is positioned inside a Vitreous Humour that mimics a human eyeball. However, it would not be possible to replicate this scenario in the reality due to the difficulty in obtaining an ethic approval. Instead, case D was proposed to provide a close representation of this case C.

In *case D*, the encapsulated antenna is positioned inside a sphere that is filled with Vitreous Humour mimicking liquid. The sphere would have a larger diameter at 40 mm to create an accurate representation of a table tennis ball. That is where the antenna and the Vitreous Humour liquid are positioned for the measurement process. Table tennis ball is a hollow sphere with a skin material of Celluloid (electrical characteristic in Table 5.1) and a skin thickness of 0.35 mm. A small experiment has also been done in an attempt to find the most suitable PDMS layer thickness for achieving the most optimal antenna performance. More detail about this will be presented later in this Section.

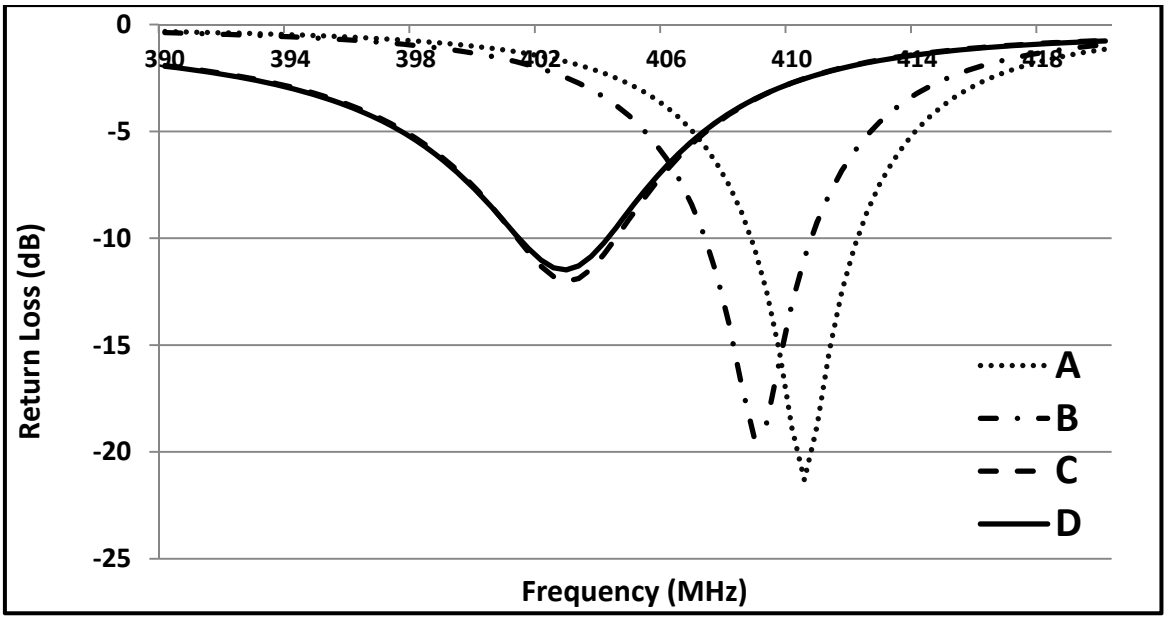

Figure 5.30. Return losses of the antenna in four different simulation setups. The letters A to D correspond to the case A to case D of the configuration.

Figure 5.30 shows a comparison of the antenna return loss in the four setups (case A to case D). As expected, shifts of resonance frequencies were evident for different setup and lower values of return loss were achieved for free space configuration. This is due to the lossless property of the free space, in contrary to the lossy Vitreous Humour. These values will be used as references for the antenna measurements. More information about the antenna performance in four different cases can be observed in Table 5.4.

Table 5.4. Simulated antenna performance on four different scenarios.

Case	Frequency (MHz)	Min Return Loss (dB)	Gainϕ = 0° (dB)	Gainϕ = 180° (dB)	Efficiency
A	410.4	-21.31	-38.83	-38.88	0.57%
B	408.8	-19.35	-38.63	-38.59	0.6%
C	402.8	-12	-41.43	-41.02	0.32%
D	402.8	-11.48	-40.57	-39.89	0.4%

The maximum simulated gains achieved by the antenna were in the region of -40 dB with the PDMS layer and -43.5 dB without the extra layer (Table 5.3). The presence of extra PDMS layer provided significant improvement to the antenna gain, but there was not much variation to the antenna gain when different extra layer heights were applied. From the result in Table 5.4, it can also be inferred that the addition of PDMS layer in free space did not affect the antenna gain performance. The immersion of the encapsulated antenna

(case C) degraded the gain by approximately 3 dB and the use of bigger eyeball size (case D) produced a 1 dB improvement. The explanation on gain at $\phi = 0°$ and at $\phi = 180°$ will be provided on the next chapter.

The radiation pattern is always omnidirectional regardless the presence of PDMS layer in any of the 4 cases, with the maximum values lie in *x* and *y* axis direction while the nulls occur at both end of the *z*-axis (Figure 5.31). This is a typical pattern of an electrically small antenna [70].

With this kind of radiation pattern, placing the antenna right in the middle of the sphere with the antenna facing upwards or downwards is the best possible set up since the signal will travel sideway, through to the external antenna. Since the interest is to deliver signal transmission in one direction (+*y* axis), the gain in any other directions are ignored.

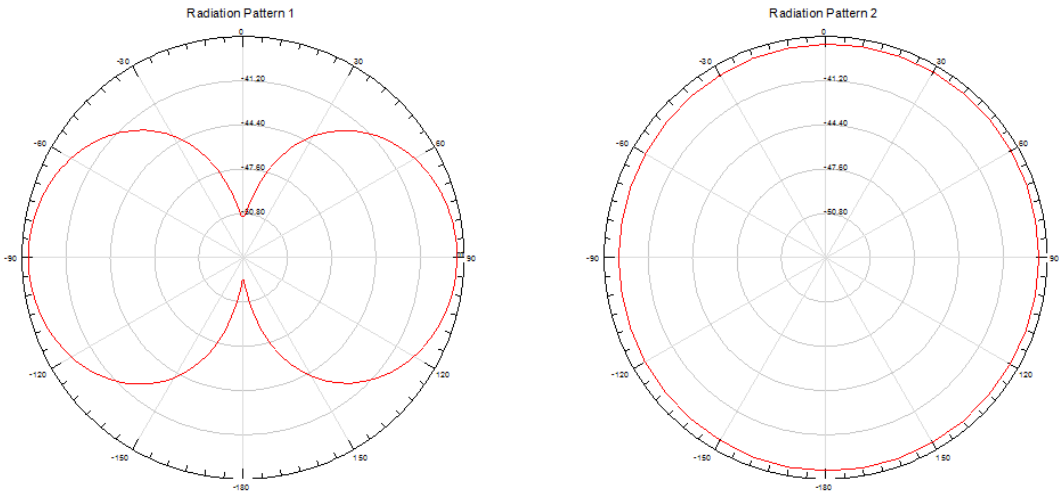

Figure 5.31. 2D Representation of simulated radiation pattern in (a) YZ plane and (b) XY plane.

In Table 5.4, a column showing radiation efficiency of the antenna is presented. Radiation efficiency is a parameter that can be obtained in HFSS with a radiated fields post processing. It means that an additional computation is executed on the values of the fields, which have already been calculated on the simulation process, over the radiation surface. As presented in Table 5.3, the efficiency values obtained from the simulation were in the region of 0.38% - 0.39% with the extra PDMS layer. The efficiency was reduced by a factor of 2 when the extra layer was removed. The antenna efficiency comparison in 4 different cases revealed that the introduction of PDMS layer in free space did not alter the efficiency. However, once the antenna was immersed inside the liquid (case C), the

efficiency degraded by 35%. A slight improvement on the efficiency was observed when a bigger eyeball size was utilized (case D).

Another parameter obtained with a post processing in HFSS software is SAR values. According to the HFSS simulation, the 10 g average SAR of this antenna at the Vitreous cavity was 45 W/kg and 33 W/kg at case C and case D, respectively. The calculation was done under the condition that the input power to the antenna was 1 W. It means, to comply with the SAR safety limit of 2 W/kg, the input power should not exceed 44.4 mW and 60.6 mW for case C and D, respectively.

5.4. Summary

In this chapter, the simulation phase of the project has been comprehensively discussed. It began with a review of the most popular techniques for solving Maxwell's Equations. A software package incorporating one of these techniques was then selected to obtain the parameters of the proposed antenna, followed by a set of information on the pre-simulation configuration to achieve results that accurately reflect the actual antenna. The chapter was finalised by the presentation of the antenna parameters obtained by the simulation. In the next chapter, the fabrication and the measurement procedure of the designed antenna will be demonstrated. That will include the coverage of the measurement on case A, B, and D as specified in this chapter.

Chapter 6
Measurement

In previous chapter, a course of simulations and optimisations process has been executed in an attempt to achieve the desired antenna performance in terms of the specified parameters. The next step would be a fabrication of the proposed antenna and a measurement procedure as part of simulation data verification. This chapter will be divided into three main parts: antenna fabrication, free space measurement, and measurement inside the Vitreous Humour liquid. The measurement procedure and equipment configuration will be explained for each measurement set up and the results will be disclosed at the end of each Section.

6.1. Antenna Fabrication

The fabrication of the antenna was initiated by etching each substrate separately. The first substrate is a double-sided Printed Circuit Board (PCB) with Rogers 3210 material, accommodating the ground layer on one side (Figure 6.1) and the layer 2 on the other side (refer to Figure 5.25 and 5.26). The second and the third substrate are regular one-sided PCBs with the same material to accommodate layer 3 and layer 4 conductor paths. The fourth substrate is purely a dielectric material without any conductor strips attached to it after the etching process. This layer acts as the supersrate of the antenna.

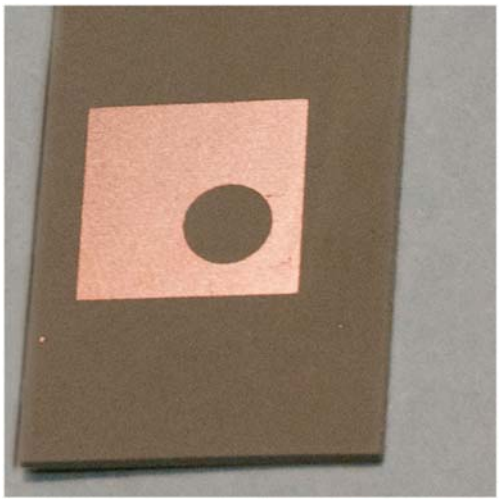

Figure 6.1. Ground plane of the antenna after the etching process.

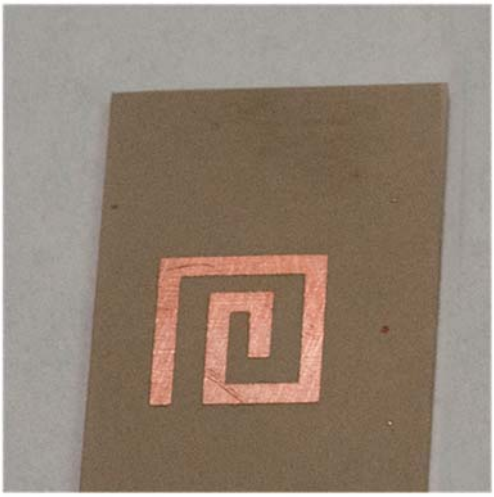

Figure 6.2. Layer 2 of the antenna after the etching process.

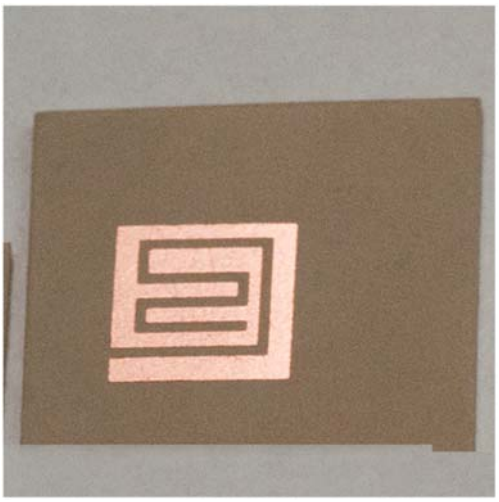

Figure 6.3. Layer 3 of the antenna after the etching process.

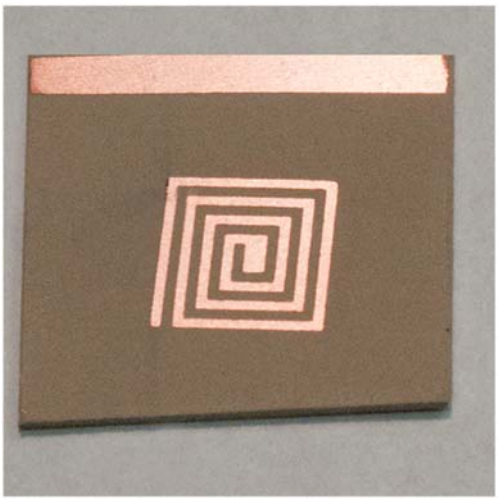

Figure 6.4. Layer 4 of the antenna after the etching process.

The next step was drilling all the holes where the feed and ground pin will be placed. Accuracy on the drilling is highly prioritised since it greatly affects the feeding placement

of the antenna. It was achieved by positioning each layer under microscope and putting a mark on the desired position of the pin holes with the help of vernier calliper. Drill bits with specific diameter sizes of 0.65 mm and 1 mm were selected to provide an exact fit to the inserted pins.

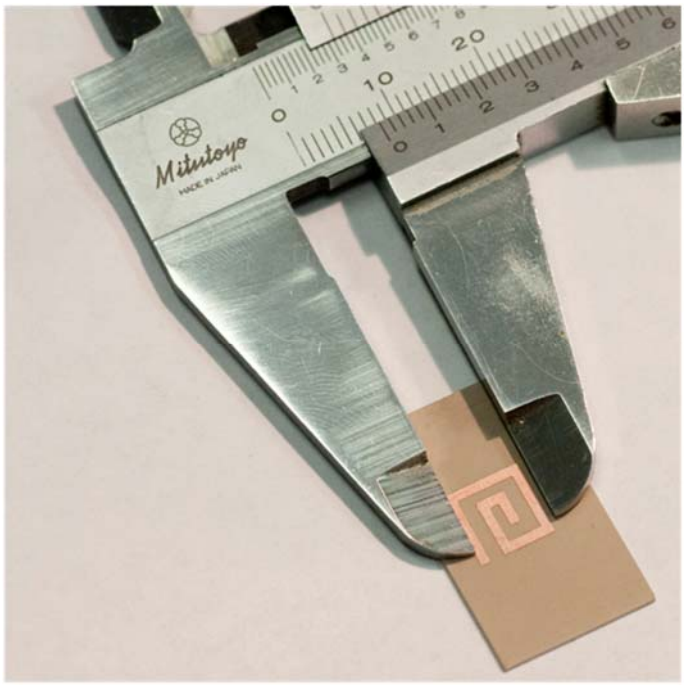

Figure 6.5. Vernier calliper was utilized to accurately mark the pin hole positions before the drilling.

The feed pin (d = 0.65 mm) was originated from the extension of the Radiall R124.463.000 SMA connector pin (Figure 6.6) and the purpose was to connect ground, layer 2, and layer 3 conductor paths. The technical specification of the connector can be found on Appendix 1. The ground pin, on the other hand, was created from a thin copper wire with a diameter of 1 mm and is responsible for connecting the ground and the layer 2 conductor path through the substrate 1. It is critical that both pins do not extend beyond the conductor line on layer 3or layer 2 to avoid excessive cross-polarized radiation [91]. To accomplish that, each pin was carefully cut to have an approximate length equivalent to the thickness of substrate 1 for the ground pin and the sum of substrate 1 and 2 thickness for the feed pin. Any protruding part of the feed pin was filed to leave just enough length of the pin to be soldered on to the conductor track on layer 3. In the case of the ground pin, both ends of the wire were soldered to their respective surface to gain contact with the conductor track.

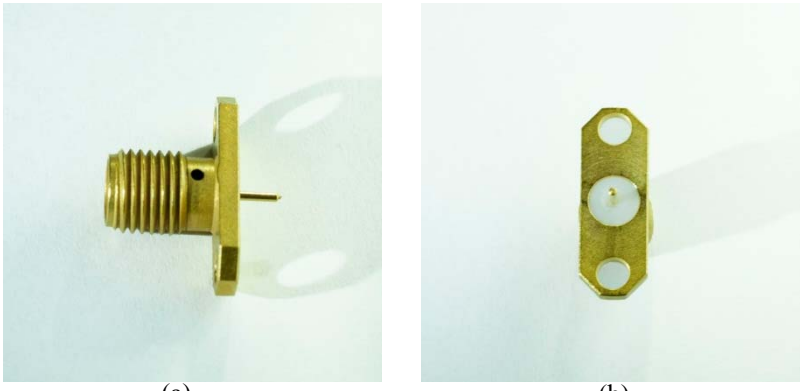

(a) (b)

Figure 6.6. Radiall R124.463.000 SMA Connector on (a) side view and (b) top view.

Once all the pins had been soldered, the rest of the substrates were stacked together and compressed with a vertical clamp to minimize any air gap in between each layer. A thin layer of epoxy resin was then applied to all 4 sides of the antenna to ensure rigidity. The resulting antenna can be seen in Figure 6.7. In Figure 6.7b, the presence of the thin transparent epoxy resin layer can be observed at the edge of the antenna along with solder tin that had been melted between the connector and the ground layer.

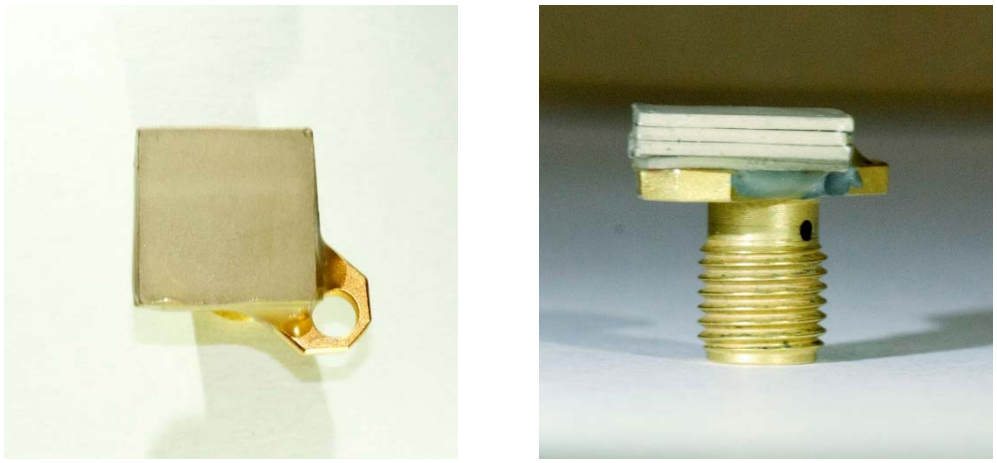

(a) (b)

Figure 6.7. The fabricated multilayer microstrip antenna seen from (a) top view and (b) side view. It can be seen that with a dimension of 10 x 10 mm, the antenna is clearly overwhelmed by the connector size.

The final phase of the antenna fabrication was the PDMS encapsulation to seal the antenna from the surrounding medium as well as to provide biocompatibility characteristic. The process was initiated after the case A antenna measurement had been completed. The whole process was conducted inside the Microelectronics and Materials Technology Centre (MMTC) clean room facility at RMIT University. The encapsulation process was divided into two stages: the development of the top layer and the development of the lateral layers.

The whole process was started with the development of the top encapsulation layer. Sylgard® 184 Silicone Elastomer from Dow Corning was used as the PDSM elastomer and it is composed of 2 parts: pre-polymer and its curing agent. Initially, the pre-polymer was mixed with the curing agent in a weight ratio of 10 by 1. The ratio was selected based on the recommended use in the datasheet (Appendix 2). A modification to the ratio would result in different product flexibility in the way that a less curing agent proportion would result in more flexible layer. The mixture was poured into a Petri dish until the desired thickness was reached and then it was left for a few minutes in order for the mixture to spread evenly. After an even surface level was achieved, the dish was entered into a vacuum chamber as an attempt to lift the air bubbles to the gel surface. Ten to fifteen minutes later, it can be noticed that most of the air bubbles had surfaced and they were ready to be eliminated with the aid of an air blower. The bubble*less* mixture was then baked inside the oven for approximately 15 minutes at the temperature of 70°C to speed up the hardening process of the elastomer.

A top encapsulation layer had been created according to the specified thickness and the next step would be the development of the lateral layers of the encapsulation. It began by placing the antenna on the hardened gel mixture, with the antenna superstrate in direct contact with the gel (refer to Figure 6.8a). Additional PDMS gel mixture was then poured onto the dish with enough thickness to cover the entire 4 layers of the antenna and occupying all its lateral sides (Figure 6.8b). The same procedure is repeated for eliminating the air bubbles as well as for hardening the mixture inside the oven. At the end of the process, the antenna would have the correct thickness of encapsulation at the top layer with infinite encapsulation on sideways. A final step of trimming the lateral layer was conducted to obtain the right thickness of 1.5 mm on each lateral layer. When executed properly, the PDMS would cover the entire 4 layers of the antenna as well as a thin layer on the ground plane (Figure 6.9) to provide hermetic attribute to the antenna.

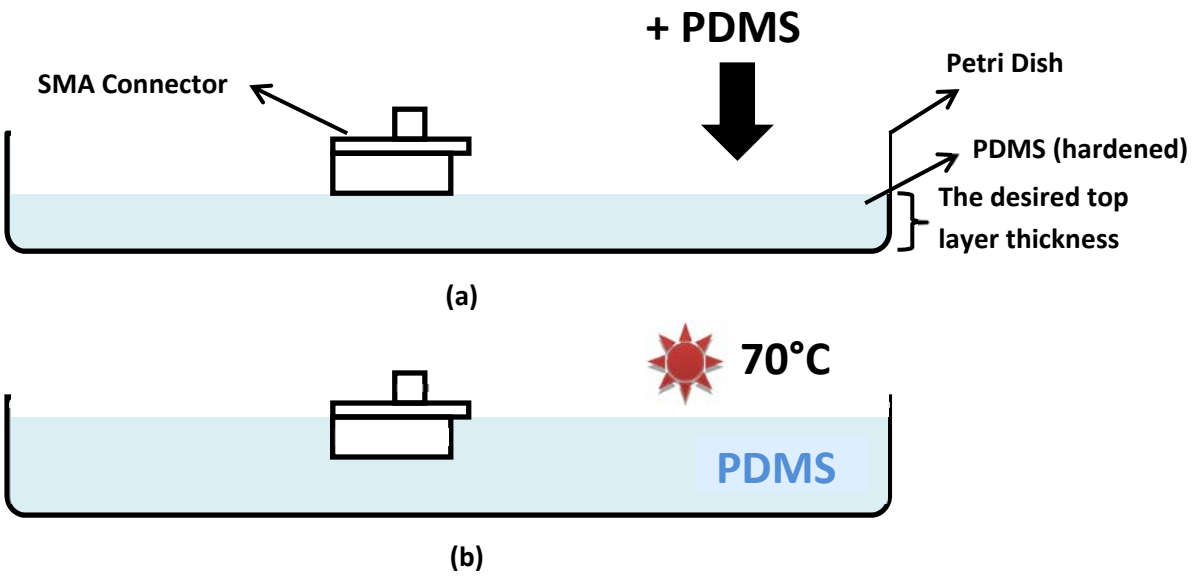

Figure 6.8. The diagram of the antenna placement during the PDMS encapsulation process. Initially the antenna was positioned upside down on the hardened PDMS (a), and then more PDMS mixture was poured into the dish until all the antenna sides were covered (b).

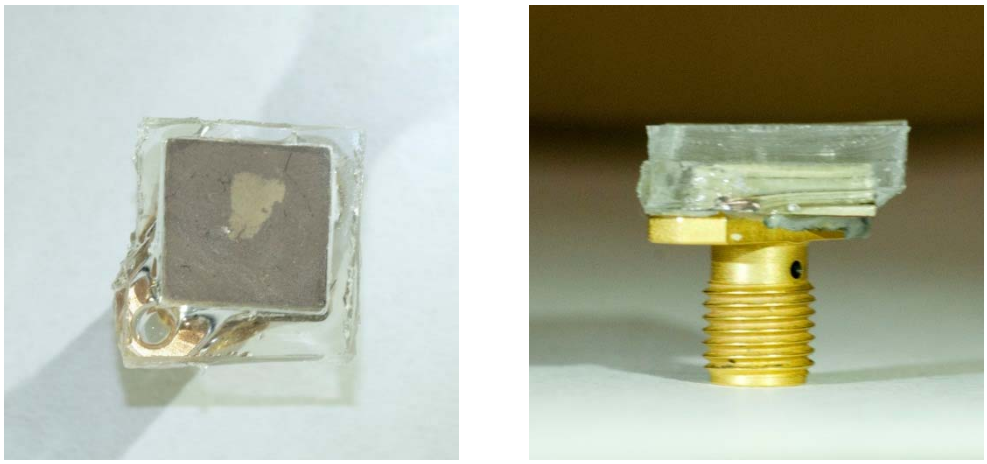

(a) (b)

Figure 6.9. The fabricated multilayer microstrip antenna after the PDMS encapsulation, seen from (a) top view and (b) side view.

6.2. Free Space Measurement

The free space measurement of the fabricated antenna was conducted as a verification process to the simulation results on the case A and case B antenna configuration. The aim was to investigate the actual antenna performance in three different parameters: return loss, radiation pattern, and gain. The measurement configuration to achieve each parameter will be presented in this Section, followed by the result of each measurement.

6.2.1. Return Loss

The free space return loss measurement was done with the aid of Agilent E5071B Network Analyzer. In Figure 6.10, the measurement set-up is presented and it shows that the antenna under test (AUT) was connected to Channel 1 of the analyser through a semi-rigid coaxial cable. During the procedure, it is of paramount importance for the antenna to have clear line of sight on all its propagation directions to achieve accurate results. After the frequency sweep had been specified and the return loss function had been selected on the machine, the return loss of the antenna was displayed on the screen. Two displays were selected, one in a normal Cartesian chart and another one in a Smith chart, to signify different information from the dataset. The return loss of case A configuration in Cartesian format can be observed in Figure 6.11 while the Smith chart format can be observed from Figure 6.12.

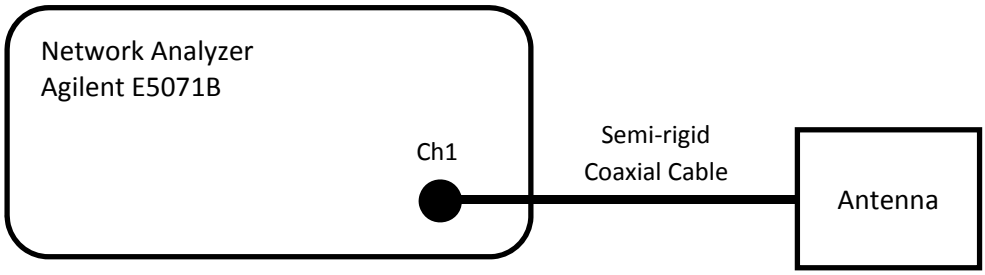

Figure 6.10. The equipment configuration of the return loss measurement.

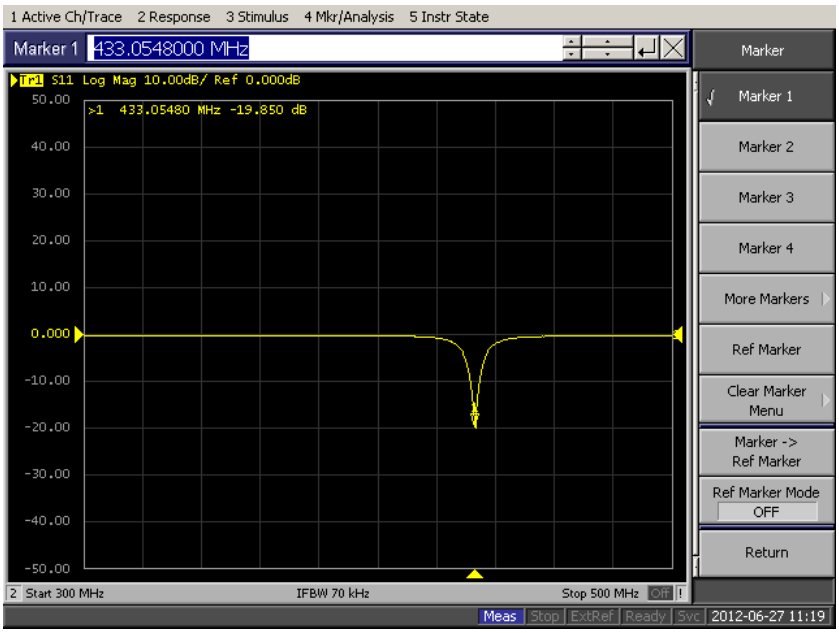

Figure 6.11. A screenshot of case A return loss measurement using Agilent E5071B Network Analyzer.

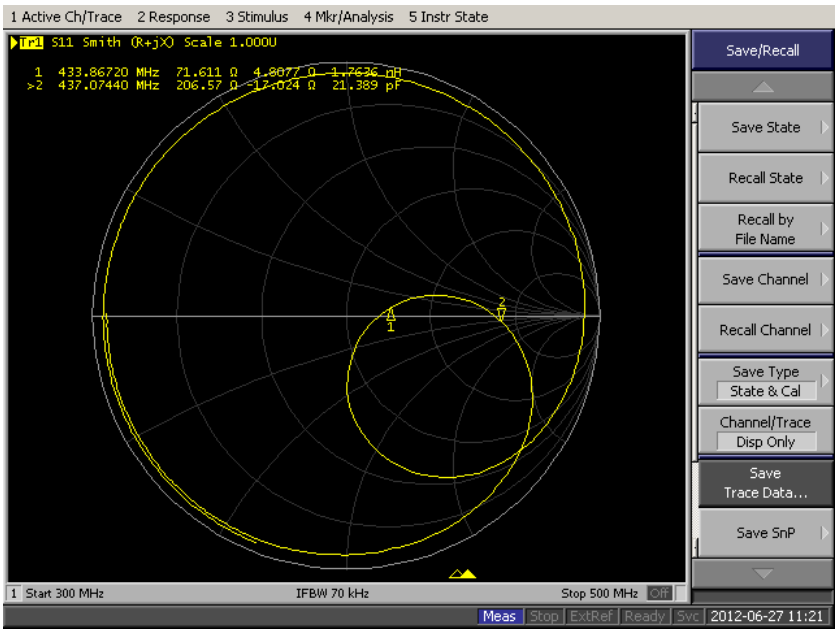

Figure 6.12. A screenshot of case A return loss measurement using Agilent E5071B Network Analyzer, displaying the data in Smith Chart.

The same measurement set-up was applied for acquiring the return loss of the antenna in the case B configuration, in which the antenna was encapsulated with the PDMS layer. The screenshot of the return loss dataset on case B measurement are presented in Figure 6.13 and Figure 6.14 for Cartesian and Smith chart format, respectively.

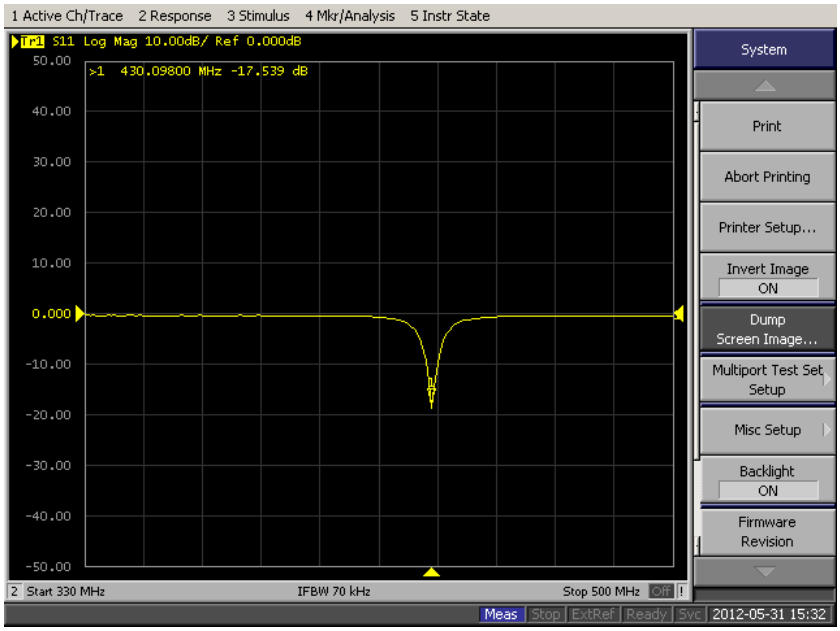

Figure 6.13. A screenshot of case B return loss measurement using Agilent E5071B Network Analyzer.

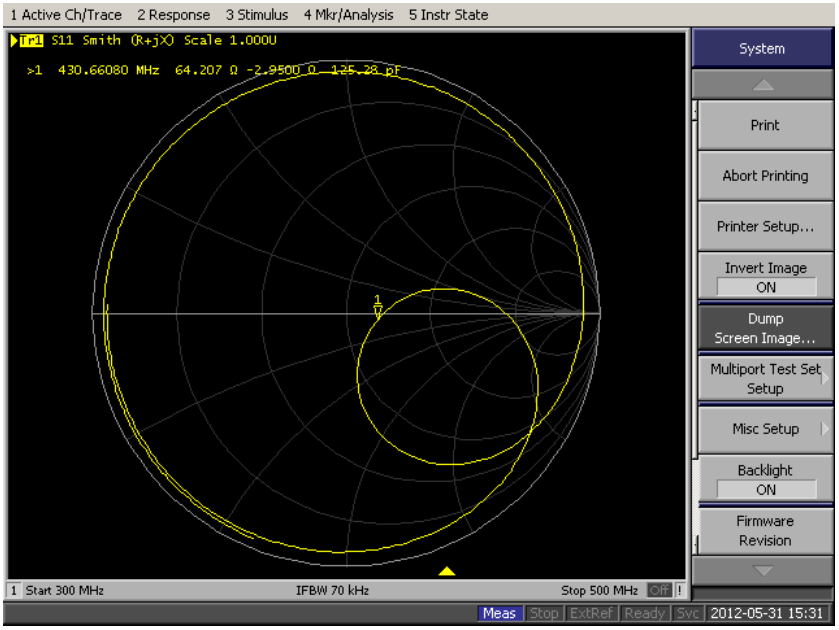

Figure 6.14. A screenshot of case B return loss measurement using Agilent E5071B Network Analyzer, displaying the data in Smith Chart.

Table 6.1 showed the measured return losses of the case A and case B in terms of the resonant frequency and the minimum return loss value in each case. The resonant frequency was determined as a frequency at which the return loss was at its lowest point. Between each case, there was a slight decrease on the resonant frequency (3.2 MHz) as well as a small increase on the return loss magnitude (1.23 dB). By analysing the dataset, the 10 dB bandwidth for each case can also be determined. For case A, the 10 dB return loss spanned from 431.2 to 434.8 MHz to constitute a 3.6 MHz bandwidth. The 10 dB region on case B ranged from 428.6 to 432 MHz to produce a bandwidth of 3.4 MHz. The datasets resulted from the network analyzer can be found in the Appendix (Appendix 3 for case A datasets and Appendix 4 for case B datasets).

Table 6.1. Measured Antenna Performance on 2 different configurations.

Case	Frequency (MHz)	Min. Return Loss (dB)	Bandwidth (MHz)
A	433.2	-20.12	3.6
B	430	-18.89	3.4

6.2.2. Radiation Pattern

The measurement of the gain and the radiation of the antenna in both cases were conducted inside an anechoic chamber. An adjustable half wave dipole antenna manufactured by Singer was selected as a source antenna and located at a distance such that both antennas

are at each other's far field zone. This is to ensure that the AUT is exposed to a plane wave of uniform amplitude, phase, and polarization [98]. The far field distance for both antennas was calculated using the following formula [99]:

$$R = \frac{2D^2}{\lambda} \tag{6.1}$$

where D is the maximum aperture of the antenna, λ is the wavelength, and R is the far field distance. Based on this formula, the far field boundary of the dipole antenna and the antenna under test (AUT) were calculated to be 0.37 m and 0.27 mm, respectively. It implies that the minimum distance between the two antennas should be around 0.37 m to ensure far field transmission. The measurements were conducted inside a 6 m length anechoic chamber, which exceeds the required separation between the two antennas.

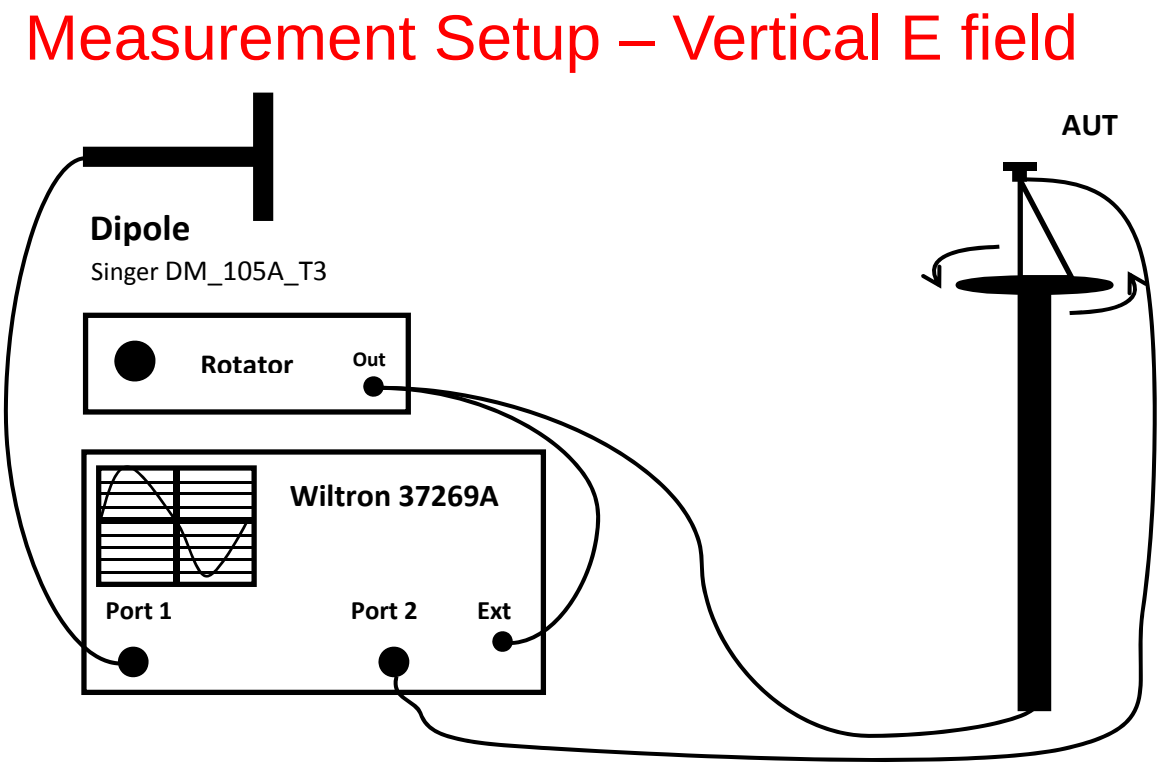

Figure 6.15. The equipment and cable configuration of the vertical E-field radiation pattern and gain measurement of the AUT for all the 3 cases. The measurement was conducted inside an anechoic chamber.

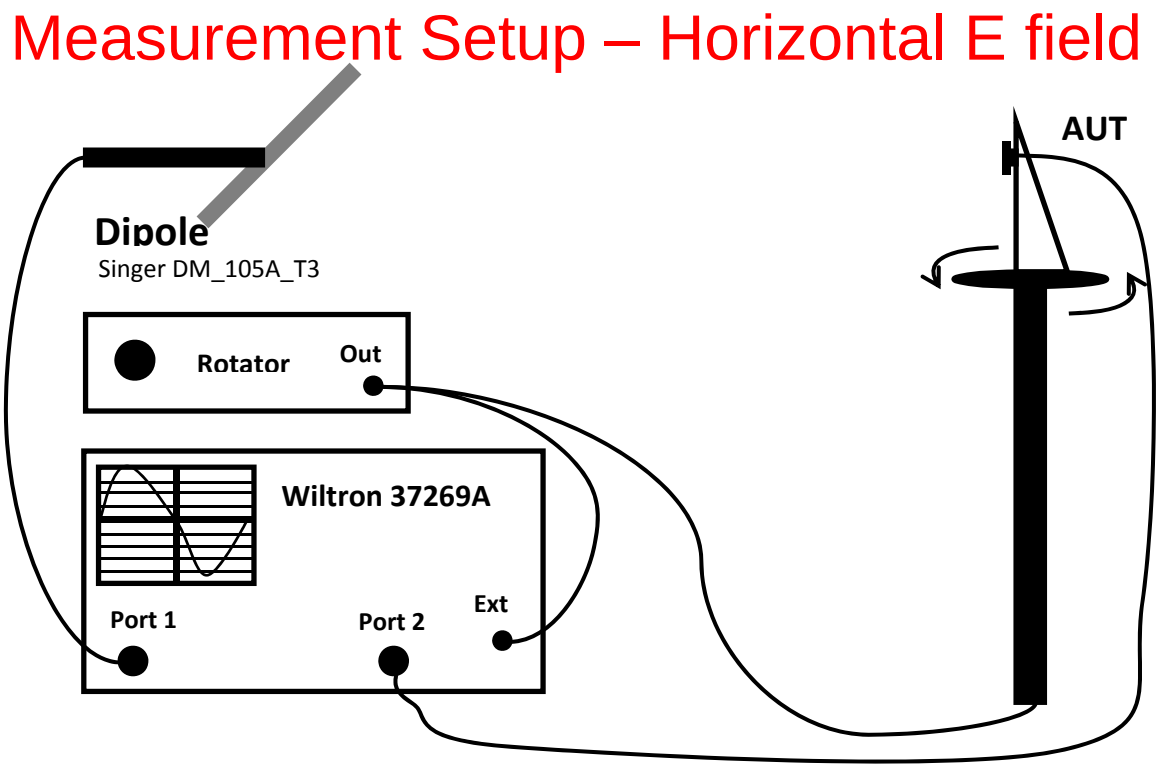

Figure 6.16. The equipment and cable configuration of the horizontal E-field radiation pattern and gain measurement of the AUT for all the 3 cases. The measurement was conducted inside an anechoic chamber.

Figure 6.15 and Figure 6.16 illustrate the configuration of the radiation pattern measurement of the AUT inside the anechoic chamber. The apparatuses used in both configurations are identical and the set-up only differed in the position of the antenna. The main equipment was the Wiltron 37269A Network Analyzer. The port 1 of this device was connected to the dipole antenna to supply transmission power. The signal source was set at the frequency 433 MHz (case A) and 430 MHz (case B) based on the return loss measurement of the AUT and each dipole arms' length was set to 17 cm correspondingly. The port 2 was connected to the AUT to measure the power received by the antenna in the course of 360° rotation. An external triggering signal was supplied by the rotator to ensure synchronicity between the antenna rotation and the data capturing process by the analyzer. In one full rotation, there were 450 steps in which the data was captured by the analyzer, which was mathematically equivalent to data resolution of 0.8° between each data point. To establish accurate data sampling at each particular angle, an averaging of 50 points was performed. This means that 50 points were measured at one particular angle and were averaged in order to minimize the chance of an outlier being collected and identified as the real data. The dipole antenna, Singer DM_105A_T3, was stationary during the whole process and was placed at the same height of the AUT.

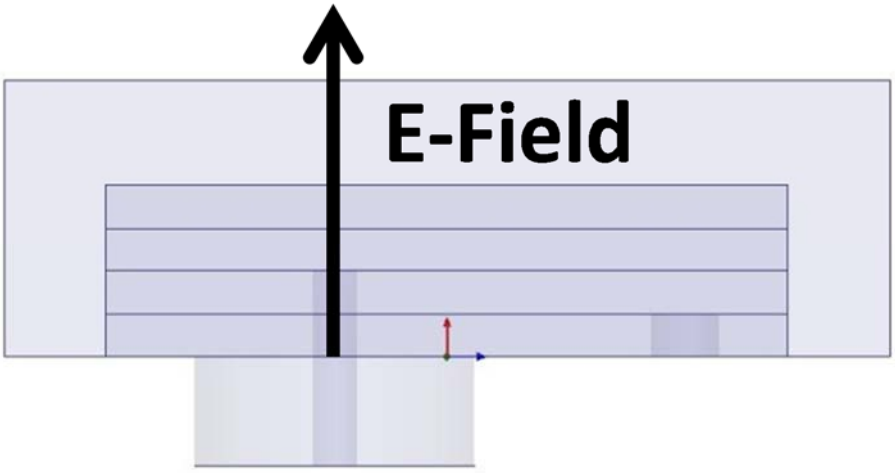

Figure 6.17. The E-field orientation with respect to the antenna position.

Several testings were conducted prior to the real measurement to determine the polarization of the antenna. It is critical that the data was recorded under a co-polarization mode to ensure that the real characteristic of the antenna was captured. Based only on the simulation results, it was not clear which way the E-field of the antenna was propagating due to the spiral pattern at the layer 3 as well as the small feeding pin size. The E-field was finally determined to be propagating vertically, parallel to the pin and perpendicular to the antenna layers (Figure 6.17). With this knowledge, co-polarization transmission can be assured on every measurement.

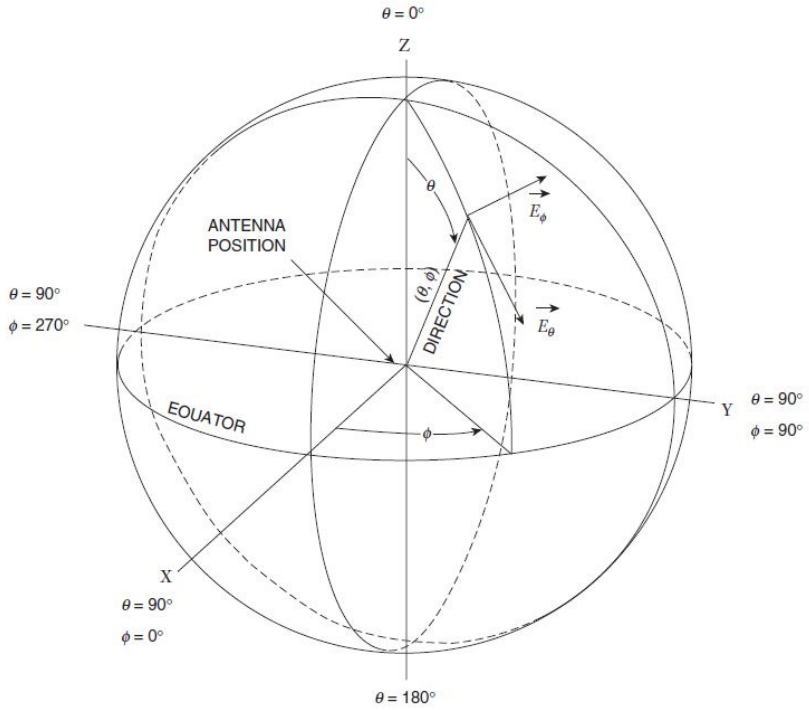

Figure 6.18. Standard spherical coordinate system used in antenna measurement [IEEE, 1979]

The radiation pattern was carefully measured following the guidelines published on IEEE Standard for Antenna Measurement [100] with its spherical coordinate system (Figure 6.18). It was recommended that 2 patterns were measured to obtain important characteristic on the antenna radiation pattern: a 360° rotation along the equator (ϕ = 0° to 360°) at θ = 0° and a 360° rotation along the equator (ϕ = 0° to 360°) at θ = 90°. The realization of this concept was a configuration in which both antenna are in vertical E-field mode (Figure 6.15) and in which both antenna are in horizontal E-field mode (Figure 6.16). A complete set of data from those two rotations would allow an approximate reconstruction of the 3D radiation pattern of the AUT. For a better understanding on the polar plots, the AUT's initial position was always set at 90° off the source antenna (clockwise). This way, the 90° position at the polar plot always signifies the main lobe of the antenna under test.

Figure 6.19 and 6.20 display the measured radiation patterns inside the chamber for case A antenna. Figure 6.19 visualizes the co-polarization transmission of horizontal E-field while figure 6.20 shows the vertical E-field transmission. The polar plot was created by running a Matlab code for creating a 2D radiation pattern based on the acquired measurement data. The code can be found in Appendix 6. It can be observed that an omnidirectional pattern was acquired on case A antenna, with a pair of nulls around ϕ = 100° and ϕ = 290°.

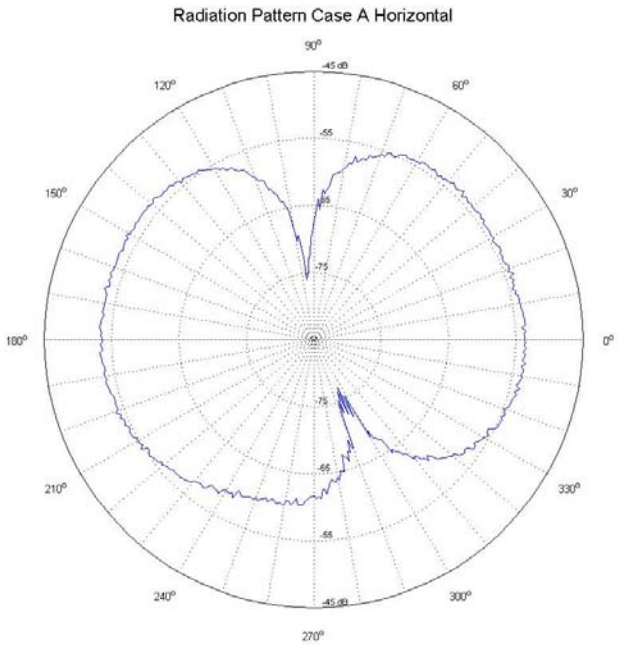

Figure 6.19. The radiation pattern of the antenna in case A with horizontal E-field.

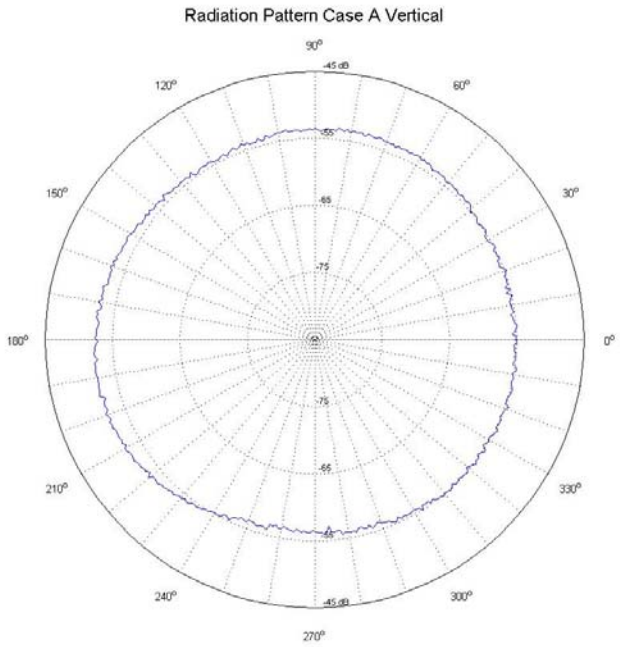

Figure 6.20. The radiation pattern of the antenna in case A with vertical E-field.

With the addition of PDMS layer in case B, an omnidirectional pattern can still be observed, with the two nulls positioned at $\phi = 90°$ and $\phi = 280°$ (Figure 6.21). However, in this case, one of the lobes lost its gain and became moderately smaller than the other lobe. Just like on the previous case, the horizontal E-field pattern was a circular, which signified the omnidirectional characteristic of the antenna.

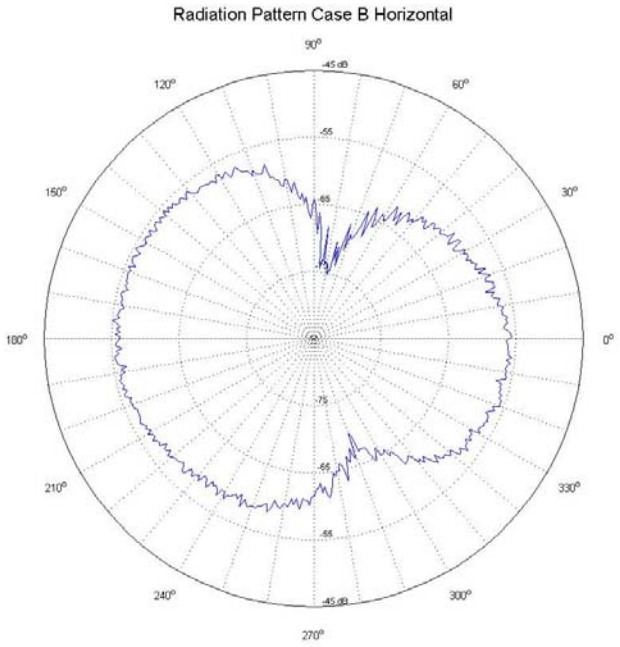

Figure 6.21. The radiation pattern of the antenna in case B with horizontal E-field.

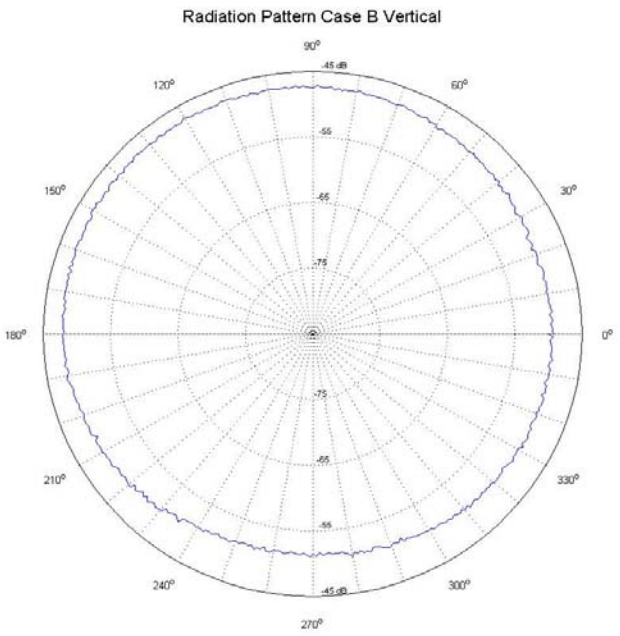

Figure 6.22. The radiation pattern of the antenna in case B with vertical E-field.

6.2.3. Gain

To find the gain of the AUT, the following formula was used:

$$G\ (dBi) = G_{standard} + (G_{AUT} - G_{ref}) \qquad (6.2)$$

where $G_{standard}$ is the known gain of the reference antenna (dBi), G_{AUT} is the measured gain of the tested antenna (dB), and G_{ref} is the measured gain of the reference antenna (dB). The reference antenna in this case was half wave dipole, which has a gain of 2.15 dBi.

The gain of the reference antenna in use, $G_{standard}$, was not initially known. A set of measurements were conducted in order to find the gain of the dipole antenna, both in horizontal E-field and vertical E-field. The equipment configurations are the same as the radiation pattern measurement of the AUT, except that another dipole antenna was sitting in place of the AUT (Figure 6.23 and Figure 6.24). As it was in AUT radiation pattern measurement, the configurations were set to produce co-polarization communication link between the two antennas. This procedure was always applied every time a measurement configuration was set up to obtain the utmost accuracy from the results. As a consequence, the $G_{standard}$ values are varied between each measurement. The datasets of reference antenna gain measurements can be found in the Appendix (Appendix 7 and 8 for case A and B, respectively).

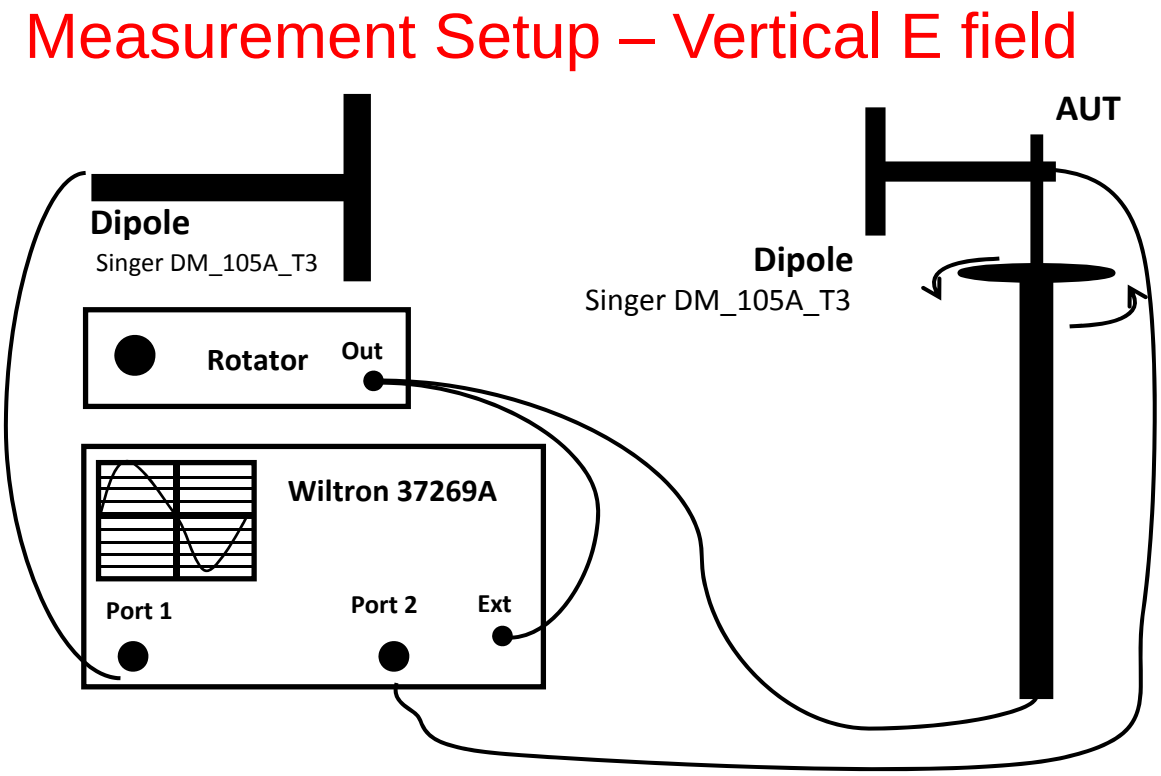

Figure 6.23. The equipment and cable configuration of the vertical E-field reference antenna gain measurement. Both the transmit and the receive antenna in this configuration are identical (half-wave dipole Singer DM_105_T3). The measurement was conducted inside an anechoic chamber.

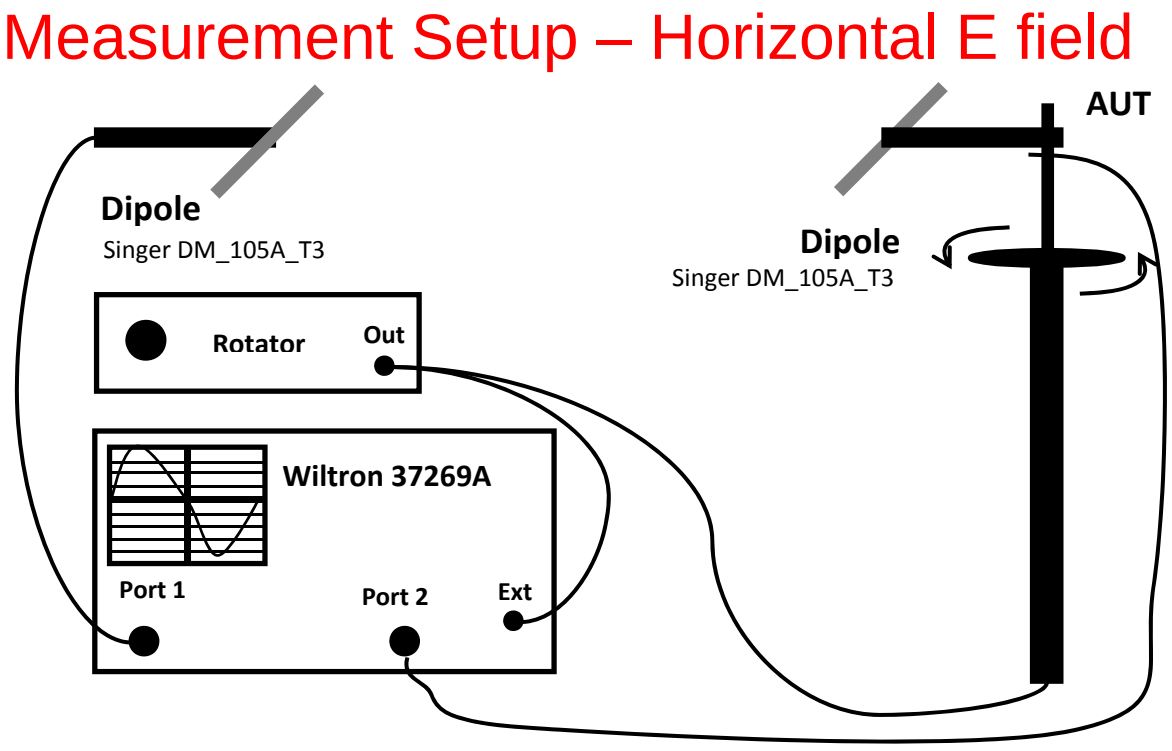

Figure 6.24. The equipment and cable configuration of the vertical E-field reference antenna gain measurement. Both the transmit and the receive antenna in this configuration are identical (half-wave dipole Singer DM_105_T3). The measurement was conducted inside an anechoic chamber.

As explained on the previous chapter (Figure 5.15), the most significant points of gain from the measured radiation pattern were the ones at ϕ = 0° and ϕ = 180°. Those positions are where the highest gain should occur on this antenna. Theoretically, the two points should overlap between the vertical and the horizontal E-field (refer to Figure 6.18). An exact pair is very difficult to achieve in the real situation due to a number of aspects, which will be discussed in the next chapter. The calculation of the two points for all the cases can be seen in Table 6.2.

Table 6.2. Measured gain of the antenna in case A and B

Case	**Horizontal E-field**		**Vertical E-field**	
Gain	**Φ = 0°**	**Φ = 180°**	**Φ = 0°**	**Φ = 180°**
A	-32.35	-32.17	-36.75	-33.84
B	-35.93	-36.07	-31.21	-30.09

The data in Table 6.2 provided useful information about the antenna characteristic in terms of the radiation pattern and the gain values. Initially, it is important to look at the gain values of each antenna at ϕ = 0° and ϕ = 180° at one E-field direction and compare them against the gains of the same angle with another E-field direction. It is evident that there are various discrepancies on the data with the range of 2 dB up to 6 dB. Possible contributing factors to the inconsistencies include alignment issues, non-symmetrical anechoic chamber, as well as spurious radiation from the coaxial cable.

6.3. Measurement inside the Vitreous Humour Liquid

The measurements of the antenna in case A and case B configuration have been discussed on the previous Section. It is now time to find out the antenna performance on the scenario at which the antenna was initially designed for. The proposal of case D was created to resemble the antenna performance inside a human Vitreous Humour due to the difficulty to secure an approval from the ethic committee. Instead of using a real human eyeball, a table tennis ball with a Vitreous Humour mimicking liquid was implemented. Despite its bigger size (d = 40 mm), the performance of the antenna was relatively unaffected compared to the performance using original configuration. Therefore, the model was employed to construct a representation on the antenna performance inside a human eyeball.

6.3.1. Fluid and Model Generation

It has been discussed previously that human tissues possess an interesting characteristic of being frequency dependent. For example, Vitreous Humour has a characteristic of $\varepsilon_r = 69$, $\sigma = 1.53$ S/m at 402 MHz while it is $\varepsilon_r = 68.24$, $\sigma = 2.44$ S/m at 2.4 GHz [64]. While the relative permittivity of the material remains the same, the conductivity is increased by 59.5%, which is very significant in this case. Therefore, a generation of fluid with a defined operating frequency is crucial for the accuracy of the outcomes.

The tissue mimicking material generation in this experiment was based on the relative permittivity and conductivity values of the fluid. A study has been conducted on creating a liquid with certain ε_r and σ values by modifying the sugar and salt contents [80]. After running a frequency sweep of 300 MHz to 3 GHz for the investigation, it was found out that the sugar content lowered the ε_r of the liquid significantly (Figure 6.25), while at the same time increasing the σ slightly (Figure 6.26). On the other hand, the salt substance was found to have a characteristic of significantly increasing the σ (Figure 6.28) while slightly lowering ε_r in process (Figure 6.27).

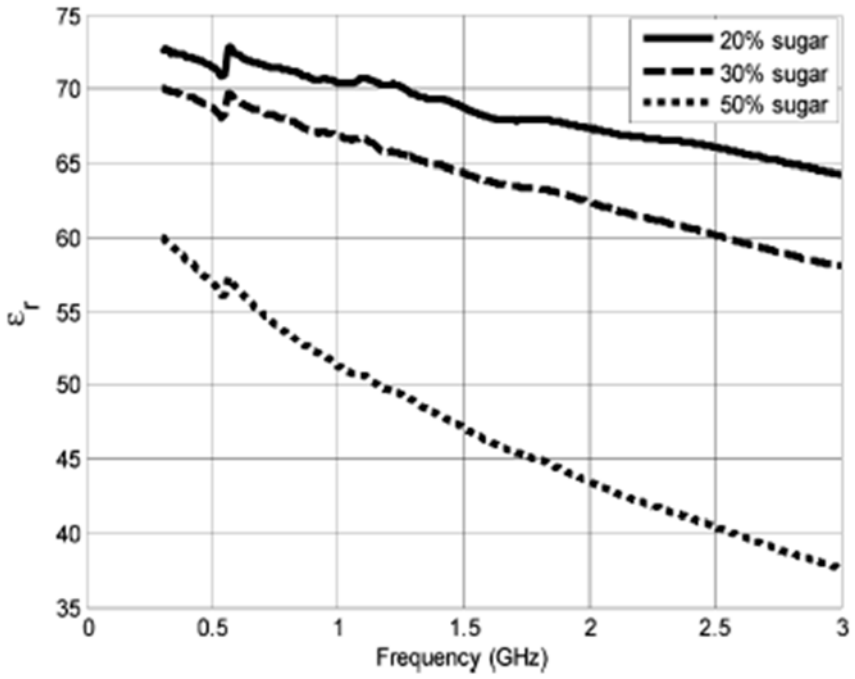

Figure 6.25. Relative permittivity of the fluid as a function of frequency for different sugar contents [Karacolak, 2008]. It can be observed that relative permittivity is significantly reduced with a higher concentration of sugar.

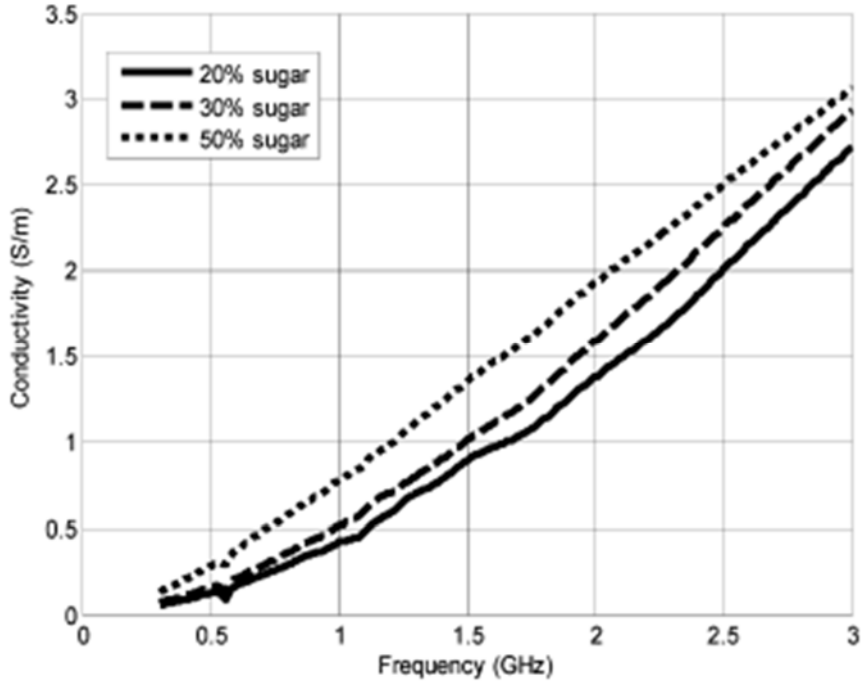

Figure 6.26. Conductivity of the fluid as a function of frequency for different sugar contents [Karacolak, 2008]. Only slight increase on the conductivity was observed as a result of higher sugar concentration.

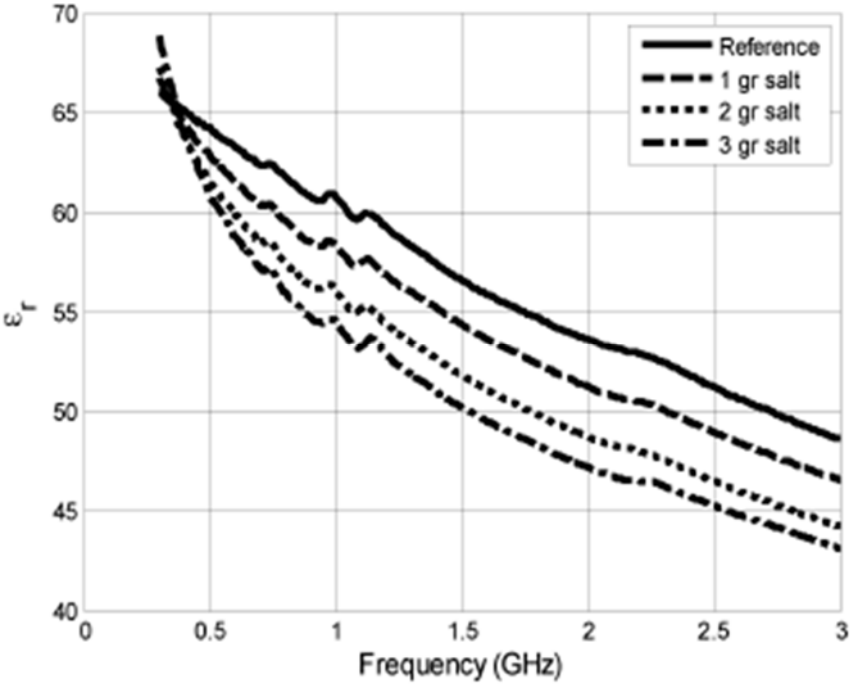

Figure 6.27. Relative permittivity of the fluid as a function of frequency for different salt contents [Karacolak, 2008]. Only slight decrease on the conductivity was observed as a result of higher salt concentration.

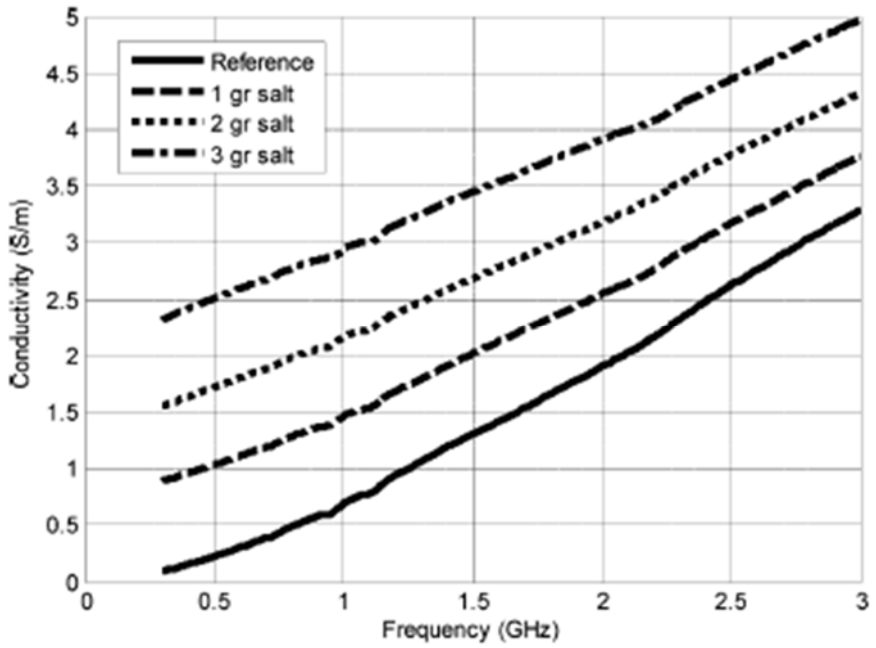

Figure 6.28. Conductivity of the fluid as a function of frequency for different salt contents [Karacolak, 2008]. It can be observed that conductivity is significantly increased with a higher concentration of salt.

This means that both substances can be used to control the permittivity and the conductivity of the liquid, which is based on deionized water (ε_r = 81, σ = 0.0002 S/m). The task of generating the right recipe was completed by Mr. Peter Jakubiec from EMC Technologies, Melbourne, Australia, with the assistance of a network analyser with a dielectric probe. A batch of liquid was generated with a characteristic of ε_r = 65.2, σ = 1.59 S/m at 22.1°C at 400 MHz. These attributes were considered very close to the required values and were therefore employed for the measurement.

The eyeball model used in the simulation was realized by a table tennis ball. A table tennis ball is made of a very thin celluloid layer (thickness = 0.35 mm) and has a uniform spherical geometry, which makes it a perfect substitution of a human eyeball. The existence of the celluloid layer was not expected to create a significant impact to the antenna performance due to its thickness relative to the wavelength. The idea was to insert the antenna and the liquid into the ball while still keeping the geometry unchanged. This involved an initial task of removing parts of the ball (Figure 6.29) and attaching it to the rigid coaxial cable that holds the antenna (Figure 6.30). Thin layers of power glue and sealant were applied to the joined area to prevent any leakage. Finally, the liquid was injected into the ball by using a syringe through a designated hole (Figure 6.30) and a strip of masking tape was put in place to avoid any fluid leaking. The resulting configuration can be observed from Figure 6.31.

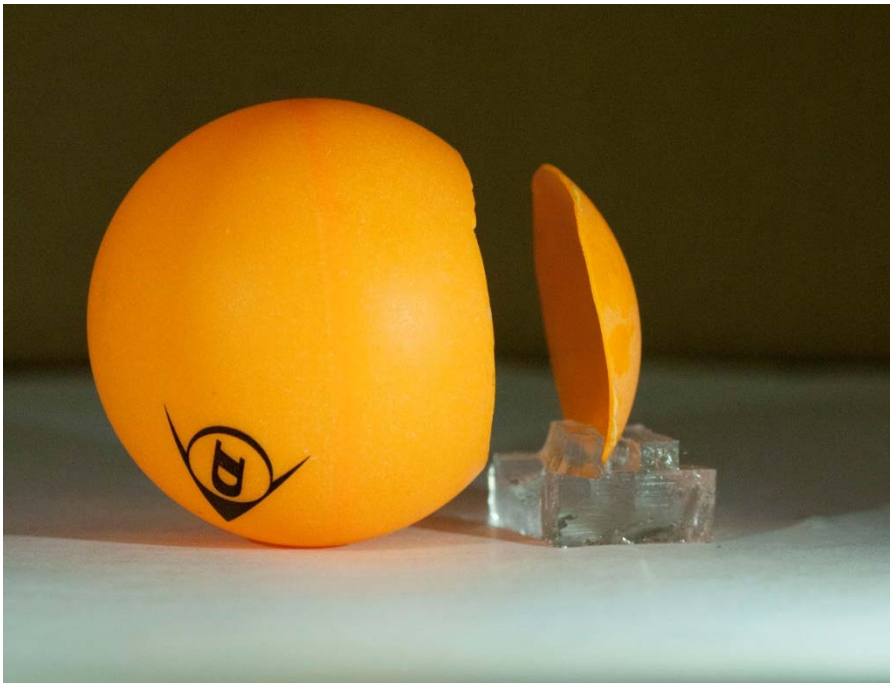

Figure 6.29. The top part of the ball was cut with the aid of a Dremel. The cutting line has to be carefully measured to ensure enough gap for the antenna.

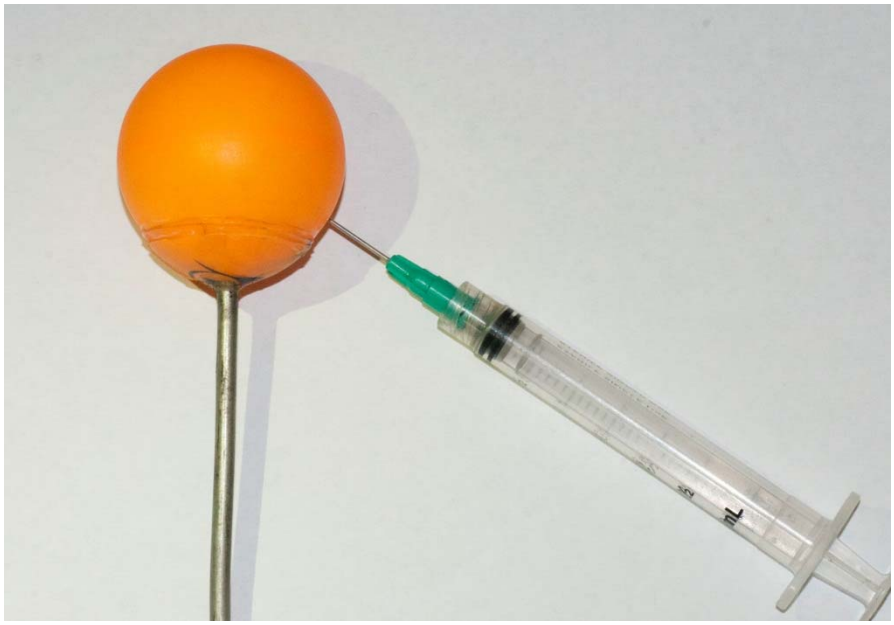

Figure 6.30. The artificial Vitreous Humour liquid was injected through a small hole on the ball surface. The process was done repeatedly until the ball was completely filled with the liquid.

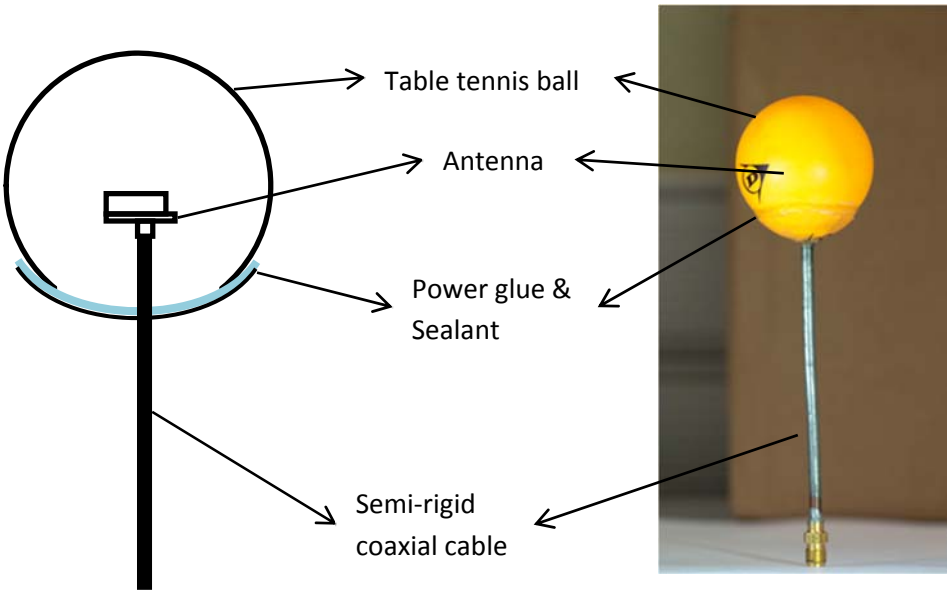

Figure 6.31. The configuration of the antenna inside the table tennis ball. The antenna was positioned right at the centre of the table tennis ball to resemble the exact configuration as the simulation.

6.3.2. Return Loss

The return loss of the antenna was measured using the free space configuration, with the antenna already submerged into the liquid. The minimum measured return loss was -12.05 dB at 421.2 MHz (Figures 6.32 and 6.33). The 10 dB bandwidth spanned from 420 to 422.8 MHz.

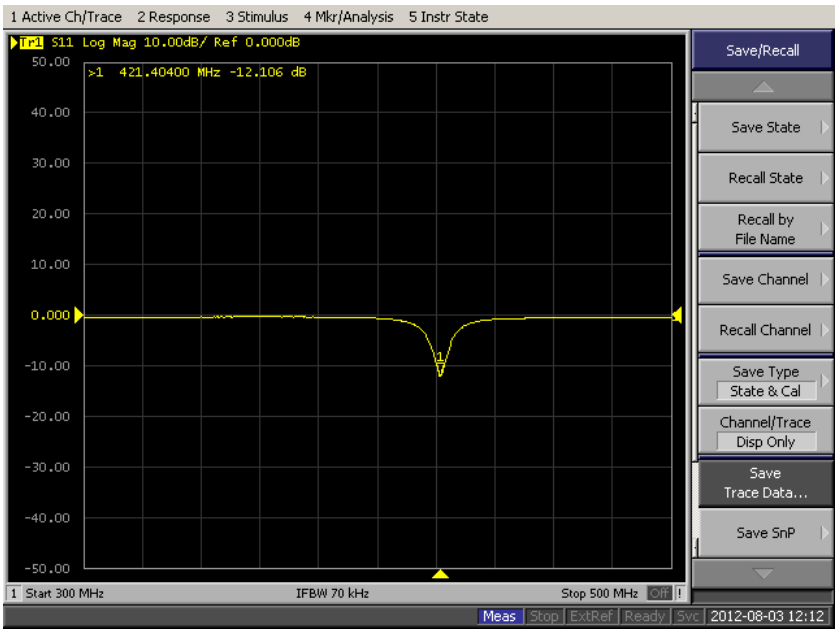

Figure 6.32. A screenshot of case D return loss measurement using Agilent E5071B Network Analyzer.

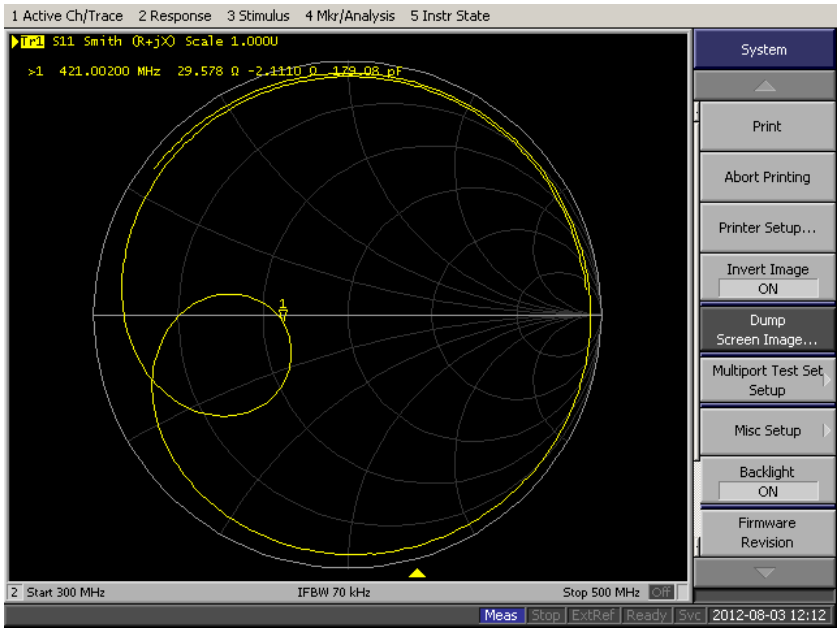

Figure 6.33. A screenshot of case D return loss measurement using Agilent E5071B Network Analyzer, displaying the data in Smith Chart.

6.3.3. Radiation Pattern

The radiation pattern and the gain of the AUT with its table tennis ball were measured using the same configuration as the free space measurement (Figure 6.15 and 6.16). However, special attention had to be paid to the orientation of the antenna since it was not visible from the outside. Figure 6.34a and 6.34b show the configuration of the measurement inside the anechoic chamber for vertical and horizontal E-field transmission, respectively.

(a) (b)

Figure 6.34. Measurement configuration of case D on (a) vertical E-field and (b) horizontal E-field inside an anechoic chamber.

Figures 6.35 and 6.36 present the measured radiation pattern of the AUT in case D configuration in horizontal and vertical E-field, respectively. The patterns resembled asymmetric omnidirectional shapes with nulls occurring at $\phi = 90°$ and $\phi = 320°$.

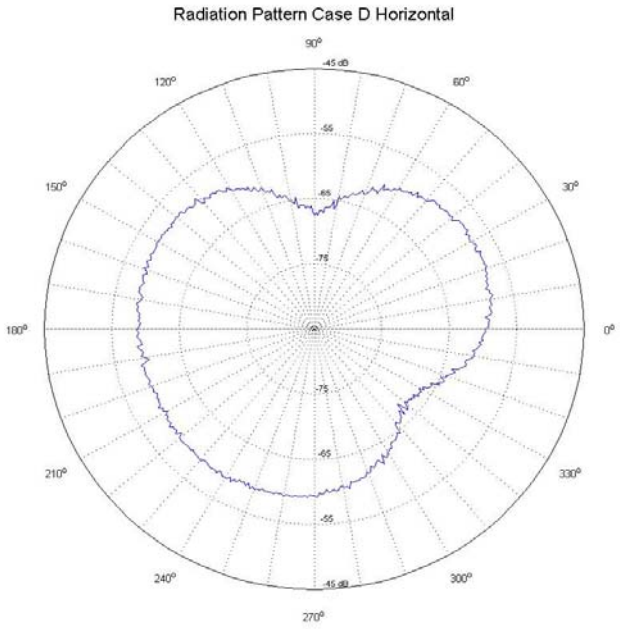

Figure 6.35. The radiation pattern of the antenna in case B with horizontal E-field.

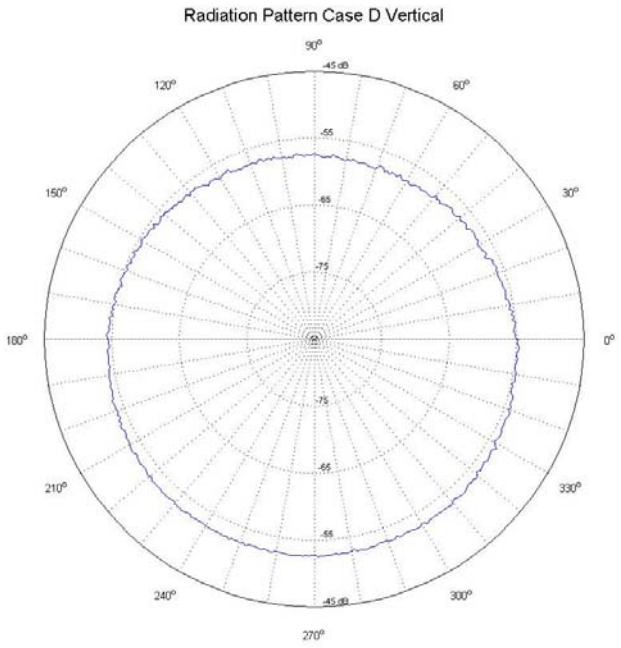

Figure 6.36. The radiation pattern of the antenna in case B with vertical E-field.

6.3.4. Gain

The gain of the AUT was obtained at $\phi = 0°$ and $\phi = 180°$ of both E-field orientations, and then the formula 6.2 was applied. For the horizontal E-field, the gain was -39.89 dB and -39.29 dB for $\phi = 0°$ and $\phi = 180°$, respectively. For the vertical E-field set up, it was -37.89 dB and -37.36 dB, respectively. As expected, the gain values with the Vitreous Humour surrounding the antenna were lower compared to the free space measurements.

6.4. Summary

In this chapter, the measurement process has been presented. The chapter was initiated by the antenna fabrication procedure. On the next Section, the measurement configuration of the antenna in free space was discussed, which included the equipment configuration, device settings, as well as data analysis process. The antenna performance in terms of return loss, radiation pattern, and gain, was then presented. The following Section provided an insight on the measurement inside the Vitreous Humour liquid, started by some background on the mimicking liquid and the model generation. The measurement procedure for each parameter was also presented, and this chapter was finalised by the demonstration of the results on each respective variable. In the next chapter, these results will be discussed and analysed. The discrepancies between them and the simulation results will also be explained.

Chapter 7

Data Interpretation and Analysis

In Chapter 5, the antenna performance with three different parameters was presented following a run of simulations. Subsequently, the designed antenna was manufactured and was encapsulated with PDMS material. The simulation data was validated by a measurement on the real antenna. In Chapter 6, the measurement procedure to obtain the value of each parameter (return loss, radiation pattern, and gain) was discussed for each antenna configuration (case A, case B, and case D). The measurement results were presented at the end of each Section. In this chapter, the simulated and measured data will be revisited and analysed to see the actual performance in comparison with the simulation data. Each parameter will be investigated separately in a head to head comparison for each antenna case. At the end of the chapter, the performance of the antenna will be compared against other implantable antennas that have been studied for similar purposes.

7.1. Return Loss

Table 7.1. Simulated antenna performance on different setups

Case	Simulation			Measurement		
	Frequency (MHz)	**Min Return Loss (dB)**	**Bandwidth (MHz)**	**Frequency (MHz)**	**Min Return Loss (dB)**	**Bandwidth (MHz)**
A	410.4	-21.31	3.2	433.2	-20.12	3.6
B	408.8	-19.35	3.6	430	-18.89	3.4
C	402.8	-10.86	3.2	N/A	N/A	N/A
D	402.8	-11.17	3.2	421.2	-12.05	2.8

Table 7.1 gives a summary on the antenna return losses based on the simulation and the measurement results. It shows the resonance frequency as well as the minimum return loss of each case both from the simulation and the measurement. Based on the simulation results, the encapsulation of the antenna shifted the resonant frequency down by 1.6 MHz with an increase in 10 dB bandwidth from 3.2 MHz to 3.6 MHz. The measurement confirmed the effect of additional PDMS layer on the antenna performance, shown by a

decrease of 3.2 MHz on its resonant frequency with a slight bandwidth decrease of 0.2 MHz. Despite a slight variation on the resonant frequency drop, this occurrence has revealed that the presence of PDMS layer around the antenna produces a small drop on the antenna resonant frequency.

Case C is obviously only applicable in the simulation due to the permit issue, but the simulation results on case C and D suggested that the implementation of a table tennis ball instead of a human eyeball produced minimum effect on the resonant frequency and the bandwidth of the antenna, with unchanged resonant frequency and bandwidth and 0.31 dB shift on the return loss. Therefore, the adoption of table tennis model can be considered as an accurate representation on *in vivo* measurement of the antenna. The introduction of Vitreous Humour liquid as the surrounding medium expectedly lowered the frequency in the simulation (6 MHz). The measurement agreed with this scenario, where a decrease of 8.8 MHz was observed on the resonant frequency and 0.6 MHz drop on the 10 dB bandwidth. Figure 7.1 to Figure 7.3 provide comparisons on the simulated and measured return loss for each antenna configuration in frequency domain based on the datasets acquired from the network analyser (Appendix 3-5).

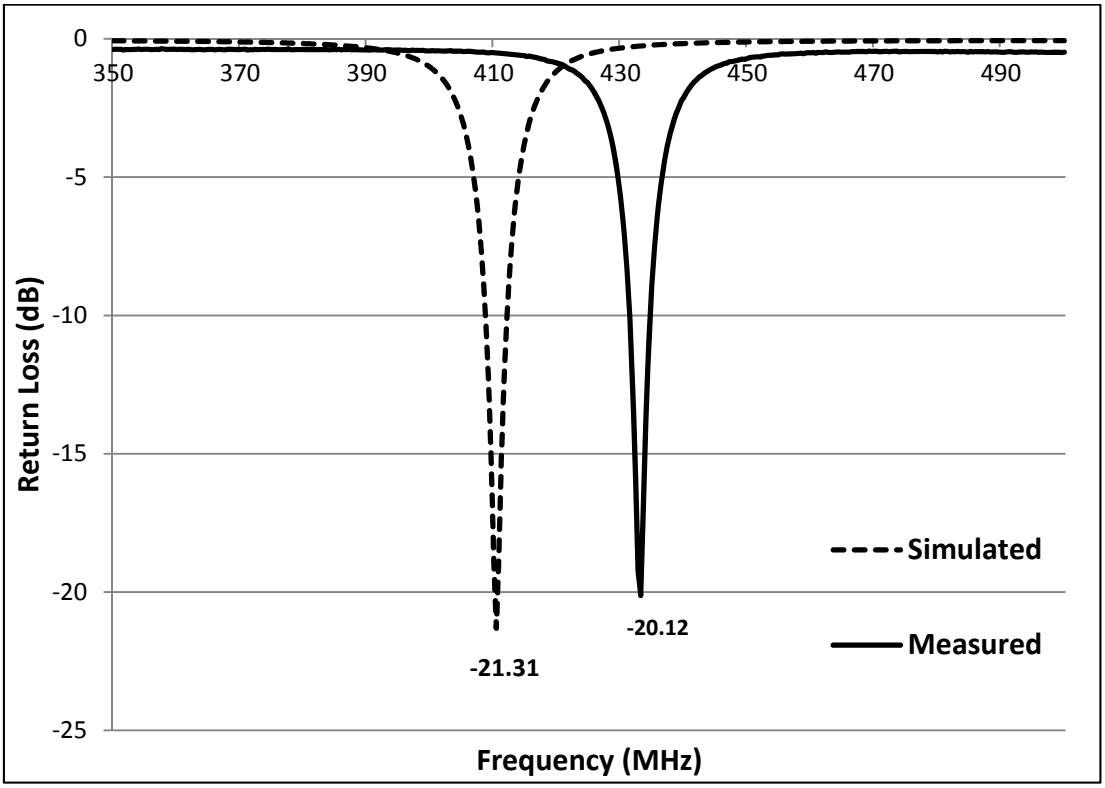

Figure 7.1. Return loss comparison between the simulation and the measurement results for case A configuration.

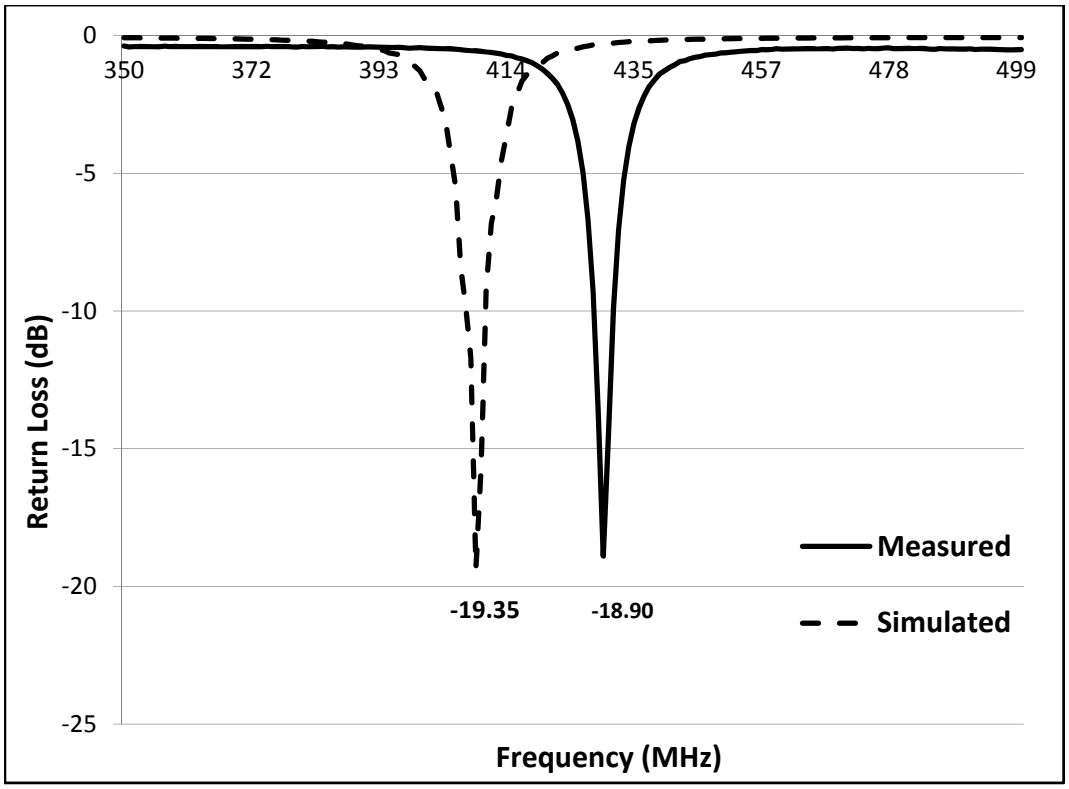

Figure 7.2. Return loss comparison between the simulation and the measurement results for case B configuration.

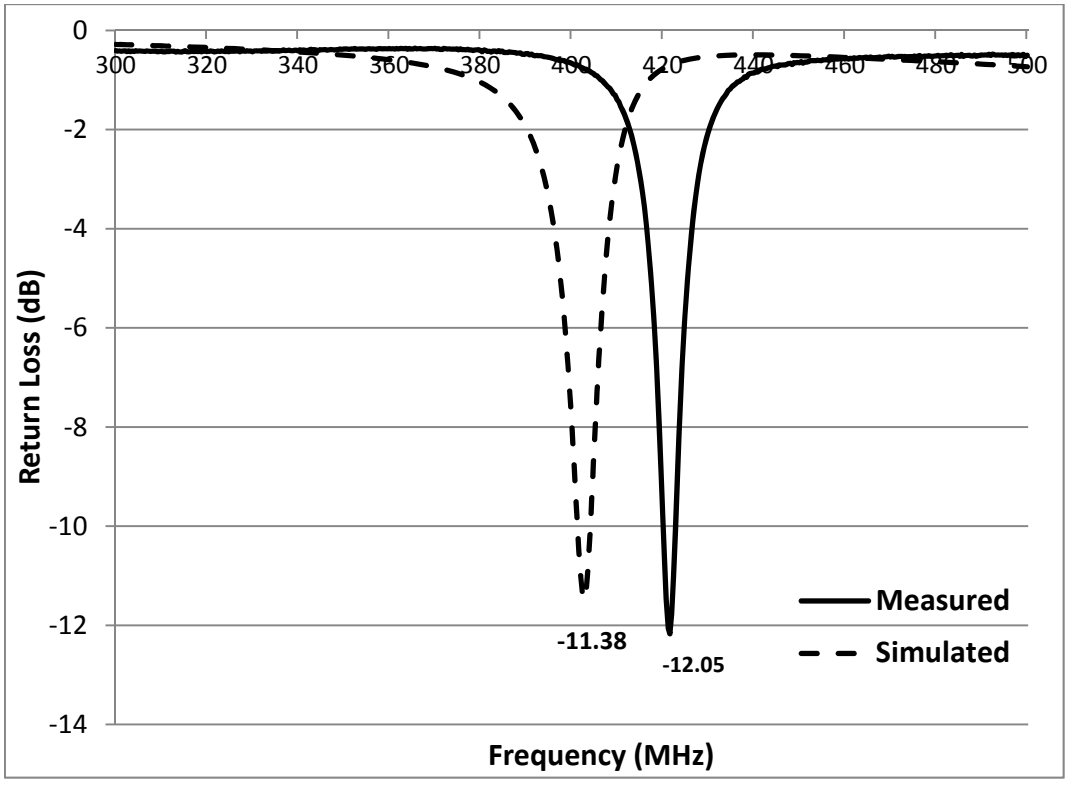

Figure 7.3. Return loss comparison between the simulation and the measurement results for case D configuration.

In cases A and B, it is evident based on the figures in Table 7.1 and the plot in Figure 7.2 that, apart from the resonant frequency, the return loss characteristic of both the simulation and the measurement were identical. The resonance discrepancy was 21.2 MHz or 5.16% relative to the simulation result. Case D is the most important configuration because this is the condition in which the antenna is designed for. In this case, the actual resonant frequency was 4.67% higher than the one resulted from the simulation with a 0.8 MHz increase on the 10dB bandwidth.

Overall, it can be concluded that the simulation provided a good reference on how the actual antenna would perform. The consistent 20 dB shift on the resonant frequencies can be attributed to the small flaws resulted by the manufacturing process. The most significant one would be the air gap created in the solder joints on layer 3 (feed pin) and layer 2 (ground pin). The antenna was manufactured with manual assembling technique, hence the existence of these air gaps is mechanically difficult to eliminate. Misalignment between each layer is another unpreventable issue as a result of this manual manufacturing procedure and it is also a contributing element on the resonant frequency inconsistency. Another factor that possibly contributed to the discrepancies was the application of the adhesive layer to join all the four layers. The addition of the adhesive layer on the sides of the antenna was not reflected in the simulation design and might have influenced the antenna performance, due to its distinct relative permittivity value (around 3.6) compared to the substrates of the antenna.

7.2. Radiation Pattern

Based on the simulation, the radiation pattern of the antenna in all cases was omnidirectional with the nulls located at both end of z-axis (Figure 7.4). The simulation results showed that the antenna produced the same radiation pattern for each case with variation only on the gain values.

Figures 6.19 to 6.22 and Figures 6.36 & 6.37 in Chapter 6 displayed the polar plot of the antenna's radiation pattern in cases A, B, and D, consecutively. In figure 6.19, the omnidirectional pattern can be observed despite the nulls being slightly off the z-axis. The reason for this variation was the alignment issue during the antenna measurement due to ambiguous starting point of the rotation.

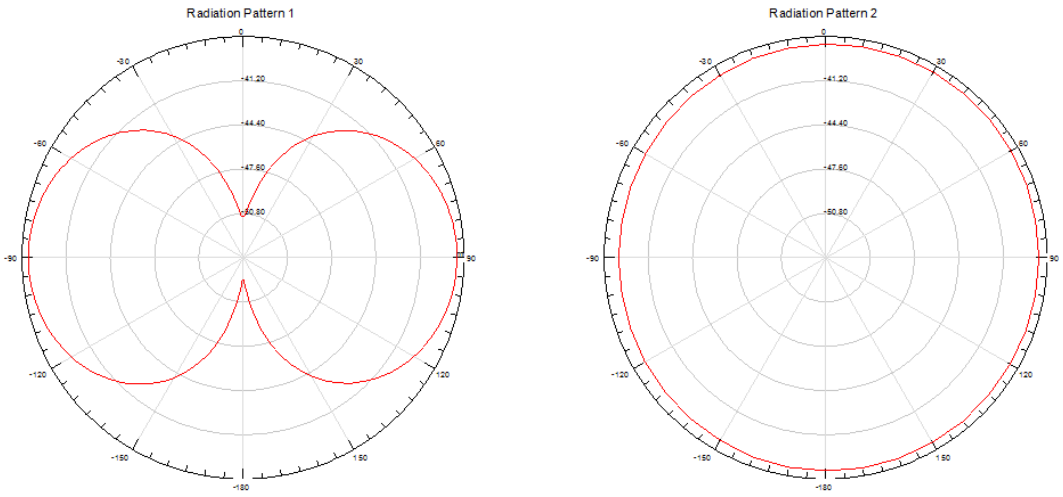

Figure 7.4. 2D Representation of simulated radiation pattern in (a) YZ plane and (b) XY plane.

The measurement of the encapsulated antenna in free space (case B) demonstrated an omnidirectional pattern with one of its lobe being smaller than the other (Figure 6.21). The position of the nulls was asymmetric, with one null at φ = 90° and the other at φ = 280°. There was also a clear alignment issue since both nulls were located off the z-axis. If this plot is observed and compared carefully with the Figure 6.19, it can be seen that this plot clearly resembled the pattern from the previous figure except for the shrinkage on one of the lobes. The most logical explanation to this phenomenon was the asymmetric dimension of the anechoic chamber (refer to Section 7.3). That, combined with the low operating frequency, was expected to cause imperfect absorption by the foam and therefore the signal reflections boosted the gain of the antenna in an irregular manner.

On the measurement of the antenna inside Vitreous Humour liquid (case D), there was a difficulty in adjusting the starting rotation point of the antenna due to the inability to see the antenna externally. As a result, the pattern was clearly off-centred judging by the nulls' position (at φ = 90° and φ = 320°).An uneven size of antenna lobes was again noticeable in this plot due to the same reason as the previous measurement. Apart from these issues, the pattern bears a resemblance to omnidirectional pattern as produced in the simulation.

7.3. Gain

Table 7.2 shows the comparison of antenna gains between the simulation and the measurement inside the anechoic chamber at two different positions, at φ = 0° and φ = 180°.

Table 7.2. The comparison between simulated and measured gain of the antenna in all four scenarios.

Case	Simulation		Measurement	
	Gain at ϕ = 0° (dB)	**Gain at ϕ = 180° (dB)**	**Gain at ϕ = 0° (dB)**	**Gain at ϕ = 180° (dB)**
A	-38.83	-38.88	-36.75	-33.84
B	-38.63	-38.59	-35.93	-36.07
C	-41.43	-41.02	N/A	N/A
D	-40.57	-39.89	-39.89	-39.29

Based on the simulation results, the addition of PDMS layer to a free space did not affect the gain of the antenna. Once Vitreous Humour liquid was introduced, a dip of approximately 3 dB was evident on the antenna gain. On case D, where a table tennis ball was utilised instead of human eyeball, there was a slight decline on the gain value. The changes between each case occurred uniformly both in $\varphi = 0°$ and $\varphi = 180°$.

There may be a question on which gain values were adopted. In Chapter 6, on the gain measurement section, it was discussed that two configurations were employed to apply vertical and horizontal E-field transmission. Theoretically, the two sets of overlapping points, $\varphi = 0°$ and $\varphi = 180°$, should have the same values. However, there were some issues that were affecting the measurement results. First of all, the anechoic chamber in which the experiments were conducted was not symmetric. With a dimension of 6m x 3m x 3m, one of its corners was slanted (Figure 7.5), resulting inconsistent readings when the antenna was in close proximity to the slanted wall. Another factor that may have contributed to the inconsistency was the fact that the foam material used to cover the chamber was designed for optimal operation above 1 GHz frequency. As a consequence, the foams were not able to absorb the entire incident signals and subsequently signal reflections occurred. Signal reflections created a hike in some part of the radiation pattern and therefore, some of the gain values were higher than expected. To signify the gain values with the least influence from the reflections, the lower gain values were selected for the comparison with the simulation results.

In terms of the actual antenna gains versus the simulations', there were variations on the level of discrepancies. For example, in case A and B, the margins were around 2 to 5 dB, whereas in case D there was only 1 dB difference in comparison to the simulation values. The discrepancies were mainly caused by spurious radiations on the coaxial cable as a result of it being connected to the AUT with its small ground plane. In a normal operation, differential mode current flows through to both conductors on the cable, with each current

flowing in opposite direction to cancel each other out. However, the introduction of an antenna at the end of the cable produced a current at the coax shield that flowed with the same direction of the current at the centre conductor. As a result, there was nothing to cancel out the alternating current at the coax and therefore the energy radiated. This radiation greatly affected the radiation and the gain values of the AUT. The contribution of the radiation to the gain values may have been as high as 10 dB [101]. To minimize this effect, a ferrite core was applied as an electromagnetic shielding on the coaxial cable. The clamp shaped ferrite core is made of ferrite, which has a characteristic of high magnetic permeability and low conductivity that are effective for isolating the cable radiation (Figure 7.6). The implementation of ferrite core to the measurement set up prompted a decrease on the overall gain values of the antenna, although it has to be admitted that the results presented in Table 7.2 are 100% free from this radiation effect.

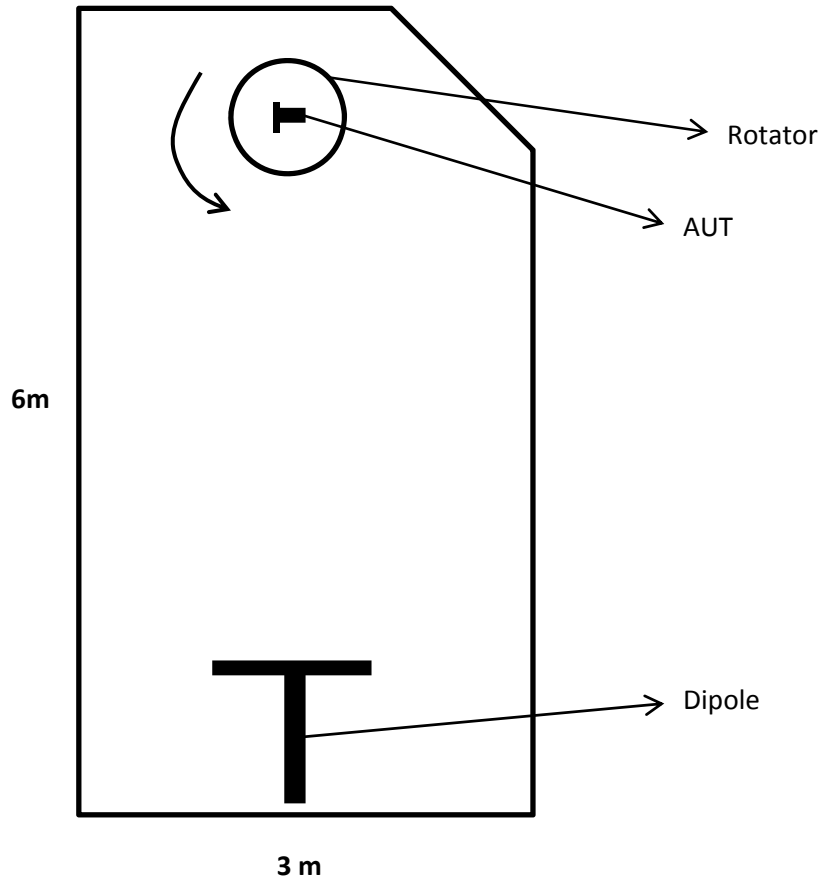

Figure 7.5. Top view schematic of the anechoic chamber. The slope on the wall edge was evident at the top right corner in this schematic.

Figure 7.6. Ferrite Core clamp that was utilised to minimize the spurious radiation of the coaxial cable.

7.4. Comparison with Other Antennas

Finally, it is important to develop a comparison between the performance of the current antenna and the previous investigated antennas as listed in Table 4.2, Chapter 4, to see at what level the proposed antenna performed. The comparison will focus only on the measurement parameters of the antennas, which were selected from the list (Table 4.2), based on the level of relevancy to the current antenna. Refer to Table 7.3 for a recap on the attribute aggregation of the previously investigated antenna as well as the proposed antenna.

There are many ways to analyse the table. The most relevant case to the current design was antenna 6 in the way it was designed for an operation inside Vitreous Humour liquid. However, this antenna was designed for operation at ISM 2.4 GHz frequency band and achieved minimum return loss at 2.33 GHz. The dimension of the antenna was much smaller compared with the current design at 5.25 x 5.25 x 4 mm^3 due to lower signal wavelength. This antenna also covered wider bandwidth in order to cope with the ISM band. This was the only study that implemented Vitreous Humour as the surrounding medium, as the other studies were focusing more on the implantation inside human muscle and skin tissues.

Based on the information in Table 7.3, it is clear that in some cases (antennas 1, 2, 4, 5, and 9) the measurement did not represent the simulation results accurately. In these cases, resonant frequency shifts between 20 to 50 MHz were present. The rest of the antennas were able to reproduce the simulation results on the measurement. The key to obtain these

results was probable a perfect manufacturing process of the antenna. In regards to the performance of the antenna proposed in this thesis, the shift of approximately 20 MHz is classified as average. There was antenna with higher resonance deviation than this, but it was certainly not the best and can still be improved.

Table 7.3. Simulated antenna performance on different setups

No	Antenna	Medium	Size	*f*	s_{11}	BW	G
1	[71]	Skin Tissue (49.6)	40 x 32 x 8	420	-6	0	N/A
2	[52]	Human Tissue (56)	pi/4 x 10.1 x 10.1 x 3	450	-30	70	N/A
3	[77]	Human Tissue (45.2)	pi x 7.5 x 7.5 x 1.9	402	-28	50	-26
4	[78]	Skin Tissue (46.7)	22.5 x 22.5 x 1.27	425	-20	132	-25
5	[79]	Pork Leg	22.5 x 18.5 x 1.9	440	-34	132	-27
6	[16]	Vitreous Humour (66)	5.25 x 5.25 x 4	2330	-32.4	151	-32.4
7	[83]	Skin Tissue (46.7)	10 x 10 x 1.9	402	-36	50	-26
8	[84]	Skin Tissue (46.7)	8 x 8 x 1.9	402	-21	122	-37.96
9	[85]	Muscle Tissue (57.1)	14 x 14 x 15	430	-37	225	-28.5
10	[86]	Muscle Tissue (43.5)	13.1 x 8 x 5.2	402	-22	12	-28.8
11	[89]	Muscle Tissue (55.2)	15.9 x 12.9 x 1.6	405	-16	9	-38
12	Current	Vitreous Humour (69)	13 x 13 x 4.06	421.2	-12.05	2.8	-39

Medium denotes the surrounding medium in which the antenna was submerged during the measurement. The number inside the bracket signifies its relative permittivity (ε_r).
Size denotes the dimension of the antenna in mm^3.
f denotes the resonant frequency of the antenna in MHz.
s_{11} denotes the minimum return loss value of the antenna in dB.
BW denotes the 10dB bandwidth of the antenna in MHz.

In terms of dimension, the proposed antenna ranked 4th on the number of space occupied with the volume of 0.687 cm^3. The smallest antenna on the list was antenna 6 with a total volume of 0.11 cm^3, but this antenna was operating in much higher frequency which subsequently resulted on lower wavelength. For the MICS band antenna, the smallest antenna volume-wise was antenna 7, with the total volume of 0.19 cm^3. It has to be noted that, with exception to antenna 6, 9, and 10), these antennas did not integrate any encapsulations to the antenna. The proposed antenna in this thesis, however, incorporated an added layer of 1.5 mm length to all the lateral sides as well as the top side and therefore produced an addition of 0.433 cm^3 to the antenna volume. The PDMS layers constituted 63% of the total volume of the structure. From another perspective, it is also interesting to see that the volume occupied by the proposed antenna was a result of its thickness. For the other antennas, the intended operation was inside a muscle or skin tissue, in which there are no lateral constraints. A human eyeball operation, however, required the whole geometry of the antenna to be within the eyeball (diameter = 25 mm). As a result, instead

of expanding laterally, another substrate was stacked at the top to compensate unfeasible lateral expansion.

The minimum return loss values do not provide any important information except to indicate that their return losses are below the typical -10 dB threshold. The bandwidth parameters are of greater importance to signify the range at which the antenna could operate. It is clear to see that the proposed antenna has the lowest bandwidth among all antennas on the list (Table 7.3). Some of the antennas were focused specifically on achieving a high bandwidth on the design process. The proposed antenna, however, was intended to operate at MICS band with a maximum bandwidth of 300 kHz. Therefore a bandwidth of 2.8 MHz was considered adequate for the operation.

Gain is another important parameter that defines the antenna performance. Based on the information on the list (Table 7.3), the gain of the other antennas was ranging from -25 to -38 dB. Unfortunately, the maximum measured gain of the proposed antenna was -39 dB, which was lower than any of the other antennas. The main reason behind this sub-optimal performance was the implementation of Vitreous Humour as the surrounding medium. As stated on previous chapters, Vitreous Humour has a high conductivity (1.53 S/m at 402 MHz [64]), compared to skin (0.69 S/m) or muscle (0.79 S/m). As a consequence, the absorption rate by the tissue is also higher, which translates to higher loss to the signal. Even with this disadvantage, the antenna still produced a similar performance to some of the antennas operating on muscle or skin tissues (antenna 8 and 11) and it should be considered a satisfying result.

Overall, the antenna has produced satisfying results in relation to the other similar antennas. Without the PDMS encapsulation, the antenna occupied a comparable amount of space to the smallest antenna on the list. The addition of the PDMS layer made the antenna 3 times bigger, but the entire structure will still fit inside the human eyeball. The bandwidth of the antenna was not particularly impressive, but it was still compatible for a MICS band operation with the right frequency range. The gain performance of the antenna was comparable with other small size antenna even though more challenging medium was applied.

7.5. Summary

In this chapter, the simulation and measurement data of the antenna have been analysed. Each parameter was investigated individually to understand how the antenna performed with respect to the simulated results. The discrepancies were identified and discussed in order to pursue logical explanation behind them. This step was applied to all three important parameters of the antenna: return loss, radiation pattern, and gain. Finally, a comparison was drawn to see the antenna performance level against other antennas designed for similar purposes. Each attribute of the antenna was analysed and a conclusion was reached at the end on how the antenna had performed.

Chapter 8

Implantable Antenna for Implantable Body Sensor Network

The implementation of a multilayer microstrip antenna for a retinal prosthesis system has been discussed in a great detail on the previous chapters. It was clear that the adoption of multilayer structure produced an enhancement on the antenna performance, which was very weak due to the lossy surrounding medium. In this chapter, another implantable antenna for completely different purposed will be presented as part of the derivative study on the main topic. The antenna was designed to be integrated in an Implantable Body Sensor Network (IBSN) system. The design will be presented, including the tissue model and the simulation configuration. The measurement results comprise the performance of the antenna in terms of return loss, gain, and radiation pattern, as a result of the same measurement procedure as the previous antenna. A discussion on the result and a summary will conclude the structure of this chapter.

8.1. Introduction

A decade ago, body sensor network (BSN) technologies started to come into prominence with the ever increasing demand of higher people life expectancy. With a complex utilization of multiple micro-sensors, the technology was aimed at introducing a long term home-based monitoring which would result in more patient freedom as well as healthcare cost saving. While BSNs are architecturally designed with varying emphasis such as low power [102] or low cost [103], the main focus is reliable data transmission throughout the network. This technology has reached its maturity and the focus is now shifted at implementing the same idea in implantable environments.

The advancement of sensor technology introduces the possibilities of various implantable sensors for the purpose of measuring and monitoring physiological signals *in vivo*. Implantable sensors for measuring SvO_2, blood oxygen, blood glucose, neural activity, as well as internal imaging, have been investigated comprehensively [104-108]. In

an implantable body sensor network (IBSN), all the sensors were designed to exchange data wirelessly by employing master-slave mechanism [54]. To realize this, implantable communication must be considered at the core design of the architecture.

As in the retinal prosthesis system, the data communication in IBSN involves signal propagation through human tissues, which leads to similar challenges in the design process. First of all, the antenna must be capable of complying with the constraints associated with the implantable environment, such as size and safety constraints. In terms of the antenna size, there is no freedom in selecting the proper size during the design process due to the limitation imposed by the surrounding tissues or other body parts. It would be unlikely to design a traditional $\lambda/2$ or $\lambda/4$ size antenna for lower frequency bands to achieve the perfect characteristics. Therefore, miniaturization technique of the antenna will be enforced in the design process. Another limitation comes from the transmission power of the antenna in relation to the SAR value. In IBSN, there are a lot of sources that can produce thermal elevation inside the body, and one of them is the electromagnetic fields radiated by the telemetry devices [109]. As stated on the early chapter, for a frequency range of 100 kHz to 10 GHz, the 1g average has a limit of 1.6 W/kg while the 1g average has a threshold of 2 W [110]. These values will dictate the maximum power that can be applied to the antenna during the transmission, which ultimately means gain restriction.

Another issue is related to the complex geometry and characteristic of human tissues on the limbs area. Geometrically, human body is much more than just a simple basic shape and it consists of heterogeneous parts that would include something as small as blood vessels. It would be inaccurate to model a human body or a human body part as a plain model with just a single electrical characteristic value [111, 112]. Electrically, each part of human body has a certain value of permittivity and conductivity, which are both crucial components in determining signal propagation characteristic. The value of each part does not depend on where it is located, makes it difficult to generalize a heterogeneous part into a homogeneous model. Furthermore, the values are frequency dependent [64]. For those reasons, the simulation of the implantable antenna necessitates an accurate model of the surrounding material as well as a specific frequency sweeping.

This brings the next question on what frequency should be used for the antenna operation. The selection of the band is based on consideration of multiple factors such as transmission rate, suitability to the network architecture, efficiency, etc. For the purpose of IBSN, Medical Implant Communication Service (MICS) band of 402-405 MHz was

deemed more suitable for IBSN due to lower loss [113] and more efficient operation in the system [54].

8.2. Tissue Model

Once again, the selection of the model is crucial in determining the accuracy of the simulation outcome. For IBSN, where most of the sensors will be located subcutaneous, the use of body equivalent tissue model as the background material of the antenna is expected. There is a choice of implementing a 3-layer tissues model (skin, fat, and muscle) or a single layer homogeneous tissue equivalent material. There have been some studies about the adoption of 3-layer and 1-layer tissue model, with one of the arguments suggested that the 3-layer's peak SAR values occurred at similar position compared to the 1-layer's, with some additional minor hotspots due to the reflection between tissues boundary [114]. In terms of the resulting antenna gain, the single layer model tends to overestimate the pair gain of the antenna; hence it can be used as a conservative approach to the simulation [115].

It was decided that the 3-layer tissues model would be employed in the simulation for the purpose of understanding detailed localised SAR values on each layer. The variation of permittivity values would give a better representation of the system in general in terms of the SAR values [116]. Refer to Table 8.1 for the electrical characteristics of the aforementioned 3 tissues at 402 MHz. The antenna would be submerged into the fat layer to benefit from its low conductivity property [115].

Table 8.1. Electrical properties of human tissues at 402 MHz

Tissue	Thickness (mm)	Relative Permittivity ε_r	Conductivity σ (S/m)	Mass Density ρ (kg/m^3)
Skin	3	46.74	0.69	1100
Fat	10	5.58	0.04	916
Muscle	20	57.11	0.8	1041

8.3. Antenna Design

As previously mentioned, the use of $\lambda/2$ or $\lambda/4$ size antenna is just not possible for implantable operation at 402 MHz due to its massive size relative to the human tissue. Therefore, miniaturization techniques such as the use of lumped element loading, high dielectric materials, short circuit to the ground plane, geometry optimisation, as well as the utilization of surrounding environment [92] were implemented. Microstrip antenna was

selected as the antenna type due to the feasibility of both exercising these techniques in the design process as well as complying to the constraints associated with the implantable antenna.

First of all, the previously used dielectric material, Rogers RO3210 (ε_r = 10.2), was chosen for both the substrate and the superstrate of the antenna, with the factory-default thickness of 0.635 mm and the dimension of 30 mm x 20 mm. The most significant consequence of adopting thin substrate is lower bandwidth of the antenna, which in this case was not the highest priority. The next step was the design of the antenna microstrip pattern. It was generally assumed that good impedance response from an antenna will result in a good radiation pattern [117]. Therefore, getting a good return loss of less than 10 dB is the first priority to the design.

To achieve the needed return loss, the task was focused on finding the most optimized geometry for the conductor track sitting on the substrate. The conductor track must be long enough to avoid any reflections from the end of the track which subsequently reduce the radiation efficiency [118]. These pre-requisites led to a long thin conductor line extending along each side of the substrate (Figure 8.1). All the specifications were in accordance to the information discussed on the Chapter 4 of this dissertation. There is a big gap in the middle that can potentially be used for any microchips in the further development.

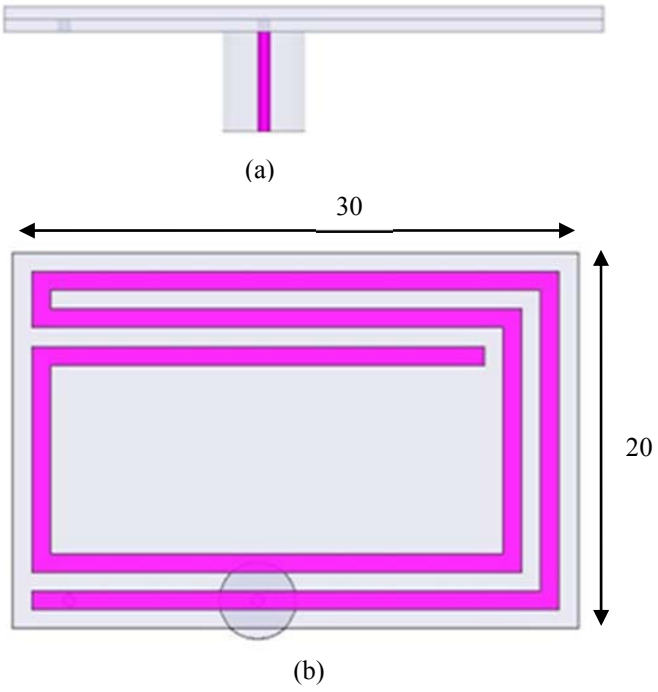

Figure 8.1. The proposed antenna design from (a) side view or YZ plane and (b) top view or XY plane. All units are in mm.

8.4. Simulation

The design was simulated using the same HFSS software which was based on Finite Element Method (FEM) numerical technique. Due to the need to discretise all the parameters in this technique, a boundary was defined with the shape of a box. The simulation was run with the centre frequency of 402 MHz, with a sweeping from 300 to 500 MHz, and a default input power of 1 W.

Three attributes of the antenna were expected from the simulation: return loss, gain and radiation pattern, and SAR value. They would determine how the antenna would perform in respect to other antennas as well as to the safety standards. This antenna was simulated in two different scenarios, the free space and the submerged simulations, due to the unavailability of the tissue mimicking material during this study. However, the measurement validation results would give a correct approximation on how the antenna behaves, as observed on the previous antenna.

8.4.1. Inside the 3-layer Tissue

Because the antenna was originally designed to operate inside 3-layer tissue, the results in this scenario will be presented first.

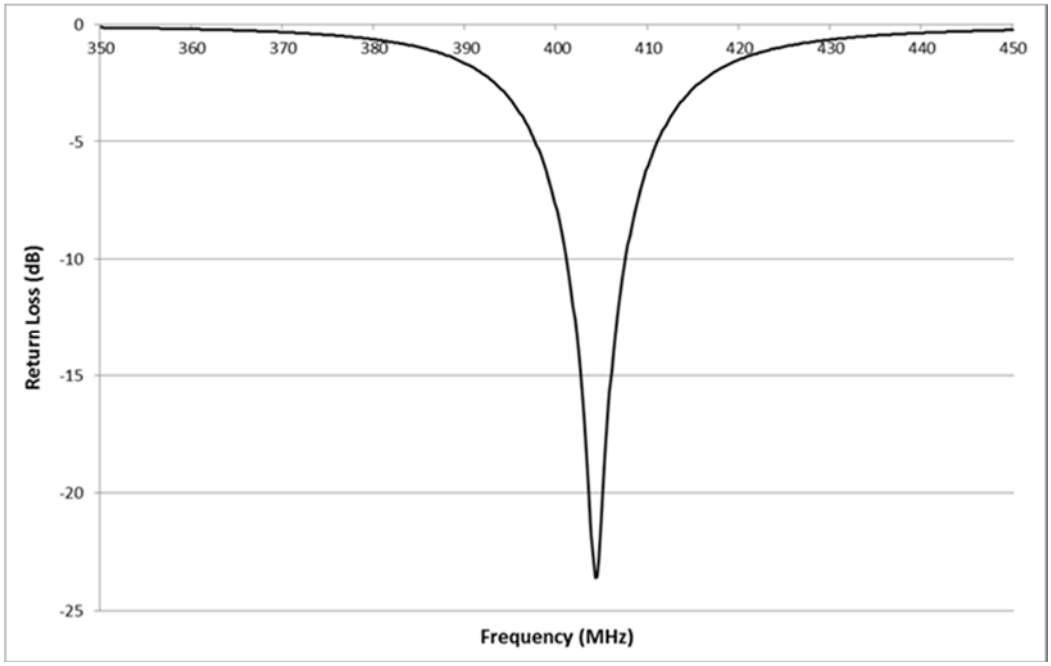

Figure 8.2. Return loss of the proposed antenna with a minimum of -23.6 dB at 404.2 MHz.

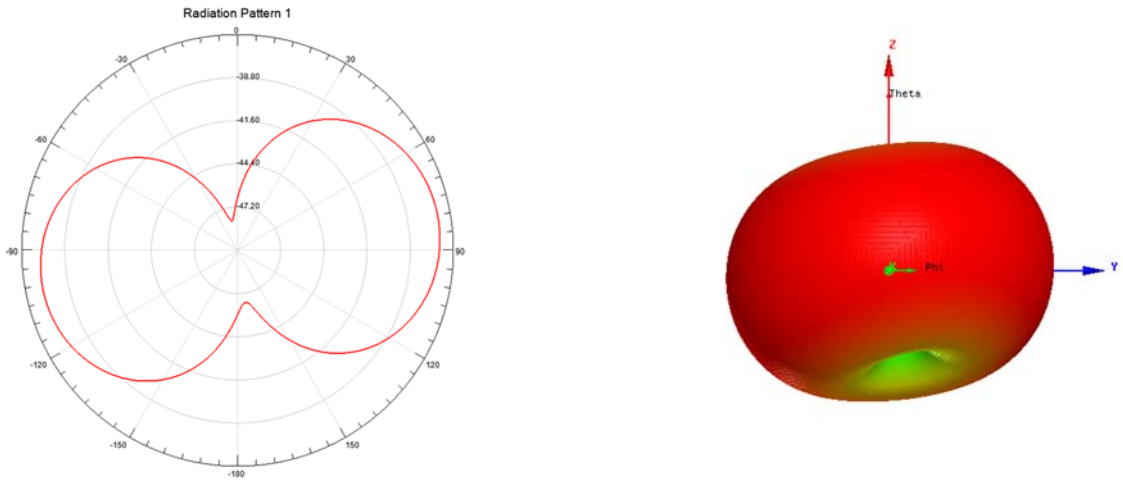

(a) (b)

Figure 8.3. Radiation pattern of the proposed antenna (a) in 2D on XZ plane and (b) in 3D view. Maximum gain was -36.55 dB.

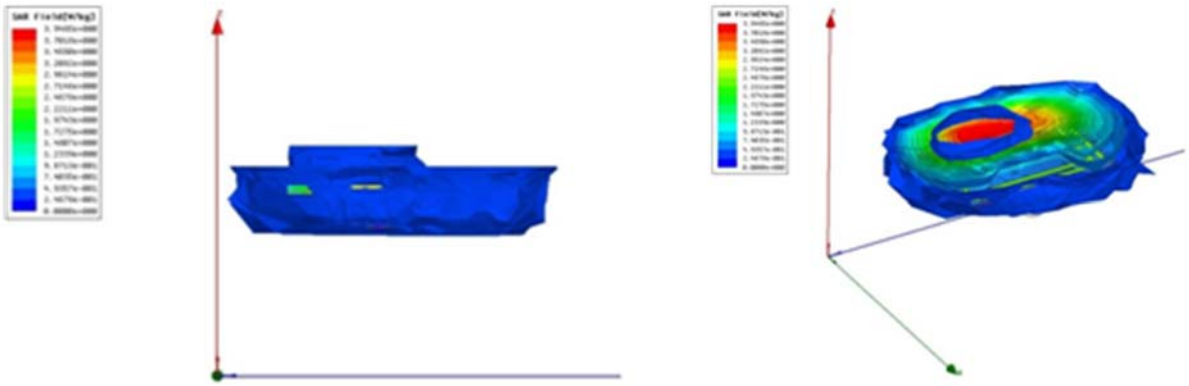

(a) (b)

Figure 8.4. 1 g average SAR on 1W input power from (a) the side view or YZ plane and (b) the 3D view.

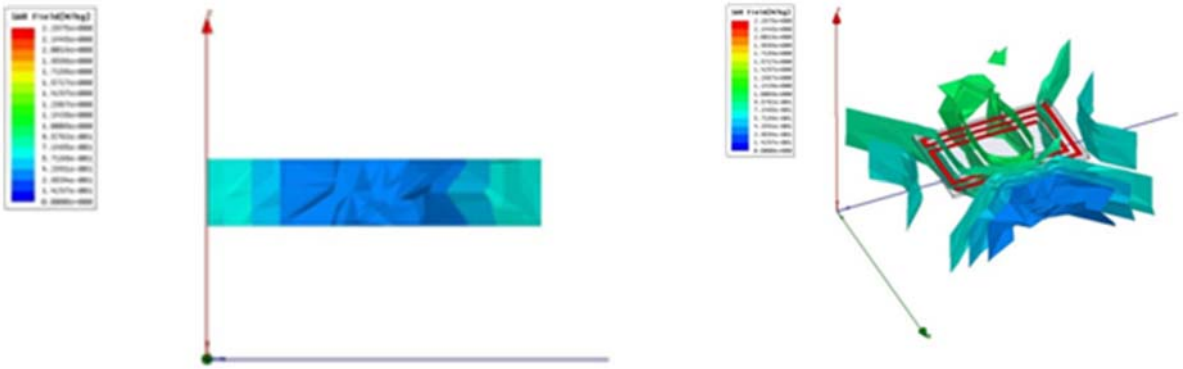

(a) (b)

Figure 8.5. 10g average SAR on 1W input power from (a) the side view or YZ plane and (b) the 3D view.

The importance of obtaining a good return loss has already been explained on the previous Section. The result of the HFSS simulation showed that the proposed antenna achieved return loss of -23.6 dB at 404.4 MHz. The 10 dB bandwidth of the antenna is 6.6 MHz, starting from 401 MHz to 407.6 MHz, well covering the MICS band (Figure 8.2).

The radiation pattern can be observed at Figure 8.3a (2D) and 8.3b (3D). It can be seen that the antenna produced an omni-directional pattern, as expected from a small antenna. The maximum gains occurred around the sideways with the maximum gain of -36.55 dB. This number is very low compared to other microstrip antennas, due to the fact that it operates inside the living tissues. Living tissues are dispersive and lossy and as a consequence they inflict losses to signal propagation and converted some of the energy into heats. The size of the antenna made it even less ideal for a good radiator, due to its inability to transform the entire electrical signal into electromagnetic wave.

The 1g and 10g average SAR values were calculated in the simulation and the resulting pattern can be seen in Figure 8.4 and 8.5.The SAR values, which indirectly indicate the temperature inclination on the tissue, were observed only at the fat layer, where the antenna was implanted. The maximum 1g average SAR value was 3.95 W/kg and it was observed at where the antenna conductor was located. The SAR values across the fat layer varied from 0.25 to 2.5 W/kg (Figure 8.4b). These values are beyond the SAR safety standard of 1.6 W/kg. Knowing about the proportion relationship between SAR and power, the power limit for safety operation of the antenna can be determined to be 0.4 W.

The 10g average SAR of the tissues can be seen in Figure 8.5a and 8.5b. In these plots, the SAR values were observed to be much less than the 1g average SAR values, due to larger averaging volume. The highest value was present at the antenna conductor with the value of 2.29 W/kg. With the safety limit of 2 W/kg, the safety power operation for this antenna is 0.87 W. Due to the size of the tissues sample, the 1g average SAR value represents more accurate values.

8.4.2. Free Space

The free space simulation was performed as an attempt to accomplish a data validation with the measurement due tothe lack of the mimicking materials. The following images will demonstrate the antenna performance in free space in terms of return loss, gain, and radiation values.

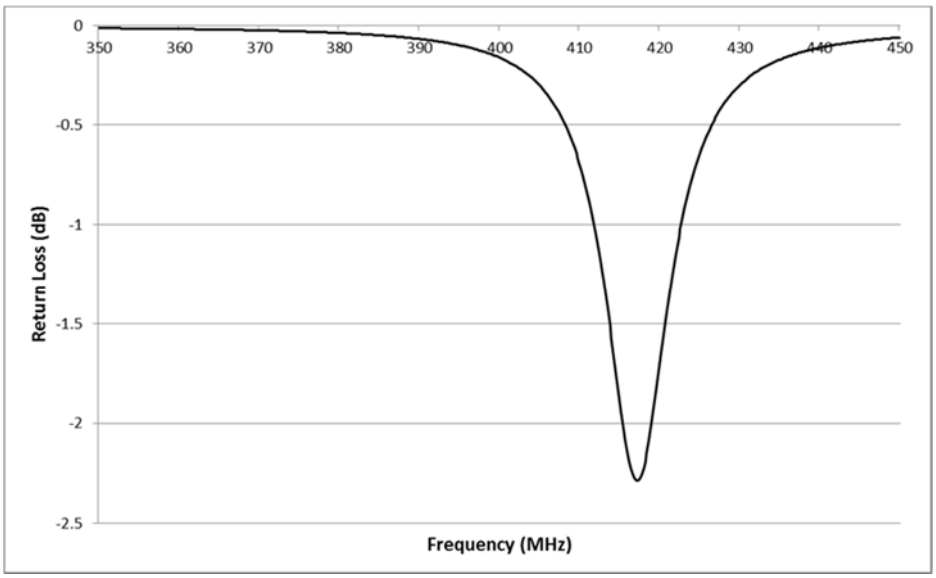

Figure 8.6. Return loss of the proposed antenna in free space with a minimum of -2.29 dB at 417.2 MHz.

It is clear from the return loss graph that this antenna performed very poorly on the free space simulation, with the minimum achieved return loss of only -2.29 dB. Due to the change of surrounding medium, the resonance of the antenna was also shifted to 417.2 MHz.

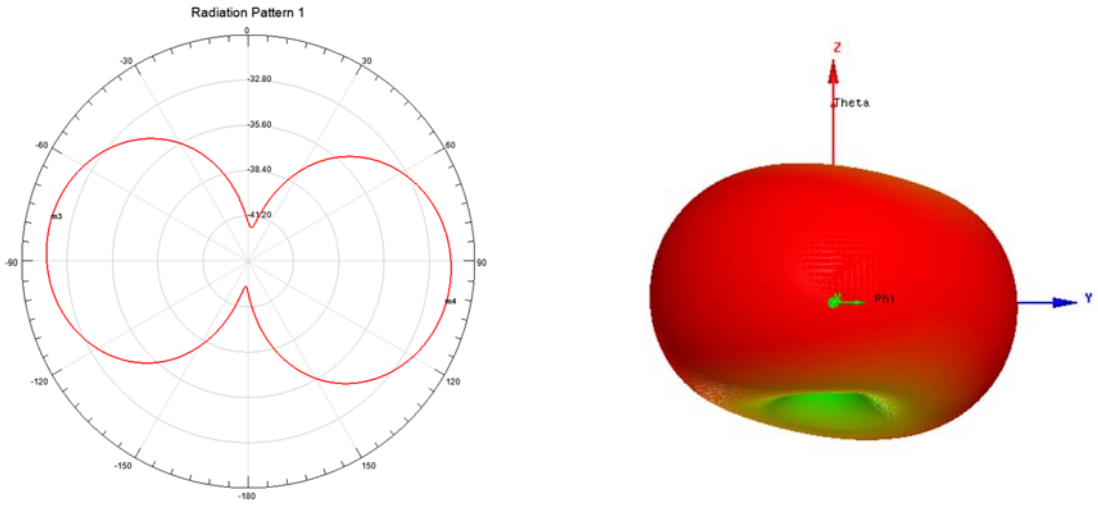

(a) (b)

Figure 8.7. Radiation pattern of the proposed antenna (a) in 2D on XZ plane and (b) in 3D view. Maximum gain was -30.9 dB

On the other hand, as expected, there was a great improvement in terms of the maximum gain to -30.9 dB. It was due to the removal of lossy medium of human skin, fat, and msucle layers. In terms of radiation pattern, there was a slight change on the direction of the maximum gain of the antenna.When the antenna was submerged (Figure 8.3a), the

left lobe of the antenna was tilted towards the –*z* axis, whereas in the free space (Figure 8.7a), the right one was tilted towards the –*z* axis. This was likely due to the variation to the Voltage Standing Wave Ratio (VSWR) value of the antenna as a result of material change. But overall, the pattern still resembled the omni-directional pattern, as expected from any small antennas.

8.5. Measurement

The measurement procedure was exactly the same as the one introduced previously for the previous antenna, involving a return loss measurement with Agilent E5071B Network Analyzer and radiation pattern measurements in both horizontal and vertical E-field configurations inside the anechoic chamber. The gain values were obtained by applying formula 6.2 with the measured gain values inside the chamber. The return loss and radiation pattern result can be observed from Figure 8.8 and Figure 8.9, respectively.

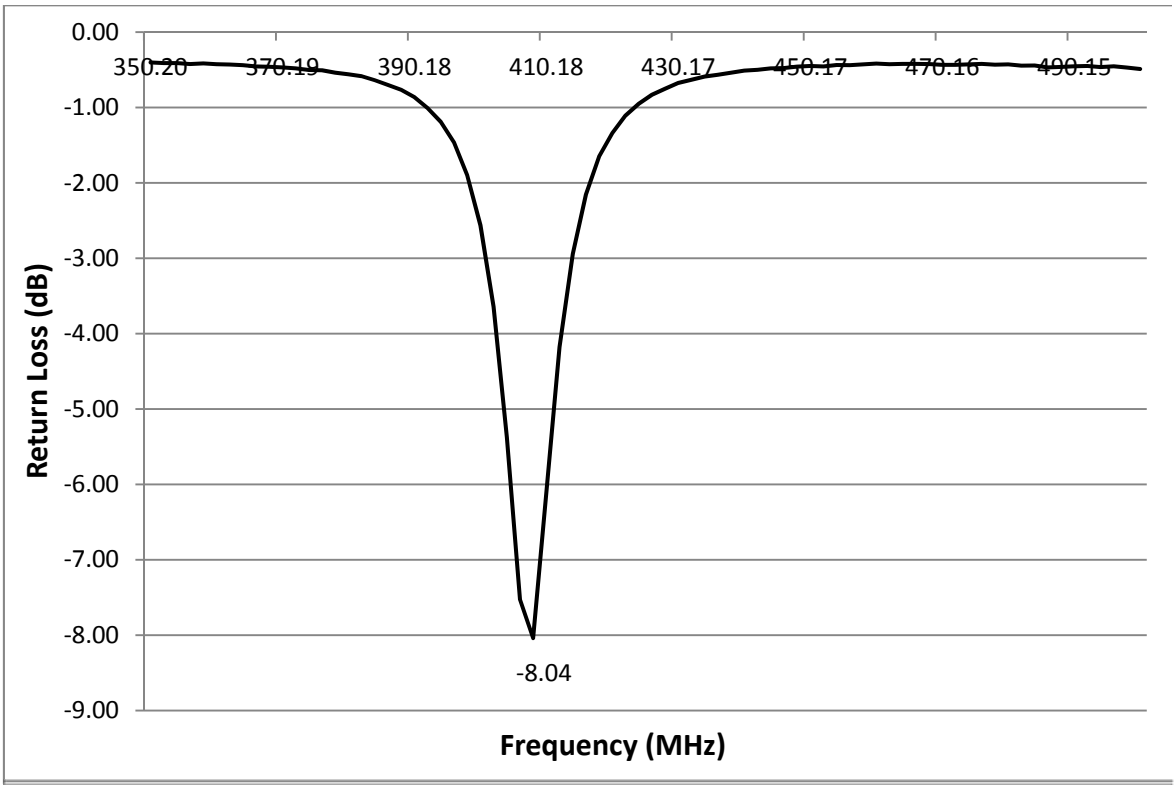

Figure 8.8. Return loss measurement result of the antenna in free space. The minimum return loss was -8.04 dB at 408.18 MHz.

The return loss measurement unexpectedly produced a better result than the simulation. Although the general performance was still weak (minimum return loss of -8.04 dB), the resonance took place at 408.18 MHz, an improvement from the simulation resonance of 417.2 MHz.

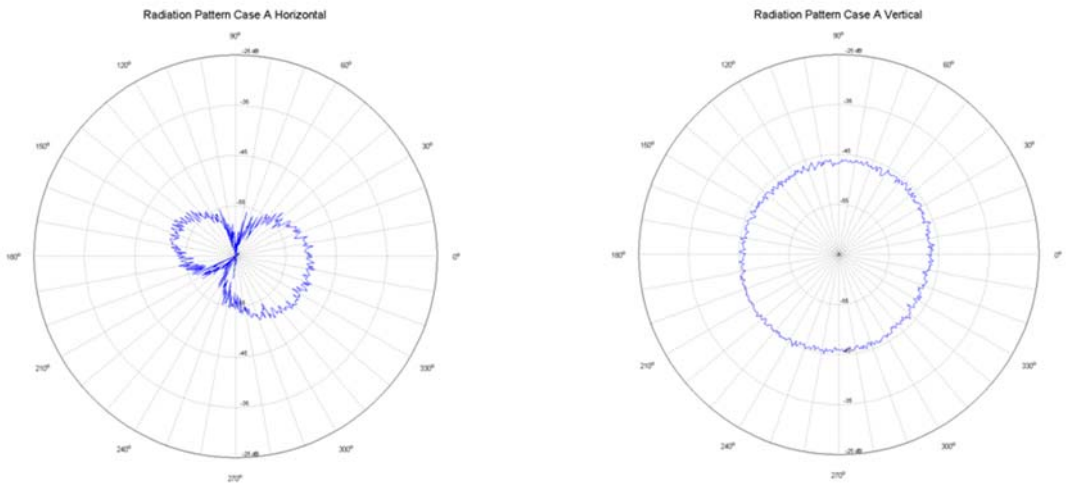

(a) (b)

Figure 8.9. The measured radiation pattern of the antenna in (a) horizontal E-field and (b) vertical E-field.

The measured radiation pattern results featured an omni-directional pattern (Figure 8.9a and 8.9b) with the right lobe of the antenna (at XZ plane) tilted towards –z axis, as observed in the simulation result. Based on the polar plot of the horizontal E-field measurement (Figure 8.9a), it was interesting that the same phenomena occurred on the measurement of the previous antenna was again noticed. One of the antenna lobes was larger than the other. It strengthened the case that this anomaly was caused by the asymmetry of the anechoic chamber rather than the mechanical characteristic of the antenna itself. A better result could be achieved by performing the measurement inside an anechoic chamber that is large enough for low frequency operation.

The gain of the antenna was obtained following a calculation with the Equation (6.2), which was stated in Chapter 6. The formula included modifications to the acquired gain data with the known information of the gain of the reference antenna by itself and in a system (2.15 dBi and -16.78 dB, respectively). The same reference antenna was utilized for this measurement, the half wave dipole antenna. Based on these values, the actual gain of the AUT was -30.11 dBi. The resulting gain was slightly stronger in comparison to the simulated value (-30.9 dB), with the discrepancy can be attributed to the imperfect absorption of the anechoic chamber. However, the combination of radiation pattern and gain values of this antenna was enough to provide a confidence on the antenna behaviour in accordance to the simulation results.

8.6. Discussion

Unfortunately, due to the inability to obtain a mimicking tissue liquid at this stage, the measurement of the antenna was only performed under free space condition. The test was performed to validate the data obtained from the simulation, and to build more confidence on the simulation result of the antenna in the human tissues environment.

To recap, the return loss measurement produced a better return loss value (-8.04 dB vs -2.29 dB) and a resonant frequency shift of 9.02 MHz or 2.2% from 417.2 MHz to 408.18 MHz. This discrepancy could possibly be attributed to the mechanical flaw that emerged during the fabrication process. The measured radiation pattern demonstrated an omni-directional pattern, but one lobe was smaller than the other. The most likely reason for this was the compatibility of the anechoic chamber for low frequency operation (under 1 GHz) that caused some irregular reflections on the absorbent walls. The measured gain showed a very close value to the simulation (-30.11 dB vs -30.9 dB).

There are important details on the antenna performance of this antenna that can be studied in comparison to the retinal prosthesis antenna. To avoid confusion, the retinal prosthesis antenna will be called RP antenna and this IBSN antenna will be called IBSN antenna from now on. First of all, both antennas were designed to operate at MICS band, but there were different level of constraints applied to each antenna. In RP antenna, there was more stringent requirement in terms of the size due to the planned placement of the antenna inside a human eyeball, whereas in IBSN antenna the planar dimension limit was more lax. The limiting factor on the dimension would be determined more on the surgical procedure and the convenience of the user. As a result the resulting dimension of the IBSN antenna was much bigger than the RP antenna (30 x 20 x 1.27 mm^3 2 layers against 10 x 10 x 2.54 mm^3 4 layers). The difference in the dimension was reflected on the antenna performance, where the IBSN antenna produced a superior performance compared to the RP antenna in terms of gain (refer to Table 8.2). In addition to the antenna dimensions, the performance imbalance was also caused by the different conductivity value of the surrounding medium. In RP antenna, the surrounding medium, Vitreous Humour, has a conductivity of 1.53 S/m, which was exceptionally larger compared to the Fat tissue (σ = 0.04 S/m). These two factors were accountable for the performance variation between the two antennas.

Table 8.2. Performance comparison between RP antenna and IBSN antenna.

Antenna Parameter	RP antenna	IBSN Antenna
Dimension	10 x 10 x 2.54 mm^3	30 x 20 x 1.27 mm^3
Surrounding Medium	Vitreous Humour (ε_r = 69, σ = 1.53 S/m)	Fat (ε_r = 5.58, σ = 0.04 S/m)
Antenna Type	multilayer microstrip	multilayer micostrip
Return Loss	-12 dB @ 402.8 MHz	-23.6 dB @ 404.2 MHz
Max Gain	-41.02 dB	-36.55 dB

8.7. Summary

As mentioned earlier, the development of this IBSN antenna was part of a derivative study on the development of the RP antenna. There were numerous applications where the knowledge of implantable antenna design could be applied, but IBSN presented its own unique and complex challenges from the antenna design perspective in terms of the applications and the placements. This was the fundamental reason why this particular system was selected as the next step of this study.

In this chapter, an implantable antenna was designed as part of a possible scenario in one of the nodes in IBSN architecture, specifically the one located on one of the limbs. The antenna adopted 2-layer microstrip structure with a rectangular spiral conductor track. The simulation was set up in two different environments, free space and inside the tissue layers, to accommodate the free space measurement of the antenna inside the anechoic chamber. The technique of the measurement was based on the knowledge obtained in the RP antenna measurement process to acquire the antenna performance in three different parameters: return loss, radiation pattern, and gain. At the end of the chapter, the antenna performance was compared to the RP antenna and several discrepancies on the parameters and performances were identified and discussed. This would provide an even deeper understanding on the behaviour of the antenna, which would benefit future development of an antenna for different purposes.

Chapter 9
Conclusion

The final chapter of this dissertation will be primarily dedicated to highlight the findings from this study. Initially, a recap in each chapter will be presented sequentially, followed by the demonstration of important findings from this study. Finally, potential future works to continue this study will be discussed at the end of the chapter.

9.1. Overview

At the beginning of this dissertation, the background and the rationale of this research was stated very clearly. In ***Chapter 2***, all aspects about retinal prosthesis system were explained, starting with the background behind the system, its role in the assistive integrated system, and the level of technology that is available or currently being research at this time. In relation to the current technology, a review from 3 major research groups covering the electrodes, wireless communications, dosimetry analysis, as well as clinical testing, was also presented. At the end of this chapter, existing implant communication technologies for various purposes were discussed. In ***Chapter 3***, four frequency bands were investigated as the first step in the antenna design process. Each band was analysed in terms of bandwidth, external interference, as well as possible antenna size and SAR values, in order to find the most suitable band for the proposed antenna. At the end, MICS band was selected as the operating frequency of the proposed antenna. Comprehensive explanation about the antenna design was presented in ***Chapter 4***. Initially, the basic principle as well as the role of an antenna in a wireless communication system was presented. It also covered the antenna operation inside a medium with high dielectric and high conductivity property. A list of previous implantable antenna designs from various researchers worldwide was compiled, highlighting their return loss, gain, and bandwidth parameters. The last Section of the chapter revealed the proposed antenna design after a thorough discussion about the constraints and the difficulties of producing an optimized operation in the specified scenario. ***Chapter 5*** covered the simulation procedure of the proposed antenna in order to obtain the specified parameters. It was started by a review of several different numerical techniques to solve Maxwell's equations, and it has been

decided that HFSS with its FEM technique would be employed to perform the computation on the antenna. A step by step procedure on the simulation process was presented and at the end of the Section, the simulation results were displayed. The next step was a manufacturing process of the antenna, which was detailed at the beginning of ***Chapter 6***. A set of measurements that comprise of two parts, free space and inside Vitreous Humour Liquid, was conducted with the fabricated antenna to acquire its return loss, radiation pattern, and gain. The measurement procedure and configuration for both scenarios were explained in detail and followed by the unveiling of the results in each case. The data was organized in such a way to allow a clear comparison against the simulation data. Finally, a discussion on the acquired data, both from the simulation and the measurement, was disclosed in ***Chapter 7***. The data was analysed to gain an understanding on how the actual antenna performed in relative to the simulation. Discrepancies on the results were investigated and possible theories behind these were postulated. To end the chapter, a compilation of previous implantable antenna performance was created and a comparison was made against the manufactured antenna to determine the actual performance level of the antenna. In ***Chapter 8***, a derivative study was also conducted where another implantable antenna for a purpose other than retinal prosthesis system was designed. Intended for the implementation in IBSN system, the antenna was developed based on the knowledge obtained on the previous process. A simulation to acquire the return loss, gain, and radiation pattern of the antenna was later validated with a free space measurement inside the anechoic chamber. Finally, the ***Final Chapter*** was written to highlight the major findings of this research, along with possible future works as a continuation of this study.

9.2. Major Findings

There are four major findings that can be reported as a result of this study:

- **MICS band has been considered as the most suited frequency band for a retinal prosthesis system**

  In Chapter 3, four frequency bands have been analysed. Based on the general SAR values, possible external interferences, as well as the size of the potential antenna, MICS has been selected as the most suitable candidate for a retinal prosthesis system.

- **Microstrip antenna has been determined as the best candidate for an implantable system**

After a thorough literature review on the antenna theory as well as the previous implantable antenna designs, microstrip antenna has been considered as the best solution for an implantable system due to the following advantages: compact, simple manufacturing process, as well as possibility of multi-band operation. The simulation and measurement results of two microstrip antenna designs strengthened this statement further with their structure and the operating performances in terms of return loss, radiation pattern, and gain.

- **A novel configuration to conduct a measurement inside Vitreous Humour liquid**

  This was the first time an antenna was measured inside a liquid-filled spherical container when undertaking a measurement, to mimic an operation inside a human eyeball. The configuration of the measurement as well as the antenna structure has been comprehensively disclosed in Chapter 6.

- **A novel implantable antenna to operate inside Vitreous Humour liquid at MICS band**

  This is the ultimate finding of this research. A small multilayer microstrip antenna with a dimension of 10 x 10 x 2.54 mm^3 (without PDMS coating) or 13 x 13 x 4.06 mm^3 (with PDMS coating) was designed, simulated, and manufactured. The measurement results of this antenna generally resembled the simulation data with a small degree of discrepancies. Compared to other implantable antennas, the performance of this antenna was at the same level with them despite more challenging constraints.

9.3. Possible Future Works

There are several ideas on how a new study can be conducted based on the knowledge acquired from this research:

- ***In vitro* and *in vivo* experiment of the antenna**

  There is no doubt that both *in vitro* and *in vivo* measurement of the antenna are the obvious next step for this project. It was unfortunately not possible to obtain permission from the ethics committee to conduct such an experiment during this project's lifecycle. *In vitro* experiment will involve the adoption of bovine's eyeball in place of a human eyeball due to the similarity between the two, structurally and dimensionally. *In vivo* experiment for only the antenna seems unlikely due to the

fact that in normal operation, the antenna will function when it is attached to the control unit. Integration with a microcontroller unit as well as collaboration with a medical team would be needed before the *in vivo* measurement can be materialized by implanting the whole unit into a living human's eyeball.

- **Designing a wireless communication link with an external antenna**

  A design of wireless communication link that comprises of an extraocular and intraocular antenna will create a solid topic for a further study. The study will include investigation of antenna placement as well as different modulation techniques on the data transmission for optimal data transfer.

- **Development of an implantable flexible antenna**

  An introduction of flexible characteristic to an implantable antenna will provide an immense benefit to the antenna in some situations. When an antenna is bendable, it is allowed to conform to the contour of the human parts, allowing it to have a larger aperture. This study will cover an investigation on the most suitable material to be employed as the substrates and superstrates and eventually the effect of bending structure to the antenna performance.

Bibliography

[1] W. H. Organisation. (2012, 1 October). Prevention of Blindness and Visual Impairment. Available: http://www.who.int/blindness/causes/priority/en/index.html

[2] D. T. Hartong, E. L. Berson, and T. P. Dryja, "Retinitis pigmentosa," Lancet, vol. 368, pp. 1795-1809, 2006.

[3] E. Margalit and S. R. Sadda, "Retinal and Optic Nerve Diseases," Artificial Organs, vol. 27, pp. 963-974, 2003.

[4] D. B. Rein, P. Zhang, K. E. Wirth, P. P. Lee, T. J. Hoerger, N. McCall, et al., "The economic burden of major adult visual disorders in the United States," Archives of Ophthalmology, vol. 124, pp. 1754-1760, 2006.

[5] U. Chakravarthy, T. Y. Wong, A. Fletcher, E. Piault, C. Evans, G. Zlateva, et al., “Clinical risk factors for age-related macular degeneration: a systematic review and meta-analysis,” BMC Opthalmology 10: 31, 2010.

[6] L. A. Remington, Clinical Anatomy of the Visual System E-Book, 3rd ed.: Elsevier Health Sciences, 2004.

[7] N. S. Peachey, "Subretinal implantation of semiconductor-based photodiodes: Progress and challenges," Journal of Rehabilitation Research and Development, vol. 36, pp. 371-376, 1999.

[8] E. Margalit, M. Maia, J. D. Weiland, R. J. Greenberg, G. Y. Fujii, G. Torres, et al., "Retinal prosthesis for the blind," Survey of Ophthalmology, vol. 47, pp. 335-356, 2002.

[9] J. S. Hayes, V. T. Yin, D. Piyathaisere, J. D. Weiland, M. S. Humayun, and G. Dagnelie, "Visually Guided Performance of Simple Tasks Using Simulated Prosthetic Vision," Artificial Organs, vol. 27, pp. 1016-1028, 2003.

[10] J. D. Weiland, M. S. Humayun, H. Eckhardt, S. Ufer, L. Laude, B. Basinger, et al., "A comparison of retinal prosthesis electrode array substrate materials," Conference proceedings : ... Annual International Conference of the IEEE Engineering in Medicine and Biology Society. IEEE Engineering in Medicine and Biology Society. Conference, vol. 2009, pp. 4140-4143, 2009.

[11] D. Nanduri, M. S. Humayun, R. J. Greenberg, M. J. McMahon, and J. D. Weiland, "Retinal prosthesis phosphene shape analysis," Conference proceedings : ... Annual International Conference of the IEEE Engineering in Medicine and Biology Society. IEEE Engineering in Medicine and Biology Society. Conference, vol. 2008, pp. 1785-1788, 2008.

[12] V. Singh, A. Roy, R. Castro, K. McClure, R. Dai, R. Agrawal, et al., "On the thermal elevation of a 60-electrode epiretinal prosthesis for the blind," IEEE Transactions on Biomedical Circuits and Systems, vol. 2, pp. 289-300, 2008.

[13] K. Gosalia, J. Weiland, M. Humayun, and G. Lazzi, "Thermal elevation in the human eye and head due to the operation of a retinal prosthesis," IEEE Transactions on Biomedical Engineering, vol. 51, pp. 1469-1477, 2004.

[14] L. Colodetti, J. D. Weiland, S. Colodetti, A. Ray, M. J. Seiler, D. R. Hinton, et al., "Pathology of damaging electrical stimulation in the retina," Experimental Eye Research, vol. 85, pp. 23-33, 2007.

[15] D. V. Piyathaisere, E. Margalit, S. J. Chen, J. S. Shyu, S. A. D'Anna, J. D. Weiland, et al., "Heat effects on the retina," Ophthalmic Surgery Lasers and Imaging, vol. 34, pp. 114-120, 2003.

[16] S. Soora, K. Gosalia, M. S. Humayun, and G. Lazzi, "A comparison of two and three dimensional dipole antennas for an implantable retinal prosthesis," IEEE Transactions on Antennas and Propagation, vol. 56, pp. 622-629, 2008.

[17] G. Wang, W. Liu, M. Sivaprakasam, M. Zhou, J. D. Weiland, and M. S. Humayun, "A dual band wireless power and data telemetry for retinal prosthesis," Conference proceedings : ... Annual International Conference of the IEEE Engineering in Medicine and Biology Society. IEEE Engineering in Medicine and Biology Society. Conference, vol. 1, pp. 4392-4395, 2006.

[18] K. Gosalia, G. Lazzi, and M. Humayun, "Investigation of a microwave data telemetry link for a retinal prosthesis," IEEE Transactions on Microwave Theory and Techniques, vol. 52, pp. 1925-1933, 2004.

[19] J. D. Weiland, B. Faraji, R. J. Greenberg, M. S. Humayun, and F. G. Shellock, "Assessment of MRI issues for the Argus II Retinal Prosthesis," Magnetic Resonance Imaging, vol. 30, pp. 382-389, 2012.

[20] K. Kagawa, K. Isakari, T. Furumiya, A. Uehara, T. Tokuda, J. Ohta, et al., "Pixel design of pulsed CMOS image sensor for retinal prosthesis with digital photosensitivity control," Electronics Letters, vol. 39, pp. 419-421, 2003.

[21] A. Uehara, K. Kagawa, T. Tokuda, J. Ohta, and M. Nunoshita, "Back-illuminated pulse-frequency-modulated photosensor using silicon-on-sapphire technology developed for use as epi-retinal prosthesis device," Electronics Letters, vol. 39, pp. 1102-1104, 2003.

[22] T. Tokuda, Y. L. Pan, A. Uehara, K. Kagawa, M. Nunoshita, and J. Ohta, "Flexible and extendible neural interface device based on cooperative multi-chip CMOS LSI architecture," Sensors and Actuators, A: Physical, vol. 122, pp. 88-98, 2005.

[23] T. Tokuda, M. Kawada, S. Sugitani, M. Taniyama, A. Uehara, K. Kagawa, et al., "A multi-chip-architecture based flexible stimulation device for retinal prosthesis with a flip-chip packaging technique," Conference proceedings : ... Annual International Conference of the IEEE Engineering in Medicine and Biology Society. IEEE Engineering in Medicine and Biology Society. Conference, vol. 1, pp. 2920-2923, 2006.

[24] T. Tokuda, R. Asano, S. Sugitani, Y. Terasawa, M. Nunoshita, K. Nakauchi, et al., "In vivo stimulation on rabbit retina using CMOS LSI-based multi-chip flexible stimulator for retinal prosthesis," Conference proceedings : ... Annual International Conference of the IEEE Engineering in Medicine and Biology Society. IEEE Engineering in Medicine and Biology Society. Conference, vol. 2007, pp. 5791-5794, 2007.

[25] T. Tokuda, K. Hiyama, S. Sawamura, K. Sasagawa, Y. Terasawa, K. Nishida, et al., "CMOS-based multichip networked flexible retinal stimulator designed for image-based retinal prosthesis," IEEE Transactions on Electron Devices, vol. 56, pp. 2577-2585, 2009.

[26] M. N. Shivdasani, C. D. Luu, R. Cicione, J. B. Fallon, P. J. Allen, J. Leuenberger, et al., "Evaluation of stimulus parameters and electrode geometry for an effective suprachoroidal retinal prosthesis," Journal of Neural Engineering, vol. 7, p. 036008, 2010.

[27] A. C. Bird, "Clinical investigation of retinitis pigmentosa," Australian and New Zealand Journal of Ophthalmology, vol. 16, pp. 189-198, 1988.

[28] L. S. Lim, P. Mitchell, J. M. Seddon, F. G. Holz, and T. Y. Wong, "Age-related macular degeneration," The Lancet, vol. 379, pp. 1728-1738, 2012.

[29] R. Klein, B. E. K. Klein, M. D. Knudtson, S. M. Meuer, M. Swift, and R. E. Gangnon, "Fifteen-Year Cumulative Incidence of Age-Related Macular Degeneration. The Beaver Dam Eye Study," Ophthalmology, vol. 114, pp. 253-262, 2007.

[30] D. B. Rein, J. S. Wittenborn, X. Zhang, A. A. Honeycutt, S. B. Lesesne, and J. Saaddine, "Forecasting age-related macular degeneration through the year 2050: The potential impact of new treatments," Archives of Ophthalmology, vol. 127, pp. 533-540, 2009.

[31] J. D. Weiland, W. Liu, and M. S. Humayun, "Retinal prosthesis," vol. 7, ed, 2005, pp. 361-401.

[32] C. C. T. Wang and S. Charles, "Microsurgical instrumentation for vitrectomy: Part II," Journal of clinical engineering, vol. 9, pp. 63-71, 1984.

[33] A. Santos, M. S. Humayun, E. De Juan Jr, R. J. Greenburg, M. J. Marsh, I. B. Klock, et al., "Preservation of the inner retina in retinitis pigmentosa:A morphometric analysis," Archives of Ophthalmology, vol. 115, pp. 511-515, 1997.

[34] S. K. Kelly, D. B. Shire, J. Chen, P. Doyle, M. D. Gingerich, W. A. Drohan, et al., "Realization of a 15-channel, hermetically-encased wireless subretinal prosthesis for the blind," 2009, pp. 200-203.

[35] G. J. Suaning and N. H. Lovell, "CMOS neurostimulation ASIC with 100 channels, scaleable output, and bidirectional radio-frequency telemetry," IEEE Transactions on Biomedical Engineering, vol. 48, pp. 248-260, 2001.

[36] J. D. Loudin, D. M. Simanovskii, K. Vijayraghavan, C. K. Sramek, A. F. Butterwick, P. Huie, et al., "Optoelectronic retinal prosthesis: System design and performance," Journal of Neural Engineering, vol. 4, pp. S72-S84, 2007.

[37] M. Schwarz, L. Ewe, N. Hijazi, B. J. Hosticka, J. Huppertz, S. Kolnsberg, et al., "Micro implantable visual prostheses," in Microtechnologies in Medicine and Biology, 1st Annual International, Conference On. 2000, 2000, pp. 461-465.

[38] K. Cha, K. Horch, and R. A. Normann, "Simulation of a phosphene-based visual field: Visual acuity in a pixelized vision system," Annals of Biomedical Engineering, vol. 20, pp. 439-449, 1992.

[39] R. W. Thompson Jr, G. D. Barnett, M. S. Humayun, and G. Dagnelie, "Facial Recognition Using Simulated Prosthetic Pixelized Vision," Investigative Ophthalmology and Visual Science, vol. 44, pp. 5035-5042, 2003.

[40] Y. Terasawa, A. Uehara, E. Yonezawa, T. Saitoh, K. Shodo, M. Ozawa, et al., "A visual prosthesis with 100 electrodes featuring wireless signals and wireless power transmission," IEICE Electronics Express, vol. 5, pp. 574-580, 2008.

[41] M. S. Humayun, J. D. Dorn, L. Da Cruz, G. Dagnelie, J. A. Sahel, P. E. Stanga, et al., "Interim results from the international trial of second sight's visual prosthesis," Ophthalmology, vol. 119, pp. 779-788, 2012.

[42] M. P. Barry and G. Dagnelie, "Use of the Argus II retinal prosthesis to improve visual guidance of fine hand movements," Investigative Ophthalmology and Visual Science, vol. 53, pp. 5095-5101, 2012.

[43] L. Mertz, "Sight restoration comes into focus: Versions of visual prostheses," IEEE Pulse, vol. 3, pp. 10-16, 2012.

[44] M. Mahadevappa, J. D. Weiland, D. Yanai, I. Fine, R. J. Greenberg, and M. S. Humayun, "Perceptual thresholds and electrode impedance in three retinal prosthesis subjects," IEEE Transactions on Neural Systems and Rehabilitation Engineering, vol. 13, pp. 201-206, 2005.

[45] Y. A. Kerdraon, J. A. Downie, G. J. Suaning, M. R. Capon, M. T. Coroneo, and N. H. Lovell, "Development and surgical implantation of a vision prosthesis model into the ovine eye," Clinical and Experimental Ophthalmology, vol. 30, pp. 36-40, 2002.

[46] N. Dommel, Y. T. Wong, P. J. Preston, T. Lehmann, N. H. Lovell, and G. J. Suaning, "The design and testing of an epi-retinal vision prosthesis neurostimulator capable of concurrent parallel stimulation," Conference proceedings : ... Annual International Conference of the IEEE Engineering in Medicine and Biology Society. IEEE Engineering in Medicine and Biology Society. Conference, vol. 1, pp. 4700-4709, 2006.

[47] Y. T. Wong, N. Dommel, P. J. Preston, T. Lehmann, N. H. Lovell, and G. J. Suaning, "Microelectronic retinal prosthesis: I. A neurostimulator for the concurrent activation of multiple electrodes," Conference proceedings : ... Annual International Conference of the IEEE Engineering in Medicine and Biology Society. IEEE Engineering in Medicine and Biology Society. Conference, vol. 1, pp. 4647-4650, 2006.

[48] Y. T. Wong, L. E. Hallum, S. C. Chen, N. Dommel, S. L. Cloherty, J. W. Morley, et al., "Optical imaging of electrically evoked visual signals in cats: I. Responses to corneal and intravitreal electrical stimulation," Conference proceedings : ... Annual International Conference of the IEEE Engineering in Medicine and Biology Society. IEEE Engineering in Medicine and Biology Society. Conference, vol. 2007, pp. 1635-1638, 2007.

[49] Y. T. Wong, S. C. Chen, J. M. Seo, J. W. Morley, N. H. Lovell, and G. J. Suaning, "Focal activation of the feline retina via a suprachoroidal electrode array," Vision Research, vol. 49, pp. 825-833, 2009.

[50] L. E. Hallum, S. L. Cloherty, and N. H. Lovell, "Image analysis for microelectronic retinal prosthesis," IEEE Transactions on Biomedical Engineering, vol. 55, pp. 344-346, 2008.

[51] D. Tsai, J. W. Morley, G. J. Suaning, and N. H. Lovell, "A wearable real-time image processor for a vision prosthesis," Computer Methods and Programs in Biomedicine, vol. 95, pp. 258-269, 2009.

[52] S. I. Kwak, K. Chang, and Y. J. Yoon, "Small spiral antenna for wideband capsule endoscope system," Electronics Letters, vol. 42, pp. 1328-1329, 2006.

[53] S. H. Lee, J. Lee, Y. J. Yoon, S. Park, C. Cheon, K. Kim, et al., "A wideband spiral antenna for ingestible capsule endoscope systems: Experimental results in a human phantom and a pig," IEEE Transactions on Biomedical Engineering, vol. 58, pp. 1734-1741, 2011.

[54] Q. Fang, S. Y. Lee, H. Permana, K. Ghorbani, and I. Cosic, "Developing a wireless implantable body sensor network in MICS band," IEEE Transactions on Information Technology in Biomedicine, vol. 15, pp. 567-576, 2011.

[55] D. C. Ng, S. Bai, J. Yang, N. Tran, and E. Skafidas, "Wireless technologies for closed-loop retinal prostheses," Journal of Neural Engineering, vol. 6, 2009.

[56] L. W. Couch, Digital and analog communication systems: Pearson/Prentice Hall, 2007.

[57] W. Liu, K. Vichienchom, M. Clements, S. C. DeMarco, C. Hughes, E. McGucken, et al., "Neuro-stimulus chip with telemetry unit for retinal prosthetic device," IEEE Journal of Solid-State Circuits, vol. 35, pp. 1487-1497, 2000.

[58] L. S. Theogarajan, "A low-power fully implantable 15-channel retinal stimulator chip," IEEE Journal of Solid-State Circuits, vol. 43, pp. 2322-2337, 2008.

[59] C. A. Balanis, Modern Antenna Handbook: Wiley-Interscience, 2008.

[60] A. Ahlbom, U. Bergqvist, J. H. Bernhardt, J. Cesarini, L. Court, M. Grandolfo, et al., "Guidelines for limiting exposure to time-varying electric, magnetic, and electromagnetic fields (up to 300 GHz)," Health Physics, vol. 74, pp. 494-521, 1998.

[61] FCC Policy on Human Exposure to Radiofrequency Electromagnetic Fields, FCC, 2010.

[62] FCC Rules and Regulations, FCC parts 18.301, 2012.

[63] N. Forum. (2012, 16 October). NFC and Interoperability. Available: http://www.nfc-forum.org/aboutnfc/interop/

[64] S. Gabriel, R. W. Lau, and C. Gabriel, "The dielectric properties of biological tissues: II. Measurements in the frequency range 10 Hz to 20 GHz," Physics in Medicine and Biology, vol. 41, pp. 2251-2269, 1996.

[65] K. L. Wong, Compact and Broadband Microstrip Antennas: John Wiley & Sons, 2002.

[66] FCC Rules and Regulations, FCC parts 95.627, 2012.

[67] T. Houzen, M. Takahashi, K. Saito, and K. Ito, "Implanted planar inverted F-antenna for cardiac pacemaker system," 2008, pp. 346-349.

[68] FCC Rules and Regulations, FCC parts 15, 2012.

[69] T. S. Rappaport, Wireless communications: principles and practice: Prentice Hall PTR, 2002.

[70] C. A. Balanis, Antenna Theory, 3rd ed. New Jersey: John Wiley & Sons, Inc., 2005.

[71] P. Soontornpipit, C. M. Furse, and Y. C. Chung, "Design of implantable microstrip antenna for communication with medical implants," IEEE Transactions on Microwave Theory and Techniques, vol. 52, pp. 1944-1951, 2004.

[72] J. Kim and Y. Rahmat-Samii, "Implanted antennas inside a human body: Simulations, designs, and characterizations," IEEE Transactions on Microwave Theory and Techniques, vol. 52, pp. 1934-1943, 2004.

[73] J. Leithon, "Electromagnetic simulation of a rectangular cavity: A comparison between FIT and FDTD results," in Electronics, Robotics and Automotive Mechanics Conference (CERMA) 2008, Cuernavaca, Mexico, October 2008, pp. 169-174.

[74] F. T. Ulaby, Fundamentals of applied electromagnetics: Pearson/Prentice Hall, 2007.

[75] S. J. Orfanidis, Electromagnetic Waves and Antennas Rutgers University, 2010.

[76] M. Z. Azad and M. Ali, "A miniature implanted inverted-F antenna for GPS application," IEEE Transactions on Antennas and Propagation, vol. 57, pp. 1854-1858, 2009.

[77] C. M. Lee, T. C. Yo, C. H. Luo, C. H. Tu, and Y. Z. Juang, "Compact broadband stacked implantable antenna for biotelemetry with medical devices," Electronics Letters, vol. 43, pp. 660-662, 2007.

[78] C. M. Lee, T. C. Yo, F. J. Huang, and C. H. Luo, "Dual-resonant Π-shape with double L-strips PIFA for implantable biotelemetry," Electronics Letters, vol. 44, pp. 837-839, 2008.

[79] C. M. Lee, T. C. Yo, F. J. Huang, and C. H. Luo, "Bandwidth enhancement of planar inverted-f antenna for implantable biotelemetry," Microwave and Optical Technology Letters, vol. 51, pp. 749-752, 2009.

[80] T. Karacolak, A. Z. Hood, and E. Topsakal, "Design of a dual-band implantable antenna and development of skin mimicking gels for continuous glucose monitoring," IEEE Transactions on Microwave Theory and Techniques, vol. 56, pp. 1001-1008, 2008.

[81] T. Karacolak, R. Cooper, and E. Topsakal, "Electrical properties of rat skin and design of implantable antennas for medical wireless telemetry," IEEE Transactions on Antennas and Propagation, vol. 57, pp. 2806-2812, 2009.

[82] T. Karacolak, R. Cooper, J. Butler, S. Fisher, and E. Topsakal, "In vivo verification of implantable antennas using rats as model animals," IEEE Antennas and Wireless Propagation Letters, vol. 9, pp. 334-337, 2010.

[83] W. C. Liu, F. M. Yeh, and M. Ghavami, "Miniaturized implantable broadband antenna for biotelemetry communication," Microwave and Optical Technology Letters, vol. 50, pp. 2407-2409, 2008.

[84] W. C. Liu, S. H. Chen, and C. M. Wu, "Bandwidth enhancement and size reduction of an implantable pifa antenna for biotelemetry devices," Microwave and Optical Technology Letters, vol. 51, pp. 755-757, 2009.

[85] J. Abadia, F. Merli, J. F. Zurcher, J. R. Mosig, and A. K. Skrivervik, "3D-Spiral small antenna design and realization for biomedical telemetry in the MICS band," Radioengineering, vol. 18, pp. 359-367, 2009.

[86] F. Merli, L. Bolomey, J. F. Zürcher, G. Corradini, E. Meurville, and A. K. Skrivervik, "Design, realization and measurements of a miniature antenna for implantable wireless communication systems," IEEE Transactions on Antennas and Propagation, vol. 59, pp. 3544-3555, 2011.

[87] T. F. Chien, C. M. Cheng, H. C. Yang, J. W. Jiang, and C. H. Luo, "Development of nonsuperstrate implantable low-profile CPW-fed ceramic antennas," IEEE Antennas and Wireless Propagation Letters, vol. 9, pp. 599-602, 2010.

[88] C. J. Sánchez-Fernández, O. Quevedo-Teruel, J. Requena-Carrión, L. Inclán-Sánchez, and E. Rajo-Iglesias, "Dual-band microstrip patch antenna based on short-circuited ring and spiral resonators for implantable medical devices," IET Microwaves, Antennas and Propagation, vol. 4, pp. 1048-1055, 2010.

[89] J. Ha, K. Kwon, and J. Choi, "Compact zeroth-order resonance antenna for implantable biomedical service applications," Electronics Letters, vol. 47, pp. 1267-1269, 2011.

[90] F. J. Huang, C. M. Lee, C. L. Chang, L. K. Chen, T. C. Yo, and C. H. Luo, "Rectenna application of miniaturized implantable antenna design for triple-band biotelemetry communication," IEEE Transactions on Antennas and Propagation, vol. 59, pp. 2646-2653, 2011.

[91] R. Waterhouse, Microstrip Patch Antennas: A Designer's Guide: Springer, 2003.

[92] A. K. Skrivervik, J. F. Zürcher, O. Staub, and J. R. Mosig, "PCS antenna design: The challenge of miniaturization," IEEE Antennas and Propagation Magazine, vol. 43, pp. 12-27, 2001.

[93] J. W. Hand, "Modelling the interaction of electromagnetic fields (10 MHz-10 GHz) with the human body: Methods and applications," Physics in Medicine and Biology, vol. 53, pp. R243-R286, 2008.

[94] Y. Kane, "Numerical solution of initial boundary value problems involving maxwell's equations in isotropic media," Antennas and Propagation, IEEE Transactions on, vol. 14, pp. 302-307, 1966.

[95] A. Taflove, Computational electrodynamics: the finite-difference time-domain method: Artech House, 1995.

[96] R. Marklein, "11. The Finite Integration Technique as a General Tool to Compute Acoustic, Electromagnetic, Elastodynamic, and Coupled Wave Fields," in Review of Radio Science: 1999-2002 URSI, W. R. Stone, Ed., ed New York: John Wiley & Sons, 2002, pp. 201-244.

[97] CSGNetwork. (2012, 5 December). Dielectric Constants Of Various Materials Table. Available: http://www.csgnetwork.com/dieconstantstable.html.

[98] L. V. Blake and M. W. Long, "Antennas - Fundamentals, Design, Measurement (3rd Edition)," ed: SciTech Publishing, 2009, pp. 371-421.

[99] R. C. Johnson, Antenna Engineering Handbook, 3rd ed. New York: McGraw-Hill, Inc, 1993.

[100] IEEE, "IEEE standard test procedures for antennas," ed: Wiley-Interscience, 1979.

[101] J. F. Zürcher, O. Staub, A. K. Skrivervik, and M. Hermanjat, "Accurate measurement of the maximum gain of electrically small antennas," Microwave and Optical Technology Letters, vol. 23, pp. 328-331, 1999.

[102] W. B. Heinzelman, A. P. Chandrakasan, and H. Balakrishnan, "An application-specific protocol architecture for wireless microsensor networks," IEEE Transactions on Wireless Communications, vol. 1, pp. 660-670, 2002.

[103] E. Jovanov, A. Milenkovic, C. Otto, and P. C. De Groen, "A wireless body area network of intelligent motion sensors for computer assisted physical rehabilitation," Journal of NeuroEngineering and Rehabilitation, vol. 2, 2005.

[104] G. Koley, J. Liu, M. W. Nomani, M. Yim, X. Wen, and T. Y. Hsia, "Miniaturized implantable pressure and oxygen sensors based on polydimethylsiloxane thin films," Materials Science and Engineering C, vol. 29, pp. 685-690, 2009.

[105] B. Kjellström, C. Linde, T. Bennett, A. Ohlsson, and L. Ryden, "Six years follow-up of an implanted SvO2 sensor in the right ventricle," European Journal of Heart Failure, vol. 6, pp. 627-634, 2004.

[106] D. A. Gough, L. S. Kumosa, T. L. Routh, J. T. Lin, and J. Y. Lucisano, "Function of an implanted tissue glucose sensor for more than 1 year in animals," Science Translational Medicine, vol. 2, 2010.

[107] G. Iddan, G. Meron, A. Glukhovsky, and P. Swain, "Wireless capsule endoscopy," Nature, vol. 405, pp. 417-418, 2000.

[108] M. Han, P. S. Manoonkitiwongsa, C. X. Wang, and D. B. McCreery, "In vivo validation of custom-designed silicon-based microelectrode arrays for long-term neural recording and stimulation," IEEE Transactions on Biomedical Engineering, vol. 59, pp. 346-354, 2012.

[109] G. Lazzi, "Thermal effects of bioimplants," IEEE Engineering in Medicine and Biology Magazine, vol. 24, pp. 75-81, 2005.

[110] "Erratum: International commission on non-ionizing radiation protection (ICNIRP). Guidelines for limiting exposure to time-varying electric, magnetic, and electromagnetic fields (Up to 300 GHz) (Health Physics (1998) 74 (494-522))," Health Physics, vol. 75, p. 442, 1998.

[111] C. C. Johnson and A. W. Guy, "Nonionizing electromagnetic wave effects in biological materials and systems," Proceedings of the IEEE, vol. 60, pp. 692-718, 1972.

[112] K. S. Nikita, M. Cavagnaro, G. Cerri, S. Chiarandini, R. De Leo, and P. Russo, "A study of uncertainties in modeling antenna performance and power absorption in the head of a cellular phone user," IEEE Transactions on Microwave Theory and Techniques, vol. 48, pp. 2676-2685, 2000.

[113] L. C. Chirwa, P. A. Hammond, S. Roy, and D. R. S. Cumming, "Electromagnetic radiation from ingested sources in the human intestine between 150 MHz and 1.2 GHz," IEEE Transactions on Biomedical Engineering, vol. 50, pp. 484-492, 2003.

[114] E. Gjonaj, M. Bartsch, M. Clemens, S. Schupp, and T. Weiland, "High-resolution human anatomy models for advanced electromagnetic field computations," IEEE Transactions on Magnetics, vol. 38, pp. 357-360, 2002.

[115] J. Gemio, J. Parrón, and J. Soler, "Human body effects on implantable antennas for ism bands applications: Models comparison and propagation losses study," Progress in Electromagnetics Research, vol. 110, pp. 437-452, 2010.

[116] P. Gajšek, J. M. Ziriax, W. D. Hurt, T. J. Walters, and P. A. Mason, "Predicted SAR in Sprague-Dawley rat as a function of permittivity values," Bioelectromagnetics, vol. 22, pp. 384-400, 2001.

[117] W. S. T. Rowe, "Multilayered Patch Antennas," in Printed Antennas for Wireless Communications, ed: John Wiley & Sons, Ltd, 2007, pp. 37-68.

[118] C.-C. Chen and J. Volakis, "Printed Spiral Antennas," in Printed Antennas for Wireless Communications, ed: John Wiley & Sons, Ltd, 2007, pp. 103-132.

[119] E. Zrenner, K. U. Bartz-Schmidt, H. Benav, D. Besch, A. Bruckmann, V. Gabel, et al., “Subretinal electronic chips allow blind patients to read letters and combine them to words,” Proceedings of the Royal Society B: Biological Sciences 278 (1711), pp. 1489-1497, 2011.

Appendix 1 - Radiall R124.463.000 SMA Connector datasheet

TECHNICAL DATA SHEET 1 / 2

2 HOLES FLANGE JACK RECEPTACLE

WITH SHOULDER CONTACT

R125.463.000

Series : **SMA**

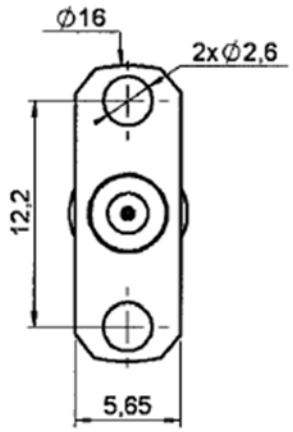

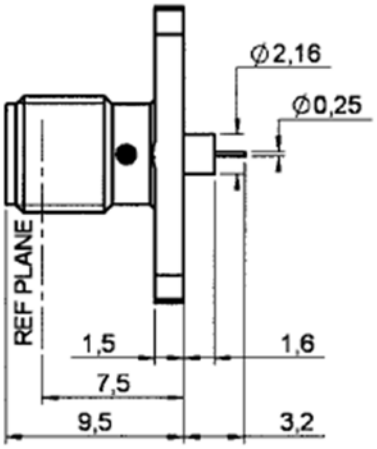

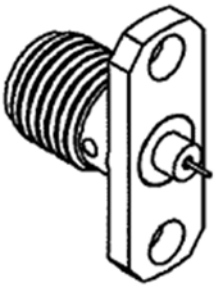

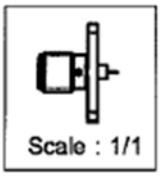

All dimensions are in mm.

COMPONENTS	MATERIALS	PLATING (µm)
BODY	STAINLESS STEEL	GOLD 0.5 OVER NICKEL 2
CENTER CONTACT	BERYLLIUM COPPER	GOLD 1.3 OVER NICKEL2
OUTER CONTACT	-	-
INSULATOR	PTFE	
GASKET	-	
OTHERS PARTS	-	-
-	-	-
-	-	-

Issue : 9840 E

In the effort to improve our products, we reserve the right to make changes judged to be necessary.

RADIALL

2 HOLES FLANGE JACK RECEPTACLE WITH SHOULDER CONTACT

R125.463.000

Series : SMA

PACKAGING

Standard	Unit	Other
100	'W' option	Contact us

SPECIFICATION

ELECTRICAL CHARACTERISTICS

Impedance		50	Ω
Frequency		0-18	GHz
VSWR	1.05 +	0,0030	x F(GHz) Maxi
Insertion loss		0.07	√F(GHz) dB Maxi
RF leakage	- (	NA	- F(GHz)) dB Maxi
Voltage rating		500	Veff Maxi
Dielectric withstanding voltage		1000	Veff mini
Insulation resistance		5000	MΩ mini

ENVIRONMENTAL

Operating temperature	-65/+165	° C
Hermetic seal	NA	Atm.cm3/s
Panel leakage	NA	

OTHER CHARACTERISTICS

Assembly instruction

Others :

-

MECHANICAL CHARACTERISTICS

Center contact retention		
Axial force – Mating end	27	N mini
Axial force – Opposite end	27	N mini
Torque	2.8	N.cm mini
Recommended torque		
Mating	NA	N.cm
Panel nut	NA	N.cm
Mating life	500	Cycles mini
Weight	2,6000	g

Issue : 9840 E

In the effort to improve our products, we reserve the right to make changes judged to be necessary.

RADIALL

Appendix 2 - Dow Corning® 184 Silicone Elastomer datasheet

Product Information

DOW CORNING

Encapsulants

Dow Corning® 184 Silicone Elastomer

Transparent encapsulant with good flame resistance

FEATURES

- Flowable
- RT and heat cure
- High tensile strength
- Same as Sylgard 182 but with RT cure capability
- UL and Mil Spec tested

BENEFITS

- Rapid, versatile cure processing controlled by temperature
- High transparency allows easy inspection of components
- Can be considered for uses requiring UL and Mil Spec requirements

COMPOSITION

- 2-part
- 10:1 mix ratio
- Polydimethylsiloxane elastomer

APPLICATION METHODS

- Automated metered mixing and dispensing
- Manual mixing

APPLICATIONS

- General potting applications
- Power supplies
- Connectors
- Sensors
- Industrial controls
- Transformers
- Amplifiers
- High voltage resistor packs
- Relays
- Adhesive/encapsulant for solar cells
- Adhesive handling beam lead integrated circuits during processing

TYPICAL PROPERTIES

Specification Writers: These values are not intended for use in preparing specifications. Please contact your local Dow Corning sales office or your Global Dow Corning Connection before writing specifications on this product.

Property	Unit	Value
Viscosity (Part A)	cP	5175
	mPa-sec	5175
	Pa-sec	5.2
Viscosity (Mixed)	cP	3500
	mPa-sec	3500
	Pa-sec	3.5
Specific Gravity (Uncured Base)	-	1.03
Specific Gravity (Cured)	-	1.04
Working Time at 25°C (Pot Life - hours)	hr	1.4
Cure Time at 25°C	hrs	48
Heat Cure Time @ 100°C	minutes	35
Heat Cure Time @ 125°C	minutes	20
Heat Cure Time @ 150°C	minutes	10

DESCRIPTION

Dow Corning® silicone encapsulants are supplied as two-part liquid component kits. When liquid components are thoroughly mixed, the mixture cures to a flexible elastomer, which is well suited for the protection of electrical/electronic applications. Dow Corning silicone encapsulants cure without exotherm at a constant rate regardless of sectional thickness or degree of confinement. Dow Corning silicone elastomers require no post cure and can be placed in service immediately following the completion of the cure schedule. Standard silicone encapsulants require a surface treatment with a primer in addition to good cleaning for adhesion while primerless silicone encapsulants require only good cleaning. Underwriters Laboratory (UL) 94 recognition is based on minimum thickness requirements. Please consult the UL Online Certifications Directory for the most accurate certification information.

MIXING AND DE-AIRING

The 10:1 mix ratio these products are supplied in gives one latitude to tune the modulus and hardness for specific application needs and production lines. In most cases de-airing is not required.

PREPARING SURFACES

In applications requiring adhesion, priming will be required for many of the silicone encapsulants. See the Primer Selection Guide for the correct primer to use with a given product. For best results, the primer should be applied in a very thin, uniform coating and then wiped off after application. After application, it should be thoroughly cured prior to application of the silicone elastomer. Additional instructions for primer usage can be found in the information sheets specific to the individual primers.

PROCESSING/CURING

Thoroughly mixed Dow Corning silicone encapsulant may be poured/dispensed directly into the container in which it is to be cured. Care should be taken to minimize air entrapment. When practical, pouring/dispensing should be done under vacuum, particularly if the component being potted or encapsulated has many small voids. If this technique cannot be used, the unit should be evacuated after the silicone encapsulant has been poured/dispensed. Dow Corning silicone encapsulants may be either room temperature (25°C/77°F) or heat cured. Room temperature cure encapsulants may also be heat accelerated for faster cure. Ideal cure conditions for each product are given in the product selection table. Two-part condensation cure encapsulants should not be heat accelerated above 60°C (140°F).

TYPICAL PROPERTIES, continued

Property	Unit	Value
Tensile Strength	psi MPa kg/cm2	1025 7.1 71
Elongation	%	120
Tear Strength (Die B)	ppi N/cm	5 2
Durometer Shore A	-	44
Dielectric Strength	volts/mil kV/mm	475 19
Volume Resistivity	ohm*cm	2.9E+14
Dielectric Constant at 100 Hz	-	2.72
Dielectric Constant at 100 kHz	-	2.68
Dissipation Factor at 100 hz	-	0.00257
Dissipation Factor at 100 kHz	-	0.00133
Mil Specification	NA	Mil Spec
Agency Listing	-	UL 94V-0
Shelf Life at 25°C	months	24
Refractive Index @ 589 nm	-	1.4118
Refractive Index @ 632.8 nm	-	1.4225
Refractive Index @ 1321 nm	-	1.4028
Refractive Index @ 1554 nm	-	1.3997

POT LIFE AND CURE RATE

Cure reaction begins with the mixing process. Initially, cure is evidenced by a gradual increase in viscosity, followed by gelation and conversion to a solid elastomer. Pot life is defined as the time required for viscosity to double after Parts A and B (base and curing agent) are mixed and is highly temperature and application dependent. Please refer to the data table.

USEFUL TEMPERATURE RANGES

For most uses, silicone elastomers should be operational over a temperature range of -45 to 200°C (-49 to 392°F) for long periods of time. However, at both the low- and high temperature ends of the spectrum, behavior of the materials and performance in particular applications can become more complex and require additional considerations. For low-temperature performance, thermal cycling to conditions such as -55°C (-67°F) may be possible, but performance should be verified for your parts or assemblies. Factors that may influence performance are configuration and stress sensitivity of components, cooling rates and hold times, and prior temperature history. At the high-temperature end, the durability of the cured silicone elastomer is time and temperature dependent. As expected, the higher the temperature, the shorter the time the material will remain useable.

COMPATIBILITY

Certain materials, chemicals, curing agents and plasticizers can inhibit the cure of addition cure adhesives. Most notable of these include: Organotin and other organometallic compounds, Silicone rubber containing organotin catalyst, Sulfur, polysulfides, polysulfones or other sulfur containing materials, unsaturated hydrocarbon plasitcizers, and some solder flux residues. If a substrate or material is questionable with respect to potentially causing inhibition of cure, it is recommended that a small scale compatibility test be run to ascertain suitability in a given application. The presence of liquid or uncured product at the interface between the questionable substrate and the cured gel indicates incompatibility and inhibition of cure.

REPAIRABILITY

In the manufacture of electrical/electronic devices it is often desirable to salvage or reclaim damaged or defective units. With most non-silicone rigid potting/encapsulating materials, removal or entry is difficult or impossible without causing excessive damage to internal circuitry. Dow Corning silicone encapsulants can be selectively removed with relative ease, any repairs or changes accomplished, and the repaired area repotted in place with additional product. To remove silicone elastomers, simply cut with a sharp blade or knife and tear and remove unwanted material from the area to be repaired. Sections of the adhered elastomer are best removed from substrates and circuitry by mechanical action such as scraping or rubbing and can be assisted by applying Dow Corning® brand OS Fluids. Before applying additional encapsulant to a repaired device, roughen the exposed surfaces of the cured encapsulant with an abrasive paper and rinse with a suitable solvent. This will enhance adhesion and permit the repaired material to become an integral matrix with the existing encapsulant. Silicone prime coats are not recommended for adhering products to themselves.

PACKAGING

In general, Dow Corning silicone 1:1 mix ratio encapsulants are supplied in nominal 0.45-, 3.6-, 18- and 200-kg (1-, 8-, 40- and 440-lb) containers, net weight. Dow Corning silicone 10:1 mix ratio encapsulants are supplied in nominal 0.5-, 5-, 25- and 225-kg (1.1-, 11-, 55- and 495-lb) containers, net weight. Packaging options may vary by product. Consult Dow Corning Customer Service at (989) 496-6000 for additional packaging options.

USABLE LIFE AND STORAGE

Shelf life is indicated by the "Use Before" date found on the product label. Refer to the product label for storage temperature requirements. Special precautions must be taken to prevent moisture from contacting these materials. Containers should be kept tightly closed and head or air space minimized. Partially filled containers should be purged with dry air or other gases, such as nitrogen. Exposure to moisture could reduce adhesion and cause bubbles to form.

HANDLING PRECAUTIONS

PRODUCT SAFETY INFORMATION REQUIRED FOR SAFE USE IS NOT INCLUDED IN THIS DOCUMENT. BEFORE HANDLING, READ PRODUCT AND MATERIAL SAFETY DATA SHEETS AND CONTAINER LABELS FOR SAFE USE, PHYSICAL AND HEALTH HAZARD INFORMATION. THE MATERIAL SAFETY DATA SHEET IS AVAILABLE ON THE DOW CORNING WEBSITE AT WWW.DOWCORNING.COM, OR FROM YOUR DOW CORNING REPRESENTATIVE, OR DISTRIBUTOR, OR BY CALLING YOUR GLOBAL DOW CORNING CONNECTION.

HEALTH AND ENVIRONMENTAL INFORMATION

To support Customers in their product safety needs, Dow Corning has an extensive Product Stewardship organization and a team of Product Safety and Regulatory Compliance (PS&RC) specialists available in each area. For further information, please see our website, www.dowcorning.com or consult your local Dow Corning representative.

LIMITATIONS

This product is neither tested nor represented as suitable for medical or pharmaceutical uses.

LIMITED WARRANTY INFORMATION PLEASE READ CAREFULLY

The information contained herein is offered in good faith and is believed to be accurate. However, because conditions and methods of use of our products are beyond our control, this information should not be used in substitution for customer's tests to ensure that our products are safe, effective, and fully satisfactory for the intended end use. Suggestions of use shall not be taken as inducements to infringe any patent. Dow Corning's sole warranty is that our products will meet the sales specifications in effect at the time of shipment. Your exclusive remedy for breach of such warranty is limited to refund of purchase price or replacement of any product shown to be other than as warranted.

DOW CORNING SPECIFICALLY DISCLAIMS ANY OTHER EXPRESS OR IMPLIED WARRANTY OF FITNESS FOR A PARTICULAR PURPOSE OR MERCHANTABILITY.

DOW CORNING DISCLAIMS LIABILITY FOR ANY INCIDENTAL OR CONSEQUENTIAL DAMAGES.

We help you invent the future. ™

dowcorning.com

2010, Month 01
Ref. No. 11-1792-01

Appendix 3 - Dataset of return loss measurement on case A

f (MHz)	Return Loss (dB)
350.00	-0.39
350.40	-0.38
350.80	-0.38
351.20	-0.38
351.60	-0.40
352.00	-0.39
352.40	-0.39
352.80	-0.39
353.20	-0.39
353.60	-0.38
354.00	-0.37
354.40	-0.39
354.80	-0.38
355.20	-0.38
355.60	-0.38
356.00	-0.39
356.40	-0.38
356.80	-0.38
357.20	-0.39
357.60	-0.36
358.00	-0.37
358.40	-0.39
358.80	-0.38
359.20	-0.38
359.60	-0.37
360.00	-0.39
360.40	-0.38
360.80	-0.38
361.20	-0.39
361.60	-0.39
362.00	-0.38
362.40	-0.40
362.80	-0.39
363.20	-0.39
363.60	-0.38
364.00	-0.39
364.40	-0.40
364.80	-0.39

f (MHz)	Return Loss (dB)
365.20	-0.39
365.60	-0.38
366.00	-0.40
366.40	-0.39
366.80	-0.38
367.20	-0.39
367.60	-0.40
368.00	-0.38
368.40	-0.38
368.80	-0.38
369.20	-0.39
369.60	-0.39
370.00	-0.39
370.40	-0.38
370.80	-0.37
371.20	-0.40
371.60	-0.40
372.00	-0.40
372.40	-0.38
372.80	-0.39
373.20	-0.38
373.60	-0.38
374.00	-0.39
374.40	-0.38
374.80	-0.39
375.20	-0.39
375.60	-0.39
376.00	-0.39
376.40	-0.39
376.80	-0.39
377.20	-0.39
377.60	-0.37
378.00	-0.39
378.40	-0.40
378.80	-0.38
379.20	-0.39
379.60	-0.39
380.00	-0.39
380.40	-0.39

f (MHz)	Return Loss (dB)
380.80	-0.39
381.20	-0.39
381.60	-0.39
382.00	-0.39
382.40	-0.39
382.80	-0.39
383.20	-0.39
383.60	-0.39
384.00	-0.40
384.40	-0.39
384.80	-0.39
385.20	-0.39
385.60	-0.38
386.00	-0.40
386.40	-0.39
386.80	-0.40
387.20	-0.38
387.60	-0.40
388.00	-0.39
388.40	-0.39
388.80	-0.40
389.20	-0.40
389.60	-0.41
390.00	-0.41
390.40	-0.41
390.80	-0.40
391.20	-0.40
391.60	-0.41
392.00	-0.41
392.40	-0.41
392.80	-0.40
393.20	-0.40
393.60	-0.40
394.00	-0.41
394.40	-0.41
394.80	-0.41
395.20	-0.41
395.60	-0.42
396.00	-0.42

f (MHz)	Return Loss (dB)
396.40	-0.42
396.80	-0.43
397.20	-0.41
397.60	-0.42
398.00	-0.41
398.40	-0.42
398.80	-0.41
399.20	-0.43
399.60	-0.44
400.00	-0.44
400.40	-0.43
400.80	-0.44
401.20	-0.44
401.60	-0.44
402.00	-0.44
402.40	-0.44
402.80	-0.44
403.20	-0.43
403.60	-0.45
404.00	-0.45
404.40	-0.45
404.80	-0.45
405.20	-0.46
405.60	-0.46
406.00	-0.46
406.40	-0.46
406.80	-0.47
407.20	-0.47
407.60	-0.49
408.00	-0.48
408.40	-0.48
408.80	-0.50
409.20	-0.51
409.60	-0.50
410.00	-0.51
410.40	-0.51
410.80	-0.51
411.20	-0.53
411.60	-0.54

f (MHz)	Return Loss (dB)
412.00	-0.54
412.40	-0.55
412.80	-0.56
413.20	-0.58
413.60	-0.58
414.00	-0.59
414.40	-0.60
414.80	-0.61
415.20	-0.64
415.60	-0.62
416.00	-0.65
416.40	-0.67
416.80	-0.68
417.20	-0.71
417.60	-0.73
418.00	-0.74
418.40	-0.80
418.80	-0.81
419.20	-0.83
419.60	-0.85
420.00	-0.88
420.40	-0.91
420.80	-0.93
421.20	-0.98
421.60	-1.05
422.00	-1.10
422.40	-1.13
422.80	-1.19
423.20	-1.26
423.60	-1.32
424.00	-1.41
424.40	-1.52
424.80	-1.58
425.20	-1.71
425.60	-1.83
426.00	-1.99
426.40	-2.16
426.80	-2.34
427.20	-2.58

f (MHz)	Return Loss (dB)
427.60	-2.82
428.00	-3.13
428.40	-3.48
428.80	-3.88
429.20	-4.38
429.60	-4.98
430.00	-5.69
430.40	-6.57
430.80	-7.63
431.20	-8.98
431.60	-10.68
432.00	-12.91
432.40	-15.83
432.80	-19.26
433.20	-20.12
433.60	-17.06
434.00	-13.86
434.40	-11.41
434.80	-9.56
435.20	-8.07
435.60	-6.94
436.00	-5.99
436.40	-5.24
436.80	-4.62
437.20	-4.11
437.60	-3.66
438.00	-3.29
438.40	-2.98
438.80	-2.69
439.20	-2.47
439.60	-2.25
440.00	-2.11
440.40	-1.94
440.80	-1.80
441.20	-1.68
441.60	-1.56
442.00	-1.48
442.40	-1.39
442.80	-1.33

f (MHz)	Return Loss (dB)
443.20	-1.25
443.60	-1.19
444.00	-1.13
444.40	-1.08
444.80	-1.04
445.20	-1.00
445.60	-0.97
446.00	-0.93
446.40	-0.89
446.80	-0.88
447.20	-0.83
447.60	-0.82
448.00	-0.80
448.40	-0.78
448.80	-0.76
449.20	-0.73
449.60	-0.75
450.00	-0.71
450.40	-0.68
450.80	-0.67
451.20	-0.66
451.60	-0.65
452.00	-0.66
452.40	-0.63
452.80	-0.62
453.20	-0.60
453.60	-0.60
454.00	-0.60
454.40	-0.58
454.80	-0.58
455.20	-0.55
455.60	-0.54
456.00	-0.56
456.40	-0.55
456.80	-0.55
457.20	-0.54
457.60	-0.54
458.00	-0.53
458.40	-0.52

f (MHz)	Return Loss (dB)
458.80	-0.54
459.20	-0.52
459.60	-0.50
460.00	-0.51
460.40	-0.50
460.80	-0.52
461.20	-0.49
461.60	-0.50
462.00	-0.49
462.40	-0.48
462.80	-0.49
463.20	-0.50
463.60	-0.49
464.00	-0.48
464.40	-0.47
464.80	-0.49
465.20	-0.49
465.60	-0.48
466.00	-0.49
466.40	-0.47
466.80	-0.46
467.20	-0.46
467.60	-0.46
468.00	-0.46
468.40	-0.46
468.80	-0.47
469.20	-0.45
469.60	-0.46
470.00	-0.45
470.40	-0.45
470.80	-0.47
471.20	-0.47
471.60	-0.46
472.00	-0.45
472.40	-0.47
472.80	-0.46
473.20	-0.45
473.60	-0.45
474.00	-0.47

f (MHz)	Return Loss (dB)
474.40	-0.46
474.80	-0.46
475.20	-0.46
475.60	-0.47
476.00	-0.46
476.40	-0.45
476.80	-0.46
477.20	-0.46
477.60	-0.46
478.00	-0.46
478.40	-0.46
478.80	-0.46
479.20	-0.46
479.60	-0.46
480.00	-0.47
480.40	-0.45
480.80	-0.48
481.20	-0.45
481.60	-0.45
482.00	-0.47
482.40	-0.46
482.80	-0.47
483.20	-0.45
483.60	-0.47
484.00	-0.46
484.40	-0.47
484.80	-0.48
485.20	-0.46
485.60	-0.47
486.00	-0.47
486.40	-0.47
486.80	-0.47
487.20	-0.47
487.60	-0.48
488.00	-0.46
488.40	-0.48
488.80	-0.47
489.20	-0.47
489.60	-0.48

f (MHz)	Return Loss (dB)
490.00	-0.48
490.40	-0.49
490.80	-0.48
491.20	-0.47
491.60	-0.47
492.00	-0.48
492.40	-0.49
492.80	-0.48
493.20	-0.48
493.60	-0.48
494.00	-0.49
494.40	-0.48
494.80	-0.47
495.20	-0.48
495.60	-0.47
496.00	-0.49
496.40	-0.48
496.80	-0.49
497.20	-0.49
497.60	-0.49
498.00	-0.49
498.40	-0.49
498.80	-0.49
499.20	-0.49
499.60	-0.50
500.00	-0.49

Appendix 4 - Dataset of from return loss measurement on case B

f (MHz)	Return Loss (dB)
350.40	-0.37
351.25	-0.41
352.10	-0.40
352.95	-0.41
353.80	-0.39
354.65	-0.40
355.50	-0.41
356.35	-0.41
357.20	-0.38
358.05	-0.40
358.90	-0.39
359.75	-0.39
360.60	-0.41
361.45	-0.40
362.30	-0.39
363.15	-0.40
364.00	-0.40
364.85	-0.41
365.70	-0.40
366.55	-0.41
367.40	-0.41
368.25	-0.40
369.10	-0.40
369.95	-0.40
370.80	-0.40
371.65	-0.41
372.50	-0.40
373.35	-0.40
374.20	-0.39
375.05	-0.40
375.90	-0.40
376.75	-0.40
377.60	-0.40
378.45	-0.41
379.30	-0.41
380.15	-0.39

f (MHz)	Return Loss (dB)
381.00	-0.41
381.85	-0.40
382.70	-0.40
383.55	-0.39
384.40	-0.41
385.25	-0.40
386.10	-0.41
386.95	-0.41
387.80	-0.41
388.65	-0.42
389.50	-0.42
390.35	-0.42
391.20	-0.41
392.05	-0.42
392.90	-0.42
393.75	-0.43
394.60	-0.43
395.45	-0.43
396.30	-0.43
397.15	-0.44
398.00	-0.46
398.85	-0.45
399.70	-0.44
400.55	-0.45
401.40	-0.46
402.25	-0.47
403.10	-0.48
403.95	-0.48
404.80	-0.47
405.65	-0.49
406.50	-0.51
407.35	-0.53
408.20	-0.55
409.05	-0.55
409.90	-0.57
410.75	-0.60

f (MHz)	Return Loss (dB)
411.60	-0.61
412.45	-0.64
413.30	-0.66
414.15	-0.72
415.00	-0.74
415.85	-0.80
416.70	-0.85
417.55	-0.91
418.40	-0.98
419.25	-1.09
420.10	-1.21
420.95	-1.37
421.80	-1.54
422.65	-1.76
423.50	-2.09
424.35	-2.50
425.20	-3.05
426.05	-3.84
426.90	-4.97
427.75	-6.67
428.60	-9.28
429.45	-13.60
430.30	-18.90
431.15	-14.55
432.00	-9.89
432.85	-7.06
433.70	-5.25
434.55	-4.04
435.40	-3.20
436.25	-2.63
437.10	-2.19
437.95	-1.84
438.80	-1.62
439.65	-1.40
440.50	-1.28
441.35	-1.15

f (MHz)	Return Loss (dB)
442.20	-1.06
443.05	-0.94
443.90	-0.91
444.75	-0.83
445.60	-0.79
446.45	-0.76
447.30	-0.71
448.15	-0.69
449.00	-0.67
449.85	-0.63
450.70	-0.62
451.55	-0.60
452.40	-0.58
453.25	-0.57
454.10	-0.55
454.95	-0.55
455.80	-0.54
456.65	-0.51
457.50	-0.52
458.35	-0.50
459.20	-0.47
460.05	-0.49
460.90	-0.49
461.75	-0.48
462.60	-0.48
463.45	-0.47
464.30	-0.48
465.15	-0.47
466.00	-0.49
466.85	-0.47
467.70	-0.47
468.55	-0.48
469.40	-0.46
470.25	-0.46
471.10	-0.46
471.95	-0.47

f (MHz)	Return Loss (dB)
472.80	-0.47
473.65	-0.48
474.50	-0.46
475.35	-0.47
476.20	-0.48
477.05	-0.45
477.90	-0.44
478.75	-0.48
479.60	-0.47
480.45	-0.47
481.30	-0.46
482.15	-0.47
483.00	-0.47
483.85	-0.47
484.70	-0.49
485.55	-0.50
486.40	-0.47
487.25	-0.48
488.10	-0.49
488.95	-0.49
489.80	-0.49
490.65	-0.49
491.50	-0.48
492.35	-0.50
493.20	-0.49
494.05	-0.50
494.90	-0.50
495.75	-0.50
496.60	-0.52
497.45	-0.52
498.30	-0.52
499.15	-0.52
500.00	-0.51

Appendix 5 - Dataset of return loss measurement on case D

f (MHz)	Return Loss (dB)
350.00	-0.37
350.40	-0.37
350.80	-0.37
351.20	-0.38
351.60	-0.37
352.00	-0.37
352.40	-0.36
352.80	-0.38
353.20	-0.37
353.60	-0.38
354.00	-0.37
354.40	-0.38
354.80	-0.38
355.20	-0.37
355.60	-0.37
356.00	-0.38
356.40	-0.37
356.80	-0.37
357.20	-0.38
357.60	-0.37
358.00	-0.36
358.40	-0.37
358.80	-0.37
359.20	-0.37
359.60	-0.37
360.00	-0.36
360.40	-0.37
360.80	-0.37
361.20	-0.37
361.60	-0.36
362.00	-0.37
362.40	-0.37
362.80	-0.36
363.20	-0.37
363.60	-0.36
364.00	-0.38
364.40	-0.36
364.80	-0.37

f (MHz)	Return Loss (dB)
365.20	-0.37
365.60	-0.36
366.00	-0.37
366.40	-0.37
366.80	-0.36
367.20	-0.37
367.60	-0.37
368.00	-0.37
368.40	-0.37
368.80	-0.37
369.20	-0.37
369.60	-0.37
370.00	-0.36
370.40	-0.37
370.80	-0.37
371.20	-0.39
371.60	-0.39
372.00	-0.36
372.40	-0.37
372.80	-0.37
373.20	-0.37
373.60	-0.38
374.00	-0.38
374.40	-0.38
374.80	-0.37
375.20	-0.39
375.60	-0.37
376.00	-0.39
376.40	-0.39
376.80	-0.39
377.20	-0.38
377.60	-0.39
378.00	-0.39
378.40	-0.40
378.80	-0.39
379.20	-0.39
379.60	-0.39
380.00	-0.40

f (MHz)	Return Loss (dB)
380.40	-0.43
380.80	-0.39
381.20	-0.41
381.60	-0.42
382.00	-0.42
382.40	-0.44
382.80	-0.42
383.20	-0.42
383.60	-0.43
384.00	-0.41
384.40	-0.43
384.80	-0.42
385.20	-0.45
385.60	-0.45
386.00	-0.45
386.40	-0.43
386.80	-0.44
387.20	-0.44
387.60	-0.45
388.00	-0.46
388.40	-0.45
388.80	-0.45
389.20	-0.48
389.60	-0.48
390.00	-0.47
390.40	-0.47
390.80	-0.49
391.20	-0.48
391.60	-0.50
392.00	-0.51
392.40	-0.50
392.80	-0.51
393.20	-0.51
393.60	-0.52
394.00	-0.53
394.40	-0.53
394.80	-0.54
395.20	-0.55

f (MHz)	Return Loss (dB)
395.60	-0.56
396.00	-0.56
396.40	-0.58
396.80	-0.59
397.20	-0.60
397.60	-0.61
398.00	-0.60
398.40	-0.61
398.80	-0.63
399.20	-0.63
399.60	-0.65
400.00	-0.66
400.40	-0.68
400.80	-0.70
401.20	-0.69
401.60	-0.71
402.00	-0.74
402.40	-0.75
402.80	-0.77
403.20	-0.78
403.60	-0.81
404.00	-0.82
404.40	-0.85
404.80	-0.87
405.20	-0.91
405.60	-0.92
406.00	-0.96
406.40	-0.99
406.80	-1.02
407.20	-1.06
407.60	-1.10
408.00	-1.14
408.40	-1.16
408.80	-1.22
409.20	-1.28
409.60	-1.31
410.00	-1.40
410.40	-1.44

f (MHz)	Return Loss (dB)
410.80	-1.54
411.20	-1.61
411.60	-1.69
412.00	-1.78
412.40	-1.89
412.80	-2.00
413.20	-2.13
413.60	-2.28
414.00	-2.44
414.40	-2.61
414.80	-2.81
415.20	-3.03
415.60	-3.28
416.00	-3.57
416.40	-3.89
416.80	-4.25
417.20	-4.69
417.60	-5.17
418.00	-5.71
418.40	-6.33
418.80	-7.03
419.20	-7.83
419.60	-8.73
420.00	-9.67
420.40	-10.63
420.80	-11.47
421.20	-12.05
421.60	-12.17
422.00	-11.78
422.40	-11.01
422.80	-10.07
423.20	-9.11
423.60	-8.18
424.00	-7.34
424.40	-6.58
424.80	-5.93
425.20	-5.36
425.60	-4.83

f (MHz)	Return Loss (dB)
426.00	-4.39
426.40	-4.02
426.80	-3.66
427.20	-3.37
427.60	-3.11
428.00	-2.87
428.40	-2.66
428.80	-2.49
429.20	-2.31
429.60	-2.18
430.00	-2.06
430.40	-1.94
430.80	-1.84
431.20	-1.73
431.60	-1.65
432.00	-1.57
432.40	-1.50
432.80	-1.43
433.20	-1.38
433.60	-1.33
434.00	-1.28
434.40	-1.21
434.80	-1.18
435.20	-1.14
435.60	-1.10
436.00	-1.08
436.40	-1.04
436.80	-1.03
437.20	-1.00
437.60	-0.98
438.00	-0.94
438.40	-0.95
438.80	-0.89
439.20	-0.87
439.60	-0.86
440.00	-0.86
440.40	-0.84
440.80	-0.84

f (MHz)	Return Loss (dB)
441.20	-0.82
441.60	-0.79
442.00	-0.78
442.40	-0.78
442.80	-0.77
443.20	-0.76
443.60	-0.75
444.00	-0.73
444.40	-0.72
444.80	-0.72
445.20	-0.73
445.60	-0.69
446.00	-0.70
446.40	-0.70
446.80	-0.70
447.20	-0.68
447.60	-0.67
448.00	-0.66
448.40	-0.69
448.80	-0.65
449.20	-0.65
449.60	-0.65
450.00	-0.65
450.40	-0.63
450.80	-0.66
451.20	-0.64
451.60	-0.64
452.00	-0.62
452.40	-0.61
452.80	-0.61
453.20	-0.61
453.60	-0.61
454.00	-0.60
454.40	-0.61
454.80	-0.61
455.20	-0.59
455.60	-0.59
456.00	-0.59

f (MHz)	Return Loss (dB)
456.40	-0.60
456.80	-0.59
457.20	-0.59
457.60	-0.58
458.00	-0.58
458.40	-0.58
458.80	-0.57
459.20	-0.57
459.60	-0.56
460.00	-0.57
460.40	-0.56
460.80	-0.58
461.20	-0.56
461.60	-0.57
462.00	-0.55
462.40	-0.56
462.80	-0.56
463.20	-0.55
463.60	-0.55
464.00	-0.55
464.40	-0.54
464.80	-0.54
465.20	-0.56
465.60	-0.53
466.00	-0.55
466.40	-0.55
466.80	-0.55
467.20	-0.55
467.60	-0.53
468.00	-0.55
468.40	-0.54
468.80	-0.53
469.20	-0.53
469.60	-0.52
470.00	-0.53
470.40	-0.52
470.80	-0.54
471.20	-0.54

f (MHz)	Return Loss (dB)
471.60	-0.53
472.00	-0.53
472.40	-0.52
472.80	-0.53
473.20	-0.53
473.60	-0.53
474.00	-0.53
474.40	-0.53
474.80	-0.54
475.20	-0.52
475.60	-0.53
476.00	-0.52
476.40	-0.51
476.80	-0.53
477.20	-0.52
477.60	-0.52
478.00	-0.52
478.40	-0.51
478.80	-0.52
479.20	-0.52
479.60	-0.52
480.00	-0.51
480.40	-0.51
480.80	-0.51
481.20	-0.51
481.60	-0.51
482.00	-0.50
482.40	-0.51
482.80	-0.51
483.20	-0.49
483.60	-0.50
484.00	-0.51
484.40	-0.50
484.80	-0.50
485.20	-0.52
485.60	-0.49
486.00	-0.52
486.40	-0.51

f (MHz)	Return Loss (dB)
486.80	-0.50
487.20	-0.50
487.60	-0.51
488.00	-0.52
488.40	-0.50
488.80	-0.52
489.20	-0.51
489.60	-0.51
490.00	-0.49
490.40	-0.50
490.80	-0.49
491.20	-0.50
491.60	-0.48
492.00	-0.50
492.40	-0.48
492.80	-0.49
493.20	-0.50
493.60	-0.49
494.00	-0.50
494.40	-0.49
494.80	-0.50
495.20	-0.49
495.60	-0.50
496.00	-0.50
496.40	-0.50
496.80	-0.49
497.20	-0.51
497.60	-0.50
498.00	-0.49
498.40	-0.51
498.80	-0.50
499.20	-0.48
499.60	-0.52
500.00	-0.50

Appendix 6 - Matlab code for radiation pattern plot

```
data =a;
x_offset=-0.1;
[maximum,max_pos]=max(a(:,1));
[minimum,min_pos]=min(a(:,1));

max_pos=max_pos*(360/180);
min_pos=min_pos*(360/180);

figure (1)
Dirplot(a(:,2),a(:,1),[-25 -65 4]);
title('Radiation Pattern Case D Vertical','FontSize',16)
```

Appendix 7 – Dataset of gain and radiation pattern measurement on case A

Horizontal E-field co-polarization

Phase (deg)	Magnitude (dB)	Phase (deg)	Magnitude (dB)	Phase (deg)	Magnitude (dB)	Phase (deg)	Magnitude (dB)
0.00	-53.64	32.07	-54.27	64.14	-54.47	96.21	-75.97
0.80	-53.63	32.87	-54.30	64.94	-54.55	97.02	-72.69
1.60	-53.76	33.68	-54.41	65.75	-55.11	97.82	-70.03
2.41	-53.49	34.48	-54.53	66.55	-55.36	98.62	-69.23
3.21	-54.12	35.28	-54.05	67.35	-54.94	99.42	-70.00
4.01	-53.48	36.08	-54.30	68.15	-54.99	100.22	-67.97
4.81	-53.51	36.88	-53.92	68.95	-55.75	101.02	-65.38
5.61	-53.53	37.68	-54.14	69.76	-55.57	101.83	-64.79
6.41	-53.65	38.49	-54.30	70.56	-56.03	102.63	-63.92
7.22	-53.67	39.29	-54.17	71.36	-56.21	103.43	-63.78
8.02	-53.65	40.09	-54.20	72.16	-56.53	104.23	-62.73
8.82	-53.82	40.89	-54.09	72.96	-56.23	105.03	-62.45
9.62	-53.78	41.69	-54.27	73.76	-57.06	105.84	-61.71
10.42	-53.96	42.49	-54.07	74.57	-56.92	106.64	-61.81
11.23	-53.87	43.30	-53.88	75.37	-57.16	107.44	-60.17
12.03	-53.85	44.10	-54.37	76.17	-57.78	108.24	-59.93
12.83	-54.31	44.90	-53.56	76.97	-57.08	109.04	-59.91
13.63	-54.07	45.70	-53.88	77.77	-58.23	109.84	-59.45
14.43	-54.58	46.50	-54.09	78.58	-58.19	110.65	-59.02
15.23	-54.06	47.31	-54.02	79.38	-58.81	111.45	-58.45
16.04	-54.17	48.11	-53.70	80.18	-59.17	112.25	-57.73
16.84	-54.03	48.91	-53.99	80.98	-59.67	113.05	-57.60
17.64	-54.42	49.71	-54.05	81.78	-59.85	113.85	-57.56
18.44	-53.76	50.51	-53.94	82.58	-59.99	114.66	-57.18
19.24	-54.39	51.31	-54.29	83.39	-60.16	115.46	-56.60
20.05	-54.15	52.12	-54.10	84.19	-61.97	116.26	-56.62
20.85	-54.03	52.92	-54.47	84.99	-62.55	117.06	-56.63
21.65	-54.31	53.72	-54.08	85.79	-63.15	117.86	-56.05
22.45	-54.51	54.52	-53.94	86.59	-62.64	118.66	-56.09
23.25	-54.48	55.32	-54.19	87.39	-65.63	119.47	-55.73
24.05	-54.36	56.13	-54.19	88.20	-64.07	120.27	-55.45
24.86	-54.46	56.93	-53.98	89.00	-66.20	121.07	-55.39
25.66	-54.20	57.73	-53.99	89.80	-67.28	121.87	-55.10
26.46	-54.08	58.53	-53.96	90.60	-69.07	122.67	-55.02
27.26	-54.39	59.33	-54.41	91.40	-69.79	123.47	-54.78
28.06	-54.51	60.13	-54.46	92.21	-72.25	124.28	-54.48
28.86	-54.64	60.94	-54.37	93.01	-72.89	125.08	-54.76
29.67	-54.20	61.74	-54.48	93.81	-72.87	125.88	-54.49
30.47	-54.38	62.54	-54.58	94.61	-75.06	126.68	-54.41
31.27	-54.23	63.34	-54.29	95.41	-75.09	127.48	-54.33

Phase (deg)	Magnitude (dB)
128.29	-54.20
129.09	-54.05
129.89	-54.41
130.69	-53.99
131.49	-53.85
132.29	-53.88
133.10	-53.57
133.90	-53.70
134.70	-53.85
135.50	-53.63
136.30	-53.82
137.11	-53.77
137.91	-53.35
138.71	-53.28
139.51	-53.65
140.31	-53.60
141.11	-53.25
141.92	-53.50
142.72	-53.43
143.52	-53.46
144.32	-53.41
145.12	-53.43
145.92	-53.52
146.73	-53.39
147.53	-53.47
148.33	-53.64
149.13	-53.43
149.93	-53.37
150.74	-53.06
151.54	-53.60
152.34	-53.32
153.14	-53.51
153.94	-53.52
154.74	-53.75
155.55	-53.38
156.35	-53.36
157.15	-53.42
157.95	-53.53
158.75	-53.57
159.56	-53.55

Phase (deg)	Magnitude (dB)
160.36	-53.52
161.16	-53.41
161.96	-53.22
162.76	-53.51
163.56	-53.34
164.37	-53.52
165.17	-53.72
165.97	-53.01
166.77	-53.27
167.57	-53.52
168.37	-53.45
169.18	-53.57
169.98	-53.37
170.78	-53.44
171.58	-53.42
172.38	-53.40
173.19	-53.68
173.99	-53.42
174.79	-53.32
175.59	-53.35
176.39	-53.16
177.19	-53.19
178.00	-53.45
178.80	-53.37
179.60	-53.46
180.40	-53.62
181.20	-53.23
182.00	-53.51
182.81	-53.66
183.61	-53.16
184.41	-53.32
185.21	-53.42
186.01	-53.39
186.82	-53.59
187.62	-53.69
188.42	-53.69
189.22	-53.51
190.02	-53.49
190.82	-53.65
191.63	-53.51

Phase (deg)	Magnitude (dB)
192.43	-53.62
193.23	-53.63
194.03	-53.84
194.83	-53.85
195.64	-54.05
196.44	-54.23
197.24	-54.14
198.04	-54.03
198.84	-54.17
199.64	-54.04
200.45	-53.74
201.25	-54.27
202.05	-53.95
202.85	-54.46
203.65	-54.35
204.45	-54.27
205.26	-54.63
206.06	-54.55
206.86	-54.37
207.66	-54.49
208.46	-54.44
209.27	-54.94
210.07	-54.78
210.87	-54.80
211.67	-55.16
212.47	-54.64
213.27	-55.58
214.08	-55.53
214.88	-55.14
215.68	-55.11
216.48	-55.28
217.28	-55.44
218.09	-55.56
218.89	-56.01
219.69	-55.74
220.49	-55.98
221.29	-56.22
222.09	-56.15
222.90	-56.48
223.70	-56.49

Phase (deg)	Magnitude (dB)
224.50	-56.45
225.30	-56.46
226.10	-56.47
226.90	-56.64
227.71	-56.68
228.51	-56.94
229.31	-57.04
230.11	-57.50
230.91	-57.61
231.72	-57.75
232.52	-57.70
233.32	-57.49
234.12	-57.79
234.92	-58.52
235.72	-58.53
236.53	-58.29
237.33	-58.33
238.13	-58.09
238.93	-58.94
239.73	-59.11
240.54	-58.91
241.34	-59.02
242.14	-59.11
242.94	-58.56
243.74	-59.91
244.54	-59.64
245.35	-59.28
246.15	-59.34
246.95	-59.58
247.75	-59.71
248.55	-59.66
249.35	-59.55
250.16	-59.97
250.96	-59.56
251.76	-60.04
252.56	-60.16
253.36	-60.36
254.17	-59.91
254.97	-60.37
255.77	-60.47

Phase (deg)	Magnitude (dB)
256.57	-60.15
257.37	-59.83
258.17	-60.15
258.98	-59.99
259.78	-59.96
260.58	-60.70
261.38	-60.58
262.18	-60.17
262.98	-60.65
263.79	-61.19
264.59	-60.26
265.39	-60.27
266.19	-60.31
266.99	-60.88
267.80	-61.18
268.60	-61.54
269.40	-61.54
270.20	-61.83
271.00	-61.36
271.80	-61.59
272.61	-61.32
273.41	-62.64
274.21	-62.74
275.01	-61.98
275.81	-62.75
276.62	-63.59
277.42	-63.98
278.22	-63.64
279.02	-63.57
279.82	-64.08
280.62	-63.81
281.43	-64.92
282.23	-64.92
283.03	-64.83
283.83	-67.39
284.63	-66.86
285.43	-66.84
286.24	-66.17
287.04	-67.63
287.84	-67.40

Phase (deg)	Magnitude (dB)
288.64	-69.24
289.44	-68.00
290.25	-67.81
291.05	-73.08
291.85	-75.12
292.65	-73.29
293.45	-75.17
294.25	-76.47
295.06	-72.78
295.86	-77.04
296.66	-75.78
297.46	-72.10
298.26	-75.45
299.07	-72.02
299.87	-68.21
300.67	-69.21
301.47	-67.91
302.27	-67.75
303.07	-67.05
303.88	-67.06
304.68	-64.49
305.48	-64.93
306.28	-64.16
307.08	-64.09
307.88	-63.22
308.69	-63.29
309.49	-61.98
310.29	-61.73
311.09	-62.13
311.89	-60.95
312.70	-60.95
313.50	-60.21
314.30	-60.95
315.10	-60.39
315.90	-59.42
316.70	-59.07
317.51	-58.93
318.31	-58.56
319.11	-58.48
319.91	-58.04

Phase (deg)	Magnitude (dB)
320.71	-58.16
321.51	-57.20
322.32	-57.14
323.12	-56.90
323.92	-57.22
324.72	-56.94
325.52	-56.15
326.33	-56.15
327.13	-56.66
327.93	-56.27
328.73	-56.02
329.53	-55.96
330.33	-55.71
331.14	-55.37
331.94	-55.76
332.74	-55.82
333.54	-55.18
334.34	-54.63
335.15	-54.76
335.95	-54.64
336.75	-54.53
337.55	-54.82
338.35	-54.49
339.15	-54.64
339.96	-54.85
340.76	-54.40
341.56	-54.30
342.36	-54.19
343.16	-54.28
343.96	-54.00
344.77	-53.79
345.57	-54.19
346.37	-53.51
347.17	-54.20
347.97	-53.87
348.78	-53.71
349.58	-53.50
350.38	-53.77
351.18	-53.55
351.98	-53.60

Phase (deg)	Magnitude (dB)
352.78	-53.86
353.59	-53.37
354.39	-53.84
355.19	-53.68
355.99	-53.47
356.79	-53.78
357.60	-53.43
358.40	-53.77
359.20	-53.49
360.00	-53.59

Vertical E-field co-polarization

Phase (deg)	Magnitude (dB)
0.00	-54.79
0.80	-54.53
1.60	-54.98
2.41	-54.85
3.21	-54.57
4.01	-54.59
4.81	-54.37
5.61	-54.68
6.41	-54.03
7.22	-54.24
8.02	-54.05
8.82	-54.18
9.62	-54.33
10.42	-54.09
11.23	-53.72
12.03	-53.81
12.83	-53.98
13.63	-53.75
14.43	-53.84
15.23	-53.88
16.04	-53.95
16.84	-53.73
17.64	-53.75
18.44	-53.71
19.24	-53.63
20.05	-53.70
20.85	-53.57
21.65	-53.60
22.45	-53.86
23.25	-53.31
24.05	-53.69
24.86	-53.78
25.66	-53.69
26.46	-53.62
27.26	-53.90
28.06	-54.04
28.86	-54.05
29.67	-54.08
30.47	-53.96
31.27	-53.79

Phase (deg)	Magnitude (dB)
32.07	-54.02
32.87	-54.05
33.68	-54.39
34.48	-53.75
35.28	-54.30
36.08	-54.19
36.88	-54.10
37.68	-53.78
38.49	-54.39
39.29	-54.66
40.09	-54.11
40.89	-54.43
41.69	-54.40
42.49	-54.59
43.30	-54.81
44.10	-54.71
44.90	-54.84
45.70	-54.90
46.50	-54.97
47.31	-55.29
48.11	-54.78
48.91	-54.74
49.71	-54.91
50.51	-54.99
51.31	-54.92
52.12	-54.78
52.92	-55.14
53.72	-55.14
54.52	-55.41
55.32	-55.03
56.13	-55.10
56.93	-55.15
57.73	-55.10
58.53	-54.63
59.33	-54.74
60.13	-55.31
60.94	-55.10
61.74	-55.10
62.54	-54.78
63.34	-54.81

Phase (deg)	Magnitude (dB)
64.14	-54.64
64.94	-54.77
65.75	-54.66
66.55	-54.28
67.35	-54.19
68.15	-54.49
68.95	-54.32
69.76	-54.25
70.56	-53.86
71.36	-53.83
72.16	-53.79
72.96	-53.79
73.76	-53.71
74.57	-53.76
75.37	-53.73
76.17	-53.42
76.97	-53.56
77.77	-53.16
78.58	-52.87
79.38	-52.96
80.18	-52.73
80.98	-52.74
81.78	-52.73
82.58	-52.64
83.39	-52.59
84.19	-52.46
84.99	-52.46
85.79	-52.39
86.59	-52.22
87.39	-51.99
88.20	-52.18
89.00	-52.20
89.80	-52.20
90.60	-51.70
91.40	-51.84
92.21	-51.92
93.01	-51.83
93.81	-51.85
94.61	-51.75
95.41	-51.51

Phase (deg)	Magnitude (dB)
96.21	-51.70
97.02	-51.70
97.82	-51.70
98.62	-51.53
99.42	-51.68
100.22	-51.84
101.02	-51.79
101.83	-51.92
102.63	-51.56
103.43	-51.88
104.23	-51.81
105.03	-51.84
105.84	-51.83
106.64	-52.03
107.44	-52.24
108.24	-51.99
109.04	-52.30
109.84	-52.11
110.65	-52.28
111.45	-52.50
112.25	-52.43
113.05	-52.44
113.85	-52.57
114.66	-52.74
115.46	-52.79
116.26	-53.34
117.06	-53.16
117.86	-53.39
118.66	-53.06
119.47	-53.38
120.27	-53.57
121.07	-53.60
121.87	-53.82
122.67	-54.09
123.47	-54.23
124.28	-54.39
125.08	-54.21
125.88	-54.79
126.68	-54.96
127.48	-54.71

Phase (deg)	Magnitude (dB)
128.29	-54.96
129.09	-54.93
129.89	-55.06
130.69	-55.39
131.49	-55.75
132.29	-55.62
133.10	-55.63
133.90	-55.86
134.70	-56.09
135.50	-56.02
136.30	-55.88
137.11	-56.20
137.91	-56.14
138.71	-55.73
139.51	-56.23
140.31	-56.25
141.11	-55.49
141.92	-55.52
142.72	-55.34
143.52	-55.77
144.32	-55.49
145.12	-55.76
145.92	-55.29
146.73	-55.12
147.53	-54.69
148.33	-55.18
149.13	-55.07
149.93	-55.25
150.74	-54.85
151.54	-54.74
152.34	-54.50
153.14	-53.96
153.94	-54.50
154.74	-53.98
155.55	-54.01
156.35	-54.02
157.15	-53.95
157.95	-53.57
158.75	-53.78
159.56	-53.18

Phase (deg)	Magnitude (dB)
160.36	-53.06
161.16	-52.92
161.96	-53.14
162.76	-52.70
163.56	-52.95
164.37	-52.60
165.17	-52.23
165.97	-52.45
166.77	-52.24
167.57	-52.11
168.37	-51.99
169.18	-52.09
169.98	-51.93
170.78	-51.63
171.58	-51.64
172.38	-51.54
173.19	-51.47
173.99	-51.32
174.79	-51.59
175.59	-51.08
176.39	-51.33
177.19	-51.03
178.00	-50.72
178.80	-50.70
179.60	-50.65
180.40	-50.64
181.20	-50.66
182.00	-50.65
182.81	-50.54
183.61	-50.70
184.41	-50.45
185.21	-50.73
186.01	-50.56
186.82	-50.20
187.62	-50.21
188.42	-50.25
189.22	-50.10
190.02	-50.10
190.82	-50.03
191.63	-50.14

Phase (deg)	Magnitude (dB)
192.43	-50.16
193.23	-50.13
194.03	-50.13
194.83	-50.02
195.64	-50.19
196.44	-49.75
197.24	-50.14
198.04	-49.88
198.84	-49.88
199.64	-50.12
200.45	-49.53
201.25	-49.80
202.05	-49.85
202.85	-49.94
203.65	-50.03
204.45	-49.89
205.26	-50.07
206.06	-49.71
206.86	-49.93
207.66	-50.12
208.46	-49.94
209.27	-49.92
210.07	-49.96
210.87	-50.17
211.67	-50.01
212.47	-50.26
213.27	-50.27
214.08	-50.31
214.88	-50.24
215.68	-50.44
216.48	-50.25
217.28	-50.35
218.09	-50.39
218.89	-50.45
219.69	-50.50
220.49	-50.28
221.29	-50.53
222.09	-50.71
222.90	-50.38
223.70	-50.72

Phase (deg)	Magnitude (dB)
224.50	-50.66
225.30	-50.63
226.10	-50.73
226.90	-50.74
227.71	-51.05
228.51	-51.11
229.31	-50.91
230.11	-51.13
230.91	-51.20
231.72	-51.23
232.52	-51.25
233.32	-51.57
234.12	-51.02
234.92	-51.36
235.72	-51.18
236.53	-51.53
237.33	-51.57
238.13	-51.57
238.93	-51.67
239.73	-51.78
240.54	-51.70
241.34	-51.83
242.14	-51.77
242.94	-52.04
243.74	-52.14
244.54	-52.17
245.35	-52.18
246.15	-52.13
246.95	-52.34
247.75	-52.35
248.55	-52.62
249.35	-52.48
250.16	-52.60
250.96	-52.80
251.76	-52.85
252.56	-52.63
253.36	-52.88
254.17	-52.78
254.97	-52.74
255.77	-52.94

Phase (deg)	Magnitude (dB)
256.57	-52.86
257.37	-53.21
258.17	-53.04
258.98	-52.87
259.78	-53.53
260.58	-53.38
261.38	-53.65
262.18	-53.69
262.98	-53.84
263.79	-53.87
264.59	-53.66
265.39	-53.79
266.19	-53.91
266.99	-53.65
267.80	-54.29
268.60	-54.30
269.40	-54.18
270.20	-54.31
271.00	-54.67
271.80	-54.54
272.61	-54.53
273.41	-54.74
274.21	-54.80
275.01	-54.83
275.81	-54.83
276.62	-54.94
277.42	-55.33
278.22	-55.15
279.02	-55.11
279.82	-55.49
280.62	-55.81
281.43	-55.66
282.23	-55.83
283.03	-56.48
283.83	-56.08
284.63	-56.21
285.43	-56.57
286.24	-57.22
287.04	-56.58
287.84	-56.93

Phase (deg)	Magnitude (dB)
288.64	-57.10
289.44	-57.60
290.25	-57.57
291.05	-57.51
291.85	-58.25
292.65	-57.95
293.45	-57.83
294.25	-58.38
295.06	-58.97
295.86	-58.72
296.66	-59.62
297.46	-59.88
298.26	-60.57
299.07	-60.38
299.87	-61.00
300.67	-60.42
301.47	-60.82
302.27	-61.98
303.07	-61.31
303.88	-62.03
304.68	-62.11
305.48	-63.21
306.28	-63.94
307.08	-63.61
307.88	-63.93
308.69	-64.92
309.49	-65.81
310.29	-65.35
311.09	-65.26
311.89	-68.27
312.70	-68.58
313.50	-71.42
314.30	-70.00
315.10	-70.67
315.90	-70.40
316.70	-74.46
317.51	-78.24
318.31	-73.42
319.11	-74.66
319.91	-71.16

Phase (deg)	Magnitude (dB)
320.71	-70.65
321.51	-75.23
322.32	-70.94
323.12	-71.24
323.92	-69.06
324.72	-68.77
325.52	-68.52
326.33	-67.37
327.13	-65.14
327.93	-65.80
328.73	-66.38
329.53	-63.58
330.33	-64.77
331.14	-63.17
331.94	-62.85
332.74	-62.41
333.54	-62.22
334.34	-62.34
335.15	-62.07
335.95	-61.02
336.75	-61.14
337.55	-60.40
338.35	-60.50
339.15	-59.75
339.96	-58.97
340.76	-59.37
341.56	-58.93
342.36	-57.57
343.16	-58.34
343.96	-58.39
344.77	-57.30
345.57	-57.50
346.37	-57.41
347.17	-57.20
347.97	-57.29
348.78	-57.09
349.58	-56.56
350.38	-56.09
351.18	-56.56
351.98	-55.93

Phase (deg)	Magnitude (dB)
352.78	-56.27
353.59	-56.08
354.39	-56.20
355.19	-55.39
355.99	-55.73
356.79	-55.32
357.60	-55.07
358.40	-55.07
359.20	-55.04
360.00	-55.00

Appendix 8 - Dataset of gain and radiation pattern measurement on case B

Horizontal E-field co-polarization

Phase (deg)	Magnitude (dB)	Phase (deg)	Magnitude (dB)	Phase (deg)	Magnitude (dB)	Phase (deg)	Magnitude (dB)
0.00	-55.89	32.07	-60.44	64.14	-63.26	96.21	-63.55
0.80	-55.50	32.87	-60.31	64.94	-68.23	97.02	-61.54
1.60	-55.80	33.68	-58.74	65.75	-66.36	97.82	-62.02
2.41	-56.13	34.48	-58.94	66.55	-64.43	98.62	-62.97
3.21	-56.70	35.28	-60.63	67.35	-66.98	99.42	-60.82
4.01	-56.59	36.08	-60.02	68.15	-68.18	100.22	-60.83
4.81	-56.09	36.88	-58.91	68.95	-68.98	101.02	-61.84
5.61	-56.39	37.68	-59.99	69.76	-69.10	101.83	-61.67
6.41	-56.05	38.49	-60.04	70.56	-68.43	102.63	-60.71
7.22	-56.73	39.29	-60.33	71.36	-71.00	103.43	-60.65
8.02	-56.68	40.09	-60.53	72.16	-67.12	104.23	-60.02
8.82	-56.75	40.89	-60.10	72.96	-70.83	105.03	-60.11
9.62	-56.45	41.69	-60.12	73.76	-73.73	105.84	-58.04
10.42	-57.26	42.49	-60.88	74.57	-70.80	106.64	-58.81
11.23	-57.20	43.30	-60.15	75.37	-72.79	107.44	-59.28
12.03	-56.71	44.10	-60.21	76.17	-70.18	108.24	-59.22
12.83	-57.63	44.90	-61.83	76.97	-74.69	109.04	-59.01
13.63	-57.89	45.70	-61.55	77.77	-74.51	109.84	-58.28
14.43	-57.26	46.50	-60.65	78.58	-75.27	110.65	-59.09
15.23	-58.51	47.31	-61.29	79.38	-73.64	111.45	-58.19
16.04	-56.96	48.11	-60.65	80.18	-73.76	112.25	-57.99
16.84	-57.26	48.91	-61.46	80.98	-73.44	113.05	-58.01
17.64	-56.95	49.71	-62.44	81.78	-73.59	113.85	-57.59
18.44	-58.04	50.51	-61.93	82.58	-68.16	114.66	-56.80
19.24	-57.96	51.31	-62.81	83.39	-73.35	115.46	-57.29
20.05	-57.07	52.12	-61.78	84.19	-73.22	116.26	-57.70
20.85	-57.76	52.92	-61.36	84.99	-74.33	117.06	-58.02
21.65	-58.70	53.72	-62.43	85.79	-68.88	117.86	-56.88
22.45	-57.43	54.52	-64.23	86.59	-67.17	118.66	-57.15
23.25	-58.89	55.32	-62.07	87.39	-66.18	119.47	-57.56
24.05	-58.73	56.13	-63.84	88.20	-69.23	120.27	-56.65
24.86	-58.36	56.93	-62.38	89.00	-64.94	121.07	-56.70
25.66	-58.99	57.73	-61.78	89.80	-64.22	121.87	-57.68
26.46	-58.82	58.53	-64.12	90.60	-65.33	122.67	-57.19
27.26	-59.49	59.33	-64.64	91.40	-67.02	123.47	-57.07
28.06	-59.00	60.13	-64.08	92.21	-65.93	124.28	-57.17
28.86	-58.93	60.94	-63.72	93.01	-63.88	125.08	-56.86
29.67	-59.42	61.74	-65.86	93.81	-64.66	125.88	-56.88
30.47	-58.86	62.54	-66.17	94.61	-63.23	126.68	-56.83
31.27	-59.73	63.34	-64.45	95.41	-64.04	127.48	-56.89

Phase (deg)	Magnitude (dB)
128.29	-57.18
129.09	-57.11
129.89	-56.78
130.69	-56.04
131.49	-56.29
132.29	-56.93
133.10	-56.37
133.90	-56.17
134.70	-56.69
135.50	-56.39
136.30	-55.91
137.11	-56.27
137.91	-55.80
138.71	-56.44
139.51	-55.68
140.31	-56.40
141.11	-56.09
141.92	-55.85
142.72	-56.57
143.52	-55.80
144.32	-55.98
145.12	-56.68
145.92	-56.44
146.73	-55.72
147.53	-56.42
148.33	-56.04
149.13	-55.84
149.93	-56.24
150.74	-56.36
151.54	-56.00
152.34	-55.48
153.14	-55.31
153.94	-56.31
154.74	-56.00
155.55	-55.53
156.35	-55.59
157.15	-55.71
157.95	-56.47
158.75	-55.44
159.56	-56.06

Phase (deg)	Magnitude (dB)
160.36	-55.69
161.16	-55.73
161.96	-55.89
162.76	-55.86
163.56	-56.15
164.37	-55.90
165.17	-56.50
165.97	-55.88
166.77	-55.61
167.57	-55.87
168.37	-55.97
169.18	-55.82
169.98	-56.17
170.78	-56.43
171.58	-55.92
172.38	-55.77
173.19	-55.58
173.99	-55.99
174.79	-54.96
175.59	-55.65
176.39	-56.25
177.19	-55.65
178.00	-56.24
178.80	-55.53
179.60	-56.23
180.40	-56.03
181.20	-55.67
182.00	-55.52
182.81	-56.43
183.61	-55.57
184.41	-55.97
185.21	-55.24
186.01	-55.40
186.82	-55.63
187.62	-55.78
188.42	-56.85
189.22	-56.05
190.02	-56.53
190.82	-55.77
191.63	-55.95

Phase (deg)	Magnitude (dB)
192.43	-55.50
193.23	-55.74
194.03	-55.97
194.83	-55.69
195.64	-56.27
196.44	-55.63
197.24	-55.72
198.04	-56.46
198.84	-56.12
199.64	-56.27
200.45	-56.39
201.25	-56.33
202.05	-56.82
202.85	-56.69
203.65	-56.74
204.45	-56.65
205.26	-56.50
206.06	-56.28
206.86	-56.66
207.66	-56.93
208.46	-56.68
209.27	-57.19
210.07	-56.54
210.87	-57.20
211.67	-57.24
212.47	-56.71
213.27	-57.23
214.08	-57.31
214.88	-57.12
215.68	-58.13
216.48	-57.43
217.28	-57.40
218.09	-58.04
218.89	-57.14
219.69	-57.49
220.49	-57.68
221.29	-57.84
222.09	-57.82
222.90	-57.91
223.70	-58.26

Phase (deg)	Magnitude (dB)
224.50	-57.86
225.30	-57.20
226.10	-57.30
226.90	-58.41
227.71	-58.14
228.51	-57.64
229.31	-58.22
230.11	-58.47
230.91	-57.66
231.72	-58.99
232.52	-58.80
233.32	-58.19
234.12	-57.67
234.92	-58.97
235.72	-58.46
236.53	-58.79
237.33	-58.47
238.13	-57.56
238.93	-58.70
239.73	-58.56
240.54	-57.71
241.34	-58.45
242.14	-58.30
242.94	-58.77
243.74	-59.07
244.54	-58.68
245.35	-59.48
246.15	-57.69
246.95	-59.05
247.75	-58.43
248.55	-58.06
249.35	-58.28
250.16	-58.41
250.96	-58.26
251.76	-58.70
252.56	-58.79
253.36	-59.20
254.17	-59.44
254.97	-58.22
255.77	-59.03

Phase (deg)	Magnitude (dB)
256.57	-60.24
257.37	-59.79
258.17	-59.36
258.98	-59.31
259.78	-59.97
260.58	-59.82
261.38	-59.56
262.18	-61.02
262.98	-60.02
263.79	-61.08
264.59	-59.90
265.39	-59.53
266.19	-61.16
266.99	-60.76
267.80	-60.79
268.60	-60.06
269.40	-61.45
270.20	-61.45
271.00	-62.50
271.80	-62.64
272.61	-63.38
273.41	-62.02
274.21	-62.88
275.01	-61.63
275.81	-61.21
276.62	-62.00
277.42	-63.22
278.22	-64.79
279.02	-64.23
279.82	-64.94
280.62	-64.94
281.43	-65.97
282.23	-65.79
283.03	-65.13
283.83	-63.16
284.63	-64.95
285.43	-66.70
286.24	-65.81
287.04	-66.34
287.84	-67.81

Phase (deg)	Magnitude (dB)
288.64	-66.52
289.44	-66.09
290.25	-69.89
291.05	-69.26
291.85	-66.95
292.65	-67.16
293.45	-67.11
294.25	-67.17
295.06	-66.97
295.86	-65.76
296.66	-64.57
297.46	-64.64
298.26	-65.52
299.07	-66.33
299.87	-65.18
300.67	-64.96
301.47	-65.10
302.27	-65.45
303.07	-64.12
303.88	-64.58
304.68	-64.28
305.48	-63.01
306.28	-61.88
307.08	-61.97
307.88	-62.18
308.69	-62.59
309.49	-62.25
310.29	-60.79
311.09	-61.11
311.89	-60.25
312.70	-61.08
313.50	-60.20
314.30	-59.44
315.10	-58.84
315.90	-60.01
316.70	-59.05
317.51	-58.70
318.31	-59.02
319.11	-58.23
319.91	-58.49

Phase (deg)	Magnitude (dB)
320.71	-58.75
321.51	-57.32
322.32	-57.42
323.12	-57.91
323.92	-56.69
324.72	-57.37
325.52	-57.38
326.33	-57.86
327.13	-57.17
327.93	-57.65
328.73	-57.45
329.53	-58.15
330.33	-56.62
331.14	-57.09
331.94	-57.02
332.74	-56.56
333.54	-56.76
334.34	-56.37
335.15	-56.56
335.95	-56.57
336.75	-57.16
337.55	-56.77
338.35	-56.10
339.15	-56.58
339.96	-55.53
340.76	-55.72
341.56	-55.54
342.36	-56.03
343.16	-55.80
343.96	-56.29
344.77	-56.20
345.57	-56.46
346.37	-56.31
347.17	-57.23
347.97	-55.81
348.78	-55.76
349.58	-56.07
350.38	-55.95
351.18	-56.14
351.98	-55.98

Phase (deg)	Magnitude (dB)
352.78	-55.52
353.59	-56.23
354.39	-55.39
355.19	-56.02
355.99	-56.00
356.79	-56.04
357.60	-56.14
358.40	-56.17
359.20	-56.43
360.00	-56.07

Vertical E-field co-polarization

Phase (deg)	Magnitude (dB)
0.00	-49.22
0.80	-49.31
1.60	-49.39
2.41	-49.58
3.21	-49.33
4.01	-49.36
4.81	-49.69
5.61	-49.20
6.41	-49.48
7.22	-49.49
8.02	-49.62
8.82	-49.58
9.62	-49.62
10.42	-49.76
11.23	-49.52
12.03	-49.49
12.83	-49.43
13.63	-49.79
14.43	-49.60
15.23	-49.39
16.04	-49.46
16.84	-49.58
17.64	-49.95
18.44	-49.78
19.24	-49.68
20.05	-49.54
20.85	-49.58
21.65	-50.08
22.45	-49.61
23.25	-49.66
24.05	-49.88
24.86	-50.09
25.66	-49.44
26.46	-49.32
27.26	-49.42
28.06	-49.54
28.86	-49.53
29.67	-49.22
30.47	-49.42
31.27	-49.78

Phase (deg)	Magnitude (dB)
32.07	-49.49
32.87	-49.22
33.68	-49.46
34.48	-49.21
35.28	-49.27
36.08	-48.88
36.88	-49.22
37.68	-49.43
38.49	-49.08
39.29	-49.37
40.09	-48.79
40.89	-49.23
41.69	-48.86
42.49	-48.84
43.30	-49.13
44.10	-49.04
44.90	-48.93
45.70	-48.75
46.50	-48.91
47.31	-48.69
48.11	-48.92
48.91	-48.45
49.71	-48.79
50.51	-48.84
51.31	-48.68
52.12	-48.53
52.92	-48.81
53.72	-48.49
54.52	-48.42
55.32	-48.47
56.13	-48.41
56.93	-48.62
57.73	-48.33
58.53	-48.46
59.33	-48.77
60.13	-48.25
60.94	-48.26
61.74	-48.36
62.54	-48.04
63.34	-48.11

Phase (deg)	Magnitude (dB)
64.14	-48.24
64.94	-48.28
65.75	-48.09
66.55	-47.91
67.35	-47.96
68.15	-47.84
68.95	-47.80
69.76	-47.86
70.56	-47.99
71.36	-47.90
72.16	-47.87
72.96	-47.68
73.76	-47.71
74.57	-47.72
75.37	-47.71
76.17	-47.64
76.97	-47.60
77.77	-47.73
78.58	-47.61
79.38	-47.38
80.18	-47.73
80.98	-47.51
81.78	-47.58
82.58	-47.50
83.39	-47.79
84.19	-47.38
84.99	-47.70
85.79	-47.33
86.59	-47.42
87.39	-47.48
88.20	-47.40
89.00	-47.19
89.80	-47.51
90.60	-47.46
91.40	-47.36
92.21	-47.30
93.01	-47.51
93.81	-47.24
94.61	-47.40
95.41	-47.48

Phase (deg)	Magnitude (dB)
96.21	-47.25
97.02	-47.34
97.82	-47.43
98.62	-47.28
99.42	-47.21
100.22	-47.30
101.02	-47.32
101.83	-47.34
102.63	-47.50
103.43	-47.35
104.23	-47.22
105.03	-47.49
105.84	-47.32
106.64	-47.36
107.44	-47.47
108.24	-47.33
109.04	-47.06
109.84	-47.19
110.65	-47.05
111.45	-47.20
112.25	-47.40
113.05	-47.36
113.85	-47.36
114.66	-47.25
115.46	-47.26
116.26	-47.42
117.06	-47.17
117.86	-47.24
118.66	-47.35
119.47	-47.17
120.27	-46.97
121.07	-47.36
121.87	-47.46
122.67	-47.19
123.47	-47.29
124.28	-47.41
125.08	-47.26
125.88	-47.56
126.68	-47.33
127.48	-47.23

Phase (deg)	Magnitude (dB)
128.29	-47.54
129.09	-47.50
129.89	-47.26
130.69	-47.34
131.49	-47.39
132.29	-47.34
133.10	-47.34
133.90	-47.16
134.70	-47.19
135.50	-47.61
136.30	-47.32
137.11	-47.35
137.91	-47.29
138.71	-47.75
139.51	-47.39
140.31	-47.32
141.11	-47.59
141.92	-47.40
142.72	-47.16
143.52	-47.31
144.32	-47.66
145.12	-47.42
145.92	-47.47
146.73	-47.57
147.53	-47.54
148.33	-47.21
149.13	-47.53
149.93	-47.18
150.74	-47.31
151.54	-47.65
152.34	-47.75
153.14	-47.45
153.94	-47.48
154.74	-47.74
155.55	-47.58
156.35	-47.64
157.15	-47.78
157.95	-47.48
158.75	-47.57
159.56	-47.36

Phase (deg)	Magnitude (dB)
160.36	-47.54
161.16	-47.76
161.96	-47.70
162.76	-47.57
163.56	-47.82
164.37	-47.40
165.17	-47.96
165.97	-47.56
166.77	-47.73
167.57	-47.69
168.37	-47.75
169.18	-47.70
169.98	-47.70
170.78	-47.71
171.58	-47.67
172.38	-47.94
173.19	-47.82
173.99	-48.03
174.79	-47.89
175.59	-47.65
176.39	-47.89
177.19	-47.86
178.00	-47.86
178.80	-47.87
179.60	-48.10
180.40	-47.86
181.20	-47.89
182.00	-47.95
182.81	-48.02
183.61	-48.01
184.41	-48.11
185.21	-48.04
186.01	-48.16
186.82	-48.01
187.62	-47.88
188.42	-48.28
189.22	-48.24
190.02	-47.99
190.82	-47.88
191.63	-48.14

Phase (deg)	Magnitude (dB)
192.43	-48.32
193.23	-48.55
194.03	-48.41
194.83	-48.34
195.64	-48.43
196.44	-48.46
197.24	-48.68
198.04	-48.48
198.84	-48.70
199.64	-48.87
200.45	-48.68
201.25	-48.66
202.05	-48.67
202.85	-48.85
203.65	-48.76
204.45	-48.73
205.26	-48.75
206.06	-49.39
206.86	-48.93
207.66	-48.96
208.46	-49.06
209.27	-49.06
210.07	-48.94
210.87	-49.20
211.67	-49.10
212.47	-49.31
213.27	-49.16
214.08	-49.02
214.88	-49.51
215.68	-49.63
216.48	-49.41
217.28	-49.34
218.09	-49.63
218.89	-49.52
219.69	-49.37
220.49	-49.23
221.29	-49.95
222.09	-49.42
222.90	-49.69
223.70	-50.19

Phase (deg)	Magnitude (dB)
224.50	-49.68
225.30	-50.11
226.10	-49.49
226.90	-49.96
227.71	-50.09
228.51	-49.73
229.31	-49.86
230.11	-49.97
230.91	-50.63
231.72	-50.32
232.52	-50.45
233.32	-50.75
234.12	-50.66
234.92	-50.10
235.72	-50.89
236.53	-50.95
237.33	-50.88
238.13	-51.15
238.93	-50.92
239.73	-50.78
240.54	-50.91
241.34	-50.79
242.14	-51.16
242.94	-51.15
243.74	-51.03
244.54	-51.21
245.35	-51.43
246.15	-51.07
246.95	-51.22
247.75	-51.15
248.55	-50.97
249.35	-51.26
250.16	-51.42
250.96	-51.29
251.76	-51.56
252.56	-51.57
253.36	-51.34
254.17	-51.54
254.97	-51.13
255.77	-51.34

Phase (deg)	Magnitude (dB)
256.57	-51.30
257.37	-51.86
258.17	-51.23
258.98	-51.21
259.78	-51.53
260.58	-51.60
261.38	-51.60
262.18	-51.35
262.98	-51.29
263.79	-51.49
264.59	-51.62
265.39	-51.48
266.19	-51.36
266.99	-51.43
267.80	-51.50
268.60	-51.15
269.40	-51.11
270.20	-51.51
271.00	-51.06
271.80	-51.67
272.61	-51.29
273.41	-51.33
274.21	-51.57
275.01	-51.33
275.81	-51.38
276.62	-51.36
277.42	-51.56
278.22	-51.22
279.02	-51.17
279.82	-50.60
280.62	-51.27
281.43	-50.83
282.23	-51.31
283.03	-50.80
283.83	-50.93
284.63	-50.72
285.43	-51.24
286.24	-51.28
287.04	-51.12
287.84	-50.91

Phase (deg)	Magnitude (dB)
288.64	-50.67
289.44	-50.51
290.25	-50.93
291.05	-50.94
291.85	-50.70
292.65	-51.31
293.45	-50.65
294.25	-50.91
295.06	-50.67
295.86	-50.72
296.66	-50.53
297.46	-50.54
298.26	-50.53
299.07	-50.61
299.87	-50.39
300.67	-50.60
301.47	-50.26
302.27	-50.32
303.07	-50.49
303.88	-50.29
304.68	-50.07
305.48	-50.34
306.28	-50.04
307.08	-50.26
307.88	-50.21
308.69	-49.89
309.49	-50.31
310.29	-49.95
311.09	-50.19
311.89	-49.72
312.70	-49.98
313.50	-50.23
314.30	-49.83
315.10	-49.86
315.90	-50.05
316.70	-50.00
317.51	-50.07
318.31	-49.90
319.11	-50.11
319.91	-49.82

Phase (deg)	Magnitude (dB)
320.71	-49.76
321.51	-49.84
322.32	-49.89
323.12	-49.84
323.92	-50.18
324.72	-49.98
325.52	-49.84
326.33	-49.68
327.13	-49.55
327.93	-49.84
328.73	-49.71
329.53	-49.80
330.33	-49.91
331.14	-49.33
331.94	-49.71
332.74	-49.41
333.54	-49.32
334.34	-49.56
335.15	-49.70
335.95	-49.49
336.75	-49.81
337.55	-49.83
338.35	-49.57
339.15	-49.46
339.96	-49.76
340.76	-49.33
341.56	-49.60
342.36	-49.33
343.16	-49.40
343.96	-49.31
344.77	-49.76
345.57	-49.28
346.37	-49.42
347.17	-49.47
347.97	-49.76
348.78	-49.41
349.58	-49.38
350.38	-49.46
351.18	-49.31
351.98	-49.66

Phase (deg)	Magnitude (dB)
352.78	-49.53
353.59	-49.18
354.39	-49.45
355.19	-49.52
355.99	-49.40
356.79	-49.44
357.60	-49.56
358.40	-49.74
359.20	-49.26
360.00	-49.97

Appendix 9 - Dataset of gain and radiation pattern measurement on case D

Horizontal E-field co-polarization

Phase (deg)	Magnitude (dB)	Phase (deg)	Magnitude (dB)	Phase (deg)	Magnitude (dB)	Phase (deg)	Magnitude (dB)
0.00	-59.53	32.07	-57.84	64.14	-61.30	96.21	-65.89
0.80	-59.06	32.87	-58.23	64.94	-60.54	97.02	-66.28
1.60	-59.15	33.68	-57.65	65.75	-62.19	97.82	-64.53
2.41	-59.10	34.48	-57.81	66.55	-61.81	98.62	-65.51
3.21	-58.97	35.28	-57.77	67.35	-61.94	99.42	-65.37
4.01	-59.54	36.08	-57.75	68.15	-61.57	100.22	-65.07
4.81	-58.79	36.88	-57.91	68.95	-62.37	101.02	-64.60
5.61	-58.55	37.68	-57.81	69.76	-62.95	101.83	-64.09
6.41	-58.68	38.49	-58.31	70.56	-63.04	102.63	-64.13
7.22	-58.74	39.29	-58.65	71.36	-62.47	103.43	-64.27
8.02	-58.37	40.09	-58.19	72.16	-63.08	104.23	-63.76
8.82	-58.42	40.89	-58.44	72.96	-63.32	105.03	-64.11
9.62	-58.62	41.69	-58.27	73.76	-63.57	105.84	-63.76
10.42	-58.32	42.49	-58.24	74.57	-63.44	106.64	-62.64
11.23	-58.06	43.30	-58.38	75.37	-63.85	107.44	-63.03
12.03	-58.40	44.10	-58.56	76.17	-64.33	108.24	-62.68
12.83	-58.38	44.90	-58.67	76.97	-64.07	109.04	-62.80
13.63	-58.86	45.70	-58.41	77.77	-64.13	109.84	-61.98
14.43	-58.45	46.50	-58.55	78.58	-64.69	110.65	-62.08
15.23	-58.39	47.31	-58.40	79.38	-64.34	111.45	-62.39
16.04	-58.39	48.11	-58.49	80.18	-65.75	112.25	-61.42
16.84	-58.10	48.91	-58.91	80.98	-66.36	113.05	-61.69
17.64	-58.35	49.71	-59.33	81.78	-64.98	113.85	-62.00
18.44	-58.02	50.51	-59.29	82.58	-66.01	114.66	-61.08
19.24	-58.03	51.31	-59.25	83.39	-66.21	115.46	-61.47
20.05	-57.95	52.12	-59.27	84.19	-66.25	116.26	-60.83
20.85	-57.69	52.92	-59.57	84.99	-66.23	117.06	-60.97
21.65	-57.98	53.72	-59.02	85.79	-67.15	117.86	-60.57
22.45	-57.76	54.52	-59.87	86.59	-66.80	118.66	-60.54
23.25	-57.84	55.32	-59.56	87.39	-66.79	119.47	-60.67
24.05	-57.86	56.13	-59.73	88.20	-67.48	120.27	-60.25
24.86	-57.93	56.93	-59.91	89.00	-67.00	121.07	-59.72
25.66	-57.59	57.73	-60.04	89.80	-67.51	121.87	-60.25
26.46	-58.22	58.53	-60.20	90.60	-67.15	122.67	-59.91
27.26	-58.20	59.33	-60.02	91.40	-66.08	123.47	-59.51
28.06	-57.75	60.13	-60.48	92.21	-66.47	124.28	-59.38
28.86	-57.88	60.94	-60.33	93.01	-66.01	125.08	-59.59
29.67	-58.11	61.74	-60.89	93.81	-66.36	125.88	-59.29
30.47	-58.16	62.54	-60.92	94.61	-65.84	126.68	-59.17
31.27	-58.22	63.34	-60.99	95.41	-65.87	127.48	-59.63

Phase (deg)	Magnitude (dB)
128.29	-59.34
129.09	-59.06
129.89	-59.75
130.69	-59.44
131.49	-58.35
132.29	-58.78
133.10	-59.02
133.90	-59.07
134.70	-58.65
135.50	-58.53
136.30	-58.72
137.11	-58.77
137.91	-58.13
138.71	-58.37
139.51	-58.51
140.31	-58.29
141.11	-58.37
141.92	-58.49
142.72	-58.24
143.52	-58.72
144.32	-58.44
145.12	-58.58
145.92	-58.30
146.73	-58.26
147.53	-58.17
148.33	-58.34
149.13	-58.27
149.93	-58.15
150.74	-58.21
151.54	-58.36
152.34	-58.45
153.14	-58.38
153.94	-58.40
154.74	-58.10
155.55	-58.38
156.35	-58.60
157.15	-58.07
157.95	-58.39
158.75	-58.69
159.56	-58.01

Phase (deg)	Magnitude (dB)
160.36	-58.70
161.16	-58.78
161.96	-58.22
162.76	-58.43
163.56	-58.49
164.37	-58.84
165.17	-58.64
165.97	-58.35
166.77	-58.43
167.57	-58.33
168.37	-58.66
169.18	-59.10
169.98	-58.85
170.78	-58.73
171.58	-58.39
172.38	-58.59
173.19	-58.55
173.99	-58.66
174.79	-59.02
175.59	-58.97
176.39	-59.05
177.19	-58.81
178.00	-59.28
178.80	-59.16
179.60	-58.93
180.40	-58.63
181.20	-58.95
182.00	-58.79
182.81	-58.69
183.61	-59.01
184.41	-59.31
185.21	-59.42
186.01	-58.60
186.82	-58.96
187.62	-59.40
188.42	-59.28
189.22	-59.07
190.02	-59.52
190.82	-60.09
191.63	-59.25

Phase (deg)	Magnitude (dB)
192.43	-58.74
193.23	-59.20
194.03	-59.12
194.83	-59.08
195.64	-58.95
196.44	-59.19
197.24	-59.31
198.04	-59.34
198.84	-59.00
199.64	-59.18
200.45	-59.41
201.25	-59.41
202.05	-59.29
202.85	-59.71
203.65	-59.64
204.45	-59.33
205.26	-59.48
206.06	-59.36
206.86	-59.46
207.66	-58.83
208.46	-59.50
209.27	-59.22
210.07	-59.90
210.87	-59.24
211.67	-59.53
212.47	-59.11
213.27	-59.23
214.08	-59.30
214.88	-58.79
215.68	-59.28
216.48	-59.16
217.28	-59.40
218.09	-58.87
218.89	-59.64
219.69	-58.99
220.49	-58.97
221.29	-58.83
222.09	-58.99
222.90	-58.92
223.70	-59.02

Phase (deg)	Magnitude (dB)
224.50	-59.05
225.30	-58.85
226.10	-59.15
226.90	-58.92
227.71	-58.88
228.51	-58.90
229.31	-58.79
230.11	-58.68
230.91	-59.12
231.72	-59.14
232.52	-58.99
233.32	-58.82
234.12	-58.64
234.92	-58.88
235.72	-58.85
236.53	-58.66
237.33	-59.09
238.13	-58.93
238.93	-58.67
239.73	-58.70
240.54	-58.62
241.34	-59.05
242.14	-58.49
242.94	-59.07
243.74	-58.86
244.54	-59.27
245.35	-59.07
246.15	-59.34
246.95	-58.88
247.75	-59.45
248.55	-58.70
249.35	-59.15
250.16	-58.82
250.96	-59.02
251.76	-58.88
252.56	-59.26
253.36	-59.01
254.17	-59.15
254.97	-59.12
255.77	-59.07

Phase (deg)	Magnitude (dB)
256.57	-59.01
257.37	-59.26
258.17	-59.17
258.98	-59.26
259.78	-58.95
260.58	-59.19
261.38	-59.27
262.18	-59.06
262.98	-59.05
263.79	-59.31
264.59	-59.14
265.39	-59.20
266.19	-59.26
266.99	-59.41
267.80	-59.19
268.60	-59.55
269.40	-59.47
270.20	-59.43
271.00	-59.20
271.80	-59.92
272.61	-59.63
273.41	-59.68
274.21	-60.24
275.01	-59.81
275.81	-60.02
276.62	-60.20
277.42	-59.93
278.22	-60.00
279.02	-60.56
279.82	-60.49
280.62	-60.31
281.43	-60.33
282.23	-59.92
283.03	-60.93
283.83	-60.68
284.63	-60.91
285.43	-60.76
286.24	-60.87
287.04	-61.09
287.84	-60.94

Phase (deg)	Magnitude (dB)
288.64	-61.15
289.44	-61.63
290.25	-61.46
291.05	-61.55
291.85	-62.30
292.65	-61.88
293.45	-62.25
294.25	-62.69
295.06	-62.75
295.86	-62.40
296.66	-61.80
297.46	-63.25
298.26	-62.54
299.07	-62.68
299.87	-63.21
300.67	-63.23
301.47	-63.49
302.27	-63.38
303.07	-64.19
303.88	-64.10
304.68	-64.13
305.48	-64.17
306.28	-64.42
307.08	-64.65
307.88	-64.86
308.69	-64.59
309.49	-65.95
310.29	-66.29
311.09	-65.72
311.89	-65.83
312.70	-66.05
313.50	-66.32
314.30	-66.74
315.10	-67.34
315.90	-66.27
316.70	-68.15
317.51	-68.00
318.31	-66.38
319.11	-66.72
319.91	-67.55

Phase (deg)	Magnitude (dB)
320.71	-67.06
321.51	-67.26
322.32	-67.36
323.12	-66.94
323.92	-67.07
324.72	-66.74
325.52	-67.23
326.33	-66.31
327.13	-66.65
327.93	-66.62
328.73	-66.36
329.53	-66.94
330.33	-66.32
331.14	-66.56
331.94	-65.73
332.74	-65.63
333.54	-65.56
334.34	-65.81
335.15	-64.49
335.95	-64.92
336.75	-64.20
337.55	-64.11
338.35	-64.87
339.15	-64.10
339.96	-64.12
340.76	-63.65
341.56	-63.39
342.36	-63.06
343.16	-63.67
343.96	-62.61
344.77	-62.43
345.57	-61.85
346.37	-61.81
347.17	-61.96
347.97	-61.94
348.78	-61.38
349.58	-61.00
350.38	-61.07
351.18	-60.84
351.98	-61.28

Phase (deg)	Magnitude (dB)
352.78	-60.74
353.59	-60.45
354.39	-60.10
355.19	-60.42
355.99	-59.90
356.79	-60.11
357.60	-59.97
358.40	-59.88
359.20	-59.46
360.00	-59.86

Vertical E-field co-polarization

Phase (deg)	Magnitude (dB)
0.00	-55.01
0.80	-55.14
1.60	-55.14
2.41	-55.42
3.21	-55.25
4.01	-55.11
4.81	-54.98
5.61	-55.55
6.41	-55.07
7.22	-55.51
8.02	-55.22
8.82	-55.80
9.62	-55.49
10.42	-55.54
11.23	-55.57
12.03	-55.93
12.83	-55.86
13.63	-55.81
14.43	-55.63
15.23	-55.80
16.04	-55.91
16.84	-55.80
17.64	-56.09
18.44	-56.11
19.24	-56.26
20.05	-56.06
20.85	-56.21
21.65	-55.92
22.45	-56.13
23.25	-56.13
24.05	-56.01
24.86	-56.46
25.66	-56.88
26.46	-56.50
27.26	-56.54
28.06	-56.81
28.86	-56.85
29.67	-56.84
30.47	-56.96
31.27	-56.55

Phase (deg)	Magnitude (dB)
32.07	-56.65
32.87	-56.64
33.68	-56.42
34.48	-56.52
35.28	-56.60
36.08	-57.05
36.88	-56.74
37.68	-56.67
38.49	-56.84
39.29	-57.08
40.09	-56.54
40.89	-57.06
41.69	-57.13
42.49	-57.09
43.30	-56.78
44.10	-56.71
44.90	-56.93
45.70	-56.99
46.50	-57.31
47.31	-57.52
48.11	-57.18
48.91	-57.32
49.71	-56.98
50.51	-57.60
51.31	-57.59
52.12	-57.63
52.92	-57.55
53.72	-57.53
54.52	-57.74
55.32	-57.41
56.13	-57.54
56.93	-57.64
57.73	-57.87
58.53	-57.91
59.33	-57.64
60.13	-57.65
60.94	-57.87
61.74	-57.62
62.54	-57.35
63.34	-57.85

Phase (deg)	Magnitude (dB)
64.14	-57.62
64.94	-57.57
65.75	-57.93
66.55	-57.65
67.35	-57.93
68.15	-57.45
68.95	-57.37
69.76	-57.64
70.56	-58.12
71.36	-57.83
72.16	-58.05
72.96	-57.90
73.76	-57.72
74.57	-57.69
75.37	-57.81
76.17	-57.85
76.97	-57.62
77.77	-57.59
78.58	-57.75
79.38	-57.74
80.18	-57.96
80.98	-57.94
81.78	-57.69
82.58	-57.64
83.39	-57.59
84.19	-57.28
84.99	-57.74
85.79	-57.71
86.59	-57.87
87.39	-57.88
88.20	-57.63
89.00	-57.55
89.80	-57.35
90.60	-57.44
91.40	-57.60
92.21	-57.33
93.01	-57.74
93.81	-57.45
94.61	-57.47
95.41	-57.32

Phase (deg)	Magnitude (dB)
96.21	-57.36
97.02	-57.84
97.82	-57.58
98.62	-57.71
99.42	-57.51
100.22	-57.60
101.02	-57.45
101.83	-57.40
102.63	-57.13
103.43	-57.44
104.23	-57.08
105.03	-57.22
105.84	-57.43
106.64	-56.90
107.44	-57.02
108.24	-57.43
109.04	-57.12
109.84	-57.14
110.65	-57.25
111.45	-57.25
112.25	-57.29
113.05	-57.43
113.85	-57.31
114.66	-57.34
115.46	-57.16
116.26	-57.13
117.06	-56.68
117.86	-56.88
118.66	-56.82
119.47	-57.12
120.27	-57.28
121.07	-57.11
121.87	-56.86
122.67	-56.86
123.47	-56.84
124.28	-57.27
125.08	-56.94
125.88	-56.68
126.68	-56.59
127.48	-56.57

Phase (deg)	Magnitude (dB)
128.29	-56.33
129.09	-56.50
129.89	-56.40
130.69	-56.76
131.49	-56.30
132.29	-56.43
133.10	-56.47
133.90	-56.67
134.70	-56.25
135.50	-56.46
136.30	-56.14
137.11	-56.26
137.91	-56.12
138.71	-56.19
139.51	-55.78
140.31	-56.05
141.11	-55.79
141.92	-56.02
142.72	-56.14
143.52	-56.27
144.32	-55.68
145.12	-56.09
145.92	-55.70
146.73	-55.63
147.53	-55.80
148.33	-55.66
149.13	-55.52
149.93	-55.37
150.74	-55.63
151.54	-55.77
152.34	-55.61
153.14	-55.65
153.94	-55.13
154.74	-55.59
155.55	-55.52
156.35	-55.36
157.15	-55.67
157.95	-55.22
158.75	-55.22
159.56	-55.41

Phase (deg)	Magnitude (dB)
160.36	-55.18
161.16	-55.13
161.96	-55.03
162.76	-54.96
163.56	-55.15
164.37	-55.35
165.17	-55.03
165.97	-54.95
166.77	-54.78
167.57	-54.74
168.37	-54.72
169.18	-55.10
169.98	-54.80
170.78	-54.69
171.58	-54.84
172.38	-54.51
173.19	-54.95
173.99	-54.44
174.79	-54.60
175.59	-54.64
176.39	-54.47
177.19	-54.59
178.00	-54.44
178.80	-54.17
179.60	-54.29
180.40	-54.47
181.20	-54.48
182.00	-54.64
182.81	-54.36
183.61	-54.33
184.41	-54.36
185.21	-54.32
186.01	-54.32
186.82	-54.24
187.62	-54.41
188.42	-54.28
189.22	-54.16
190.02	-54.11
190.82	-54.01
191.63	-54.02

Phase (deg)	Magnitude (dB)
192.43	-54.10
193.23	-53.87
194.03	-54.03
194.83	-54.09
195.64	-53.88
196.44	-53.88
197.24	-53.59
198.04	-53.82
198.84	-53.86
199.64	-53.68
200.45	-53.94
201.25	-53.66
202.05	-54.05
202.85	-53.55
203.65	-53.74
204.45	-53.43
205.26	-53.52
206.06	-53.81
206.86	-53.66
207.66	-53.44
208.46	-53.47
209.27	-53.49
210.07	-53.41
210.87	-53.33
211.67	-53.21
212.47	-53.29
213.27	-53.56
214.08	-53.37
214.88	-53.32
215.68	-53.08
216.48	-53.29
217.28	-53.34
218.09	-53.33
218.89	-53.08
219.69	-53.01
220.49	-53.28
221.29	-52.90
222.09	-53.01
222.90	-53.07
223.70	-53.05

Phase (deg)	Magnitude (dB)
224.50	-53.10
225.30	-52.89
226.10	-52.97
226.90	-52.87
227.71	-52.98
228.51	-53.00
229.31	-53.09
230.11	-52.94
230.91	-52.84
231.72	-52.88
232.52	-52.72
233.32	-52.76
234.12	-52.94
234.92	-52.96
235.72	-52.78
236.53	-52.93
237.33	-52.84
238.13	-52.85
238.93	-52.95
239.73	-52.84
240.54	-52.82
241.34	-52.77
242.14	-52.79
242.94	-52.75
243.74	-52.76
244.54	-52.81
245.35	-52.69
246.15	-52.81
246.95	-52.58
247.75	-52.80
248.55	-52.73
249.35	-52.81
250.16	-52.57
250.96	-52.85
251.76	-52.50
252.56	-52.82
253.36	-52.88
254.17	-52.83
254.97	-52.74
255.77	-52.58

Phase (deg)	Magnitude (dB)
256.57	-52.77
257.37	-52.75
258.17	-52.52
258.98	-52.62
259.78	-52.81
260.58	-52.79
261.38	-52.77
262.18	-52.69
262.98	-52.63
263.79	-52.57
264.59	-52.59
265.39	-52.63
266.19	-52.64
266.99	-52.60
267.80	-52.74
268.60	-52.65
269.40	-52.76
270.20	-52.82
271.00	-52.52
271.80	-52.63
272.61	-52.62
273.41	-52.72
274.21	-52.66
275.01	-52.78
275.81	-52.85
276.62	-52.59
277.42	-52.84
278.22	-52.78
279.02	-52.74
279.82	-52.82
280.62	-53.12
281.43	-52.74
282.23	-52.86
283.03	-52.80
283.83	-52.62
284.63	-52.74
285.43	-52.84
286.24	-52.79
287.04	-52.92
287.84	-53.06

Phase (deg)	Magnitude (dB)
288.64	-53.00
289.44	-53.08
290.25	-52.87
291.05	-52.90
291.85	-52.78
292.65	-53.20
293.45	-52.83
294.25	-52.95
295.06	-53.03
295.86	-53.02
296.66	-53.00
297.46	-52.91
298.26	-52.89
299.07	-52.84
299.87	-53.04
300.67	-53.24
301.47	-52.81
302.27	-52.99
303.07	-53.02
303.88	-53.12
304.68	-53.04
305.48	-53.17
306.28	-53.03
307.08	-53.10
307.88	-53.07
308.69	-52.99
309.49	-52.99
310.29	-53.24
311.09	-53.35
311.89	-53.22
312.70	-53.10
313.50	-53.04
314.30	-53.06
315.10	-53.14
315.90	-53.43
316.70	-53.46
317.51	-53.32
318.31	-53.45
319.11	-53.24
319.91	-53.34

Phase (deg)	Magnitude (dB)
320.71	-53.81
321.51	-53.52
322.32	-53.59
323.12	-53.64
323.92	-53.88
324.72	-53.57
325.52	-53.54
326.33	-53.71
327.13	-53.88
327.93	-53.84
328.73	-53.38
329.53	-53.83
330.33	-54.26
331.14	-54.02
331.94	-53.88
332.74	-53.89
333.54	-54.01
334.34	-54.16
335.15	-54.05
335.95	-54.11
336.75	-54.17
337.55	-54.10
338.35	-53.98
339.15	-54.03
339.96	-54.28
340.76	-54.07
341.56	-54.36
342.36	-54.30
343.16	-54.24
343.96	-54.33
344.77	-54.73
345.57	-54.86
346.37	-54.74
347.17	-54.89
347.97	-54.57
348.78	-54.65
349.58	-54.71
350.38	-54.50
351.18	-54.83
351.98	-54.86

Phase (deg)	Magnitude (dB)
352.78	-54.91
353.59	-54.71
354.39	-54.74
355.19	-54.79
355.99	-54.89
356.79	-54.69
357.60	-54.58
358.40	-54.71
359.20	-54.89
360.00	-54.69